

Characterisation of woodwind instrument reed (*Arundo donax L*) degradation and mechanical behaviour

Connor Kemp



Computational Acoustic Modeling Laboratory – Music Technology Area

Department of Music Research, Schulich School of Music

McGill University

Montreal, Quebec, Canada

March 2019

A thesis submitted to McGill University in partial fulfillment of the requirements
for the degree of Doctor of Philosophy

© 2019 Connor Kemp

Abstract

In the present study, reeds and reed material *Arundo donax L* are evaluated in a long-term degradation study. Investigations into the macroscopic and microscopic behaviour of reeds suggests several deterioration mechanisms. Results can be used to inform manufacturers as to methods by which product quality control could be improved. The anatomical and material properties evaluated could be used to inform the design of synthetic reeds exhibiting more authentic static and dynamic behaviour.

Spatially dependent bending stiffness is analysed for reeds over their useful life and compared with objective rankings by a professional musician. Characterisation of cross-sectional anatomical structures is also performed. Objective measurements from the musician's set are compared with a larger set of reeds of various manufacturer rating. Experimental techniques include cantilever bending testing, optical microscopy and image analysis. Results show a stark decrease in bending stiffness with increasing reed age and overall stiffness is shown to be accurately predicted by the spatial density of specific anatomical structures. A model is developed to predict reed stiffness with improved accuracy over manufacturer methods. The musician's rankings are also found to be dependent on stiffness asymmetry, illustrating the importance of more accurate stiffness characterisation.

Evaluation of reed degradation at multiple length scales is performed using a series of material characterisation methods. Experiments are performed on new and used reed samples, as well as on raw *Arundo donax L* samples. Nanoindentation results show differences in the nano-mechanical behaviour of anatomical structures tested in the longitudinal direction (cross-section) of samples. Elasticity and viscoelasticity are assessed, specifically. The behaviour of the two structures of interest is found to depend on exposure to moisture cycles, and each exhibit fundamentally different trends with increasing moisture exposure. Changes in elasticity and viscoelasticity are associated with chemical degradation of different *Arundo* phases in the cell wall. Significant differences between new and used samples are found in terms of chemical constituents, and results are compared with a control sample to verify findings. These material property changes are thought to contribute to changing damping properties, measured macroscopically.

In-situ swelling of *Arundo donax L* is analysed using micro-computed tomography at different relative humidity. The effects of moisture cycling on anatomical morphology are also considered during this experiment. *Arundo donax L* swelling is found to be linearly dependent on relative humidity, with little difference in tangential and radial swelling. Longitudinal swelling is comparatively negligible. Swelling in the tangential-radial plane is highly heterogeneous and large local strains surrounding specific anatomical structures suggests one mechanism for matrix deterioration during reed aging. Image analysis on tomographic stacks shows a loss of matrix material with increasing exposure to moisture cycles. Morphological changes are also noted and are primarily confined to the matrix material. The macroscopic impact of these changes is discussed in the context of bending stiffness of real reeds.

Résumé

Dans cette étude, la qualité des anches d'instruments provenant de la canne de Provence (*Arundo donax L*), est étudiée lors d'une dégradation à long terme. L'analyse du comportement macroscopique et microscopique des roseaux suggèrent plusieurs mécanismes de détérioration. Les résultats peuvent être utilisés par les fabricants pour identifier des méthodes permettant d'améliorer le contrôle de la qualité des anches. Les propriétés anatomiques et matérielles étudiées pourraient être utilisées pour la conception d'anches synthétiques pour qu'ils présentent un comportement statique et dynamique plus authentique et réaliste.

La rigidité à la flexion dépendante de la dimension spatiale est analysée pour les anches au cours de leur vie utile et comparée aux classements objectifs réalisés par un musicien professionnel. La caractérisation des structures anatomiques transversales est également effectuée. Les mesures objectives de l'ensemble du musicien sont comparées à une sélection diverse d'anches de différentes qualités. Les techniques expérimentales comprennent les essais de flexion en porte-à-faux, la microscopie optique et l'analyse d'images. Les résultats montrent une diminution de la rigidité à la flexion avec l'augmentation de l'âge des anches et la rigidité spatiale de structures anatomiques spécifiques permet de prédire avec précision la rigidité globale. Un modèle est développé pour prédire la rigidité des anches avec une précision améliorée par rapport aux méthodes du fabricant. Les classements du musicien sont également dépendant de l'asymétrie de la rigidité, illustrant l'importance d'une caractérisation plus précise de la rigidité.

L'évaluation de la dégradation des anches à plusieurs échelles de longueur est réalisée à l'aide d'une série de méthodes de caractérisation des matériaux. Les expériences sont effectuées sur des échantillons d'anches neufs et usagés, ainsi que sur des échantillons bruts d'*Arundo Donax*. Les résultats au niveau du nano-indentation montrent des différences dans le comportement nano-mécanique des structures anatomiques testées dans la direction longitudinale (coupe transversale) des échantillons. Spécifiquement, l'élasticité et la viscoélasticité sont évaluées. Le comportement des deux structures concernées dépend de l'exposition aux cycles d'humidité et chacune présente des tendances fondamentalement différentes avec une exposition accrue à l'humidité. Les changements d'élasticité et de viscoélasticité sont associés à la dégradation chimique de différentes phases d'*Arundo* dans la paroi cellulaire. Des différences significatives

entre les échantillons nouveaux et utilisés sont constatées en termes de constituants chimiques, et les résultats sont comparés à un échantillon témoin pour vérifier les résultats. Ces modifications des propriétés des matériaux contribueraient à modifier les propriétés d'étouffement, mesurées macroscopiquement.

Le gonflement in situ d'Arundo Donax est analysé en utilisant une tomodesitométrie micro-calculée à différents degrés d'humidité relative. Les effets du cycle d'humidité et séchage sur la morphologie anatomique sont également pris en compte lors de cette étude. Le gonflement d'Arundo est dépendant linéairement de l'humidité relative, avec peu de différence dans le gonflement tangentiel et radial. Le gonflement longitudinal est comparativement négligeable. Le gonflement dans le plan tangentiel-radial est très hétérogène et des tensions locales entourent des structures anatomiques spécifiques suggérant un mécanisme de détérioration de la matrice pendant le vieillissement des roseaux. L'analyse d'images sur des piles tomographiques montre une perte de matériau provenant de la matrice lors d'une exposition croissante aux cycles d'humidité. Les modifications morphologiques sont également notées et se limitent principalement au matériau de la matrice. L'impact macroscopique de ces changements est discuté dans le contexte de la rigidité à la flexion des anches.

Acknowledgements

The author is very grateful to the many people that have aided and contributed to this work in some way. It is only through the fruitful interactions with colleagues, technicians and others around McGill and abroad that this thesis was possible. Firstly, I would like to give many thanks to my supervisor, Dr. Gary Scavone. He was willing to take on a new student venturing into a project that would require expertise in many areas. The success of this work rests on his guidance and support. I would also like to thank the students at CAML who have been a pleasure to work with, and for their time in discussing the many intricacies of experimental work. The Music Technology Area and CIRMMT have also provided support in this endeavour, facilitating travel that lead to meetings and collaborative work that form significant components of this thesis. Several other labs at McGill have provided the use of equipment and space without which many experiments would not have been possible. Dr.'s Francois Barthelat and Larry Lessard of the Mechanical Engineering Department provided the use of their labs and helpful discussions in various aspects of this work. Dr. Richard Chromik of the Materials Engineering Department facilitated meetings with himself and members of his lab and the use of experimental equipment. Dr. Dominique Derome at the Swiss Federal Laboratories for Materials Science (Empa) was willing to host me in her lab after meeting at MRS in Boston. Her support and interest in this study made the results more meaningful and provided an avenue for experimental work that was not initially thought possible. Without the input and help of these people this thesis would not have fulfilled its objectives.

I would also like to acknowledge the various laboratory technicians that aided in experimental setup and sample preparation around McGill. The staff at the Goodman Cancer Research Centre are greatly acknowledged for their efforts in designing a protocol for sample preparation on a material they were seeing for the first time. The students of Luc Mongeau's lab in the Mechanical Engineering Department helped with surface probing techniques and imaging. Petr Fiurasek in the Department of Chemistry provided training and helpful discussions on the chemical characterisation of samples. Stepan Carl at Empa provided support while performing experiments as a visiting researcher there. Daryl Cameron in the Music Technology Area helped with much of the machining work in this thesis and was vital in preparing a computer for data analysis. Thanks to all.

Perhaps the most important people to which success is owed is my family. They have always provided support, despite my best efforts to become a career student. Grandparents on both sides of the family have always given me help and my gratitude cannot be overstated. The close bonds I share with all my family have given me the strength to power through this work. My only regret is that my Poppa has left us prior to the conclusion of this work. I know he would have loved to hear about all of my endeavours despite the endless “book learnin’.” And of course, thank you to Kate Fisher, my wonderful partner who has been privy to all aspects of completing a dissertation. You’ll always be my LF.

Preface and Contribution of Authors

This thesis is presented as a collection of manuscripts from three main studies that were conducted over the duration of the author's PhD studies. During this period the author was supervised by Dr. Gary Scavone of the Computational Acoustic Modeling Laboratory. Experiments were conducted in the labs of several professors at McGill University, including Dr. Francois Barthelat, Dr. Larry Lessard and Dr. Richard Chromik. Additionally, a specialized experimental setup was used for swelling analysis under the direction of Dr. Dominique Derome at the Laboratory for Multiscale Modeling in Building Physics, Swiss Federal Laboratory for Materials Science (Empa) in Zurich, Switzerland. This thesis is presented as a collection of manuscripts for publication in peer-reviewed journals (to be submitted). The detailed contributions of each co-author to the relevant thesis chapters are provided below.

- **Chapter 4**

C. Kemp performed the bending stiffness testing on all reeds and the associated optical microscopy, image analysis and manuscript writing. Sample preparation for microscopy was performed by the histology technicians at the Goodman Cancer Research Centre, McGill University. Manuscript editing was completed by G. Scavone, in addition to supervision of the research project.

- **Chapter 5**

C. Kemp performed all measurements on the samples after relevant training from L. Shang (XRD), R. Zheng (optical profiling and nanoindentation), Y. Zhang (nanoindentation) and P. Fiurasek (TGA). R. Chromik aided with discussions on nanoindentation experimental techniques. The manuscript was written by C. Kemp and edited by G. Scavone and R. Chromik.

- **Chapter 6**

C. Kemp performed the experiment with the help of S. Kolokytha and C. Stefan at the Swiss Federal Laboratory for Materials Science (Empa), Zurich, Switzerland. S. Kolokytha performed ring artifact corrections on the dataset and all subsequent analysis was performed by C. Kemp. D. Derome supervised the research and oversaw

experimental design. The manuscript was written by C. Kemp and edited by S. Kolokytha, D. Derome and G. Scavone.

- **Appendix A**

This study was performed as an exploratory investigation into the vibrational degradation of Arundo Donax samples. G. Scavone supervised the research and edited the manuscript (written by C. Kemp). This manuscript is published as follows:

Kemp, C. and Scavone, G. (2017) "Microstructure Contributions to Vibrational Damping and Identification of Damage Mechanisms in Arundo Donax L: Reed Cane for Woodwind Instruments." Materials Research Society Advances, Feb. 2017, DOI: 10.1557/adv.2017.223, pp. 1–20.

Notable Conference Contributions

The following research items represent conference contributions that are not otherwise discussed in this thesis. These projects were used as a proof-of-concept for many of the experiments that constitute this dissertation. Discussions with colleagues and acquaintances were very fruitful in these situations.

- Kemp, C. and Scavone, G. "Vibrational analysis of arundo donax L (woodwind reed cane) through internal friction measurements and microstructure evaluation" In *Proceedings of the 22nd International Congress on Acoustics*, vol. 28, no. 1, Buenos Aires, Argentina, 5-9 September 2016, POMA-D-17-00030 (accepted January 27th 2017).
- *Symposium on the Acoustic of Poro-elastic Materials, December 16th – 18th 2014, KTH, Stockholm, Sweden (International)*
Kemp, C. and Scavone, G. (2014) Observing stiffness variation in reed cane (Arundo Donax L) and the resulting frequency and flexural response (reviewed oral presentation)

Table of Contents

Abstract	i
Résumé	iii
Acknowledgements	v
Preface and Contribution of Authors	vii
Notable Conference Contributions	viii
1 Introduction and Objectives	1
1.1 Organisation of Thesis	3
2 Literature Review	5
2.1 Microstructure and the Cell Wall in Wood-Type Materials	5
2.2 Reed/Wood Microstructural Characterisation.....	9
2.3 Considerations for Arundo Material Microstructure Models and Degradation	21
2.4 Dynamic Testing of Wood Type Materials	24
3 Experimental Techniques	27
3.1 Samples and Sample Preparation	27
3.2 Experimental Setup – Additional Information.....	30
3.3 Image Analysis.....	32
4 Static Bending Stiffness and Aging Behaviour of Alto Saxophone Reeds: A Practical and Anatomical Approach	33
4.1 Introduction.....	34
4.1.1 Background and Motivation	34
4.1.2 Arundo donax L	35
4.1.3 Anatomical Structures and Quality.....	37
4.1.4 Static Stiffness	37
4.1.5 Degradation and Tip-Stiffness Importance.....	38

4.1.6	Summary	39
4.2	Experimental Design.....	39
4.2.1	Materials and Samples	39
4.2.2	Objective Stiffness Testing.....	39
4.2.3	Perceived Stiffness Testing	41
4.2.4	Bending Stiffness Measurements	42
4.2.5	Microstructure and Anatomical Evaluation.....	43
4.2.6	Comparison Reed Set.....	50
4.3	Results	50
4.3.1	Overall Tip Stiffness.....	50
4.3.2	Subjective Stiffness Evaluation	55
4.3.3	Comparison Reed Set.....	58
4.3.4	Anatomical Structures.....	60
4.3.5	Solid Fiber Density and Distribution.....	67
4.4	Analysis and Discussion.....	70
4.4.1	Bending Stiffness Modeling – Empirical Approach.....	73
4.4.2	Bending Stiffness Modeling – Anatomical Approach.....	77
4.5	Conclusions.....	85
5	Nano-mechanical and material investigations into the viscoelastic behaviour of anatomical structures in Arundo Donax L	87
5.1	Introduction.....	88
5.2	Materials and Methods	90
5.2.1	Background.....	90
5.2.2	Nanoindentation	94
5.2.3	Thermogravimetric Analysis	95

5.2.4	X-ray Diffraction Analysis	95
5.2.5	Internal Friction.....	96
5.2.6	Reed and <i>Arundo donax L</i> Samples.....	96
5.3	Results	98
5.3.1	Reed Heel – Tip Nanoindentation	98
5.3.2	Saturation Cycle Sample Nanoindentation.....	101
5.3.3	X-ray Diffraction Analysis	102
5.3.4	Thermogravimetric Analysis - TGA.....	105
5.4	Discussion.....	108
5.4.1	Reed Heel – Tip Pairs	108
5.4.2	Saturation Cycle Samples.....	109
5.4.3	Solid Fibers and Parenchyma Cells	112
5.4.4	TGA and XRD	116
5.4.5	Internal Friction.....	119
5.5	Conclusions.....	120
5.6	Appendix - Nanoindentation	121
5.6.1	Nanoindentation Modeling	121
5.6.2	Theory – Viscoelastic models.....	122
6	Swelling and Moisture Fatigue Behaviour of Arundo Donax using Micro-Computed Tomography	130
6.1	Introduction and Background.....	131
6.2	Physiology and Properties of Arundo Donax.....	132
6.3	Materials and Methods	136
6.3.1	Image Analysis.....	139
6.4	Results	141

6.5	Discussion.....	158
6.6	Conclusions.....	162
7	Conclusions	164
7.1	Contributions to Original Knowledge.....	166
7.2	Suggestions for Future Work	166
8	References	168
A.	Appendix	179
A.1	Microstructure Contributions to Vibrational Damping and Identification of Damage Mechanisms in Arundo Donax L: Reed Cane for Woodwind Instruments	180
A.2	Introduction.....	181
A.3	Experiment.....	183
A.3.1	Cyclic Mechanical Loading	185
A.3.2	Moisture Cycling.....	185
A.3.3	Internal Friction Measurements	186
A.3.4	Materials Quantification.....	188
A.4	Discussion.....	189
A.4.1	Microstructural Analysis	196
A.5	Summary and Future Work.....	204
A.6	Acknowledgments	206

Chapter 1

1 Introduction and Objectives

Arundo donax L is the natural material used for the manufacture of reeds used on clarinets, saxophones, oboes and bassoons. *Arundo donax L*, known under the vernacular name cane or giant cane or giant reed, is a perennial grass species and member of the Poaceae family that grows rapidly to produce tall (2-3 meter) shoots [1]. These shoots are primarily grown in France and South America and dried for 1 year in ambient conditions after harvesting. *Arundo donax L* has a typical monocotyledonous structure made of randomly distributed vascular bundles surrounded by cells with thick walls, with all these elements embedded in a matrix of soft parenchyma. Reeds are machined from the internode sections of the harvested culm to specific dimensions dictated by the type of reed to be manufactured (i.e., classical, jazz, clarinet, alto saxophone, baritone saxophone etc). The overall dimensions of finished reeds remain consistent for single instrument types, although the vibrating tip of the reed, known as the vamp, differs in thickness and profile.

The vibrational properties of *Arundo donax L* are considered desirable for musical purposes [2]–[4], however the material exhibits several limitations and undesirable characteristics. These include mechanical considerations such as stiffness degradation, changes in damping properties and moisture deterioration due to chemical degradation and geometric warping (from moisture related swelling and shrinkage hysteresis). Environmental effects such as temperature and humidity also contribute to changing reed properties [5]. Synthetic reeds are often used for acoustic experimentation on mouthpiece-instrument systems [6] due to their consistent properties and insensitivity to ambient conditions. It is desirable to combine this environmental insensitivity and improved durability of synthetic materials with the vibrational properties of natural *Arundo donax L*. The material properties that are most important for consistent reed performance are still not well understood, nor are the mechanisms by which these properties change with time. In order to create synthetic reeds in a truly biomimetic manner further research into reed properties, degradation and fatigue behaviour is required.

Although acoustic definitions associated with the description of sound produced by reeds is generally agreed upon by musicians (i.e., brightness and stiffness), their personal preferences vary

[7]. This variance between musicians may be related to the variability in reed behaviour and properties considered above. The general agreement on the definition of acoustic brightness and its association with reed stiffness makes bending stiffness a good candidate for static evaluation of reeds. For clarinet reeds, the dynamic modulus has been linearly related to the static modulus [8], providing further justification for the use of static evaluation of reeds. Static methods are employed by the manufacturer for reed sorting and these methods translate well to manufacturing environments where dynamic tests are too time consuming and/or too difficult to run reliably and repeatably.

Previous research on the anatomical structure of *Arundo donax L* and its relationship to musical quality have either focused on optical characterisation of the microstructure [4], [9], [10], have considered a small set of reeds chemically [3], [11] or have considered the biomechanics of the culm of *Arundo donax L* using a physiological and evolutionary approach [12]. Acoustic characterisation of *Arundo donax L* bars has been considered at various humidity levels [2], although the relationships between damping properties and anatomical structure was limited to measures of sample density. Little is known about the micro- and nano-mechanical properties of the two main anatomical constituents of the *Arundo donax L* culm, the vascular bundles and parenchyma cells, and the degradation of these properties with exposure to moisture is not understood. All of these considerations suggest that a degradation study on the properties of *Arundo donax L* anatomical structures could yield important insight as to the behaviour of real reeds during a typical lifecycle.

The primary objective of this thesis is to quantify the changing anatomical, microstructural, material and mechanical properties that alto saxophone reeds experience during their useful life. Previous research has been limited to new reeds and reed material (*Arundo donax L*) and has not considered changing material properties at multiple length scales. Through this thesis a better understanding of the objective and subjective bending stiffness rankings of alto saxophone reeds during their lifecycle is gained (as played by a professional musician). Evaluation of static bending stiffness is completed using a spatially sensitive method to quantify stiffness heterogeneity across reed tips, an approach that has not previously been utilized. This experiment constitutes the first portion of the thesis. Samples taken from played and un-played reeds are analysed at multiple length scales, including chemical analysis using thermogravimetric methods, nanoindentation on

vascular bundles and parenchyma cells and x-ray diffraction on powdered samples. Each of these techniques yields information regarding the deterioration of anatomical and chemical constituents of reed samples and quantifies the corresponding changes in local mechanical properties (indentation moduli) of these structures. These methodologies and results form the middle part of the thesis. An investigation into the swelling behaviour of *Arundo* material is also undertaken using an in-situ micro-computed tomographic approach, similar to methods previously used for wood [13]–[15]. This type of analysis has not previously been performed on *Arundo donax L* and represents an important step towards understanding the behaviour of fully saturated reeds. This swelling experiment is provided as the final component of the thesis body.

1.1 Organisation of Thesis

This thesis is comprised of six main chapters. An overview of main chapter contents is provided below.

Chapter 2 provides a literature review of pertinent studies on wood type materials and experimentation on *Arundo donax L*. Previous experimental techniques are considered as they relate to the objectives of this thesis. The constituents of wood cell walls are also described due to the similarities between the structure of woody plants and *Arundo donax L*.

Chapter 3 briefly considers some of the details of experimentation from each subsequent chapter. These details were not included in their respective manuscripts for brevity. Specifically, sample preparation techniques for microscopy, nanoindentation and X-ray diffraction are covered. The experimental setup for moisture cycling of samples with regard to in-situ swelling is also described.

Chapter 4 considers the degradation of real reeds as played by a musician and evaluates the changing stiffness parameters with respect to anatomical features obtained through cross-section image analysis. A composite model dependent on these anatomical features is presented as an alternative bending stiffness predictor versus typical methods employed by manufacturers.

Chapter 5 evaluates changes in *Arundo donax L* material properties at multiple length scales using nanoindentation, X-ray diffraction and thermogravimetric techniques. Viscoelastic indentation parameters are extracted from the results using models previously published for polymeric and

biological materials. Results are presented with respect to the number of full saturation cycles each sample was subjected to.

Chapter 6 considers the in-situ swelling of Arundo samples using X-ray micro-computed tomographic imaging. Results are analysed using a number of anatomical features to evaluate changes with increasing exposure to moisture cycling. Swelling and shrinkage strains in the tangential and radial directions are extracted from image stacks for new samples, and changes in the morphology of parenchyma matrix cells are quantified using anatomical image analysis.

Chapter 7 presents a brief summary of the results and the main conclusions that are drawn from the work. Recommendations for future work are also provided.

Appendix A provides the exploratory manuscript evaluating the impact of microstructural features on damping properties for samples exposed to short term moisture degradation.

Chapter 2

2 Literature Review

2.1 Microstructure and the Cell Wall in Wood-Type Materials

In order to consider the effect of the cane material on reed quality, modeling techniques for natural ‘wood-like’ materials must be examined. Qing and Mishnaevsky [16] have developed a micromechanical model that predicts the elastic properties of softwoods using several parameter inputs (microfibril angles, cell wall thickness, cell cross-section shape and density). The authors note that micromechanical models of wood can be divided into three categories, including cellular models, homogenization models and composite models. In their work, Qing and Mishnaevsky combine attributes of each of the aforementioned models and evaluate the effect of interface layers, microfibril angles, cell wall thickness and cross-section shape on elastic properties. In terms of geometry (Figure 2-1), their cell-level (microstructure) representation of softwood is comprised of a network of interconnected hexagonal cells with inter-cell regions of interfacial layers with varying mechanical properties. The authors examined the stress distributions within these layers when subjected to different loading modes (including tensile, compressive and pure shear).

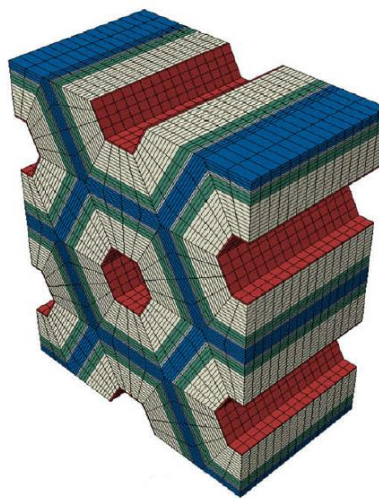


Figure 2-1: Finite element cell structure model used for experimentation (from [16]).

It was found that the thickness of the middle interface layer (the blue layer in Figure 2-1) is greatest such that support during shear loading is provided. Additionally, the surrounding layers (red layers in Figure 2-1) have increased stiffness with respect to the middle layer such that deflections due to shear loading are not excessive. In terms of microfibril angles in the surrounding cell layer (white layer in Figure 2-1) a change in elastic modulus was observed by the authors for changing angles. This was measured as a normalized fraction of the elastic modulus for isotropic behaviour. In general terms, the microfibril angle represents the orientation of cellulose fibers with respect to the cell axis (in the case of Figure 2-1, the cell axis is parallel to the red hexagonal layer). In these simulations, the authors observed the greatest deviation in tensile modulus (parallel to the cell axis) and shear modulus. In terms of magnitude, both the tensile and shear moduli were found to vary by over a factor of two for microfibril angle variations of up to 30 degrees. This indicates a strong anisotropic elastic behaviour for woods of varying microstructural orientations. It should be noted that each of the simulations performed included a moisture content of 12% in the cell structure (this is important for considering the potential effects of humidity on elasticity). Relative to the differences observed in elastic moduli for varying microfibril angles, the contribution of cell wall thickness to this effect was found to be much more subtle. In this case, simulations indicate that moduli changes of less than 1% are realized for thickness changes of up to 10%. For the influence of cell shape, the authors varied the angle of the hexagonal structure (from symmetric to an elongated cell) and found that significant elastic moduli changes were observed in the direction perpendicular to the cell wall angle. In general, the authors concluded that elastic properties were most significantly dependent on the microfibril angle of the cellulose fibers while the cell cross-sectional shape had the strongest effect on elastic anisotropy.

Mishnaevsky and Qing [17] have also considered the general micromechanical modeling of wood structures in terms of 'bio-mimicking' (the modeling of synthetic materials after their biological counterparts). They describe the macroscopic properties of wood as being primarily orthotropic with the important properties including longitudinal, radial and transverse directionality. Extending this description to the microscopic scale, the microstructure of wood contains a honeycomb-like configuration that is akin to a fibre-reinforced composite system. Here the cellulose fibrils act as a reinforcing phase while the matrix is comprised of hemicelluloses and lignin. In terms of mechanical properties, the cellulose fibrils control the longitudinal strength while the transverse strength is governed by the hemicelluloses and lignin. The authors also

consider general characteristics of wood which should be accounted for when modeling wood microstructures. These characteristics include the effects of moisture (decrease in strength), time-dependent deformation (due to the amorphous sections of cellulose microfibrils) and the large variation in properties from one species of wood to another. Mishnaevsky and Qing describe the cellular level (or mesoscale) of the wood microstructure in terms of an idealized hexagonal geometry (shown in Figure 2-2).

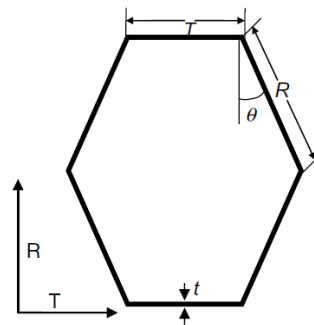


Figure 2-2: Hexagonal geometry of the cell structure depicting the shape and length parameters and the radial and tangential directions (from [17]).

In terms of elasticity, the ‘beam-like’ structure of the cell can be modeled using classical beam theory with rigid joints and deformations which are limited to in-plane deflections. Elastic stiffness in the longitudinal direction is proportional to the ratio of wall thickness to cell size, while the transverse stiffness is proportional to the cube of this ratio. Thus, the authors note that larger cells results in reduced strength and stiffness. As the authors note, the transition from micromechanical modeling to macroscopic length scales can be accomplished through homogenization schemes where representative volume elements can be used to replicate the response of lower-level material structures. For example, at the micron level fibres of crystalline and amorphous cellulose can be used in a matrix to mimic the complex interactions of hemicellulose, lignin and cellulose microfibrils using a Mori-Tanka composite regime. As the length scale is reduced, the individual contributions of the aforementioned constituents must be including in simulations. At the scale of

the cell wall itself, laminate models can be used to include the effects of multiple inter-cell wall layers. In these models, cell walls of varying microfibril orientations (generally referred to as laminae) can be overlaid on one another and the resulting structure behaves similarly to composites with various fibre orientations and can be modeled as a layered composite. Combining the meso- and micro-scale models enables very accurate mechanical response results to be obtained using the finite element approach.

Koponen et al. [18] investigated the elastic properties of wood as a result of the underlying cell structure. Using a similar beam-method as discussed in [17], Koponen et al. developed a model for softwoods that considered the internal angle of the hexagonal unit cells and their characteristic length such that the resulting meso-scale strain could be calculated for a variety of honeycomb configurations and parameters. Variations in longitudinal elastic modulus were observed for changing internal cell angles, similar to the results of [16]. The effect of density on longitudinal modulus was also considered, with modulus varying linearly with density. Interestingly, large variations in modulus were observed for models of different internal moisture percentages (results as shown in Figure 2-3).

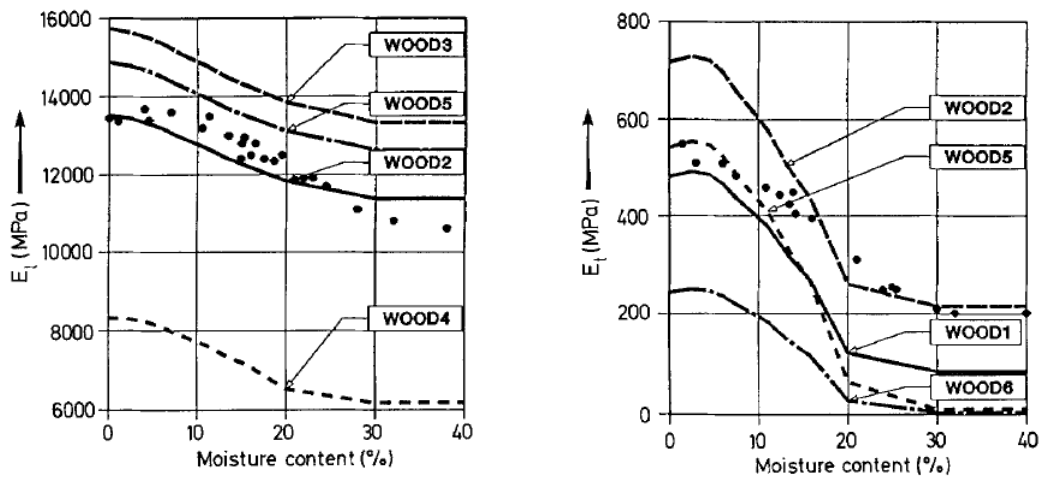


Figure 2-3: Variation of longitudinal (left) and tangential (right) elastic moduli with moisture content (from [18]).

The authors note that significant anisotropy observed for elasticity can be attributed to the molecular structure of the wood itself and the inhomogeneity of the cellular structure. Furthermore, it is suggested that the elastic properties, moisture content, microfibril properties (shape volume, orientation), cell-wall structure and cross-sectional shape are required to obtain generalized elastic constants for wood materials. The authors continue on to suggest that elastic behaviour estimation in wood can be accomplished through the analysis of microstructural constituents and morphology. This conclusion was attributed to the fact that macroscopic wood properties are directly reflective of their microstructural components' performance.

2.2 Reed/Wood Microstructural Characterisation

Studies have also been completed on the microstructural analysis of wood and cane-type materials. Obataya and Norimoto [2] have completed an acoustical analysis of *Arundo donax L* (the raw material used for reeds) and the influence of water-soluble extractives on its performance. The authors suggest that the water-soluble extractives can greatly influence the dynamic Young's modulus and internal friction of reeds in the direction of the grain due to uneven 'soaking' that create moisture gradients within the reed. Using a free-free beam flexural test, the influence of water-soluble extractives was examined by completing vibration experiments at different levels of relative humidity. By analyzing the resulting resonant frequencies, the authors were able to calculate dynamic modulus and internal friction values. Results for dynamic modulus are provided in Figure 2-4.

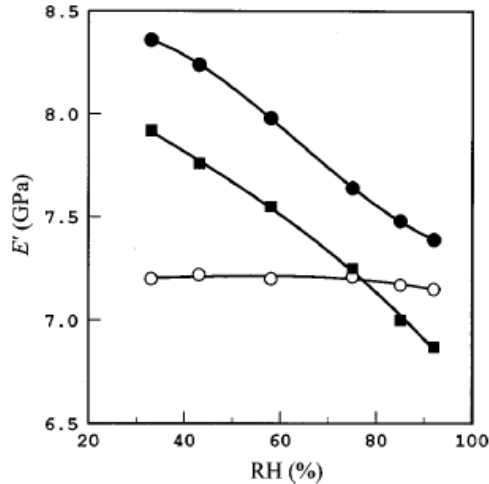


Figure 2-4: Effect of relative humidity on the dynamic Young's modulus of reed samples in the first mode of vibration. Untreated, water-extracted and glucose-impregnated reeds are represented by the black circles, open circles and black squares, respectively (from [2]).

The authors found that the extractives enhanced the dynamic modulus at low levels of relative humidity but did not significantly affect it at higher relative humidity levels. Changes in reed quality due to these effects were also considered by having professional clarinetists play each reed that had been subjected to water-extraction and glucose-impregnation. Overall, water-extraction was found to decrease the apparent richness and softness of the reeds, although ease of vibration and response increased. Additionally, glucose-impregnation only contributed to the ease of vibration and response of the reed (in which case both were reduced relative to the control). The authors reasoned that the extractives improved the tone quality of the reeds and upon removal of these constituents, tone quality could be recovered through glucose-impregnation. In general, the authors note the important relationship between reed performance and moisture content as reed wetting percentage in 'real' use would contribute significantly to variations in observed stiffness and playability.

Perdue [1] compiled a complete review of the grass species *Arundo donax L*, which has been used for the construction of musical instruments dating back 5000 years. In this review, Perdue examines the physical, morphological, chemical, environmental and historical characteristics of *Arundo donax L* (often referred to as bamboo reed). Physically, bamboo reed is

a tall, cane-like grass measuring 2 to 8 meters in height at full maturation. When examining its internal morphology, bamboo reed culms have a typical monocotyledonous structure consisting of randomly distributed vascular bundles embedded in a matrix of parenchyma. All vascular bundles share a common orientation and are surrounded by thick-walls of fiber. There is a marked difference in the morphology of these fibers at the periphery of the culm, with vascular bundles decreasing in size and increase fiber-to-wall ratios. Volumetrically, the vascular bundles occupy roughly 24% of the internal culm space, the vascular tissue and fibers 33% and the parenchyma matrix accounting for the remaining 43%. Perdue also notes that chemical analysis of bamboo reed has indicated a high silica content which can be attribute to highly silicified cells within the vascular bundles and epidermal tissue. Environmentally, the author mentions that little agreement has been reached as to the required soil conditions necessary for quality reed production (a fact illustrated by the wide variety of growth regions of bamboo reed). In terms of reed making (Figure 2-5) and physical testing, Perdue suggests that some insight as to the tone quality of reeds can be obtained through the use of bending recovery tests (similar to hysteresis type situations) during manufacturing.

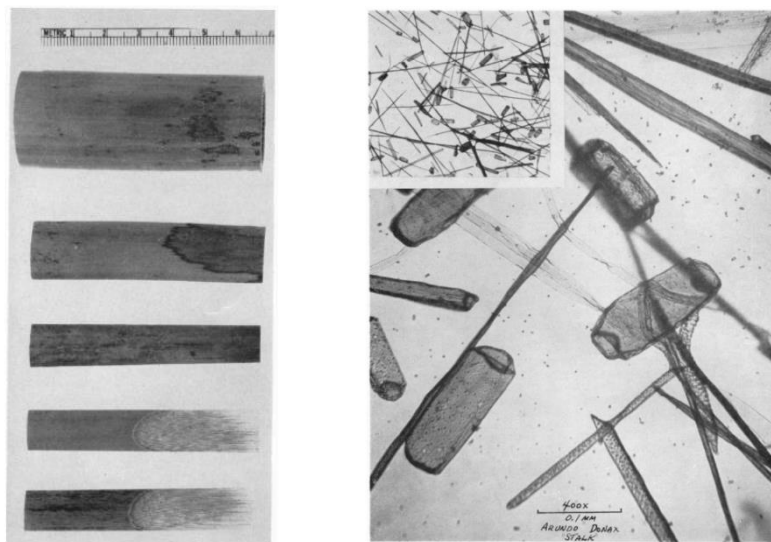


Figure 2-5: The stages of clarinet reed manufacturing (left) starting from the raw bamboo reed culm and a micrograph (right) of a fully macerated reed (from [1]).

Purdue also notes the potential variability in cut and finished reeds due to culm non-uniformities. This variability also affects the maceration (‘wetting’) potential of the reed (microstructure provided in (Figure 2-5)). Chemical analysis has shown there to be four primary constituents in the culm of bamboo reed, including cellulose, pentosans, lignin and ash. The results compiled by Purdue from a number of literature sources are provided in Table 2-1.

Table 2-1: Chemical analysis compilation of *Arundo donax L* from various literature findings (from [1]).

Source (compiled in [1])	Cellulose (%)	Pentosans (%)	Lignin (%)	Ash (%)
Raitt	42.8	33.6	9.4	7.4
Tomeo et al.	40.1 - 44.4	22.7-27.5	23.4-24.4	3.8-4.8
Jayme et al.	44.4	24.3	16.4	2.9
Bhat and Virmani	58.0	18.4	22.0	3.6
Kocevar and Javornik-Kosler	43.8	20.8	22.4	2.5

Additionally, the use of other bamboo variants (specifically *Phyllostachys bambusoides* and *Semiarundinaria fastuosa*) for reeds has yielded undesirable results. Plastic reeds have also been used, dating as far back as the 1950’s, although Purdue mentions that their lack of porosity has been considered a major hurdle to the development of synthetic reeds.

The interesting properties of wood have also been investigated in terms of wettability. Gardner et al. [19] conducted dynamic wettability experiments on red oak samples with a cellulose content (47 – 53%) similar to that of *Arundo donax L*. These experiments are important for understanding the effect of surface aging on wettability, absorption and capillarity. Gardner et al. found that the use of dynamic wettability experiments provided more accurate results compared to static measurements. This was attributed to the high levels of surface roughness (and thus high thermodynamic free energy) found on most wood surfaces. Of interest to reeds are the authors’ findings of surface aging effects. In order to simulate ‘fresh’ surface conditions, samples were sanded to remove oxide products and compared with naturally aged samples. It was found that the fresh surfaces were much more easily wetted than the aged samples. The authors correlate these results with x-ray photoelectron spectroscopy (XPS) chemical surface analysis that indicated increased levels of carbon on the surface of aged samples. This carbon content has been shown to

contribute significantly to hydrophobicity. Additionally, the critical surface tension of several wood species was examined in order to determine surface free energy. Through comparison of contact angle measurements with chemical surface analysis it was found that the lignin and cellulose content of the sample contributed most significantly to its surface tension. Generally, higher weight percentages of lignin and cellulose correlated with an increase in critical surface tension (indicating a more hydrophobic surface). These results illustrate the importance of aging and chemical considerations when characterising the mechanical behaviour of wood-like materials.

In addition to chemical analysis, the micro-mechanical behaviour of wood and other fibrous materials has been studied by Holmberg et al. [20]. Here the authors note that the microstructure of wood can be used to explain its highly non-linear stress-strain behaviour and elasticity. Similar to the findings in [1], Holmberg et al. note that the highest percentage of cell types in wood culms are all oriented nearly parallel with the axis of stem growth. The structural arrangement of these cells is such that starkly different properties are obtained in each of the longitudinal, radial and tangential directions. The structure of the cell wall is also discussed as it contains several layers (Figure 2-6) which each contribute to the macroscopic performance of the body.

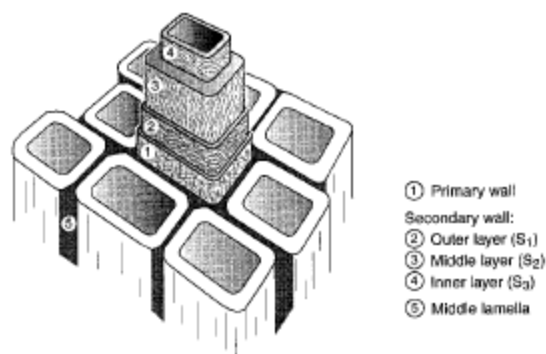


Figure 2-6: A generic schematic diagram of the layers within the cell wall (from [20]).

The authors describe this arrangement of layers as behaving similarly to a fibre-reinforced composite with cellulose chains in a hemicellulose and lignin matrix. This system forms repeating, thread-like units and represent the microfibrils of the cell. The orientations of these microfibrils are different in each layer of the cell wall as are their chemical compositions. For these reasons, wood is highly anisotropic and its elasticity can be described using the classic orthotropic compliance tensor (in terms of moduli and directionally dependent Poisson's ratios). The elasticity tensor developed by Holmberg et al. is provided in Figure 2-7.

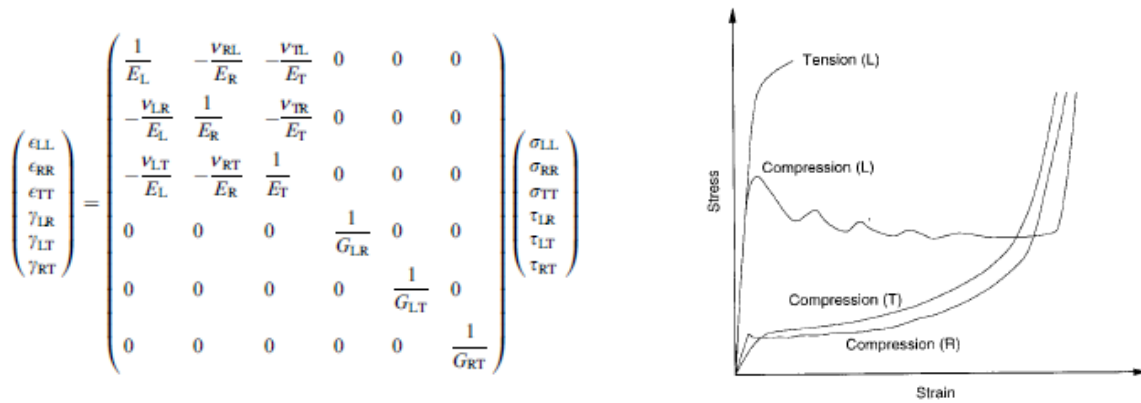


Figure 2-7: Orthotropic elasticity tensor for wood (left) and the associated stress-strain curves for wood when loaded in different orientations (right) (stress-strain curves from [20]).

The authors note that the symmetry of the compliance tensor enables one to write the relationships between radial, longitudinal and tangential compliance in the following way:

$$\frac{\nu_{RL}}{E_R} = \frac{\nu_{LR}}{E_L}, \frac{\nu_{TL}}{E_T} = \frac{\nu_{LT}}{E_L}, \frac{\nu_{TR}}{E_T} = \frac{\nu_{RT}}{E_R}. \quad (2-1)$$

Here, 'ν' represents the Poisson's ratio between the two noted directions and 'E' the corresponding elastic modulus. Due to the longitudinal orientation of most cellulose fibers, the strength and stiffness of the wood are greatest in this direction. This fact is further illustrated in the generic stress-strain behaviour of wood (Figure 2-7). Scanning electron microscopy (SEM) microstructural analysis has shown that the inter-cell bonded regions (ie. the microfibril structures from Figure 2-6) experience the greatest level of stress during loading. This can lead to failure of the cell wall, similar to delamination failure in composites. In addition to their microstructural modeling, Holmberg et al. suggest that further experimental characterisation of the wood cell-structure is required for the improvement of finite element models. These improvements could

consider geometry, chemical constituents (microfibrils), microfibril arrangement (relative lamellae angles) and moisture absorption properties.

More general characterisation of fibrous wood structures has been carried out by Justiz-Smith et al. [21] by analyzing three different natural cellulosic fiber materials. Several tests were performed in this study including fiber diameter determination, ASTM moisture content and absorption rates and chemical analysis of the samples (including natural and metallic composition). The authors found that significant variability in fiber diameter was common for all samples tested which suggests that control of mechanical properties can be difficult for cellulosic materials. Water absorption was highest for materials with the largest weight percentage of hemicellulose present in the culm. This was also found to be inversely proportional to the tensile strength of the fibers. The authors also note that this behaviour appears to be dependent on the metal ion concentration in the wood as larger water absorption rates were observed for wood species with increased weight percentages of silicon ions (Si^{4+}). The authors suggest that low values of metal ion content are often desirable as they tend to increase the brittleness of cellulose fibers. All of these factors indicate that there are complex interactions between properties at the microstructural level which contribute to the mechanical performance of wood-type materials.

Chemical and anatomical analysis of *Arundo donax L* and the corresponding effects on reed quality has been completed by Glave et al. [3]. In this study, the authors performed cross-sectional analysis of as-manufactured reeds using optical microscopy, SEM and particle induced x-ray emission (PIXE). In preparation for imaging analysis, thin (2 micron) sections were cut from the reeds and sputter coated with gold and palladium in order to provide a conductive surface for SEM. Micrographs of 'good' and 'poor' quality (as assessed by professional musicians) illustrated some subtle differences in the vascular bundles of the stems. The authors observed that reeds of poor quality contained occluded (overgrown and damaged) vessels, which were attributed to tylosis. In wood plants, a tylosis is a tissue generated by penetration through axial parenchyma cell pits and into xylem vessels. It is the result of a physiological process of the occlusion in the xylem as a response to a cyptogamic attack or other injuries. The authors continue to suggest that care should be taken when harvesting the cane to prevent such internal damage. Chemical analysis of the reed samples indicated little difference in phosphorus, sulfur, chlorine, potassium and calcium concentrations along the reed epidermis between good and poor reeds. However, silicon was found

in two major concentrations along the epidermis in the case of poor reeds. This second concentration was not observed in good reeds. Figure 2-8 provides the optical and scanning electron micrographs of the analysis samples.

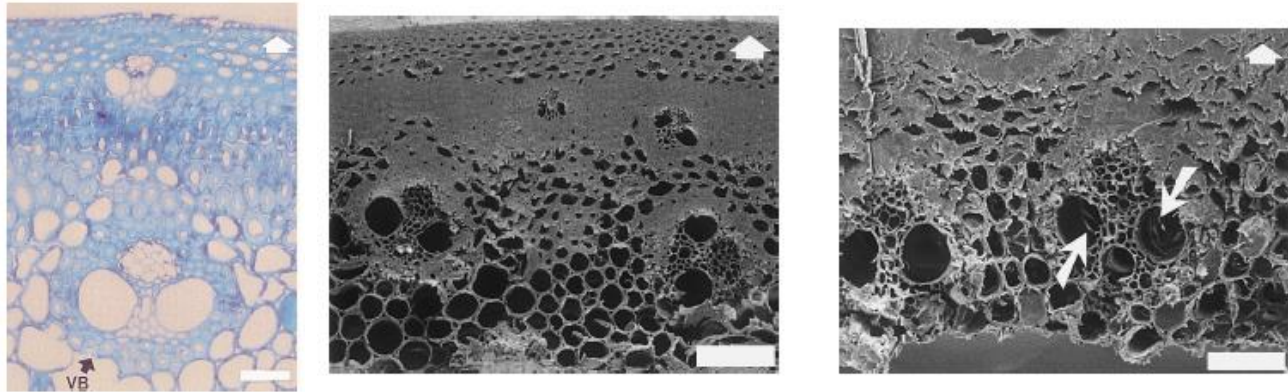


Figure 2-8: Optical (coloured) and scanning electron (greyscale) micrographs of the reed samples. Note the scale bars in each image are 50 microns. The arrows in each image at the top right indicate the orientation towards the exterior of the culm. The occluded vessels of the poor quality reed are shown on the right (from [19]).

An important microstructural feature of the so-called good reed is the twisted vascular bundles as seen in the middle image of Figure 2-8. Previous results have suggested that variation in orientation of the vascular bundles (here two bundles are observed, with one oriented radially and the other tangentially relative to the epidermis) contributes to their observed quality. It should be noted that this study did not contain a large sample size in terms of the number of reeds analysed. This fact was also mentioned by the authors as they suggest that future studies draw from a larger reed source. Pre- and post-manufacturing analysis in addition to pre- and post-harvest analysis is also suggested in order to isolate the ‘damaging’ phase of reed manufacturing (ie. natural causes, overgrowth, or harvesting damage).

A review on the structure of wood was completed by Vincent [22] in which an overview of mechanical properties, internal structure, testing and design was considered. Vincent discusses the arrangement of microfibrils within the cell wall and their orientations. X-ray diffraction methods can be used to measure these orientations throughout the entire cell wall and in the cell cross-section (due to the crystalline nature of the microstructure in these regions). These results could be used as input data for a micro-mechanical model using finite element methods. Vincent also provides insight as to the number of cells required within the cross-section of a model before

accurate wood response is observed. For structures in which the cells are geometrically isotropic, this number is approximately 16. Furthermore, micro- and nano-indentation tests (using a diamond tip indenter) can be used to measure both the hardness and isotropic Young's modulus of wood cells. In terms of internal structure, non-invasive techniques such as computed x-ray tomography have been used to evaluate the structure of stringed instrument wood species. Vincent suggests that further analysis using this and other methods is required as the consistency of the internal structure alone does not appear to correlate with perceived quality. With regards to *Arundo donax L* reeds, Vincent mentions that good musical performance has been associated with reeds containing a high proportion of vascular bundles and bundles with a high fiber to xylem and phloem ratio. In general, Vincent notes that the microstructural understanding of wood cell structures requires further development and correspondingly, the microstructural influence on micromechanical performance is essential.

Additional surface analysis on various wood species has been completed by Sinn et al. [23]. Here the authors used XPS methods to determine the surface oxygen to carbon ratio (O/C) for different wood samples prepared using both traditional sanding methods and by micotome. Morphologically, it was found (using scanning electron microscopy) that both sanded and microtomed surfaces retained many of the same features. Contrastingly, the anatomical structure of each wood sample was significantly damaged by the sanding operation. The authors suggest that this result should be taken into account when forming wood materials for applications where it is desirable to retain their 'natural' behaviour. With respect to the O/C ratio, sanded samples were found to have lower values than the microtomed ones indicating a reduction in surface oxygen content. The authors postulate that considering the lower O/C ratio observed in lignin compared to that of cellulose, sanding enriches the surface in lignin. This is important to consider as lignin is more ductile than cellulose and correspondingly has a very different elastic behaviour. This drop in O/C ratio was also found to depend on the initial wood density. This suggests that quality control of even basic material properties is critical for repeatability in manufactured wood-components.

The variability of *Arundo donax L* properties within single plants has been investigated by Neto et al. [24]. In their study, Neto et al. considered chemical composition changes as a function of morphological regions within bamboo reeds at a maturation age of approximately 6 months.

Each harvested plant was segmented into 6 sections such that intra-plant chemical variations could be analysed. General analysis on the water content, lignin percentage and holocellulose cellulose percentage in each section indicated significant variability. Specifically, water content varied by as much as 3% while lignin and holocellulose varied by 6.5% and 5% respectively. Thus the authors found that older bamboo reeds contained larger lignin amounts than younger plant sections. More specifically, the sections cut close to the bamboo joints yielded lower levels of cellulose on average when compared to the sections cut from the inter-joint regions. The same trend was observed for lignin concentrations. The authors suggest that the changing morphology of the bamboo reed microstructure could cause this segregation. Overall, these results illustrate the importance of location on resulting component behaviour (ie. for the case of reeds, where the reed is cut from the culm).

Using a more mechanistic approach, the specific vibrational and acoustical properties of wood have been analysed in relation to grain directionality by Obataya et al. [25]. In their experiments, the authors considered the dynamic Young's modulus and loss tangent ($\tan \delta$) with respect to the grain orientation of the wood. They also defined an acoustic conversion efficiency term (α) that was dependent on the dynamic Young's modulus, density and loss tangent (the relation is provided below).

$$\alpha = \sqrt{\frac{E_L' / \rho}{\tan \delta_L}} \text{ (from [25])} \quad (2-2)$$

$$\beta = \left(\frac{E_L'}{G_L'} \right) \left(\frac{\tan \delta_S}{\tan \delta_L} \right) \text{ (from [25])} \quad (2-3)$$

The acoustic efficiency can be defined as the ratio of acoustic energy radiated from the beam to its vibrational energy. Also, equation 2-3 shows the ratio developed by Obataya et al. which describes the anisotropy of the wood. As can be seen, the anisotropy parameter depends on the ratio of dynamic Young's modulus to dynamic shear modulus in the longitudinal direction. In general, the anisotropy ratio is larger in wood materials than in metals or plastics due to cell wall anisotropy at the microstructural level. The authors used an experimental setup similar to that of [2] in order to measure the flexural vibration of beam samples. Torsional vibration was also considered such that anisotropic effects would be captured, and the dynamic shear modulus could be measured. The authors found that there was a good correlation between acoustic efficiency and the anisotropy

ratio (Figure 2-9). It is also noted that the vibrational properties of wood beams discussed in the present study are nearly independent of macroscopic density and depend most significantly on the structure of the cell wall. The authors illustrate this fact by mentioning the variability in vibrational performance of multiple samples of the same species. Continuing, Obataya et al. consider the relationship between the viscoelastic properties spruce wood and its microstructure. This is performed by using a cell wall model which models the lignin constituent as an amorphous (and thus isotropic) matrix with embedded elastic fibrils which impart directionality into the model. The resulting complex equations for the Young's and shear moduli of each layer (relative to the fibril orientation) are developed such that a relation between the individual fibril moduli and fibril volume fraction is obtained. This method is similar to that utilized for carbon-fiber type composite calculations.

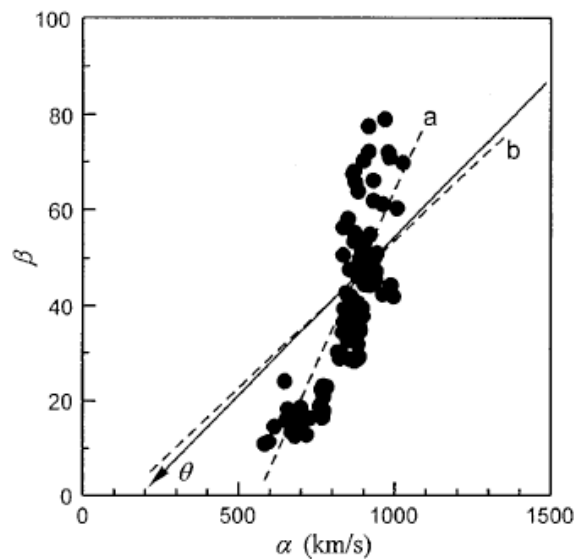


Figure 2-9: Correlation between acoustic efficiency and wood anisotropy (from [25]).

From their findings the authors suggest that for wooden soundboards, smaller fibril angles in the cell wall yield more desirable results. These findings are somewhat limited as only one wood species was examined although the cell wall models could be applicable to other wood materials.

The use of wood fibers for natural-synthetic composite systems has been evaluated in terms of mechanical behaviour by Bledzki and Faruk [26]. Specifically, the authors examined the resulting changes in properties when coupling agents were added to wood fiber prior to insertion in a polymeric matrix. These agents were used to promote interfacial adhesion between the fibers and matrix. SEM analysis of both hardwood and softwood fibers was also completed to determine any morphological discrepancies between the two. In general, large variations in fiber size and shape were observed for all samples. Damping potential measurements which considered the ratio of dissipated energy (loss energy) to stored energy (strain energy) were conducted using impact toughness tests. The authors note that loss energy can be described as internal irreversible deformation, energy dissipation from the creation of matrix cracks, delamination of layers and fiber fracture. Overall the addition of coupling agents was found to decrease the damping index considerably (up to 100% reduction in hardwood samples). The results of their experiments are shown in Figure 2-10. This is an important finding as it demonstrates the importance of matrix-fiber bonding on the resulting energy absorption. Although the authors analysed a natural-synthetic composite system in their study, it is reasonable to deduce the importance of cellulose fiber-lignin matrix bonding in bamboo cane on the resulting vibratory behaviour.

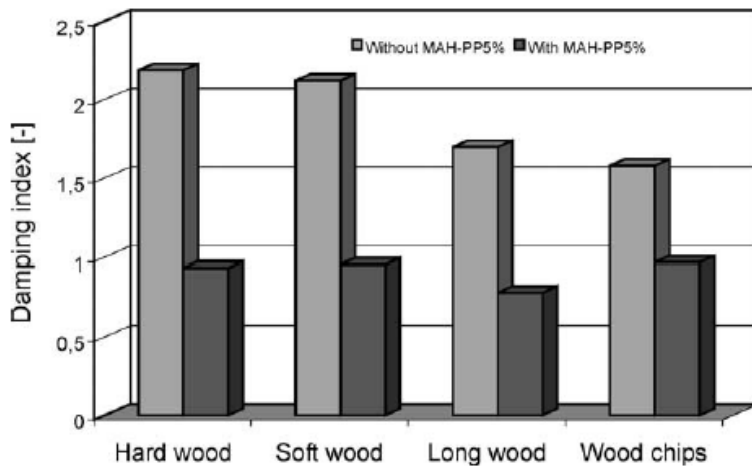


Figure 2-10: The importance of interface bonding between fiber and matrix on the resulting damping potential (from [26]).

2.3 Considerations for Arundo Material Microstructure Models and Degradation

Before a choice in multiscale modeling technique (in terms of top-down or bottom-up) can be made, consideration should be given to the attributes of each and the requirements of the system in question. Top-down methods involve the observation of system features at the macroscopic level followed by lower-level investigations to decipher which micro-scaled contributions can account for the higher-level observations [27]. A limitation of this method resides in the difficulty in isolating potential micro-scaled phenomena which could account for macro-scale behaviour. At these reduced length scales there is often a complex interplay between several mechanisms which may not be easily modeled in the top-down methodology. Examining material behaviour mechanisms at higher spatial and temporal resolutions constitutes the bottom-up method. The dynamics of material behaviour are attributed to the interactions of nano- to micro-scaled constituents (or on the potentially quantum scale for atomic and beyond resolutions). Modeling the complex details of material behaviour at these length scales can facilitate the development of models which more accurately represent macroscopic behaviour. Several limitations exist including limits of computational power (which usually increase as length scales decrease due to a reduction in the analysis volume), a lack of prior knowledge on constituent properties (lack of experimental findings) and the requirement of coupling techniques to link the micro and nano levels such that applied problems can be solved (i.e., engineering design of components at the macro-scale). Some of the typical coupling techniques used for bottom-up approaches have been discussed in previous sections. Others have noted [28] that hierarchical multiscale modeling of microstructural damage for structural analysis (macro-scale) is complicated by the complex dependencies of single damage modes to multiple spatial damage modes at meso-scale levels. Damage evolution is also difficult to consider as the length scales over which each mode is active can change during deformation [28]. Top-down methodologies may provide a more computationally convenient average behaviour, however changes in periodicity and geometry as length scale changes can complicate the analysis. Knothe Tate [29] has provided motivation as to the bottom-up modeling of bone mechanophysiology in contrast to years of research focused on the reverse engineering (top-down) of bone. Motivation for this shift comes from the desire to create new materials inspired by natural systems. This requires the development of highly accurate mathematical models coupled with experimental characterisation at the basic, cellular level in order to better predict material performance.

Extending the discussion of bottom-up modeling, there is reason to support this methodology for the case of reeds (more specifically *Arundo donax L*). Upon first inspection it is apparent that the modeling techniques used for wood-like materials would be well suited to the analysis of *Arundo donax L* (ADL). Specifically, the previously discussed softwood modeling of Bader et al. [30] could be applied to ADL modeling (that is, the general methodology). While the microstructure of ADL shares similarities with that of wood, there are some notable differences (see Figure 2-11).

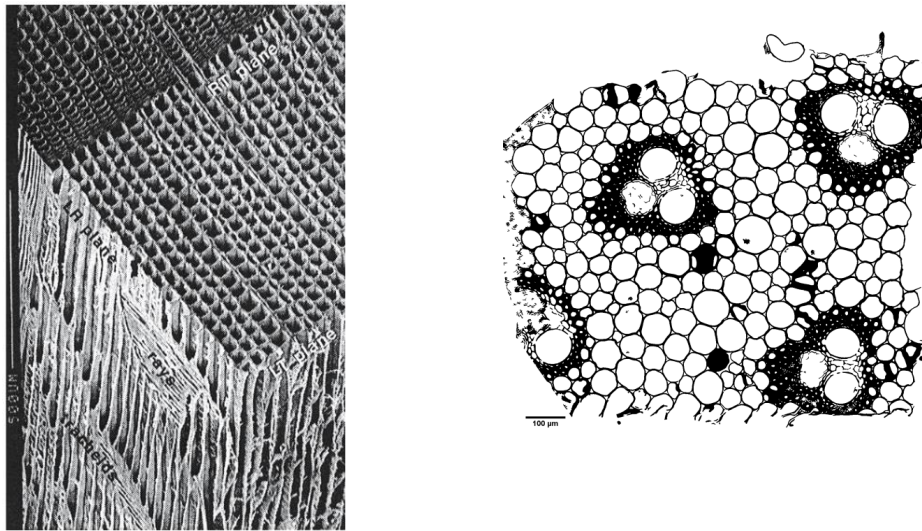


Figure 2-11: Comparison of wood (spruce) and ADL microstructure. Left: Sample of spruce wood microstructure via scanning electron microscopy. The top surface represents the radial-tangential plane (from [31]). Right: Sample *Arundo donax L* microstructure via micro-computed tomography. The illustrated sample orientation represents the radial-tangential plane.

Firstly, the micro-scaled honeycomb structure of wood (which is usually assumed periodic) is not as well-defined in ADL. Cell wall structures are prevalent around the fiber-like vascular bundles; however the microstructure is more randomly distributed. This suggests that a Mori-Tanaka approach for inclusion-matrix modeling may more accurately account for the distribution of reinforcing vascular bundles (VB) within the polymer-like matrix. Reducing the spatial scale to the sub-micron level, damage at the interface between the VB structures and the matrix would also be an important consideration. Fiber pull-out models for interface coherency strength could be used at this scale in a similar manner to those of composite materials [32]. Given the importance of microstructural damage and potential evolution, damage mechanisms should be investigated at

the micro-to nano-scales (similar to the approaches mentioned by Souza and Allen [33]). It is important to first consider these mechanisms as otherwise damage evolution can be difficult to predict using either top-down or bottom-up approaches, as previously mentioned. In ADL, damage is likely to occur in part due to moisture gradients and drying effects which suggests the use of poroelastic models to predict internal stresses and microcracking due to pore pressure and porosity variations. Given that the level of porosity changes with length scale it is important to consider the micro and nano-levels first as they contribute to lower spatial level porosity [30]. Plasticity due to the deformation of crystalline constituents (i.e., cellulose fibrils) may also contribute to deformation behaviour and damage evolution which can be modeled using self-consistent and Mori-Tanaka approaches [34]. The macroscopic geometry of the reed itself is also likely to contribute to highly non-linear gradients of damage and viscoelastic effects. At the reed tip, overall thickness is highly reduced compared to the “bulk” properties of the main body. Thus drying and wetting phenomena along the tip are likely to differ from the bulk behaviour. During excitation, the reed tip would also likely undergo more rapid changes in moisture gradients due to the increased driving force for fluid flow in the pores (a consequence of thinness). Micromechanical stiffness variations due to interfacial coherency fluctuations are also important to examine in the context of frequency dependent vibrational behaviour. Average methods (rule of mixtures, Voigt and Reuss models) would not capture these variations. Additionally, experimental characterisation of micro to nano-scaled ADL constituents could provide material inputs at a fundamental level (previous macroscopic testing has been inconclusive in terms of quantifying inter-reed behaviour [2]). Similar to the reasoning presented by Knothe Tate [29], understanding the interplay between mechanics and fluid transport, mechanics and material constituents and damage mechanisms at high spatial resolutions is required in order to reveal the phenomena behind the behaviour of natural materials. This reasoning suggest a bottom-up approach to ADL modeling.

It is also prudent to examine the microstructure and reed tip configuration more closely. In terms of microstructural constituents, it is well known that size effects can influence the results of equivalent volume analysis [35]. Analysis of RVEs with identical morphology containing different microstructural features (voids and inclusions with different absolute size) reveals that the active deformation mode depends on the size scale of the microstructure. As the microstructural size approaches a negligible level with respect to the length scale of the macroscopic deformation field the material begins to behave periodically (the contribution of higher order deformation modes to

overall response is reduced). In these cases, a first order approximation to the internal stress state (such as the aforementioned Piola-Kirchhoff stress) accurately describes material deformation [35]. Other size effects also become relevant when the given microstructural length scale (even if it is constant) becomes significant with respect to the macroscopic scale (for reeds, this would represent the thin tip region). In this case, gradients of macroscopic deformation control the overall material response due to microstructural domination of macroscopic behaviour. Similar to microstructural length scale variations, first-order homogenization schemes do not capture these effects as higher order deformation modes become important. As mentioned, these effects become important for materials exhibiting microstructural elements close to free surfaces or within thin films where surface effects significantly contribute to deformation modes.

2.4 Dynamic Testing of Wood Type Materials

Measurements of internal damping in reticulated spruce have also been completed over the audible frequency range (20Hz to 20kHz) [36]. Of interest to the authors of this study was the loss angle of a spruce sample as measured by the phase angle between stress and strain during sinusoidal time-dependent deformation. The more common loss tangent can be calculated from this angle (d) as $\tan(d)$ (elsewhere termed $\tan(\delta)$). This loss tangent represents the ratio of the imaginary and real components of the complex elastic modulus and represents a deviation from the time-independent Hookeian behaviour of linear elastic materials. In terms of experimental setup, the authors use a compression rig with piezoelectric load sensors to subject a spruce rod (5 mm diameter) to sinusoidal compressive stresses. The rig actuator allows a frequency sweep to be applied to the sample and analysis of the signal is conducted using an FFT. Results showed that the loss angle exhibits a linear dependency on frequency within the audible range; this result is expected as the viscoelastic behaviour of wood at the macro-level is known to follow the classic Kelvin-Voigt rheological model. Several peaks in the frequency domain with respect to loss angle do appear at 4000, 8000, 9000 and 17000Hz, although the authors do not provide reasoning for these observations. It is likely that other wood species would exhibit different peak locations and magnitudes due to structural differences (both material constituent distributions and porosity).

More rigorous analysis of damping and dynamic elastic moduli has been completed for Norway spruce and sycamore wood samples by [37]. Both the damping and dynamic moduli (shear and Young's) are experimentally determined by the authors using the free transverse vibration

model of a beam, including consideration of shear deformation and inertial components. Using this method, the damping factor (δ) can be computed as the ratio of the width of the resonance curve at half of the maximum amplitude (alternatively, the half power level can be used, which is the 3dB level) to the resonant frequency. The value of δ was found to increase exponentially with resonant frequency for both wood species (for a resonant frequency range of 500 to 6000Hz). Observable differences in the δ -resonant relationship between the spruce and sycamore samples were noted as the spruce wood exhibited a more drastic variation with resonant frequency. The potential mechanisms behind this difference are considered by Spycher et al. [37] in terms of the material constituents of each wood species. The authors note that previous experimental studies on organic, amorphous polymers illustrate a pronounced frequency dependence of dynamic properties (where attenuation of sound waves occurs due to synchronized movements of large molecular segments within the polymer). Given the increase in lignin (an organic polymer) content of Norway spruce versus sycamore (27% and 23%, respectively) it is estimated that the degree of crystallinity within the cell wall and the microstructural arrangement of the amorphous polymer sections contribute significantly to frequency dependent internal damping [37].

It is also prudent to consider the inherent anisotropy of wood and other natural materials within the context of viscoelasticity and damping. Amada and Lakes [38] have examined the dynamic viscoelastic properties of bamboo in both dry and wet conditions over a frequency range of 0.01 to 1000Hz. A similar testing method to that of Spycher et al. [37] was implemented for torsional and bending measurements of dynamic moduli and $\tan(\delta)$. Overall, $\tan(\delta)$ was found to exhibit little dependence on frequency within the range mentioned above. The torsional values of $\tan(\delta)$ were slightly greater than those obtained in the bending mode and both were lower than $\tan(\delta)$ measurements for wet samples. Small peaks in the $\tan(\delta)$ values are observed near the 1000Hz (dry, torsion) and 100Hz (wet, bending) spectral components which may be due to the micro-level distribution of lignin and cellulose with respect to each of these orientations, as well as the viscoelastic response of the material in each of these modes. For instance, in bending the values of $\tan(\delta)$ are dominated by the ratio of imaginary to real Young's modulus, whereas in torsion matrix contributions dominate (the matrix compliance is more important). Thus it can be reasoned that the fibrous material constituents play a major role in bending $\tan(\delta)$ measurements while the relatively compliant matrix constituents control the torsional values of $\tan(\delta)$. Given these differences and the well known anisotropy in the cellular structure of bamboo and wood

more generally, it is somewhat surprising that $\tan(\delta)$ does not differ more significantly between torsional and bending modes (as is also mentioned by Amada and Lakes [38]). In terms of modeling the frequency dependent $\tan(\delta)$ behaviour, Amada and Lakes [38] note that following the methodologies of cellular and porous composite design the $\tan(\delta)$ values of a cellular solid would correspond with those of the solid material from which it is comprised. Fluid flow within the pores for the wetted case is not considered as no significant peaks in the frequency spectrum were observed and small peaks which were observed were quite narrow ($< 10\text{Hz}$). It follows that a purely cellular model of damping would not be adequate for capturing potential anisotropy in damping behaviour as anisotropy in porosity would not alter the solid-cellular relationship of $\tan(\delta)$ values. Amada and Lakes [38] suggest that molecular orientation of material constituents may contribute to damping anisotropy as well as the existence of two solid phases at a sub-micron level.

Ultrasonic methods can also be used for the characterisation of wood orthotropic properties (including elastic moduli) [38]. This ultrasonic methodology yields nine elastic constants, representing the 9 independent orthotropic elastic moduli. In this method, wood anisotropy can be expressed as ratios of various velocities and acoustic invariants. For estimating the quality of spruce for resonant wood (as used in violins and other musical instruments), the ratio between Young's modulus in the longitudinal axis and the shear modulus of the transverse plane (radial-tangential) provides a good quality estimation index. This method of testing yields substantial elastic and acoustic data regarding the properties of wood, although sample preparation can be difficult, and for the case of *Arundo donax L* is somewhat limiting due to size constraints versus larger wooden samples.

Chapter 3

3 Experimental Techniques

This section is intended to provide additional information regarding the preparation of samples used for Chapters 4 and 5 and to give an overview of the moisture cycling setup used in Chapter 6. The experimental setup for in-situ X-ray micro CT scanning is also provided. These details are not provided in their respective journal manuscripts.

3.1 Samples and Sample Preparation

Arundo samples taken from the heels of reeds played by the musician were prepared using a modified histological approach. Microscopy samples were first removed from the reed heel using a razor blade to an approximate thickness of 3 mm. Samples were then embedded in paraffin wax for fixation and their cross-sectional surfaces prepared using a sliding microtome. All surface preparation was performed on the tangential-radial plane of each sample (corresponding to the cross-section of the Arundo culm). The samples were microtomed at a slice thickness of 20 microns until even, flat surfaces were obtained. No further surface treatments were performed to prevent unwanted surface damage to the delicate microstructure. A few samples were analysed for surface roughness prior to nanoindentation testing using an optical surface profiler (Zygo NewView 8000). This was conducted to ensure that surface roughness was acceptable for nanoindentation using the surface preparation technique. A sample profile is provided in Figure 3-1.

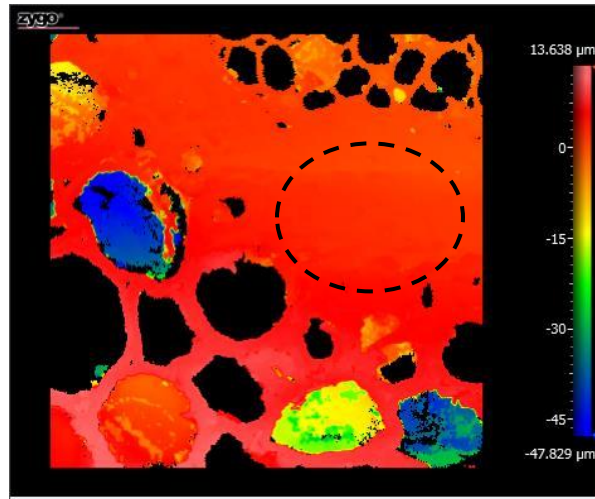


Figure 3-1: Surface profile for a vascular bundle as prepared using histological processing. The area of interest for nanoindentation testing is noted by the dashed area.

Note that large profile values are due to the open pores of the parenchyma cells. The RMS roughness of the nanoindentation area was ~ 10 nm. Although not representative of the entire material, the solid fibers of the vascular bundles contribute most significantly to the longitudinal stiffness of the reed. This longitudinal stiffness controls the bending rigidity of the reed and thus measures of fiber longitudinal modulus are important for understanding the behaviour of the macro-scaled material. Nanoindentation measurements were also performed on parenchyma cell walls, and these structures combined with the solid fibers represent all of the solid material present in the reed microstructure. Characterising the longitudinal moduli of these structures provides a basis for the development of composite models quantifying the macroscopic mechanical properties of the reed.

For comparison with reed heels, reed tips were prepared using an identical methodology, although microtome slices were limited to 10 microns as damage was found to be more significant in the tip samples if larger slices were taken (the cross-sectional width of reed heels was 2.5 to 3 mm, while tips were 1.25 to 1.5 mm). Moisture cycled samples were also prepared using this methodology. For these samples a single piece of *Arundo culm* internode (obtained from the reed manufacturer) was sectioned into 3.5 by 3.5 by 3.5 mm samples, all aligned longitudinally. This longitudinal alignment was used to minimize inter-sample variance that could impact measured

differences in nano-mechanical behaviour. A schematic of the sample orientation is shown in Figure 3-2.

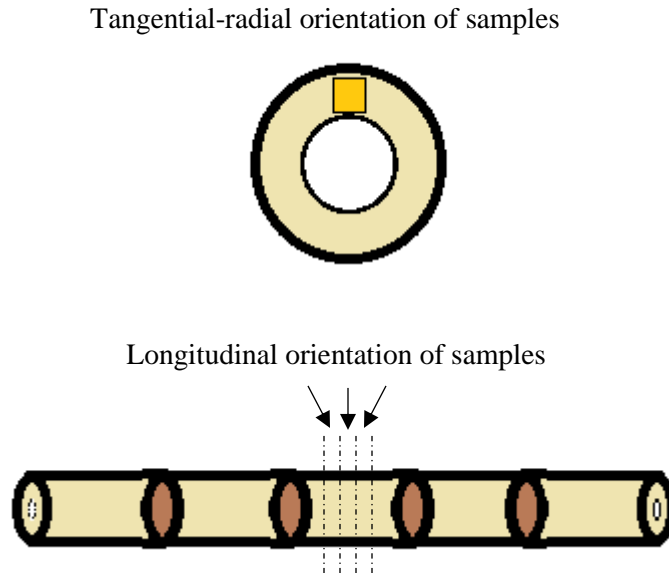


Figure 3-2: Orientation of moisture cycling samples for nanoindentation testing. In this diagram, samples were cut from a single internode (bottom) using 4 successive cuts. The position of each sample with respect to the cross-section is also shown (above).

All fixated samples were stored at 50 to 60% RH to prevent deformation due to shrinkage strains during moisture desorption.

Samples for X-ray diffraction testing were taken from the same locations as the nanoindentation samples of the used reeds. A razor blade was used to cut off equal amounts (by mass) of reed heel and tip samples from the used set. Samples were dried at 100°C for 1 hour prior to powdering to reduce residual moisture content. Samples were powdering using a razor blade and mortar and pestle (to a final size of approximately 800 microns). This procedure was used to prevent the final powder size from being too fine and impacting the XRD results. Samples were stored under vacuum desiccation prior to testing.

TGA samples were sectioned similarly to the XRD samples. Matching heel and tip samples were obtained from the played reed set using a razor blade. *Arundo donax L* exhibits strong longitudinal symmetry in terms of anatomical structures (specifically vascular bundles), therefore each TGA sample set was taken from the same location along the length of the reed. Heel and tip samples were all of equal mass (~1.5 mg) and were stored at ambient temperature and 40 to 50% RH prior to pyrolysis. Samples were not dehydrated as equilibrium moisture content for each sample was determined during the TGA ramp-up to 100°C. A diagram depicting the orientation of TGA samples relative to the reed is shown in Figure 3-3.

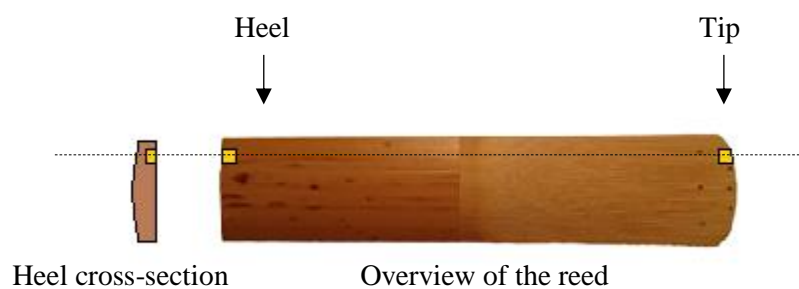


Figure 3-3: Schematic of TGA samples cut from the alto saxophone reed samples. The longitudinal alignment of both heel and tip samples is noted. The overall top view of the reed is depicted, although samples were taken from the underside where radial depth of the culm is equal (i.e., the side that clamps onto the mouthpiece).

3.2 Experimental Setup – Additional Information

Measurements of $\tan \delta$ were obtained through careful calibration of the dynamic longitudinal stress-strain setup. The experimental design included a shaker rig used to input dynamic displacement at specified frequencies. Input displacement was measured using a chromatic (white-light) confocal displacement sensor (STIL CCS-Optima+) with the sensor focused on the point of contact between the shaker stinger and the sample surface. Output force was measured using a piezoelectric transducer in contact with the opposite sample surface. The use of sandbags and foam aided in eliminating resonances of the setup between 100 and 1000 Hz. Latent lag in the system (between input and output measurements) was compensated via calibration using a solid aluminum block (assumed to contribute a negligible amount of input-output lag relative to the system). This

calibration was performed between 100 and 1000 Hz and used as a calibration curve for measurements on Arundo samples between these two frequencies.

The experimental setup for micro CT moisture cycled samples is shown in Figure 3-4. Here the process of exposing samples to saturation cycles was automated due to the precision required and the time needed to complete all cycles.

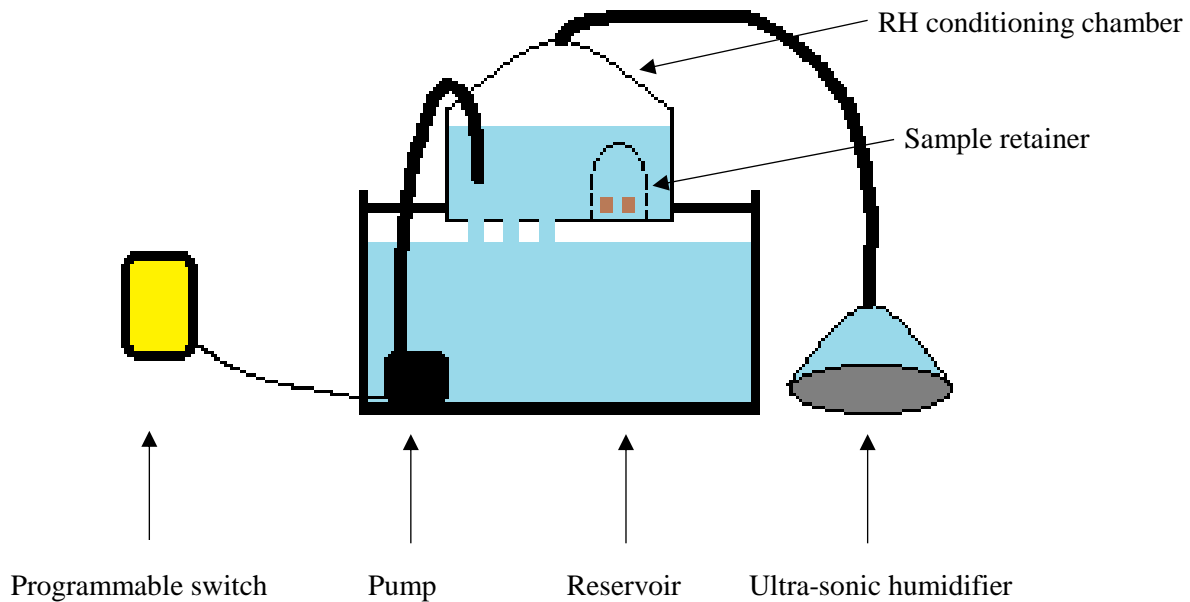


Figure 3-4: Automated moisture cycling setup for the micro CT samples. Note that only deionized water was used in the reservoir.

The power switch was programmed to cycle the pump on and off at specified intervals and the exact cycle profile is provided in Chapter 6. The ultra-sonic humidifier was set to maintain the samples at 70% RH during each desorption cycle. The flow rate of the pump was set such that the equilibrium water level of both the reservoir and sample chambers was just above the height of the sample retainer during an absorption cycle. Perforations in the sample chamber allowed water to completely flow out during desorption.

3.3 Image Analysis

Some general comments should be made with regards to the error introduced when using thresholding operations for image processing. Several anatomical and microstructural features were extracted from various micrographs during this work using thresholded binary images. Intensity thresholds were mainly used for the results of Chapter 6 where large contrast differences between the sample tissue and the surrounding air volume were obtained, facilitated by the quality of X-ray CT micrographs obtained. Features extracted from these images were obtained as averages over the entire X-ray CT stack and slight changes in threshold levels would not affect the relative differences between samples that are discussed. As an example, measures of cell diameter could fluctuate in terms of absolute value with changing threshold levels, but these fluctuations would be consistent between image and sample sets where the same threshold limits were used for binarization. Therefore, for the purposes of these comparisons the thresholding operations would not introduce significant error.

Feature extraction on images of Chapter 4 was also performed on binarized images, although the binarization process was different from the above noted method. In this case, thresholding was performed using the K-means clustering procedure in ImageJ and a training set of classifiers from each of the two regions of interest within each micrograph. In this way, small differences in intensity values between micrographs did not influence the results of the clustering segmentation as the classifying training set included samples from the entire collection of micrographs. Similar to the limitations mentioned for Chapter 6 micrographs, absolute values for fiber area fraction and cell shape parameters (such as diameter) could exhibit a dependency on the segmentation classifiers chosen, however relative values would not be affected. The differences between reeds of a set is the main point of interest for this study and the magnitude of these differences would not change due to thresholding fluctuations. The use of K-means clustering for image segmentation also eliminates any variance in binarization operations as the resulting segmented images were binary in nature (solid fibers and surrounding parenchyma tissue).

Chapter 4

4 Static Bending Stiffness and Aging Behaviour of Alto Saxophone Reeds: A Practical and Anatomical Approach

C. Kemp¹, G. Scavone¹

¹Computational Acoustic Modeling Laboratory, Department of Music Research, McGill University

This chapter is in manuscript style and intended to be published. This component of the thesis work examined the degradation behaviour of actual alto saxophone reeds using bending stiffness as a mechanical characterisation method.

Abstract:

The present study examines the static bending stiffness behaviour of alto saxophone reeds manufactured from *Arundo donax L.* Reeds are quantified both experimentally and through stiffness evaluation by a musician during their playing lifecycle. Spatially dependent stiffness is considered and stiffness asymmetry is found to be an important metric of reed performance as assessed by the musician. The reeds played by the musician are also analysed with respect to several different reeds sets ranging from soft to stiff in terms of manufacturer stiffness rating. This was conducted to examine similarities and differences between reed sets from an anatomical perspective. Correlations between bending stiffness and anatomical structures are found and a Euler beam bending stiffness model that is dependent on these anatomical structures is developed to account for minute differences between reeds. Good agreement between the model and measured results is observed. This work may lead to the development of more accurate sorting and categorization methods for currently manufactured reeds, reducing the variability often observed by musicians.

4.1 Introduction

The reed and its vibrational behaviour are a critical component of any reed instrument. The woodwind reed is manufactured from *Arundo donax L* and is clamped to the mouthpiece during playing for single reed instruments. Although reeds are sorted and categorized by the manufacturer according to stiffness, significant variability is often observed between reeds. Initial assessments of the performance (mechanical, acoustical) of reeds also does not remain constant and further contributes to reed variability and the difficulty in assessing reed behaviour (and ultimately musical performance). The proper objective classification of reeds is an interesting problem from an engineering perspective with the goal of producing reeds that are more consistent.

4.1.1 Background and Motivation

Research into the mechanical behaviour of the mouthpiece-reed system has, in general, considered the reed as a second order vibrating system with homogenous properties [39]. This model simplifies the simulation of fluid flow behaviour, although it neglects some of the intricate anatomical features of the reed that contribute to inter-reed variability. Previous studies on clarinet reeds have noted that at the tip, reed displacements are large compared to the thickness of the cross-section ($> 10\%$ strain) [40]. The cross-section of alto saxophone reed tips range from 100 to 200 microns in thickness, meaning that the inner cortex of the *Arundo culm* contributes significantly to the mechanical properties governing reed vibration, especially around the center of the reed. The inner cortex represents the inner diameter of the *Arundo culm* cross-section (the inner to outer cortex is the bottom to top direction of the Figure 4-1 micrograph) and is comprised of a composite mixture of several anatomical structures, primarily stiffening vascular bundles and more compliant parenchyma cells as a surrounding matrix. The vascular bundles contain a perimeter of solid fibers that contribute significantly to longitudinal and radial (bending) stiffness while the parenchyma cells form a cellular-like structure similar to that of a honeycomb. Both of these anatomical structures are illustrated in Figure 4-1 (the micrograph on the right). The importance of vascular bundle fibers within the inner cortex on the musical quality of clarinet reeds has previously been noted [4], although the influence of these fibers on pertinent mechanical properties such as bending stiffness has not been considered thoroughly. Additionally, comparative differences in fiber structures between individual reeds in a nominally identical set have not been analysed (i.e., only general trends of anatomical parameters and the impact on reed quality have

been considered). The distribution of vascular bundles within the parenchyma of the inner cortex is not uniform and significant differences can be observed between nominally identical reeds. It is not clear the way in which these differences contribute to either objective or subjective reed properties and is an area requiring further analysis.

Another aspect of the relationship between reed mechanical, microstructural and anatomical properties that is not well understood is the consideration of changing reed properties alongside longer-term degradation behaviour. Spatz et al. [12] considered the anatomical features that contribute to Young's modulus of the *Arundo* culm and found that, amongst other factors, the large Young's modulus in the longitudinal direction was due to both high lignification and the density of solid fibers surrounding reinforcing vascular bundles. Investigations into the dependence of reed quality on anatomical features have only considered the analysis of a small set of reeds and to the best of the authors' knowledge, no studies have considered the importance of these features to aging reed properties [4], [10], [41]. These properties are important as initial assessments of reeds do not always hold true and their behaviour changes with time.

4.1.2 *Arundo donax* L

A typical *Arundo* culm cross-section is provided in Figure 4-1. The primary material directions of interest are the radial and longitudinal directions, also noted in the figure. Reeds are manufactured such that the length of the reed is aligned with the longitudinal direction and the flat underside is closest to the inside diameter of the culm wall. A typical *Arundo* culm contains node and internode regions although only internode regions are considered in the present study as they are the sections used for woodwind reed manufacturing.

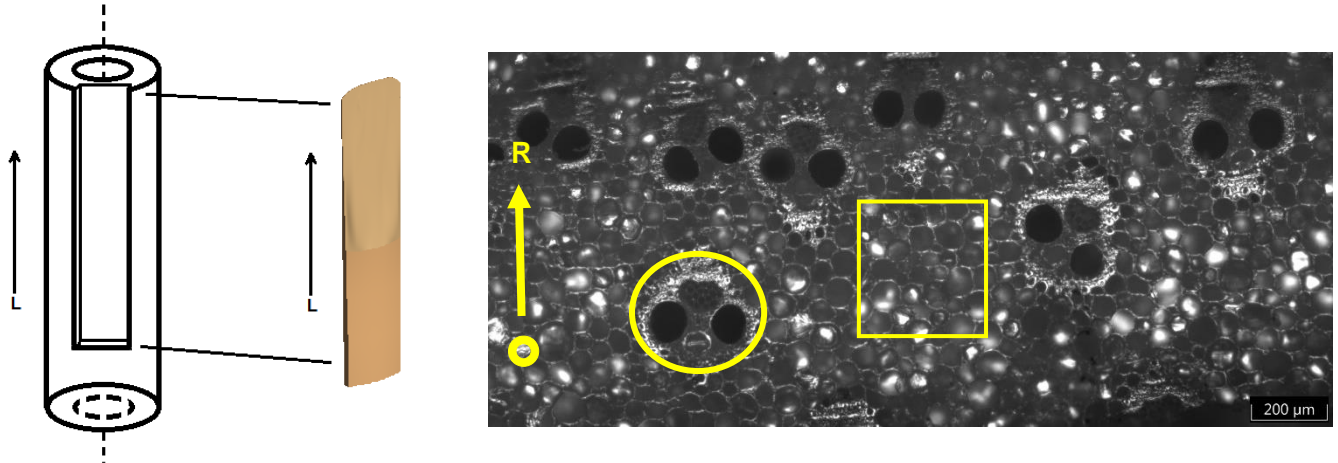


Figure 4-1: Left: Orientation of the longitudinal direction with respect to the Arundo culm and a manufactured reed. Right: Radial (R) direction and the longitudinal direction (circle, into the cross-section) with respect to a typical Arundo cross-section micrograph. The circle highlights a vascular bundle structure and the square highlights the surrounding parenchyma cells.

Biomechanically, the nodes (end caps of the culm shown on the left of Figure 4-1) are important for structural rigidity and it would be interesting to consider proximity to these regions on the influence of reed bending stiffness in future studies, although this is not considered in the present work. The main microstructural and anatomical features of interest are the vascular bundles, surrounding solid fibers and the parenchyma cells. Although the epidermal layer is important to the biomechanical strength of the Arundo culm [12] its importance is less significant for woodwind reeds where the majority of vibrating material is confined to the tip region. Manufactured reeds are machined from the outside to inside diameter of the culm with the flat underside of the vamp corresponding to the inside diameter. This results in a reed tip entirely comprised of the inner 10 to 20 % of the culm wall thickness. Previously it has been noted [12] that the density of vascular bundles is dependent on the radial position within the culm wall. This is similar to the structure observed in many types of bamboo [42], although the average size and shape of vascular bundles differs between the two species. The radial dependence of vascular bundle density results in a gradient in the structural Young's modulus of the culm, with the inner most region being an order of magnitude lower than the outer region with a logarithmic relationship with respect to radial position [12]. The importance of radial position is not just confined to the spatial density of vascular bundles, but also to the size and density of the solid fibers that surround their perimeter [4], [43]. These solid fibers provide most of the longitudinal

and bending stiffness to the Arundo culm and their density is likely important to the vibrational performance of the reed.

4.1.3 Anatomical Structures and Quality

Good quality reeds have previously been associated with a high density of vascular bundles exhibiting continuous solid fiber perimeters [43]. The solid fiber perimeter surrounds each of the vascular bundles as previously mentioned and can be seen as the small white ring surrounding the bundle depicted in Figure 4-1 (highlighted by the yellow circle). Thus, much data and insight into the structural performance of reeds can be obtained through careful analysis of the vascular bundle anatomy. The surrounding parenchyma cells form a structure that is more compliant than the vascular bundles and this coupled with the scale of the cells and vascular bundles can influence tip bending significantly. In bending, deflection of the tip is greater for regions with reduced vascular bundle density and depending of the spatial arrangement of vascular bundles, this can result in a non-uniform bending profile. This would influence the vibrational performance of the reed (in addition to other factors, such as tip-opening displacement) and is not taken into account by typical reed-mouthpiece acoustic models. All of these biomechanical contributions highlight the importance of radial positioning with respect to the strength and stiffness of machined reeds in their final geometry. The microstructural and anatomical measurements considered above have not previously been directly compared with bending stiffness measurements or stiffness ratings (by a musician) for single reeds of a specific set. The potential correlation of these measurements with reeds of varying bending stiffness is also an area requiring investigation. General studies considering the rankings of reeds (i.e., good versus poor performance) have thus far been unable to draw clear conclusions from the data [11]. Kolesik et al. [4] and other studies [9] found no statistical evidence that vascular bundle density contributed to musical quality, although for bassoon reeds Heinrich [43] found that the fiber density surrounding the vascular bundle was important.

4.1.4 Static Stiffness

Stiffness is an important parameter for sorting and comparing reeds as it is a metric that manufacturers use and one that musicians agree upon the definition of [7]. Musicians can also consistently identify reeds according to their stiffness. It has also been considered as the foundation for good acoustic performance in clarinet reeds [44] and thus is an important property to consider

in the objective classification of reeds. More recent studies on static vs dynamic compliance in clarinet reeds has shown a linear relationship between the two, at least when the dynamic compliance of the first bending mode is considered [8]. This is important as it suggests that static measurements (which are easier to perform by the manufacturer, practically speaking) can be used to categorize dynamic behaviour. These mechanical measurements of the reed were also shown to be highly correlated with ratings by musicians, including ease of playing and brightness, further highlighting their importance. Reeds of equal static compliance could not explain all of the differences in ease of playing ratings, although an arbitrary unit for static compliance was used in this case and only a single measurement position was tested. Differences due to blowing pressure, lip position and other mouthpiece-reed interactions notwithstanding, it is still of interest to test highly calibrated bending stiffness measurements with respect to tip microstructure variability to investigate potential sources of variation in nominally identical reeds. Given that stiffness is used as a baseline for sorting and anticipating reed performance, stiffness is used as the primary descriptor for reed variability in the present study.

4.1.5 Degradation and Tip-Stiffness Importance

As has been noted, reed performance changes with time and exposure to moisture. Reeds are played in a fully saturated state (at least at the tip of the reed) and then stored between sessions in an unsaturated state (although usually at elevated relative humidity to prevent warping). This repeated moisture cycling coupled with mechanical fatigue contributes to the degradation of reeds and their changing properties. Mechanically it is relatively easy to quantify reed degradation behaviour by testing changing bending stiffness values during the lifespan of a reed. It is common for musicians to report differences in reed stiffness for purchased reeds, however the magnitude of these differences in comparison with objective measurements has not been well studied to date. Manufacturers sort machined reeds according to their bending stiffness, although this measurement is only performed in one location along the length of the reed and does not capture differences due to variable anatomical distributions. These localized differences are important as several anatomical features have a length scale that is the same order of magnitude as the thickness of the reed tip. This suggests that the distribution and local material properties of anatomical features within the tip region are important for more rigorous classification of reeds. This is especially true when the modal shapes of tip vibration are considered in the context of tip deflection

magnitude [40]. If the tip is significantly heterogenous in terms of stiffness, this could lead to localized differences in tip vibration (i.e., tip stiffness asymmetry) and these differences would not be obvious from average bending stiffness values taken further away from these heterogeneities.

4.1.6 Summary

Of additional interest is the relationship between changing objective stiffness measurements and perceived stiffness values during the lifecycle of a reed. While more reliable prediction of initial reed bending stiffness is desirable, changing stiffness values are also an important measure of reed consistency. The current study observes changing objective and perceived reed stiffness over the course of several months to evaluate changes that occur during the natural lifecycle of played alto saxophone reeds. Upon completion of the playing portion of the study, anatomical features of the reeds are analysed to extract potential objective measures that better predict reed stiffness and aging behaviour as compared to typical bending stiffness values.

4.2 Experimental Design

4.2.1 Materials and Samples

For the purposes of tracking reeds over their lifecycle, a set of reeds from the same manufactured batch (i.e., same raw material and harvest) were obtained from the manufacturer. These reeds were all nominally identical according to the manufacturer specified stiffness and showed no significant differences in tip geometry. This geometry was measured in terms of tip thickness at six different locations and values between reeds were all within 5%. A total of 8 reeds from this batch were selected randomly for the study in order to observe changes during normal playing. The reeds were all specified with a stiffness of “3H”, where H is used as a ‘hard’ descriptor. Reeds of this cut are available in all different stiffnesses ranging from 2 to 4 and include intermediate ratings of soft, medium and hard (S,M and H). With this rating system the musician is able to be more precise in their selection of reeds by stiffness. The magnitude of differences in between reeds of these ratings was not well understood prior to this study, in terms of calibrated static bending stiffness.

4.2.2 Objective Stiffness Testing

In order to quantify potential stiffness asymmetry along the tip of the reed, six different measurements of bending stiffness were taken at six different spatial positions as outlined in Figure

4-2 below. A rounded dowel pin was used to perform point stiffness measurements that highlighted differences in on- and off-axis values. Two measurements per reed were taken on-axis (along the centerline of the reed vamp) and 4 measurements were taken off-axis. Note that in this context, on-axis represents measurements at A2 and B2 positions (along the reed vamp centerline) and off-axis represents all measurements taken closer to the edge of the reed (A1, A3, B1, B3). These measurements were performed at 70% relative humidity (RH) and 23 to 25°C. All 8 reeds were measured initially in as-received conditions before they were played by the musician.

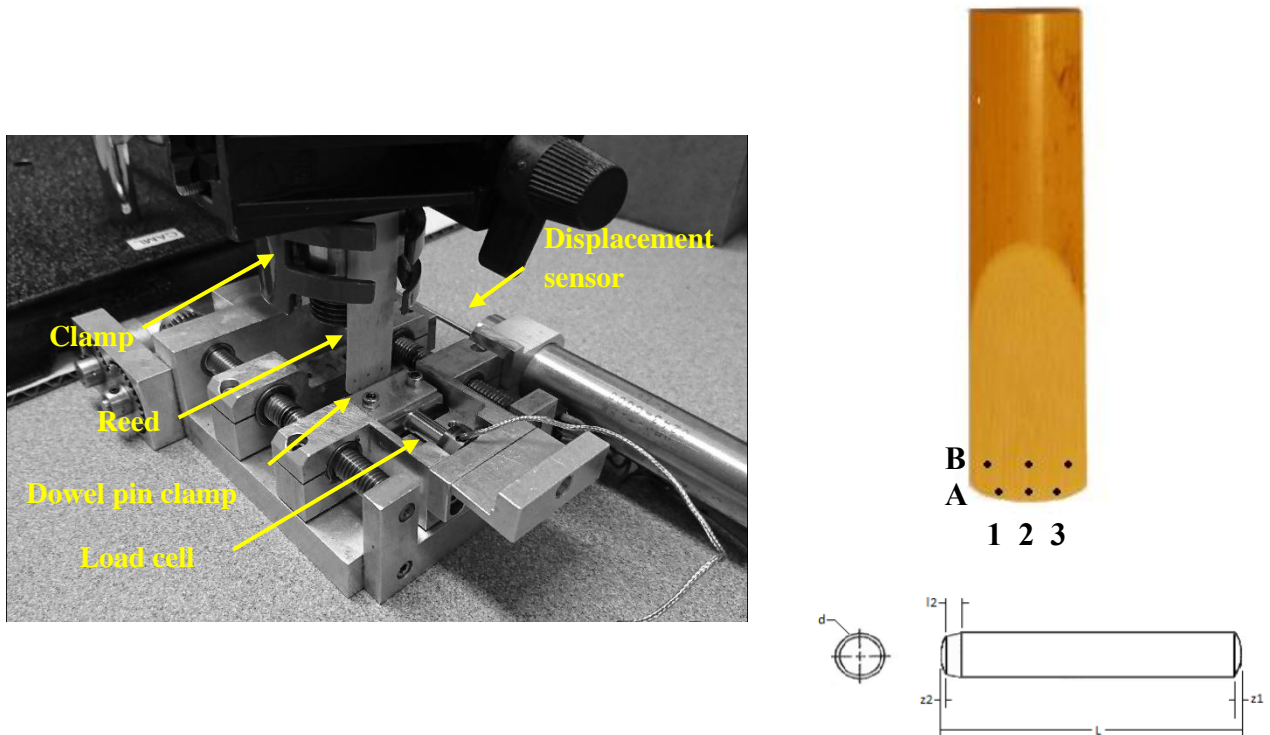


Figure 4-2: Experimental setup illustrating the stiffness testing technique along with the spatial position of stiffness tests. Note that the dowel pin is positioned in the center of the clamp (shown by the arrow). A typical dowel pin (used for probing the tip stiffness) is also illustrated (bottom right illustration, $d = 1$ mm).

Prior to beginning the study, a test reed of the same 3H stiffness ranking (also from the same set of reeds) was fitted with a strain gauge 3 mm away from the tip. This strain gauge was attached to the flat underside of the reed vamp and is shown in Figure 4-3.

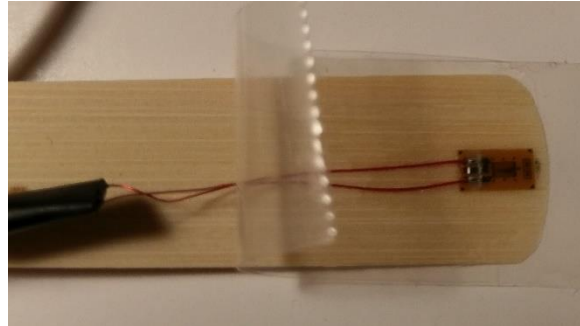


Figure 4-3: Strain gauge fitted to the underside of the alto saxophone reed. The underside of the reed normally sits against the lay of the mouthpiece.

It is difficult to make in-vivo measurements of reed bending behaviour [45] and it was desirable to obtain approximate values of strain magnitude during playing by the test musician. The placement of the strain gauge was meant to provide a measure of bending strain at the same location as one of the static bending stiffness measurement positions. The addition of a strain gauge to the tip of the reed likely influenced the overall vibrational and acoustic performance of the reed although it was noted that the musician did not find it difficult to play the reed, nor were any significant differences between this test reed and a normal reed offered by the musician. These measurements were useful for determining average bending stress values for reeds during in-vivo use. This provided an indication of the magnitude of bending induced in the reed tip during normal playing. The influence of increased lip force (in this case, style of play) on the reed tip is also considered.

4.2.3 Perceived Stiffness Testing

Reeds were evaluated for perceived stiffness by a professional alto saxophone jazz musician. Initially, the entire set was ranked by the musician after the first set of objective stiffness measurements were taken. The reeds were then entered into the musician's normal playing rotation and a stiffness ranking tracking sheet was provided. This sheet was used for recording the duration played on each reed per session and the current ranking of stiffness on a scale from 1 to 8, where

number 8 represented the stiffest reed and number 1 the softest. For consistency, the reeds were played for the same amount of time during each practise session and stored at 70% RH between sessions. The reeds were re-ranked from soft to stiff during each playing session, unless no changes in ranking were detected. The reed placed in the 4th ranking was considered to be the “concert” reed and would be selected for use in a concert performance (this system was adopted as part of the musician’s normal routine). A schedule was setup such that objective stiffness measurements could be made in conjunction with the perceived stiffness ratings and the reeds were completely re-ranked several times (without the aid of the tracking sheet) to prevent previous ranking entries from influencing the current rankings. This was done to ensure that perceived rankings were independent of previous findings.

Overall, the study tracked the life of the reeds for 2.5 months, with objective measurements of stiffness being conducted once per week. Care was taken to monitor the storage conditions of the reeds to make sure that they were held as close to 70% RH as possible. This was done through the use of a calibrated temperature/humidity logger and an 80% RH saline pack placed inside the reed container. Pre-experimental monitoring of the container found that an 80% RH pack was required to maintain the RH level of the container at 70%. Reeds were only stored indoors and thus temperature fluctuations were minimized to ambient conditions (23°C +/- 5°C). Temperature and relative humidity measurements were recorded at 1-minute intervals during storage of the reeds in the experiment so that conditions could be monitored and verified. The study was concluded when the musician felt that the reeds had reached the end of their useful life, a point at which they would normally be replaced in their normal rotation. By the end of the study, each reed had accumulated approximately 300 minutes of playing time at an average rate of 5 to 7 minutes per day.

4.2.4 Bending Stiffness Measurements

Objective stiffness measurements were conducted using a micro-tensile-compressive loading stage with a 10-pound load cell. Static loading conditions were used (similar to manufacturer testing) with an applied displacement rate of 0.025 mm/second. Each tested point along the reed tip was loaded to a constant displacement of 1.5 mm. This value was chosen to be large enough for an accurate measure of linear elastic bending stiffness to be measured while preventing damage due to fiber breakage and/or fracture.

Reeds were loaded using a cantilever beam setup (Figure 4-2) intended to mimic the way that reeds are normally mounted on the mouthpiece of a saxophone. The clamping condition of the cantilever was made to simulate a ligature on the mouthpiece with the underside of the reed pressed flat against a steel adaptor. The length of the unsupported end of the reed (as measured from the tip) was 38.25 mm and the length of the supported end was 32.55 mm. The clamp was positioned such that the boundary conditions were representative of a rigidly supported beam. Displacement measurements were taken from the linear displacement sensor of the tensile-compressive rig. The locations of the bending stiffness measurements along the reed tip are noted in Figure 4-2.

The ‘A’ position measurements were taken 1 mm from the reed tip, and the ‘B’ position measurements were 6 mm from the tip. The A2 and B2 values were aligned along the center of the reed vamp with A1, A3, B1 and B3 values taken off-axis on either side of the A2 and B2 values. The ‘A’ position measurements were each 3 mm apart, while the ‘B’ positions were 5 mm apart (refer to the diagram in Figure 4-2 for an overview). It was desirable to maintain several millimeters of distance from the edges of the reed for testing to prevent damage to the vamp. The loading condition was such that the dowel pin was perpendicular to the surface of the reed tip during deflection. A rounded dowel pin was chosen to prevent excessive localized stress from penetrating the reed surface. As previously noted, these measurements were performed at six different locations along the tip during each measurement session. Reeds were not played by the musician for 24 hours leading up to each bending stiffness measurement to allow the reeds to stabilize at the nominal storage condition. Reed masses were also recorded during each measurement session to capture potential changes in moisture content, and any mass changes related to deposition of skin or mineral materials during repeated playing sessions.

4.2.5 Microstructure and Anatomical Evaluation

All reeds of the set were analysed for several microstructural features in addition to the high spatial resolution stiffness measurements conducted. Upon completion of the playing portion of the study, samples from the heel section (the back cross-section of the reed) of each reed were taken. These samples were 1.5 to 3 mm in thickness and captured the entire cross-section of the reed. Cross-sections are indicative of the reed tip along the bottom edge due to the high longitudinal symmetry of the *Arundo culm*. This was verified by analyzing the distribution of solid fibers surround vascular bundles at both the tip and heel of the reed. Images of the underside of

several reeds were obtained and segmented to separate solid fibers from the surrounding parenchyma. Sub-sections from the tip and heel sections were then compared to check for the continuity of fibers along the longitudinal axis. Examples of this are provided in Figure 4-4 and Figure 4-5.

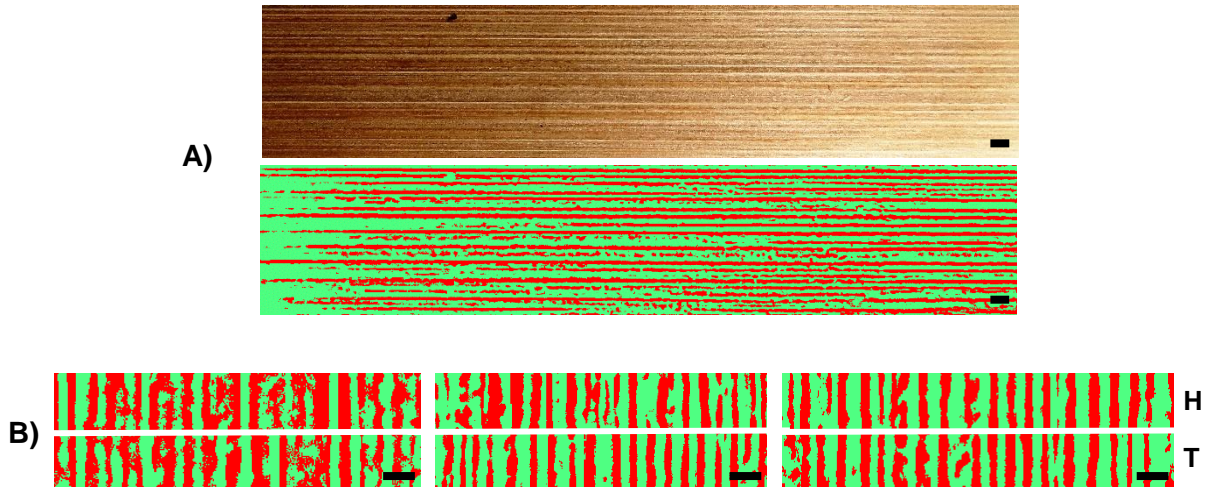


Figure 4-4: A) Optical image of the underside of an alto saxophone reed. The corresponding segmented image depicting solid fibers (red) is shown below. Solid fibers are optically opaque to white light in comparison to the parenchyma tissue (matrix material). Therefore, image segmentation was performed using thresholded grey values from the “dark” sections of the reed, separating solid fibers from the more transparent matrix. B) Sub-sections of segmented images providing a comparison between tip and heel sections for 3 reeds. The continuity of fibers along the longitudinal direction of the reed can be observed here as strong fiber symmetry between tip and heel images is apparent. Note that all scalebars are 1mm and heel versus tip sections are denoted by the “H” and “T” labels respectively.

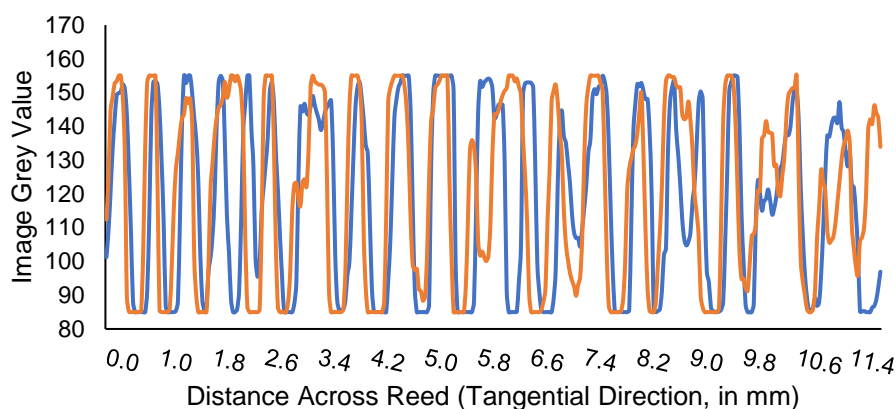


Figure 4-5: Plot of the area averaged grey value for sub-section images (as in Figure 4-B) for heel (orange) and tip (blue) locations of a sample 3H reed. Note that while the width of solid fiber bundles varies slightly, the location of bundles is uniform between the heel and tip data.

Although not shown here, slight differences in tip versus heel solid fiber distributions can be explained by the flatness of the machined reed relative to the *Arundo culm*. Within this context the longitudinal direction of the culm may not be perfectly aligned with the machining plane, and slight bending along the longitudinal axis that occurs naturally in *Arundo donax L* can cause solid fiber bundles to appear misaligned when tip and heel segmented images are compared. The locations of solid fibers in both heel and tip sections are depicted as the maxima of grey values in Figure 4-5. Overall strong continuity in fiber location between heel and tip sections is observed, confirming the assumption of high longitudinal symmetry for vascular bundles and solid fibers within the *Arundo culm*.

Samples were cut using a Struer's microtome saw and then prepared for optical microscopy using a Lecia vibrating microtome. Composite optical microscopy images for the entire heel cross-section of each reed were obtained by stitching together several individual micrographs at 10x magnification. The resulting micrographs were roughly 13 by 3.5 mm in size and were used for further identification, classification and quantification. The microstructural and anatomical features used in the analysis were centered around the vascular bundles (VB) of the reeds. Most of the analysis focused on these elements as they play an important role in determining the mechanical and vibrational properties of reeds [4], [12], [43].

All of the anatomical features extracted from the micrographs were compared analytically with measurements of stiffness for each of the spatial positions considered. It was also possible to compare changing stiffness values for each reed with these extracted features by fitting aging curves to the measured stiffness values over the duration of the study. These aging rates were calculated as a loss of bending stiffness per hour of playing. Objective aging rates were also compared with subjective changes in stiffness ranks for each reed over the duration of the study.

Reed micrographs were post-processed to extract the features of interest. The above analysis and extraction was performed in MATLAB and in ImageJ [46]–[48]. Routines were written to automatically quantify the desired properties, plot them as statistical distributions and save descriptive parameters. A general outline of this process is shown in Figure 4-6.

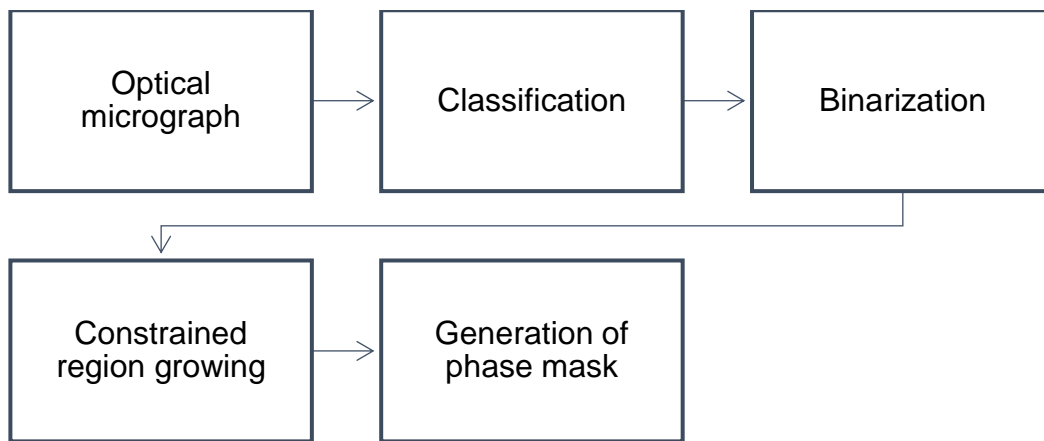


Figure 4-6: Overview of the image processing technique used to extract the desired anatomical features from each micrograph.

Classification of the optical micrographs is performed using ImageJ and a trainable segmentation procedure. The segmentation is used to create two main phases from each micrograph, specifically parenchyma and VB fibers. It is important to consider the location and density of these VB fibers, as several metrics related to the shape, density and spatial arrangement of VB's can be extracted from these segmented images in subsequent image analysis. The segmentation routine requires that a training set for classification is provided.

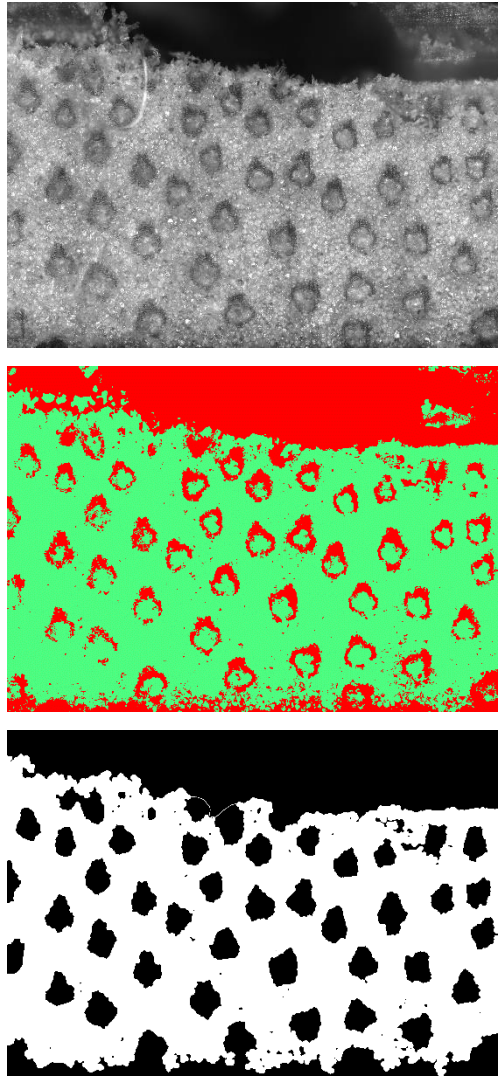


Figure 4-7: From top to bottom: Initial, unprocessed optical micrograph of the reed cross-section. Segmented image of solid fibers. Phase mask image of vascular bundles and surrounding matrix.

This training set was taken from each reed heel micrograph separately to prevent variation in exposure and brightness from influencing the results. A subsection from a typical micrograph along with its corresponding segmented image is shown in Figure 4-7.

Regions containing small, 5 to 30 μm diameter fibers surrounding the VB's were chosen at random for the first classifier training. Larger (50 to 300 μm) sections of parenchyma cells were selected for the second classifier (green portions of the middle image in Figure 4-7). Heel micrographs were also cropped to a rectangular section that captured the entire height of the reed heel (cross-section) measuring roughly 10 x 3.4 mm. The exact size of the crop was dependent on the heel cross-section being analysed as the height of reed heels was slightly variable.

The fully segmented images were then binarized to facilitate further processing including constrained region growing. This operation involved 'filling' the space between VB's such that a phase mask was produced. The growing region was confined to the limits of the cropped heel micrograph and seed points were selected to completely fill the spaces in between adjacent VB's. This mask represented a binary image that contained only shape and spatial data from the VB's (bottom image of Figure 4-7). This map of VB masks simplified the automatic recognition of VB centroids during image processes. Table 4-1 outlines the features that were analysed for each reed/micrograph and these descriptors were extracted from these VB masks using the analytical techniques mentioned above. Extracted features were found to exhibit the best goodness-of-fit to Weibull distributions and shape parameters and therefore are described using two-parameter (shape and location) Weibull curves. Some features did exhibit fits more similar to a normal distribution and were modeled as such. Normally distributed features are noted where appropriate.

Table 4-1: Overview of the anatomical and microstructural features analysed.

Microstructural Feature	Description
VB maximum distance	<ul style="list-style-type: none">• The maximum Euclidean distance between any pair of VB's
VB minimum distance	<ul style="list-style-type: none">• The minimum Euclidean distance between any pair of VB's
VB A2 density	<ul style="list-style-type: none">• The Euclidean distance of neighboring VB centroids from a centroid located at the A2 stiffness position of the cross-section. This value is computed using a nearest-neighbour approach where the closest 10 VB's surrounding the A2 position are found. A fitted Weibull curve to the results yields a location parameter that is used as the VB A2 density value.
VB area	<ul style="list-style-type: none">• The area of any VB in terms of an equivalent diameter (i.e., idealized as a circle)
VB ellipse	<ul style="list-style-type: none">• The aspect ratio of an ellipse fitted to any VB in the cross-section (where the limiting cases of 0 and 1 represent a circle and a line segment, respectively)
VB area fraction	<ul style="list-style-type: none">• The ratio of VB area to overall parenchyma (cross-sectional) area in the analysed micrograph
Fiber area	<ul style="list-style-type: none">• The ratio of solid fiber area surrounding the VB's to overall parenchyma area in the analysed micrograph
VB distribution	<ul style="list-style-type: none">• An overall metric of the Euclidean distance between all pairs of VB's
VB A1 density	<ul style="list-style-type: none">• Computed in the same way as for the A2 density but using an A1 centroid position.
VB A3 density	<ul style="list-style-type: none">• Computed in the same way as for the A2 density but using an A3 centroid position.

All features are presented as statistical distributions (primarily normal and Weibull types, depending of the fit) with distribution shape and location/center parameters used for further analysis. The distribution features were chosen as a metric of the spatial arrangement of VB's and to test for obvious microstructural differences between reed cross-sections. More specifically, the VB center metrics at the A1, A2 and A3 positions were taken to assess any asymmetry in the arrangement of VB density throughout the reed cross-section. This asymmetry was quantified by comparing the magnitudes of differences between VB A1, A2 and A3 center values.

4.2.6 Comparison Reed Set

The geometry between reeds of different static stiffness (of the same manufactured cut, such as jazz or classical) does not vary significantly in terms of tip cross-section. Given that manufacturers offer reeds in half and quarter stiffnesses it was deemed prudent to compare the set of reeds played by the musician (3H) with those of the same cut and different stiffness ratings. Thus, four additional sets of samples were compiled including 10 reeds of rating 2S, 10 of 3S, 10 of 3M and 10 of 4H. The samples were selected to provide a measure of differences in the static bending stiffness between reeds of similar and dissimilar manufacturer ratings.

These samples (referred to as the comparison set) were subjected to the same mechanical testing procedures as the musician set although only 2 spatial positions were examined, both along the central axis of the reed. In total, 80 measurements were made with 40 A2 position and 40 B2 position data points. Reeds were conditioned at 70% RH and 23°C for 48 hours prior to mechanical testing to ensure that the initial conditions were the same between all reed samples in the study. The reed heel micrograph preparation method was identical to that of the musician set, as was the image acquisition method. All of the anatomical features extracted from the musician set were also analysed for the comparison set. Overall this experimental setup provided 48 reeds of varying manufactured stiffness ratings with 5 sets (10,10,10,10 and 8) of identical stiffness ratings.

4.3 Results

4.3.1 Overall Tip Stiffness

A visualization of reed tip stiffness values for the musician set (3H set) can be found in Figure 4-8. These figures present plots of spatially dependent stiffness values for each of the 8 3H reeds played by the musician. Each plot represents one temporal position within the reed's lifecycle. Spatially dependent plots of stiffness rate of change are also presented (measured as a bending stiffness loss per hour of playing). The distance units for all of the plots are given in mm and are representative of the actual locations for bending stiffness measurements. Graphs are plotted on the same stiffness scale for all positions with each of the 6 spatial positions where measurements were made being depicted. General observations between the plots and the musician's rankings are also discussed within the context of reed preference. As previously noted, the reeds ranked between 3 and 5 of the 8-reed set were considered 'concert performance' level reeds by the musician in accordance with their normal reed maintenance technique. All values

have been normalized with respect to the thickness of the reed tip at each measured location. The measurements presented in the plots were obtained by calculating the slope of linear fittings through the origin to load-displacement data at each of the 6 spatial locations tested (assuming linear elasticity with no time-dependence over the testing duration). Therefore, the measurements presented represent a measure of linear bending stiffness for a 1.25 mm input displacement.

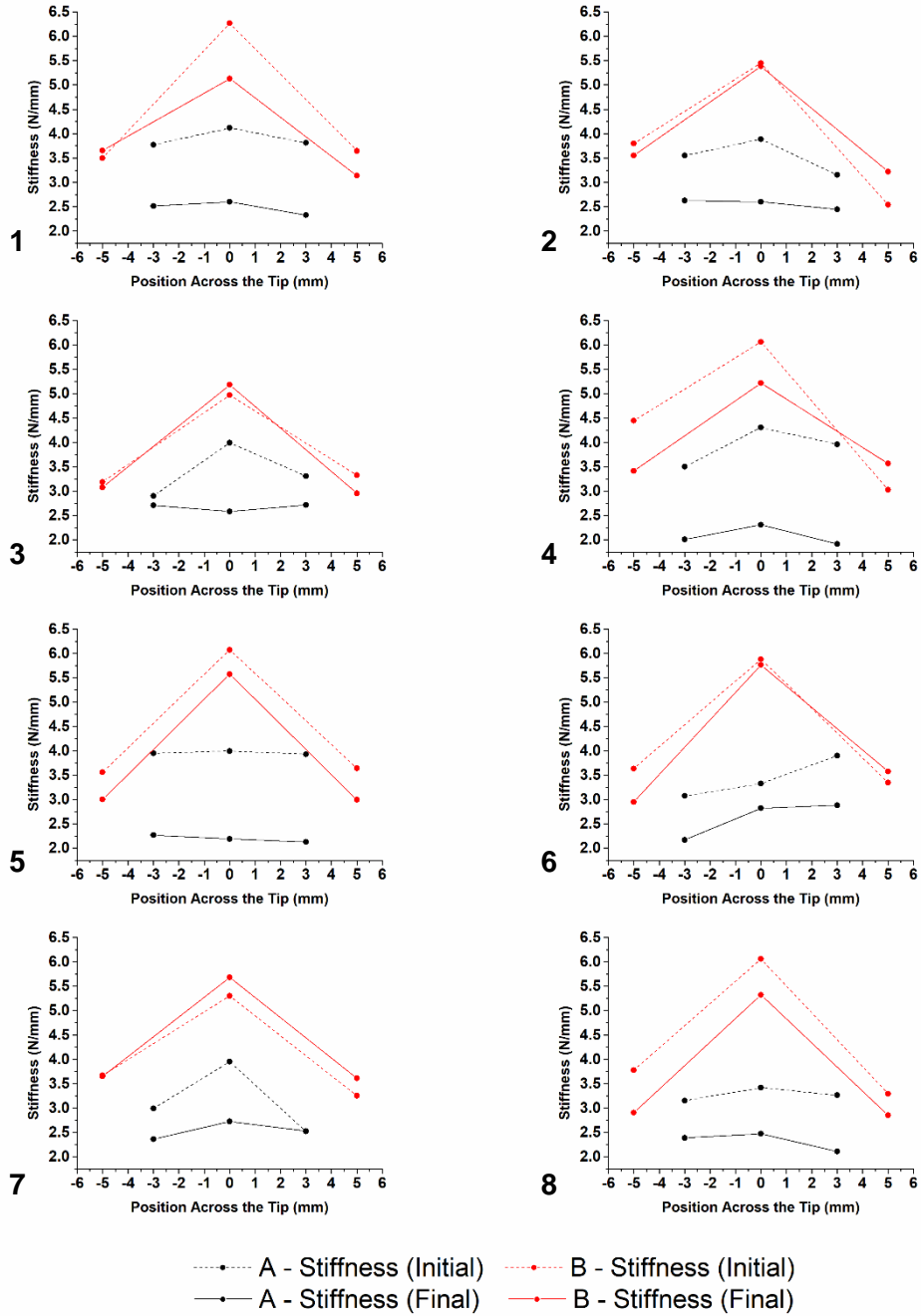


Figure 4-8: Initial (dashed) and end-of life (solid) bending stiffness (N/mm) for the 8-reed musician set. All 6 data points for each reed are used to plot spatially dependent stiffness at A and B (black and red lines, respectively) positions along the tip. Reed numbers within the set are depicted on each of the plots.

The orientation of these plots is such that the x-axis represents distance along the reed tip (in the tangential direction, with respect to the ADL culm), where the 0 mm point is located at the centerline of the reed vamp along the longitudinal direction. Using data from the A and B positions, these plots create a stiffness map of the reed vamp. The longitudinal axis is aligned with the y-axis and these plots represent spatially dependent stiffness within the longitudinal-tangential plane of the Arundo culm. Results for tip stiffness for the final measurement taken on all reeds at the end of their lifecycle are also provided. It should be noted that the influence of torsional deformation on bending stiffness was not considered here. Although torsion is likely to be induced by bending along the off-axis positions, a reduction in bending stiffness from the beginning to end of the study is still indicative of the aging process and not only due to mixed-mode deformation types. Additionally, lower off-axis bending stiffness is still an indicator of stiffness asymmetry as more symmetrical stiffness profiles along the tip would suggest simple bending dominates the deformation mode, with less torsional influence. This information is also useful towards the understanding of inter-reed variability and aging related changes.

Contour plots of stiffness rate-of-change are provided in Figure 4-9. These plots illustrate stiffness changes along the reed vamp during their lifecycle. There are two scalebars in the figure to account for relatively large changes in the stiffness of two specific reeds during the study (as mentioned in the figure caption).

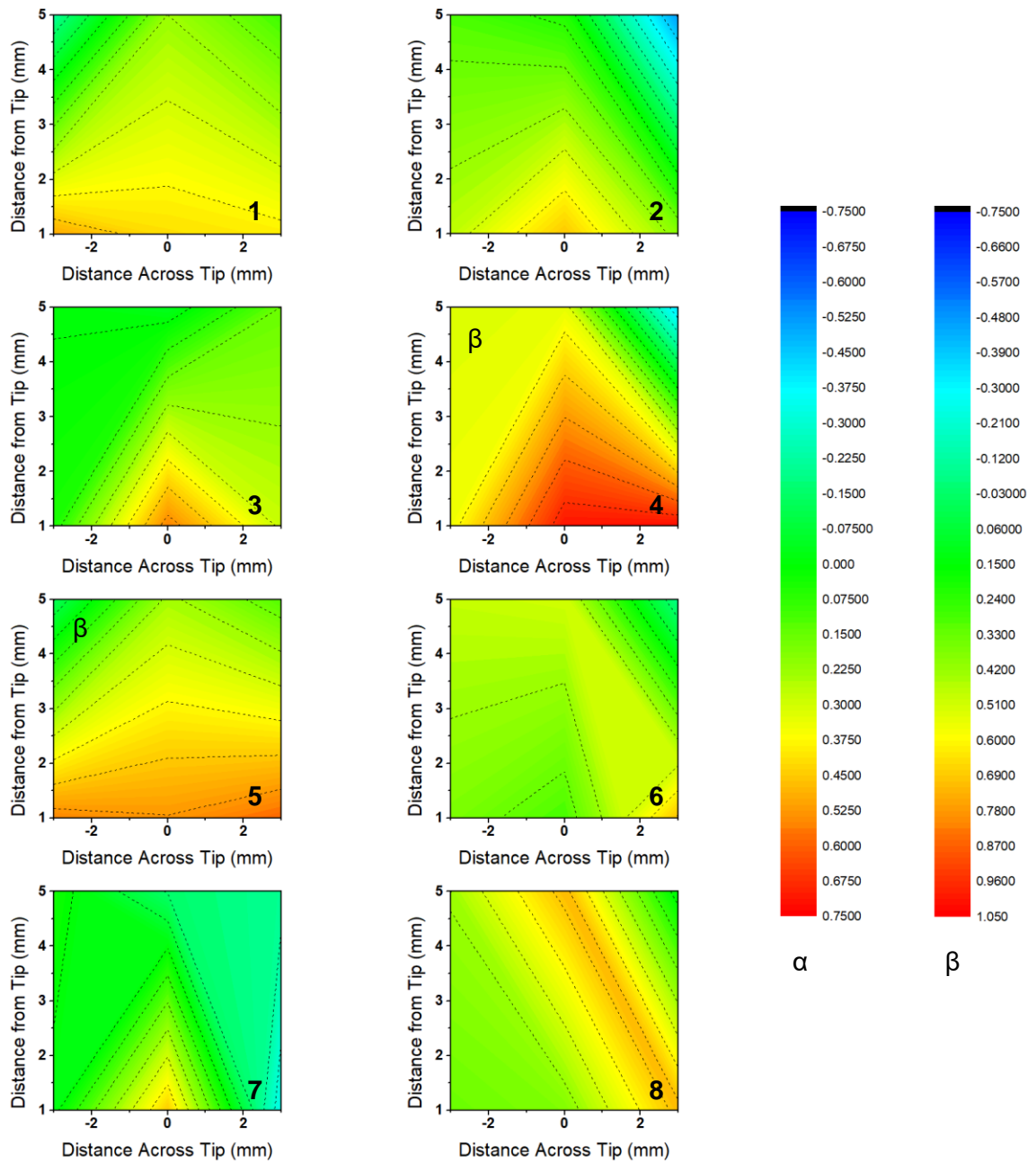


Figure 4-9: Rate of change of bending stiffness (N/mm/hr) for each of the measured spatial positions along the reed tip. Contour plots have been presented with two different scalebars due to substantial differences in stiffness degradation. Plots corresponding to the β scalebar are indicated, while all other plots are provided with respect to the α scalebar.

The plots of stiffness rate of change indicate that A-position values (i.e., the ones closest to the reed tip) deteriorate more significantly and more rapidly than B-position values. This suggests that degradation along the tip is the most significant component of deterioration during a reed's lifecycle, including mechanical and moisture/saturation fatigue. Differences between reeds within this set are quickly visualized through these degradation plots. This will be discussed in further detail with respect to the musician's rankings in the discussion section. Furthermore, this may indicate that complete reed wetting during playing is confined to the tip region of the reed vamp and thus degradation of parenchyma cells due to cell wall collapse is less prevalent as the distance from the reed tip increases (fibers do not exhibit significant elastic degradation during a complete reed lifecycle).

4.3.2 Subjective Stiffness Evaluation

Consideration is also given to the musician's subjective stiffness rankings of the reeds. Figure 4-10 provides the average stiffness rank for each reed over the duration of the study. Rankings in this plot represent temporal averages, including 24 ranking events. Reed 7 is shown without error bars as this reed was always considered to be the stiffest by the musician.

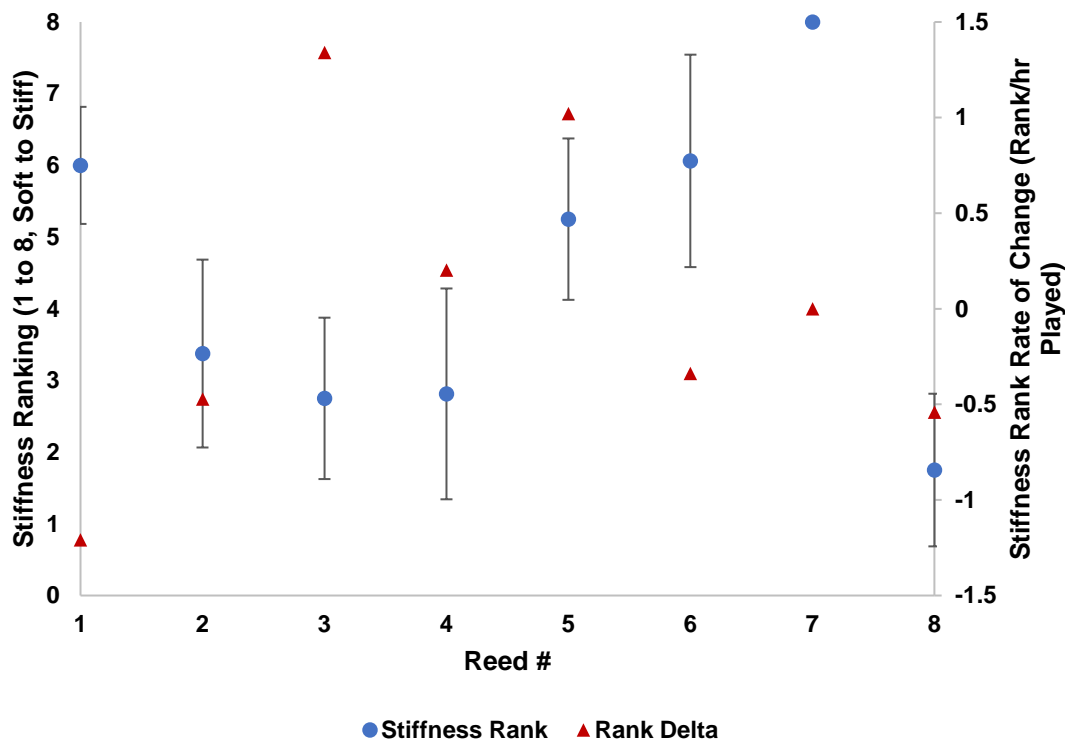


Figure 4-10: Subjective stiffness rankings over the lifespan of each reed. Stiffness rank rate of change is also shown on the right axis. Error bars are provided as standard deviation.

Temporal changes in subjective rankings are also shown in this figure via stiffness rate of change. Rate of change is provided as the change in stiffness rank per hour of playing and is an indicator of reeds that the musician found to change more significantly than others. Larger values of this metric indicate a larger net change in subjective stiffness relative to the other reeds in the set. For example, the musician considered reed #1 to vary much more significantly than reed #4 and overall found it to become softer with time. The musician also found reed #3 to vary significantly, although they found it to become stiffer with time. Reed 7 exhibited the least amount of variability in terms of musician ranking, as shown from the rank delta in Figure 4-10.

A summary of objective and subjective measurements is provided in Figure 4-11. These plots facilitate the comparison of all objective and subjective rankings per reed over the duration of the study. Here each box contains the upper and lower ranking bounds and the average rank for the entire study. The box plots also illustrate the importance of off-axis stiffness measurements in terms of predicting the subjective stiffness ranking and they provide a quick visual reference for reed variability, where large boxes indicate reeds that changed significantly during their lifecycle.

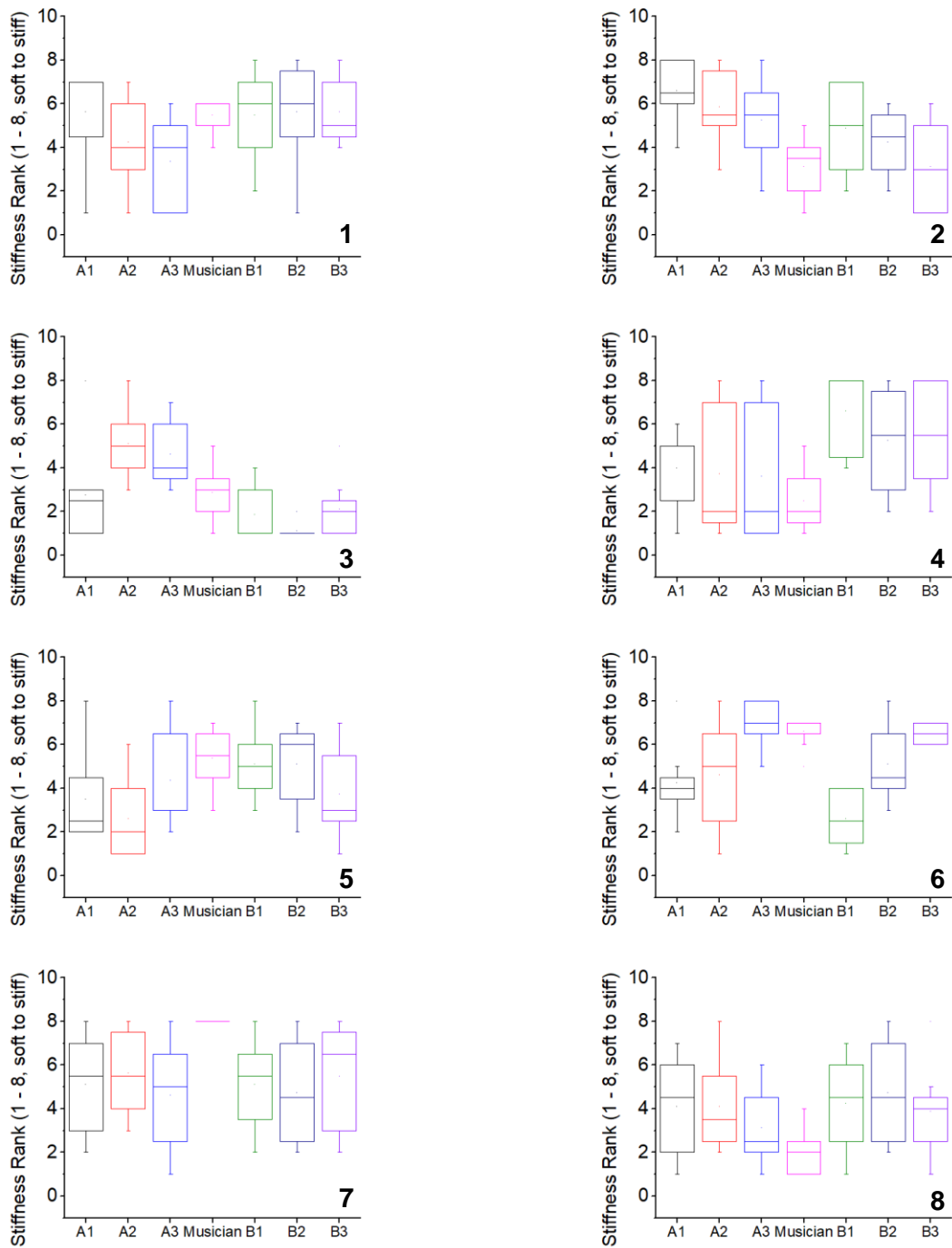


Figure 4-11: Box plots of stiffness ranks for objective measurements and the musician's assessments. The reed number is noted in the lower right quadrant of each plot. Rankings are presented on a 1 to 8 scale, where 1 and 8 represent the softest and stiffest reed, respectively.

Figure 4-12 provides a direct comparison between average stiffness rankings for the musician's ratings and bending stiffness measurements at the B3 tip position. The B3 position is depicted as it provided the strongest correlation with the musician's rankings. Statistically significant correlations between objective and subjective stiffness rankings and time dependence will be considered in the discussion. Although differences are observed for reeds 4 and 7, it appears that the musician's perception of reed stiffness is related to the off-axis value of bending stiffness 6 mm from the reed tip.

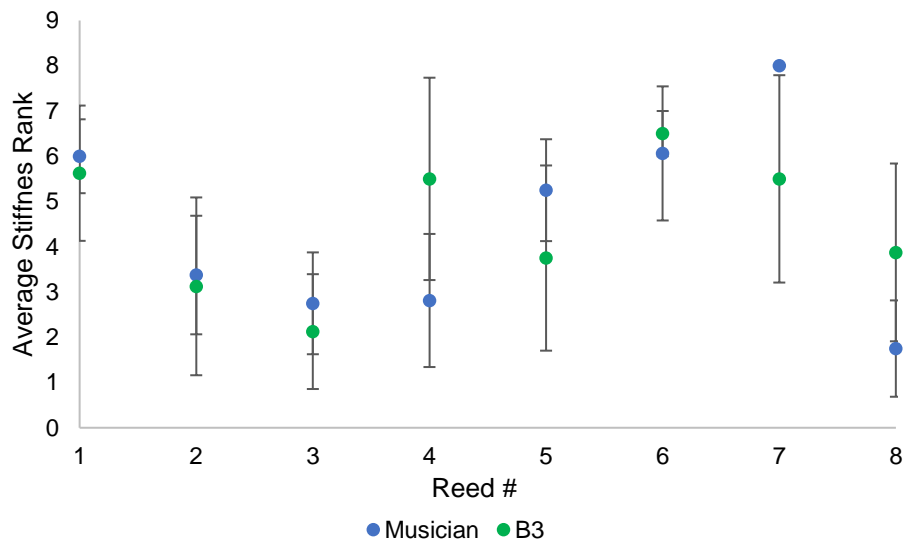


Figure 4-12: Comparison of the musician's stiffness rankings with B3 spatial location bending stiffness rankings (average values over the duration of the study). Error bars are provided as standard deviation.

4.3.3 Comparison Reed Set

Static bending stiffness values at A2 and B2 spatial positions were obtained for the 40-reed comparison set. This was performed to examine the quality control of typical stiffness sorted reeds. As previously mentioned, 10 reeds from 4 different manufacturer stiffness ratings (2S, 3S, 3M and 4H) were measured and the results are shown in Figure 4-13 for A2 and B2 stiffness positions. It was expected that the 3H reeds from the musician set would fall in between reeds of 3M and 4H rating, although the magnitude of differences was unknown. The stiffness data for the 3H reeds compared here was obtained prior to beginning the study with the musician (i.e., initial values of stiffness).

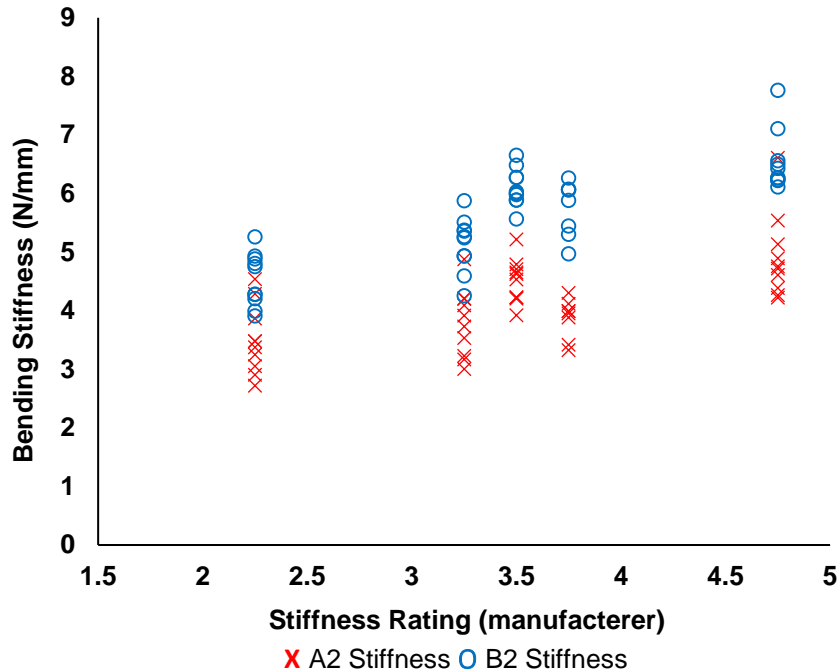


Figure 4-13: A2 (red crosses) and B2 (blue circles) position bending stiffness measurements for the comparison and musician reed sets. All measured samples are plotted.

There is a large amount of overlap in stiffness between sets measured at the A2 position. This suggests that more rigorous material classification of the tip is necessary to elucidate differences in reeds at this spatial location. For these A2 stiffness positions no single reed set was statistically different from every other set, although the 4H reeds were stiffer than all but the 3M set ($p < 0.01$). The musician's set (3H) was softer than the 4H set ($p < 0.01$), with no other differences being observed. In general, the 2S and 3S reeds were softer than the others, but not significantly different from each other. Statistically, the B2 stiffnesses for the 2S and 3S reed sets were significantly different from each other and all other sets ($p < 0.05$), indicating that on average they are indeed the softest reeds. Reed sets 3H and 4H were substantially stiffer than all but the 3M reed set. There is still significant overlap as denoted by the standard deviation suggesting that it is likely to receive reeds in a 2S box that could be found in a 3S set and it is also possible to obtain 4H rated reeds in a 3H box. Differences between reed sets of rating 3M and stiffer are not so clear and suggest that the ratings offered by manufacturers could be improved to mitigate variability. It is possible that reed stiffness changes post-sorting and packaging that could influence the results of initial testing during manufacturing. It may be worthwhile for manufacturers to

condition reeds for some time after machining and prior to sorting/packaging, although the benefits of this (in terms of mitigating variability) with regards to the current accepted method of testing bending stiffness is not known.

4.3.4 Anatomical Structures

In addition to the anatomical features considered in Table 4-1 several other metrics were also analysed. These other metrics were analysed to capture and find correlations with changes in bending stiffness over time and to analyse asymmetry in bending stiffness and anatomical structures. Asymmetry was quantified by calculating the difference between distribution means for vascular bundle (VB) centroids at three spatial locations along the tip. These were located at the A1, A2 and A3 positions along the x-axis (tangential direction) of the micrograph cross-section. A typical heel cross-section that has been processed, segmented and classified is shown in Figure 4-14. Several of the extracted anatomical metrics are also illustrated in this figure. All spatially (radial with respect to micrograph cross-section) dependent measurements such as fiber area fraction and VB area fraction have been provided with respect to a normalized (0 to 1) heel cross-section height. In these cases, the 0 position represents the flat underside of the reed vamp (i.e., the inside diameter of the Arundo culm) and the 1 position the outer epidermal layer of the reed (i.e., the outside diameter of the Arundo culm).

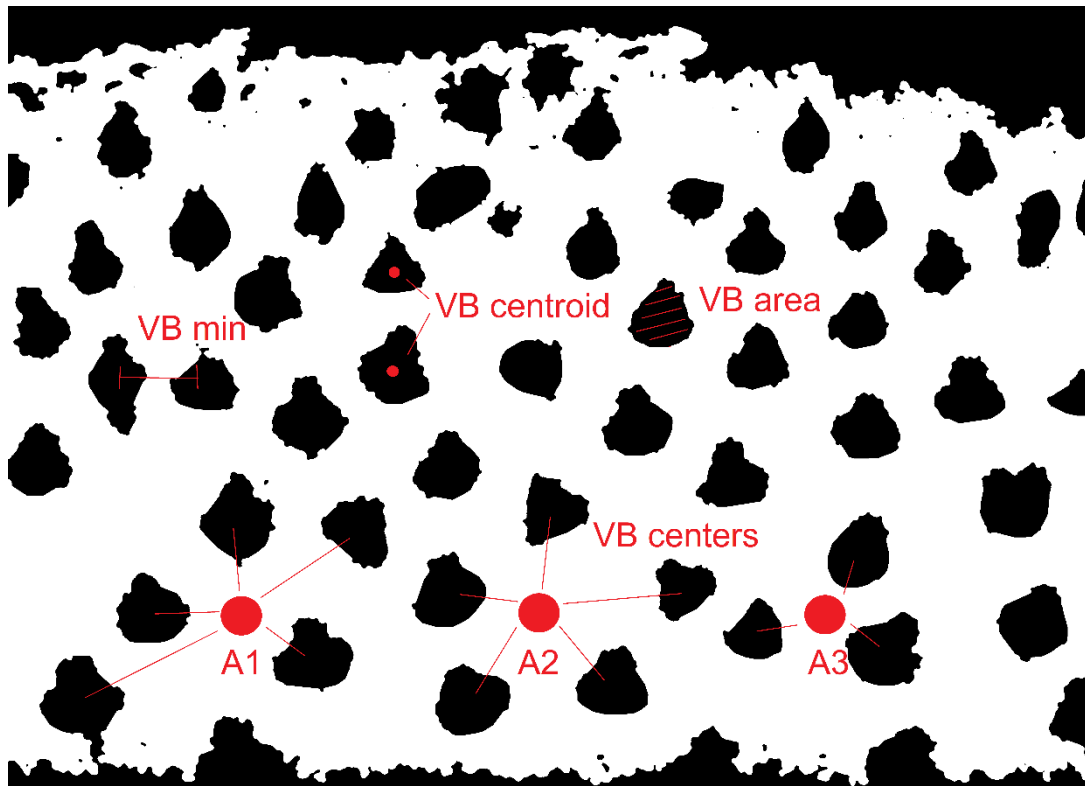


Figure 4-14: Cross-section of a typical reed heel that has been processed and segmented. Visualizations of quantification methods for several anatomical features are provided. Note that these binary images were denoised prior to automated analysis. These images represent the phase masks that were obtained from the image processing technique outlined previously. Note that the VB's surrounding points A1, A2 and A3 are only provided as an illustration and do not represent the total number of surrounding VB's analyzed. Refer to Table 1 for more details.

In this figure the VB centers are shown with respect to their corresponding spatial position. The A1, A2 and A3 positions represent centroids about which the nearest vascular bundle neighbours were located and analysed in terms of Euclidian distance.

Other metrics aimed at classifying anatomical structure size and morphology included shape parameters for VB spatial arrangement, VB centroid positions and VB area distributions. These metrics were all compared to measured bending stiffness values. The shape metrics were measured as Weibull shape parameters and their importance relates to the quantification of VB spatial distributions (i.e., skewness). Typical results for the comparison set reed heels are provided in Figure 4-15. The asymmetry of these distributions is due to the spatial density of VB's throughout the reed cross-section, with density increasing towards the inside diameter of the culm.

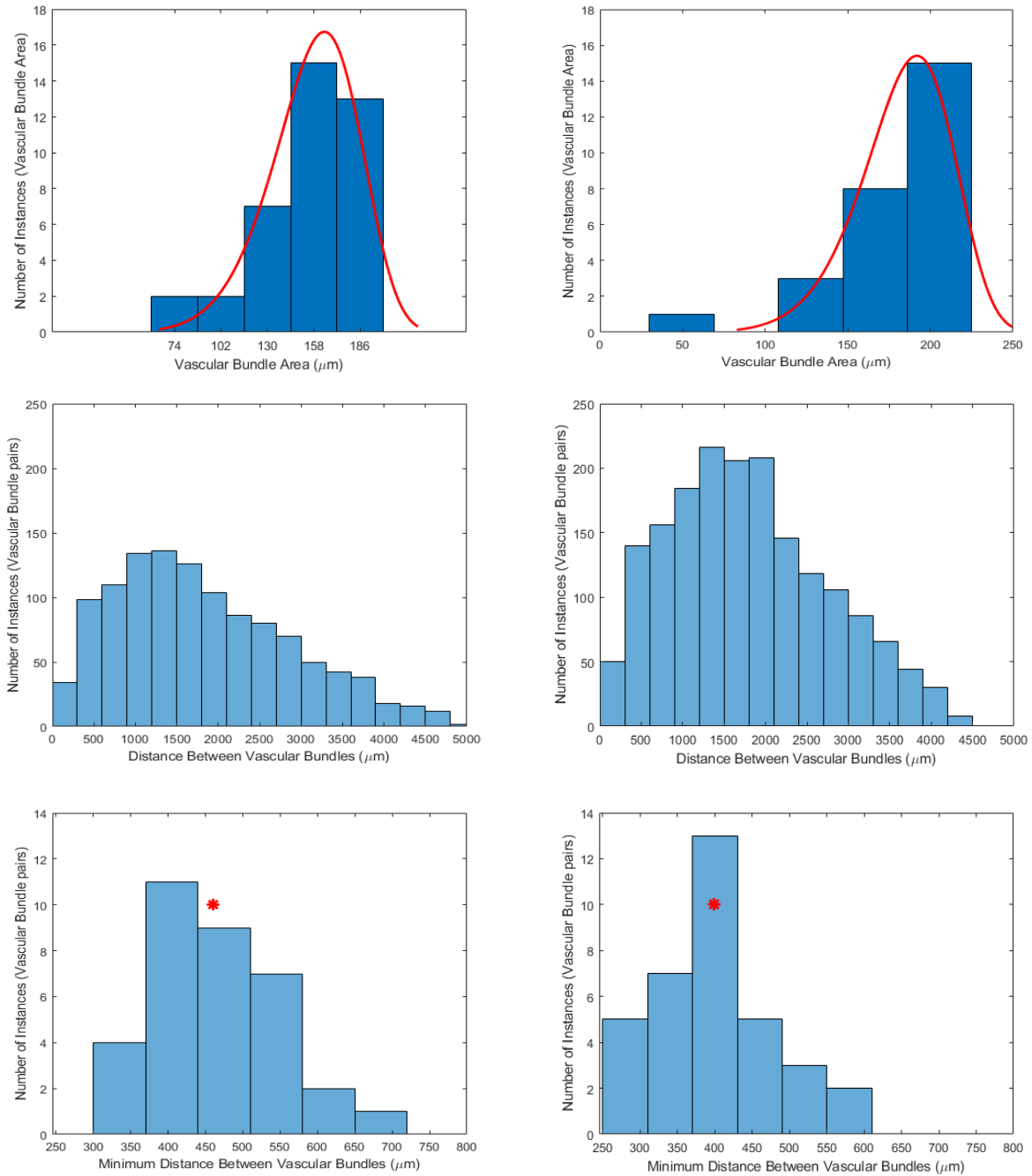


Figure 4-15: Left: Distributions of vascular bundle area, distance between vascular bundle centroids and minimum average distance (nearest neighbour) between vascular bundle centroids for a 2S reed. Right: The same distributions presented for a 4H reed. Note distance between vascular bundles is a distribution of Euclidian distance between each centroid pair within the heel cross-section. This provides a measure of average spacing and spacing density. For vascular bundle area a Weibull distribution is fit to the data and shown as a red line. The location parameter for the fitted Weibull distribution is provided for the minimum vascular bundle distance as a red asterisk. All units are in microns and the x-axis limits of each corresponding plot pair are equal.

PCA was used to visualize all the gathered anatomical and bending stiffness data for all the measured reeds. This was performed on all the reeds in a combined data set to check for overall trends of stiffness dependency on features of interest. 5 principle components were found to account for 70% of the variance in the data. From the PCA results, components 1, 2 and 3 account for 21.94%, 14.59% and 11.98% of the variance in the data, respectively. The density of VB's surrounding the central axis (VB A2 density) of the reed vamp appear to be negatively correlated with stiffness at position B2, and less significantly correlated with A2 stiffness. VB area fraction is positively correlated with stiffness at both spatial locations. Stiffness at the A2 position appears to be influenced by more localized VB morphology including VB area (i.e., size of individual bundles) and VB perimeter (indicative of the size of continuous fiber rings surrounding the inner VB). Although not analysed for the comparison reed set (and thus not studied here), it is likely that the density of VB's surrounding spatial locations A1 and A3 would be negatively correlated with stiffness at those locations, following the trend observed along the central reed axis.

Further data analysis on all reed samples using Pearson correlation coefficients has been summarized in Table 4-2. The correlation was performed on the entire reed set, regardless of manufacturer stiffness rating.

Table 4-2: Summary of correlations between A2 and B2 reed bending stiffness and anatomical structures.

Correlated Variables	Correlation Coefficient	p-value
A2 Stiffness – VB Area Fraction	0.344	< 0.03
B2 Stiffness – VB Distribution	0.299	< 0.05
B2 Stiffness – VB Maximum Centroid Separation	-0.292	< 0.05
B2 Stiffness – VB Center Density (central axis)	-0.384	< 0.01
B2 Stiffness – VB Area Fraction	0.630	< 0.0001
B2 Stiffness – VB Center Density (Off-axis A3 position)	-0.523	< 0.0001

From these correlations the spatial density, size and morphology of VB's through the reed cross-section influence central axis bending stiffness most significantly. It also suggests that reed sorting according to several VB metrics could lead to less variability in terms of stiffness. The relationship between bending stiffness and VB area fraction is shown in Figure 4-16. As previously discussed, the stiffness overlap between reeds of different manufacturer rating is evident here.

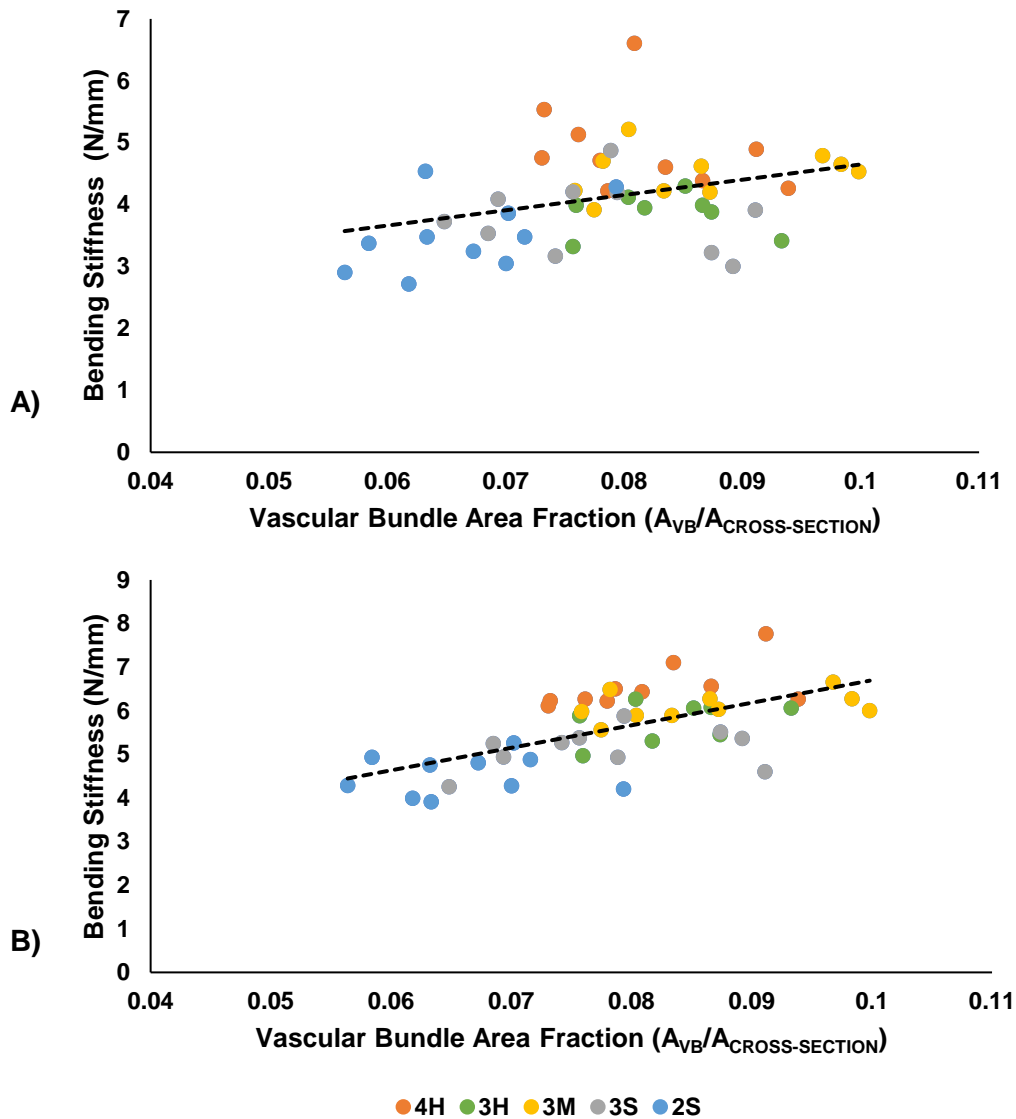


Figure 4-16: A) A2 position stiffness versus VB area fraction for all the reeds in the study (i.e., both the musician and comparison sets). Individual manufacturer stiffness ratings are colour coded according to the legend. ($r = 0.33$, $p < 0.03$). B) The same results presented for the B2 position bending stiffness measurements. ($r = 0.630$, $p < 0.0001$)

The asymmetry of reed stiffness and spatially dependent anatomical features were of specific interest for the musician reed set where more stiffness measurements per reed tip were made. To perform this comparison, stiffness metrics included the magnitude and sense (positive or negative) of differences between A1 and A2, and A3 and A2 bending stiffness values. Such metrics thus represent asymmetry about the central reed axis (along the longitudinal direction). These same differences were also calculated for the B stiffness positions. It should be reiterated that all stiffness values were normalized with respect to thickness. Stiffness measurements on this reed set were repeated 8 times over the duration of the study to examine changes with time. Considering this, Pearson correlations were computed for all anatomical variables of the musician reed set (consistent with the method outlined for Table 4-2 results), initial stiffness values and time-dependent stiffness values to examine linear relationships between the variables. This facilitated more detailed comparison of reeds of equal manufacturer stiffness rating. A summary of findings is presented in Table 4-3.

Table 4-3: Pearson correlations between anatomical structures and stiffness parameters for the musician reed set (3H rating).

Correlated Variables	Correlation Coefficient	p-value
A2 and A3 Stiffness end-of-life – Asymmetry	-0.911, -0.862	< 0.01
B2 Stiffness end-of-life – Solid Fiber Modulus	-0.761	< 0.03
A3 Stiffness end-of-life – Solid Fiber Modulus	0.800	< 0.03
A2 Stiffness Delta – VB Ellipse (aspect ratio)	-0.792	< 0.03
A3 Stiffness Delta – VB Centroid Density (A2 position)	-0.781	< 0.03
B3 Initial Stiffness – VB Perimeter	0.735	< 0.05

It was also discovered that after the time played on each reed was greater than 1.5 hours, stiffness at positions A1, A2, B1 and B2 correlated with VB Area Fraction ($r > 0.773$, $p < 0.03$ for all cases). This is interesting given that VB Area Fraction is also positively correlated with initial

stiffness for reeds of different manufacturer rating and suggests that predictions of reeds exhibiting reduced stiffness upon aging could be predicted using this metric. VB area (i.e., the area of an individual bundle and not area fraction) was also correlated with the modulus of solid fibers ($r = 0.850$, $p < 0.01$). This suggests that reeds having larger VB's also contain more stiff solid fibers, and the importance of VB size and distribution cannot be overstated with respect to bending stiffness. The A3 stiffness delta was also found to be correlated with A1, A2 and A3 stiffness when reed playing time was greater than 2 hours per reed. The growth of the *Arundo culm* may lead to anisotropy in the orientation of VB's within the cross-section, resulting in an off-axis dominated stiffness after significant fatigue. As is evidenced by the negative correlation between B2 end-of-life stiffness and solid fiber modulus and the opposite correlation for A3 end-of-life stiffness, the microstructural mechanism controlling stiffness of the tip may be different from areas closer to the heart of the vamp (further towards the heel of the reed). Directly at the tip (A-positions), this result suggests that solid fibers contribute most significantly to bending stiffness, while at the B2 positions the surrounding parenchyma cells play a more significant role. The stiffness delta for A2 positions is also negatively correlated with the aspect ratio of VB's (the VB Ellipse parameter). Here VB morphologies approaching a circular perimeter appear to age less significantly than more elliptical VB's (i.e., those with a higher aspect ratio). This may be of geometrical consequence as load sharing between the VB's and parenchyma cells may be less efficient for high aspect ratio VB's.

Comparisons with variability in musician rankings were also analysed. Variability in subjective rankings was an important metric as difficulty in assessing the current stiffness of a reed may be indicative of more rapidly changing reeds. For this the standard deviation of subjective stiffness rank per reed was used, as it was notable that one reed was continuously ranked as the stiffest by the musician, while some of the other reeds deviated during the study. For the 8 reeds in the musician set (of manufacturer rating 3H), the musician's stiffness rankings were correlated with stiffness asymmetry of the A-position measurements ($r = -0.282$, $p < 0.03$). The stiffness asymmetry at these positions is a measure of the magnitude of stiffness disparity between the A1, A2 and A3 locations. The negative correlation here indicates that the musician identifies reeds as being softer when the off-axis stiffness values (at A1 and A3) at the tip are different from the A2 values. The standard deviation of the musician's rankings of each reed during the study were positively correlated with the A3 stiffness delta of each reed. Thus, reeds that undergo more rapid

changes in bending stiffness are more difficult to assess in terms of perceived stiffness. Rate of change of subjective stiffness rankings was also considered and found to correlate with the VB Area parameter. These results are shown in Figure 4-17.

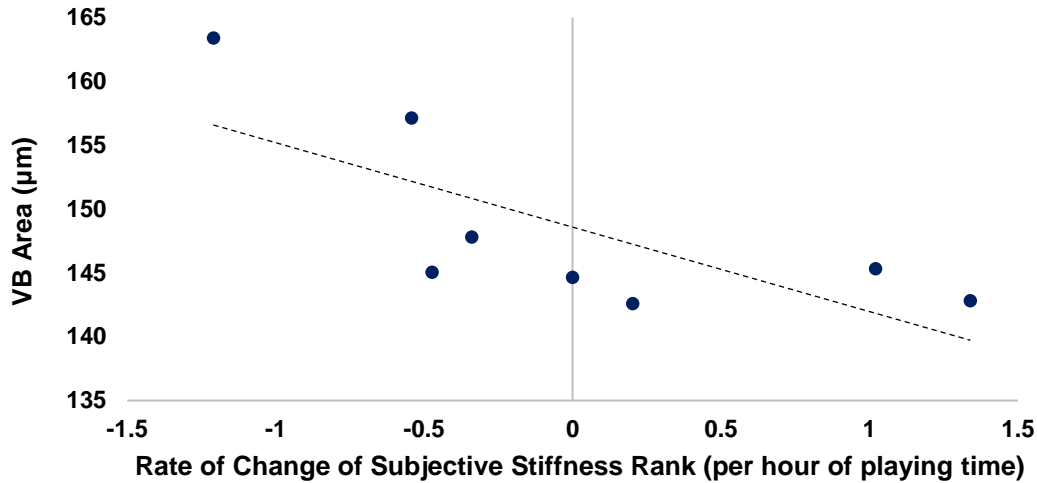


Figure 4-17: Changing stiffness rankings by the musician over the duration of the study compared with VB area. ($r = 0.736$, $p < 0.05$)

Increased measured bending stiffness towards end-of-life is correlated with reeds containing larger VB's as previously discussed. For the musician these results indicate that reeds perceived as increasing in stiffness during their life have a larger area fraction of parenchyma cells than reeds that are perceived to soften. Considering these two findings it would suggest that the musician's perception of stiffness is controlled to a greater degree by the parenchyma cells as reeds with a smaller average VB area contain a larger (in terms of area fraction) percentage of parenchyma cells.

4.3.5 Solid Fiber Density and Distribution

All the segmented reed heel images were analysed at 4 radial positions along the radial direction of the heel. In this way, the segmented heel micrographs were separated into 4 different cross-sectional slices to give radial dependent measurements of solid fiber area fraction (with respect to overall micrograph area and parenchyma). An example of these slices and the original micrograph are shown in Figure 4-18.

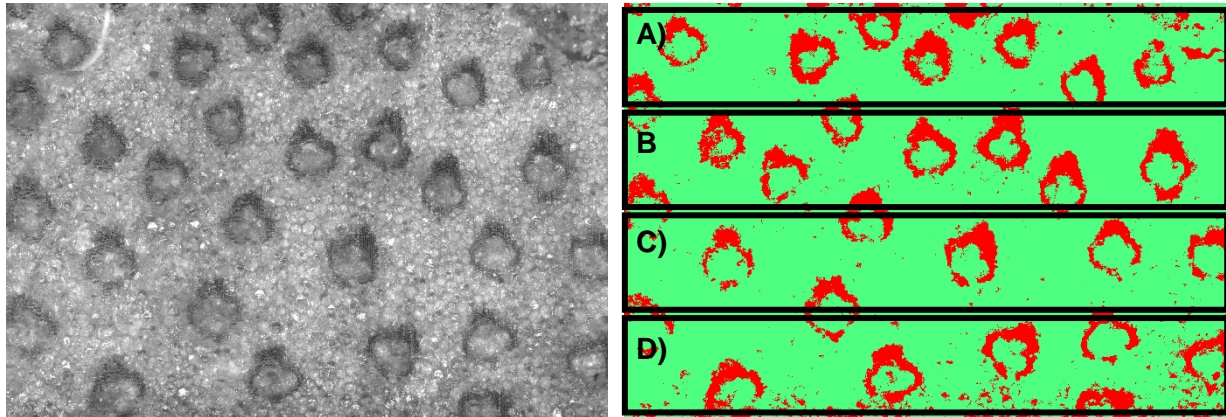


Figure 4-18: Left: Original micrograph of reed heel cross-section. Right: Segmented image to identify solid fibers surrounding the VB's. The four analyzed radial sections are shown as, from outside to inside diameter, A, B, C, D. A represents 1 in the normalized radial distance used from graphing the relationship of solid fiber area fraction and radial position.

All micrographs were obtained at the same optical magnification and thus the physical spatial distances in each micrograph is the same, and thus all reed scales are equal. All of the trendlines for fiber area fraction versus normalized radial position are presented as quadratics as they exhibited the best fit to the data. Previous measurements of solid fiber distributions in bamboo have also shown similar fits to be the most appropriate for the fiber density gradient [49]. A typical result between two reeds is shown in Figure 4-19.

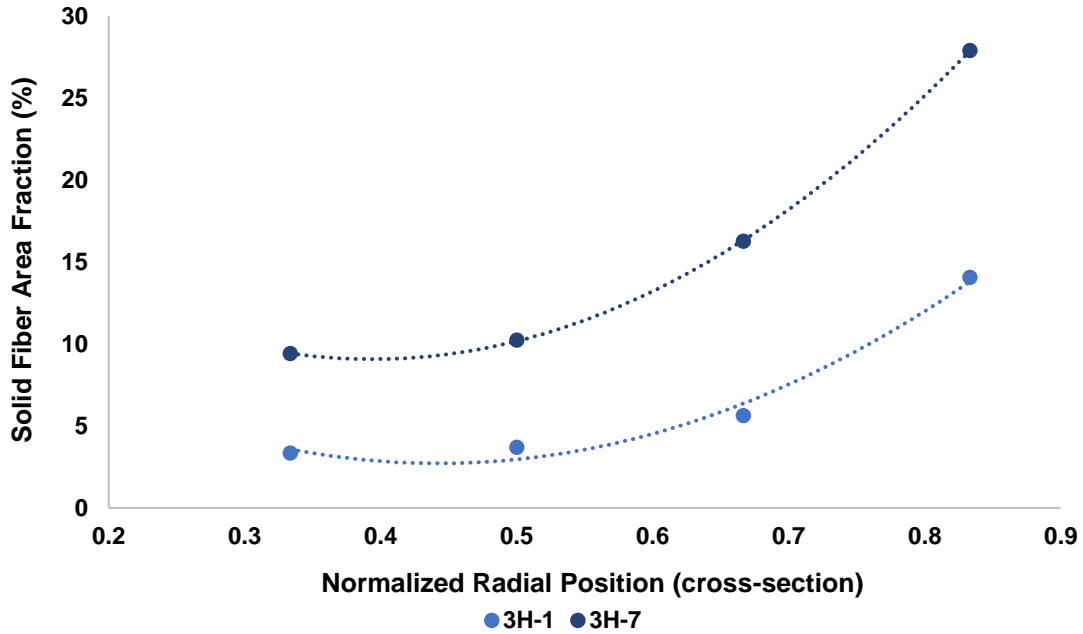


Figure 4-19: Radial dependence of solid fiber area fraction surrounding the VB's. Shown here are two reeds from the musician set.

The dependence of fiber area fraction on radial position with respect to the *Arundo culm* indicates that reed tip geometry and thickness will greatly influence the resulting bending stiffness of the finished product.

Changing reed masses during the study were also monitored to detect potential changes in moisture absorption. Moisture uptake was measured as the increase in mass relative to the initial reed mass and was found to depend on the size of VB perimeters within the cross-section (Figure 4-20).

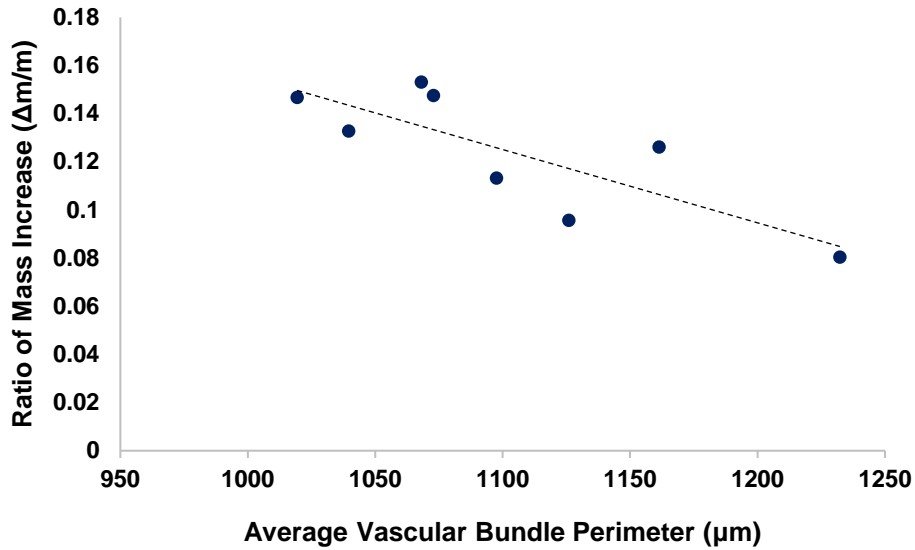


Figure 4-20: Mass increase due to moisture absorption in reeds from the musician set and the dependence on VB Perimeter.

4.4 Analysis and Discussion

The use of a strain gauge to determine average bending strain during playing was previously discussed in the introduction section. A typical strain–time curve for an arpeggio played with a crescendo is shown in Figure 4-21. Note that strain peaks represent each of the sustained notes played.

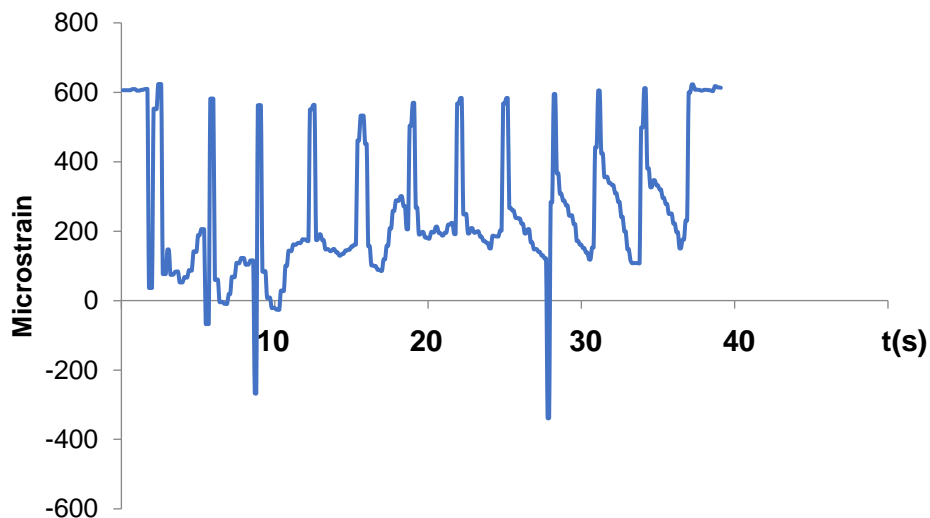


Figure 4-21: Microstrain plot of reed tip bending for a 3H rated reed in-vivo. The musical structure played on the alto saxophone was an arpeggio.

The bending strain during playing was used to calculate an average stress in the reed, assuming a bending modulus of ~ 6 GPa. This modulus was calculated from a model developed in the latter part of this section. Using the maximum value of strain from this data, an average bending stress of 4.09 MPa was calculated. During this test the musician also produced a tone that he considered to be the maximum reasonable clamping force the reed would be subjected to during a performance. Using this value of microstrain (~800 to 900) the bending stress increases to 5.45 MPa. These values show that reed fatigue is likely a complex combination of mechanical bending and moisture saturation. These values of strain also informed the prescribed displacement that reed tips were subjected to during bending stiffness testing.

Stiffness rankings of the musician set have been compared between the musician's ranks and the objective measurements. As observed from Figure 4-12, a general trend agreement between the average values of B3 stiffness for each reed and the musician's average ranking is observed. With specific regard to reeds 1, 4 and 6 from this set significant ($p < 0.05$) agreements between the subjective and B2/B3 objective rankings are found. This significance indicates that for these particular reeds the musician's stiffness ranking tracked well with the actual bending stiffness over the duration of the study. It is also worth noting that the musician found reed number 8 from this set to be "odd". It is the only reed to exhibit a net loss in stiffness at all spatial locations during the duration of the study as shown in Figure 4-22. From the stiffness rate-of-change plots in Figure 4-9 it is also observed that the spatial distribution of stiffness change across the reed vamp is highly heterogeneous, whereas other reeds exhibit a gradient of changing stiffness that is highly directional. This may suggest a more rapid collapse of parenchyma cells within the matrix of this reed that also recovers in between playing sessions, resulting in erratic changes in stiffness between tests. The collapse and recovery of parenchyma cells upon drying – re-saturation in *Arundo donax L* has previously been noted [5]. Figure 4-22 depicts the overall changes in stiffness for the musician reed set during the study.

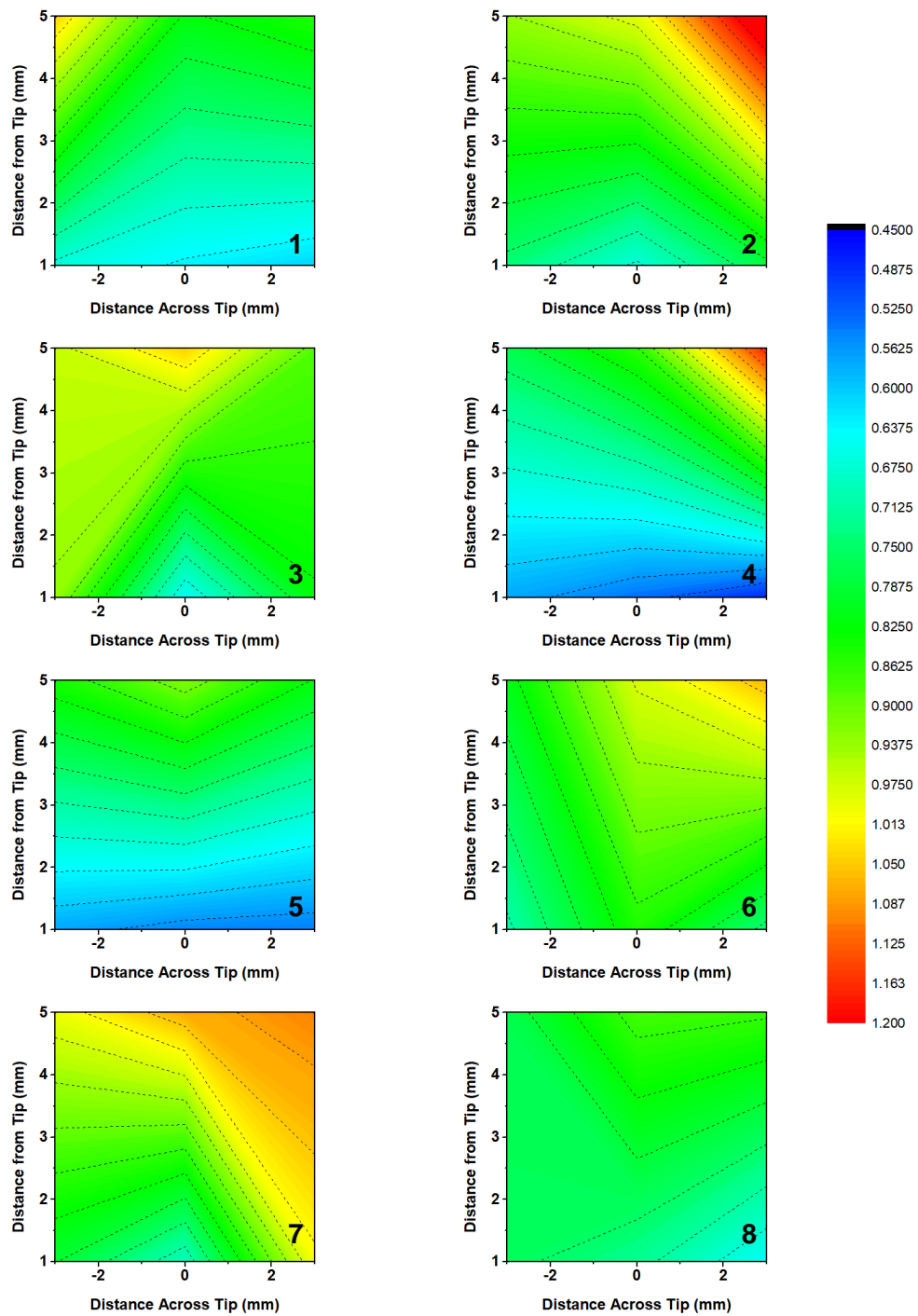


Figure 4-22: Bending stiffness change for the musician reed set over the duration of the study. Results are plotted as the fraction of initial stiffness for each spatial position (A1, A2, A3, B1, B2, B3).

In general, all reed tips along the A-positions exhibited a reduction in stiffness relative to initial values. This is not surprising given the large stresses that reeds experience in-vivo and the fact that large magnitude tip displacement is likely confined to the immediate region surrounding the A-positions [40]. As well be discussed in Chapter 5, the solid fibers of the VB's do not experience an increase in elastic modulus upon exposure to moisture cycles. It follows that reeds experiencing a slight increase in bending stiffness at the B-positions would owe this increase to the parenchyma cells of the matrix and not to the solid fibers. Similar to the correlations between A-position stiffness and anatomical structures presented in the results section, this also indicates that A-position tip stiffness is highly dependent on the VB structures. The differences observed for the aging behaviour of A- and B-position stiffness also show that a single, average value of bending stiffness taken closer to the heart of the reed (i.e., ~15 mm from the tip, along the longitudinal axis) is not sufficient to quantify the differences between reed tips. Given that this area of the reed is undergoing significant displacement during playing the differences discussed here should not be ignored.

4.4.1 Bending Stiffness Modeling – Empirical Approach

Analysis of the anatomical features of the comparison set (stiffness ratings 2S, 3S, 3M and 4H) was performed to generate fitting variables for a stiffness prediction model (for A2 and B2 stiffness measurements specifically). The importance of anatomical variables was measured using a linear correlation matrix and principal component analysis. The variables with the highest levels of correlation to static stiffness measurements at A2 and B2 positions and those accounting for the majority of variability in stiffness measurements were used to fit an empirical relation to all of the bending stiffness measurements. The most important anatomical features for bending stiffness prediction are shown in Table 2. All the correlations and fittings for this data are with respect to anatomical and bending stiffness variables obtained from all the reeds in the comparison set (i.e., not using data from the 3H set played by the musician). Only variables that were not co-dependent were used for the construction of a multi-linear regression model of no more than 4 independent variables. The purpose of constructing this model was to determine if reasonable predictions of bending stiffness along the central axis of the reed vamp could be made from only anatomical features. This would enable the use of a non-contact (i.e., optical microscopy) form of reed categorization with better stiffness resolution than presently implemented methods. It should be

noted that this type of prediction methodology is of interest for manufacturing as optical methods of reed categorization are possible to implement practically, where speed is critical to the machining and sorting process. The variables were rotated through the model until the best fit between predicted and measured values of A2 and B2 stiffness for the musician set were obtained. The goodness of fit was measured as a minimization of residuals between the actual and predicted stiffness values. Although it may be possible to categorize using other static and/or dynamic techniques, many of them are too time intensive or expensive to be practically viable for a manufacturing process.

The fitted parameters for this empirical model included VB Area Fraction, VB Center (Euclidian distance between VB's) and Fiber Area Delta (the second order term of a polynomial fit to the data shown in Figure 4-19). The general form of this linear model is shown below.

$$C_{bending} = W + X \cdot VB_{AreaFraction} + Y \cdot VB_{Center} + Z \cdot Fiber\ Area_{Delta} \quad (4-1)$$

Fitting this linear equation led to the following parameters for A2 and B2 positions:

$$A2: W = 3, X = 25.9, Y = -9.32 \times 10^{-4}, Z = -1.53 \times 10^{-5}$$

$$B2: W = 3.2, X = 46.9, Y = -1.34 \times 10^{-3}, Z = -9.12 \times 10^{-5}.$$

The results of the fittings are compared with initial A2 and B2 stiffness values in Figure 4-23.

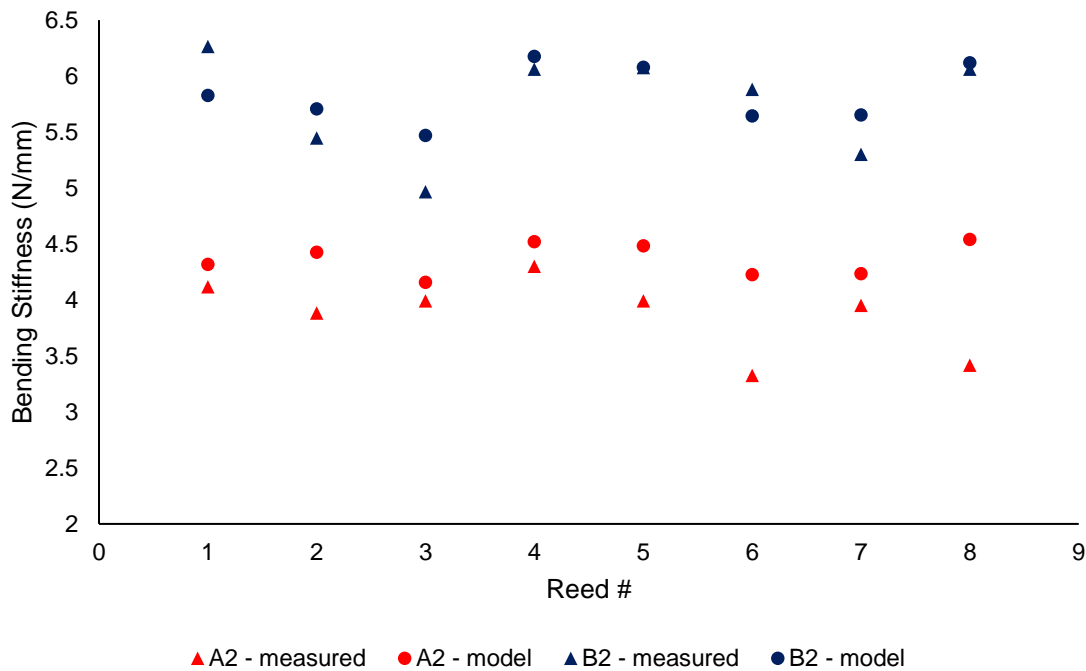


Figure 4-23: Empirical model of bending stiffness compared with measured results for A2 and B2 positions. Data is shown for the initial measurements made on the musician reed set prior to the reeds being played.

Maximum error between calculated and measured stiffness values at the A2 positions is 24% as observed for reed number 3H-8. Mean error is 13% with the general finding that stiffness is underpredicted overall. Maximum error for B2 stiffness is 9% with a mean error of 7.5%. It is worth remembering that the parameters of the model were derived from fitting to bending stiffness data from the comparison set and is independent of the results from the musician set. These findings indicate that B2 stiffness is more accurately predicted as expected. The increase in thickness of the vamp cross-section at the B2 position results in less spatial variability in terms of anatomical structures that may influence the results. The difference in the B-parameter between A2 and B2 positions suggests that A2 stiffness is more dependent on the spatial arrangement of VB's and less dependent on their size. The usefulness of this model depends on the amount of data collected for reeds of variable stiffness rating by the manufacturer. Figure 4-24 presents a comparison of the A2 and B2 models with and without parameters C and D included. This was of interest to measure the sensitivity of the model to more sophisticated anatomical metrics that may be more difficult to obtain in a manufacturing setting.

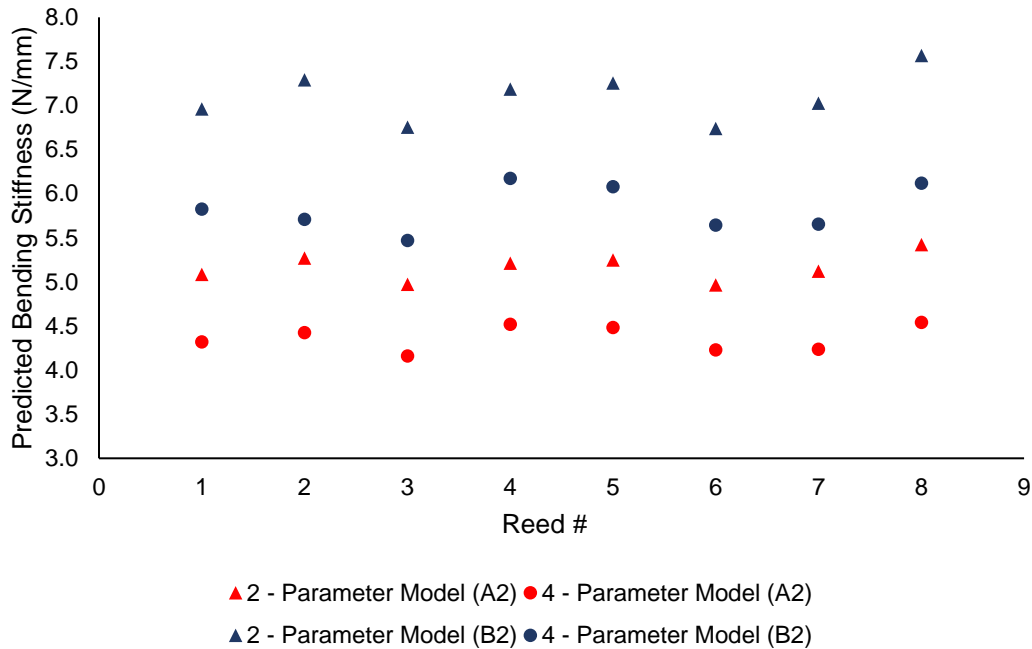


Figure 4-24: Empirical model comparison for A2 and B2 bending stiffness using 2- versus 4-parameters for model fitting (taken from Equation 4-1).

In this case, only the A and B parameters were used to calculate the expected bending stiffness of each reed. By using this two-parameter model only one anatomical metric is required, the vascular bundle area fraction. A2 stiffnesses of the two-parameter model are underpredicted by ~15% compared to the use of four parameters. This increases to ~20% for the B2 stiffnesses. Inter-reed stiffness variability remains constant when using two parameters for the A2 position, however some trend differences are observed for the B2 position (i.e., The relative stiffness of Reeds 2 and 5 decreases with respect to the entire set when the two-parameter model is used). This suggests that the distribution of solid fibers (the fourth parameter in the initial model) with respect to the reed cross-section becomes more important as distance from the tip increases. Considering that relative reed A2 stiffness remains well captured for the two-parameter model, thought should be given to practical collection of VB area fraction data at the manufacturing level. It could be possible to obtain high resolution cross-section images of raw ADL culms prior to machining as an initial sorting procedure. The downside to this method is the requirement for an additional step in the manufacturing process. It may also be possible to obtain images of VB distribution along the underside of the reed, similar to the analysis shown in Figure 4-4 and Figure 4-5. This could be accomplished during the normal sorting procedure via optical imaging. VB area fraction could

be estimated as the ratio of longitudinal VB's across the reed tip relative to the total surface area. This measurement would correlate most strongly with the inner cross-section VB area fraction of the reed and would not capture cross-section spatial dependence. As a pilot study, it would be interesting to examine the reliability of such a measurement in predicting A2 and B2 bending stiffnesses as compared to full cross-sectional analysis.

It was also desirable to consider a model based on composite mechanics that could predict the stiffness of only specific reeds of interest, and reeds without initial stiffness classification. A methodology towards this goal is presented below.

4.4.2 Bending Stiffness Modeling – Anatomical Approach

A phenomenological approach was also used to develop a model that similarly predicts stiffness along the central axis of the reed but does not require empirical fitting. This model was based on the Euler-Bernoulli beam theory where the elastic modulus of solid fiber/VB and parenchyma phases was calculated using a composite annulus model [50]. The basic premise of the model's beam component is presented below (Figure 4-25).

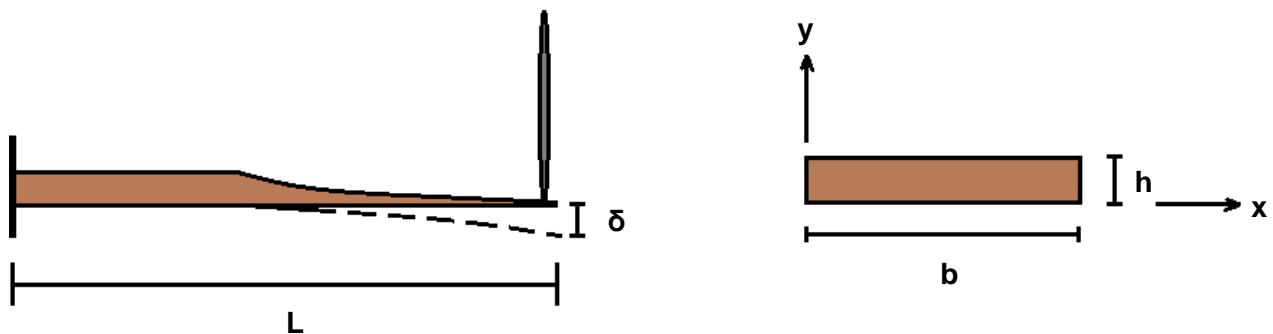


Figure 4-25: Cantilever beam setup for the Euler-composite beam model. The assumed cantilever cross-section (used for calculating the area moment of inertia) is shown on the right. The point load (dowel pin) is represented by the grey bar. The coordinate system is also shown.

It was assumed that the end of the cantilever (the reed) was a rigidly clamped boundary condition (moments at this location are unequal to zero). The length of the cantilever beam was equivalent to the experimental conditions (38.25 mm). Following Euler beam theory, it can then be written that the stiffness of the cantilever is:

$$\frac{P}{\delta} = \frac{6EI}{x^2(3L-x)}, \quad (4-2)$$

where P is the point load applied to the cantilever at location x along the length of the beam L . δ is the deflection induced by load P at x and solving for the left side of Equation 4-2 yields the bending stiffness of the beam. For the purposes of stiffness prediction relative to experimental values, x was taken along the central axis of the reed (parallel to the longitudinal direction) at locations A2 and B2, as they pertain to the experimental setup. Calculation of the area moment of inertia for the beam, I_y , is taken as:

$$I_y = \frac{b^3h}{12} \quad (4-3)$$

where b is the width of the cantilever (reed tip) at the location of the point load and h is the thickness of the cantilever at this location. Note that this model assumes a rectangular cross-section despite the slight curvature of the reed tip at the testing location. Additionally, the taper of the reed vamp was not factored into the model. Given the proximity of the clamping apparatus (from experimental bending stiffness evaluation) to the reed tip, considering the reed cross-section to be rectangular in this region is a reasonable assumption. The taper along the reed length of actual bending in this area is not significant (i.e., thickness change from tip to testing location is approximately 50 microns). Consideration of a homogenized flexural modulus through this model also serves to “average” the effects of the reed taper. Thickness measurements on either side of the central axis indicate that curvature is extremely limited at this location and given the length scale (microns) the assumption of a linear b would not significantly impact the results.

For calculation of an equivalent elastic modulus for both the VB and parenchyma cell structures two composite models were utilized. These two main structures present in the cross-section of *Arundo culms* are considered separately here and added together using a rule of mixtures composite approach. Figure 4-26 depicts the main areas of interest for the model.

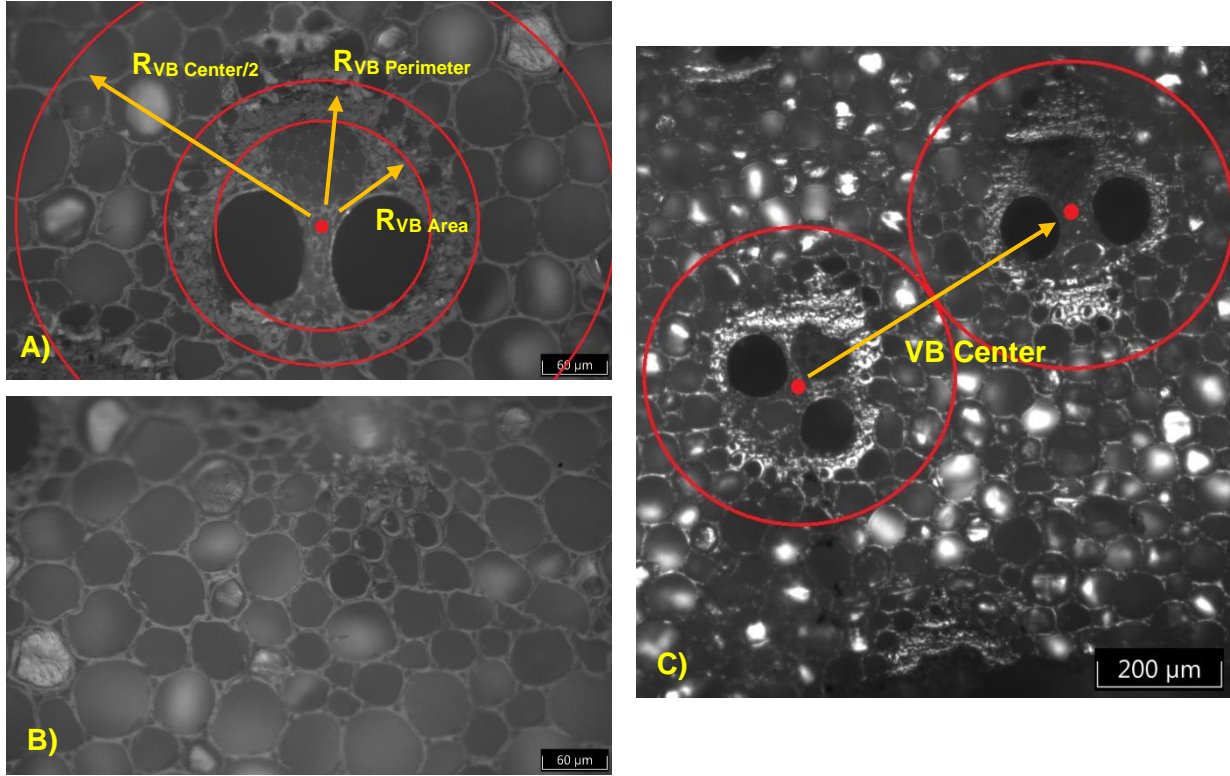


Figure 4-26: Overview of the anatomical parameters used in the bending stiffness model. A) The annulus composite model denoting the parameters used to compute inner and outer radii of the two-element composite modulus. B) The surrounding parenchyma cells used to compute the matrix component of the rule of mixtures modulus. C) An overview of the VB Center (centroid distance) parameter used to compute the outer radius of the annulus model.

In this model, the annulus composite shown in Figure 4-26-A is comprised of two layers including a thin-walled solid fiber annulus and an outer, thick-walled parenchyma annulus. The connectivity of two of these composite structures is shown in Figure 4-26-C. To calculate an equivalent modulus for the entire cross-section, the modulus of the annulus structure must be added to the equivalent modulus of the parenchyma matrix through the rule of mixtures. The most important parameters for the parenchyma equivalent modulus are the parenchyma cell wall thickness, t , and radius, R . The equivalent modulus of the annulus structure (Figure 4-26-A) is given as [50] :

$$E_A = \sum_{n=1}^N \frac{\pi[(R_O^n)^4 - (R_i^n)^4] E_n}{4 I_n}, \quad (4-4)$$

where N is the number of annulus layers (2 for the present model), R_O and R_i are the outer and inner radii of the n th layer, E_n is the elastic modulus of the n th layer and I_n is the area moment of inertia of the n th layer. I for the solid fiber layer ($n = 1$) is calculated using the thin-walled

assumption of the standard annulus area moment of inertia equation such that $I_y = \pi r^3 t$, where r is taken as R_O for the solid fiber layer. For this model, the elastic modulus of the inner solid fiber layer was taken as the modulus obtained from nanoindentation testing on the musician set reed samples. This methodology is discussed in Chapter 5. For the parenchyma annulus the equivalent modulus was calculated from the proportionality in Equation 4-5.

$$E_{Annulus\ Parenchyma} \propto I \left(\frac{t}{l}\right)^3 E_{Parenchyma\ cell} \rho_{cells} \quad (4-5)$$

This is similar to the equivalent modulus developed for honeycomb cell structures [51], [52] with an additional term to factor in the spatial density of parenchyma cells within the parenchyma annulus. Similar to E_n , $E_{Parenchyma\ cell}$ was obtained by nanoindentation testing on the cell walls of reed samples. These samples were taken from the musician reed set. For the cells shown in Figure 4-26-B, l is approximately equal to R . The area moment of inertia (I) of this phase can be approximated as $\sim t^4$ [53]. The equivalent modulus of the parenchyma matrix was calculated as:

$$E_{Parenchyma\ matrix} \propto \left(\frac{t}{l}\right)^3 E_{Parenchyma\ cell} * n_{area}, \quad (4-6)$$

where n_{area} is the average number of parenchyma cells across the entire reed tip cross-section, assuming no VB's. This results in an equivalent stiffness for a purely parenchyma cell reed tip similar to previous analysis methods on cylindrical cell lattice structures [54]. These cylindrical cells are a good physical approximation of the parenchyma cell structure. To calculate the equivalent stiffness of the reed cantilever, the area fractions of the above phases (phase 1 from Figure 4-26-A and phase 2 from Figure 4-26-B) and their equivalent moduli were combined using the rule of mixtures (Equation 4-7).

$$E_{reed\ tip} = (1 - A_{parenchyma})E_{Annulus} + (A_{parenchyma} \cdot E_{Parenchyma\ matrix}) \quad (4-7)$$

This equivalent modulus was used for E in Equation 4-2 to solve for the expected bending stiffness of each reed in the musician set. Results are also normalized with respect to reed tip density. The $A_{Parenchyma}$ area fraction term is calculated by computing the area surrounding VB centroids throughout the cross-section and assuming their combined area is equivalent to Equation 4-8.

$$A_{Parenchyma} = 1 - A_{Annulus} \quad (4-8)$$

$$A_{Annulus} = \pi \left(\frac{VB_{Centroid}}{2} \right)^2 n_{Annulus} \quad (4-9)$$

The term $n_{Annulus}$ represents the average number of VB's in the cross-section and is extracted from the distribution of VB's for each reed. This calculated area can then be used to calculate $A_{Parenchyma}$.

In terms of the anatomical variables used the outer radius of the solid fiber annulus was calculated by assuming each VB was a circle and then using the VB Perimeter parameter such that R_O for the solid fiber annulus layer was $VB_{Perimeter}/2\pi$. All told, this bending stiffness model was dependent on the anatomical variables shown in Table 4-4.

Table 4-4: Overview of the extracted reed variables used for stiffness prediction in the bending stiffness model outlined above.

Anatomical Variable	Description
$VB_{Centroid}$	Mean Euclidean distance between VB's relative to the central reed axis
t	Parenchyma cell wall thickness
R	Parenchyma cell radius
ρ_{Cells}	Number of parenchyma cells per unit area
$VB_{Perimeter}$	Mean VB perimeter length for each reed
VB_{Area}	Mean VB area for each reed
$E_{Parenchyma\ cells}, E_n$	Cell wall and solid fiber moduli of the n th layer of the annulus model

Note that variables t , R and ρ_{Cells} were taken as constants (computed from the average of all reeds in the musician set) when calculating the predicted stiffness values of each reed.

Results of this composite model are compared for A- and B-position stiffness with experimental values in Figure 4-27.

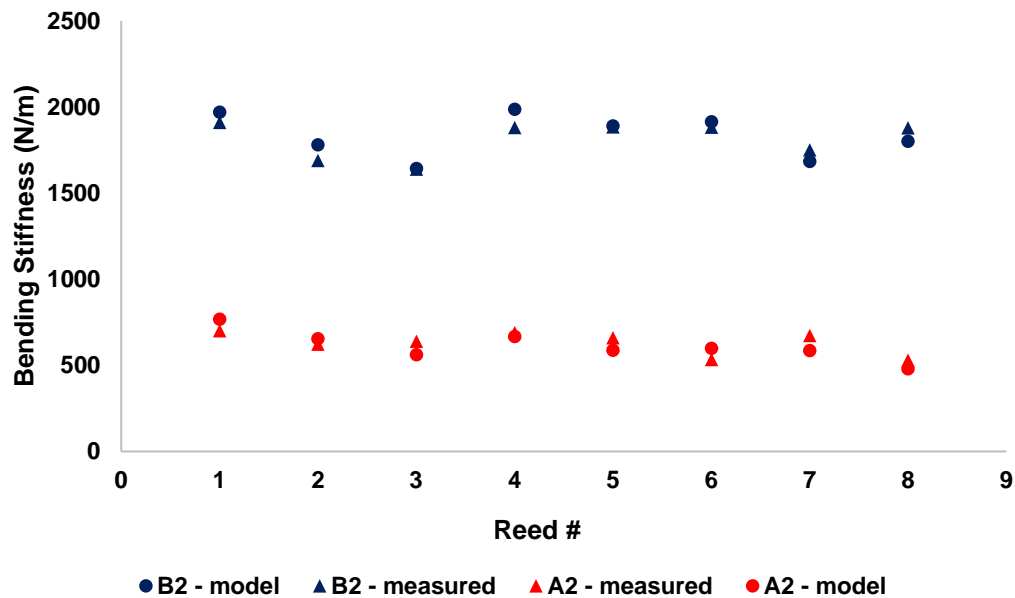


Figure 4-27: Bending stiffness composite model comparison for predicted and measured values at A2 and B2 positions.

The mean difference between the predicted and measured B2 stiffness values is -3.5% (maximum -5.5%), and the difference for the A2 position is 7.2% (maximum 12%). These reeds were all rated as having the same static stiffness by the manufacturer despite the differences observed. The usefulness of this model stems from its independence from measured values of bending stiffness. Furthermore, it only depends of the anatomical structures of analysed reeds. Consideration as to the acquisition of this data in a manufacturing scenario has been given in 4.4.1. For categorization purposes, this is useful as pre-manufactured Arundo culms could be sorted according to the distribution of their anatomical structures. These variables could be used as inputs for the model and coupled with the reed tip geometry to calculate the expected bending stiffness. Another benefit of this method is the ability to modify reed geometry and obtain a precise value of bending stiffness. The geometry of reed vamps could be tuned in this way to accommodate musician preferences.

As noted, the anatomical variables used in the model are not single values, but rather statistical distributions. It was therefore of interest to consider the impact of variable distribution

on the resulting predicted bending stiffness. In this way, the sensitivity of bending stiffness to different anatomical structures was considered.

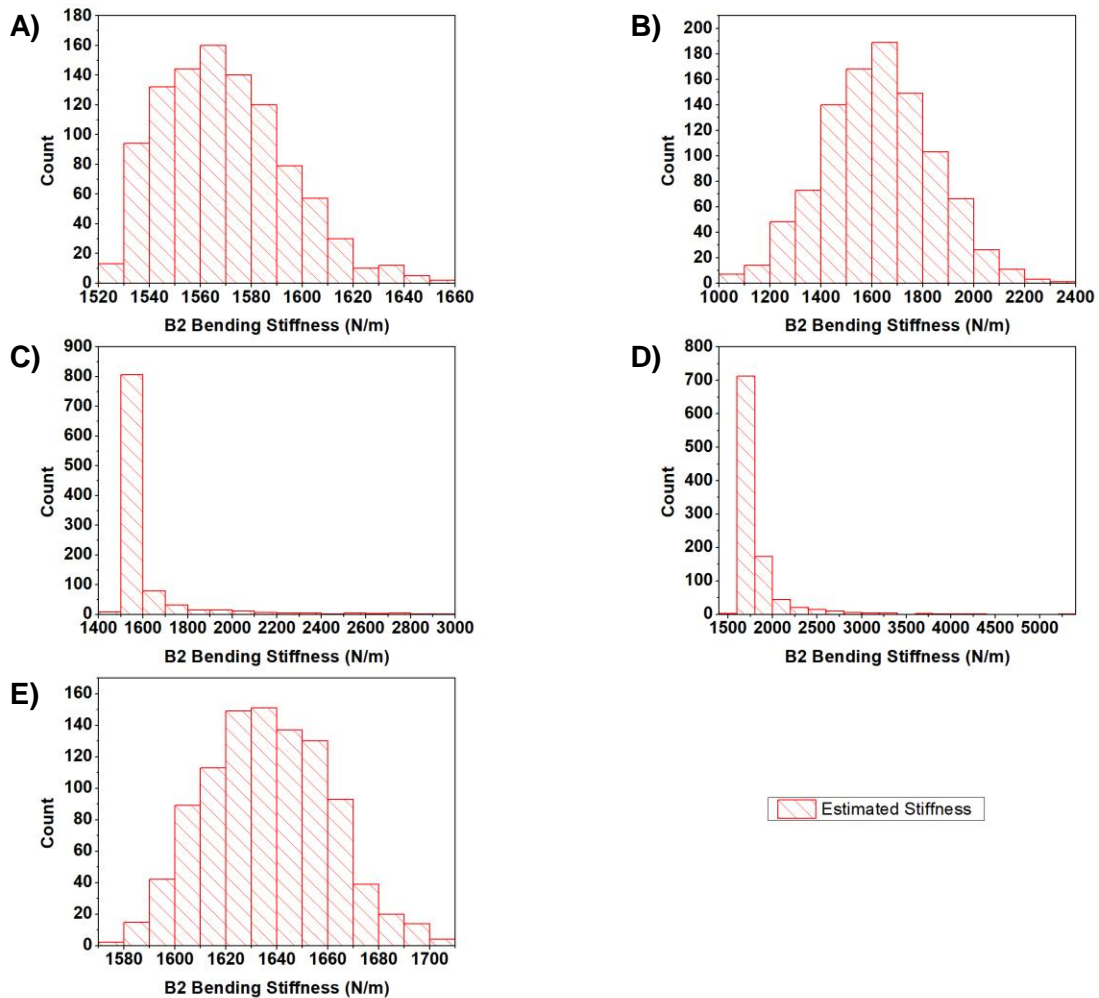


Figure 4-28: Distributions of estimated bending stiffness through modification of anatomical variables. A) Parenchyma cell modulus B) Solid fiber modulus C) VB mean centroid distance D) VB Perimeter E) VB Area

The stiffness distributions presented in Figure 4-28 were obtained by varying a single anatomical parameter and holding the additional parameters constant (i.e., average values obtained for the entire reed set). The distributions include 1000 simulated reeds and the expected bending

stiffnesses that would be obtained from such a set. All variables were fitted as Weibull curves to match the distributions found from optical microscopy analysis of reed heel cross-sections. The one exception was for solid fiber modulus as it was found to be normally distributed and thus fit using the average modulus and standard deviation. The distributions obtained for VB centroid distance and VB perimeter are much more skewed than the others and exhibit significant positive kurtosis. This would indicate that outliers in stiffness sorted reeds at the manufacturing level could be attributed to these variables. Variation of the VB area parameter generates a distribution more similar to the expected distribution of stiffness produced via standard sorting practises. The VB area fraction was found to be highly correlated with bending stiffness as discussed earlier, and this result agrees with the former.

A comparison is also made between the expected and measured bending stiffness distributions for a set of 48 reeds (i.e., comprised of both the comparison and musician reed sets) when only parenchyma and solid fiber moduli values are varied. This result is shown in Figure 4-29.

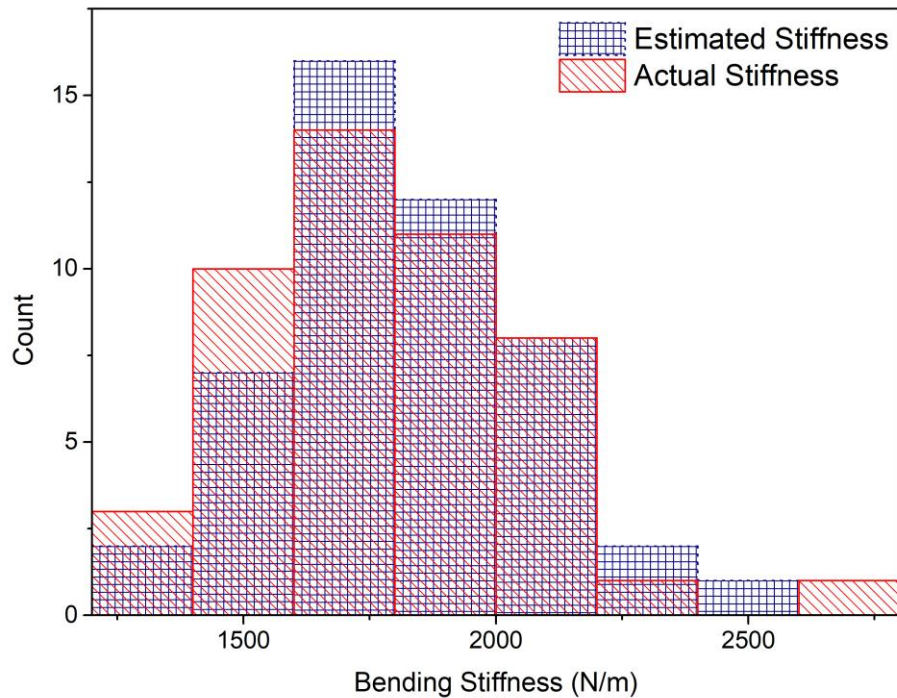


Figure 4-29: Distribution of expected bending stiffness at the B2 position for a set of 48 reeds. This is compared with the measured results from the comparison and musician reed sets.

A good fit to the measured data is observed for the simulated stiffness results. This approach would be useful to manufacturers where stiffness prediction of raw Arundo material could be made prior to machining and tailored to the type of reeds to be made.

4.5 Conclusions

In this study the static bending stiffness and aging behaviour of alto saxophone reeds has been examined. Two reed sets were used, one comprised of 8 reeds (the musician set) to analyse aging behaviour both objectively and subjectively and another comprised of 40 reeds (the comparison set) to examine differences in rated stiffness in terms of anatomical structures and objective stiffness measurements. The VB Area Fraction and VB Center density (centroid distance) parameters were found to be highly correlated with bending stiffness at positions A2 and B2. Aging behaviour was quantified through rate-of-change bending stiffness metrics, and these metrics were

correlated with stiffness asymmetry. This indicated that reeds with a large difference in tip stiffness values off-axis aged more rapidly than others. The musician's rankings of subjective stiffness were also correlated with asymmetry and the ability to accurately rank the stiffness of reeds was negatively correlated with rate-of-change in stiffness for the A3 position. This suggests that the musician was less reliable in stiffness assessments of reeds that varied considerably during their lifecycle. These results highlight the importance of stiffness asymmetry to the subjective stiffness of nominally identical reeds (from a current manufacturing perspective). Overall, VB Area Fraction was found to correlate with B2 bending stiffness across all reeds of various manufacturer rating. It is suggested that the use of this anatomical parameter to classify reeds according to bending stiffness would lead to less variability post-manufacturing.

Models were created using Euler beam theory and composite structures to predict the bending stiffness of reeds perpendicular to the longitudinal direction and good agreement was found for both A2 and B2 stiffness values. The model considers VB center density, VB area, VB perimeter and parenchyma cell dimensions as anatomical inputs. Statistical distributions (primarily Weibull) of these variables led to accurate macroscopic bending stiffness distributions when compared with all the measured reeds. Variability and outliers in conventionally sorted reed sets are likely the result of differences in solid fiber modulus, VB area and VB perimeter microstructure parameters, and the inability of average bending stiffness techniques to capture important differences in VB distributions and morphologies along the tip of the reed.

Future work could include the use of finite element analysis coupled with the homogenized flexural modulus developed here to simulate dynamic behaviour of the reed. The influence of anatomical variable distributions on bending modes around the reed tip could be investigated and compared with measured results at the A- and B-spatial positions presented here. The static bending stiffness model presented in this chapter could also be extended directly to consider dynamic reed behaviour. In this way the influence of anatomical structures on modes of bending vibration could be studied.

Chapter 5

5 Nano-mechanical and material investigations into the viscoelastic behaviour of anatomical structures in *Arundo Donax L*

C. Kemp¹, R. Chromik², G. Scavone¹

¹Computational Acoustic Modeling Laboratory, Department of Music Research, McGill University

²Department of Materials Engineering, McGill University

This chapter is provided in manuscript form and is to be published. Building on the results of Chapter 4, this chapter investigates the degradation of reed samples taken from the played reeds at different length scales. In this way, evidence is presented to explain the deterioration of reeds and their mechanical performance over their useful life.

Abstract:

The giant reed *Arundo donax L* is used for the manufacture of woodwind instrument reeds (known as reed cane). Variability in reed behaviour has been a long-standing question complicated by changing properties with time during the natural aging process. Investigations into the macroscopic performance of reeds have been variable in their findings, and literature concerning microstructural analysis is lacking. As this material shares anatomical similarities to bamboo methods previously employed for bamboo (nanoindentation) are used to quantify the properties of different anatomical structures and changes with exposure to natural aging (musical use) and well-controlled saturation cycling. Changes in the material structure are also considered through x-ray diffraction and thermogravimetric analysis. Detectable differences in elastic and viscous behaviour of

microstructural elements are discussed and considered in relation to creep response. These results will help inform the development of more naturally behaving artificial reeds (with enhanced durability and stability) and provide a starting point for understanding more rigorous categorisation methods of natural cane reeds.

5.1 Introduction

Woodwind instruments require a vibrating reed clamped to the mouthpiece in order to produce sound. For centuries, the giant reed *Arundo donax L* has been used as the material of choice for crafting these cane reeds. As a natural material *Arundo donax L* is found to have varying mechanical, chemical and vibrational properties [41], [55]–[57], some or all of which contribute to the high level of variability that musicians experience when using natural cane reeds [7]. This variability leads to changes in mechanical behaviour with time and exposure to moisture (reeds are played in a fully saturated state in the mouth) that alters the sound produced from the reed. Although synthetic reeds including polymeric, composite and metallic variants exist and offer advantages in terms of durability and environmental invariance, natural cane reeds are preferred due to their desirable sound. It is not clear why cane reeds vary so much despite manufacturer efforts to group reeds by macroscopic bending stiffness, a problem that is further complicated by their changing properties with time. The present study investigates the changing nano-mechanical properties of new and used cane reeds through nanoindentation experiments on various structures within the vascular bundles and parenchyma cells of the microstructure. These vascular bundles represent the majority of solid material within the reed microstructure and are thought to contribute to vibrational performance in bending. This nano-mechanical approach is warranted as the geometry of finished reeds is maintained to a high level of accuracy by the manufacturer and previous studies [7] on the macroscale performance of reeds have been inconclusive [41].

Reed variability has been noted in many previous studies [7], [40], [45], [58] with regards to stiffness, vibration behaviour, acoustic associations with mechanical parameters and environmental sensitivity. Variance in the stiffness of reed sets results in significant differences in the bending vibrational behaviour of nominally identical reeds. Although differences in static stiffness between reeds have been noted, the dynamic and static stiffness have been shown to be correlated with one another for individual reeds [8]. This is important as it gives validity to the classification and testing of reeds via static methods when their usage is dynamic. Changes that

reeds undergo with time have also been examined with respect to the first vibrational bending mode and shrinkage and expansion characteristics [5]. A general decrease of internal damping of the first bending mode is observed although consideration was only given to contributions from matrix cell shape changes (i.e., parenchyma cells). Anatomical studies [4] have shown so-called good reeds to be correlated with the solid fiber ring surrounding vascular bundles, specifically the continuity of such rings.

The deformation mechanisms of moso bamboo (*Phyllostachys edulis*) samples during flexural bending has recently been considered and found to depend on moisture (water) content [59]. This flexural testing showed that parenchyma matrix failure was the primary deformation mechanism at low moisture content, with increasing deformation due to solid fiber-matrix pull-out with increasing moisture content. Reeds experience moisture cycling during their lifespan as they alternate between a high ambient relative humidity state (storage conditions, usually > 50% RH) and fully saturated conditions in the mouth. The noted difference in flexural deformation mechanisms for moso bamboo between moisture states suggests that long term degradation of *Arundo* material would increasingly be due to the degradation of the solid fiber-matrix interface. The mechanical properties of these two phases are not well quantified, especially not for long term deterioration and this information is required for a better understanding of changing macroscopic mechanical properties of reeds with time. Due to the noted gradient in spatial distribution of vascular bundles throughout the cross-section of *Arundo donax L* (similar to bamboo), the mechanical properties of solid fibers and parenchyma cells may be spatially dependent. Differences in the nano-mechanical properties of solid fibers over different spatial locations within vascular bundles have been found to be insignificant for moso bamboo [60]. Nanoindentation of solid fibers showed no dependence on location within the individual vascular bundles. The cellulose microfibrils of solid fibers primarily control the longitudinal stiffness and their arrangement in the cell wall (primarily described by microfibril angle, MFA) does not vary significantly between vascular bundles. This means that the gradient in stiffness observed for solid fiber sections of vascular bundles in bamboo is the result of cell wall thickening (and tissue density) within the solid fibers where the thickness increases the composite effective stiffness [60]. Similar results are likely to be observed for *Arundo donax L* and suggest that differences in indentation moduli would be due to MFA differences or chemical changes in the cell wall during aging.

A comprehensive materials science study of *Arundo donax L* within the context of woodwind reeds is lacking in the literature and presents an opportunity to identify changes in elastic and viscoelastic material behaviour over the life of a cane reed. Previous studies [42], [61], [62] on moso bamboo (a similar grass - family natural material with a similar microstructure) have used nanoindentation methods to characterise the elastic properties of fiber bundles and similar approaches are used in the present study. Methods of time-dependent behaviour are also analysed through the use of nano-mechanical creep tests and viscoelastic modeling techniques [63]–[66]. Comparisons are made between samples taken from single cane reeds before and after their useful life as played by a professional musician. These results suggest the microstructural origins of stiffness fatigue over the life of a reed and the nano-mechanical properties that contribute to changing reed behaviour with time.

5.2 Materials and Methods

5.2.1 Background

The stem of *Arundo donax L* (ADL) contains three primary directions of interest including longitudinal, radial and transverse. Cellulose fibrils within the cell wall of vascular fiber bundles leads to a high elastic modulus in the longitudinal direction [57]. The alignment of these fibers results in orthotropic elastic symmetry and is also the direction along which reeds are machined. There are several node and internode regions along the stem of the plant similar to members of the bamboo family. The stem itself is a hollow tube with a hard epidermal layer and a softer composite wall structure [12]. Reeds are machined from the stem wall of the internode regions with the long axis of the reed aligned with the longitudinal direction of the stem (shown in Figure 5-1).

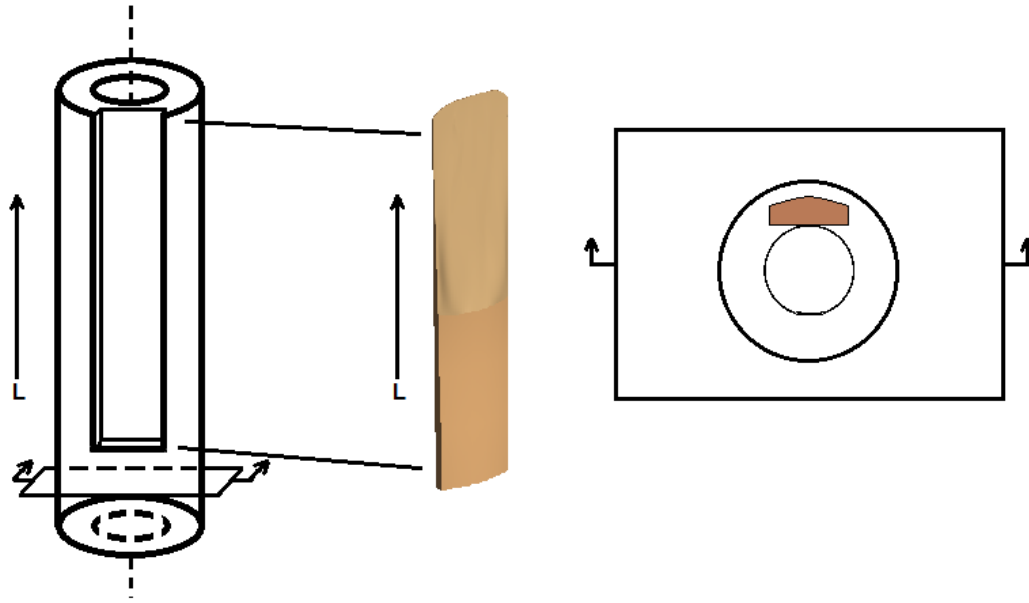


Figure 5-1: Orientation of manufactured reeds with respect to the ADL culm and cross-section. The longitudinal axis is noted as L.

The microstructure of the stem wall consists primarily of two biomechanical elements: a parenchyma matrix and a reinforcing solid fiber phase (within the regions known as vascular bundles). Analysis of the area fractions of these anatomical features has shown them to be related to the musical performance of reeds and thus are important to consider in more detail [4]. Cellulose, hemicellulose and lignin constitute the natural polymeric composition of both elements in varying amounts. Figure 5-2 illustrates the cross-section of a manufactured reed. Figure 5-3 provides optical micrographs of the vascular bundles, parenchyma cells and general culm anatomy. In terms of orientation as it relates to Figure 5-1, the micrographs are taken through the cross-section of the culm (i.e., perpendicular to the longitudinal axis).

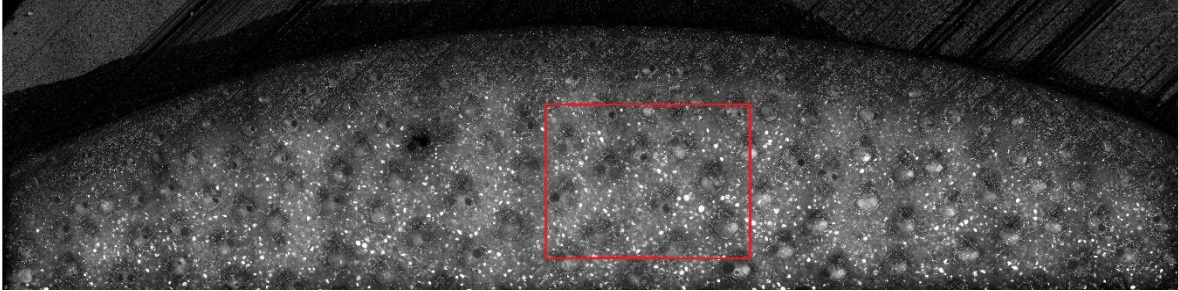


Figure 5-2: Optical micrograph cross-section of an ADL reed (for scale, the total length of the cross-section is 15 mm and height 3 mm). The orientation of this micrograph corresponds to the shaded cross-section depicted in Figure 5-1. The area outlined in red represents the area in Figure 3(A).

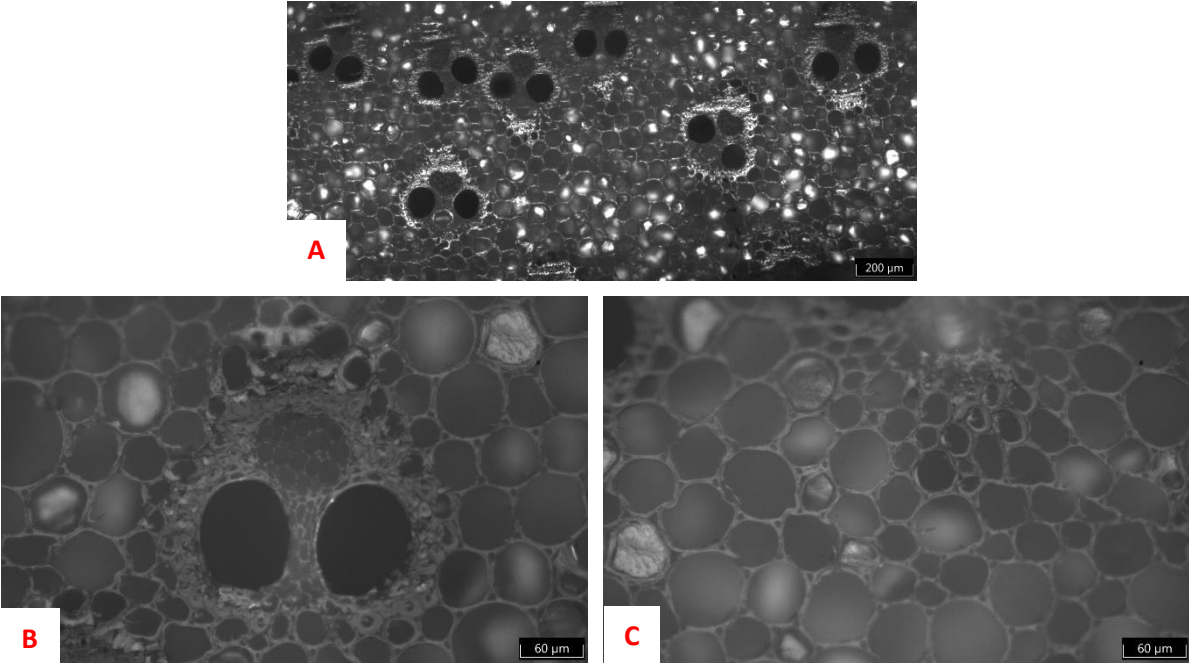


Figure 5-3: A) Optical micrograph of the typical ADL cross-section anatomy with vascular bundles and parenchyma cells. B) The vascular bundle with surrounding solid fibers and lumen vessels (dark circular structures). C) The ADL matrix of parenchyma cells.

Figure 5-4 provides an overview of a typical area of solid fibers and depicts their average diameter. Solid fibers are generally circular in shape with diameters and wall thicknesses of 20 – 30 μm and 5 – 10 μm respectively.

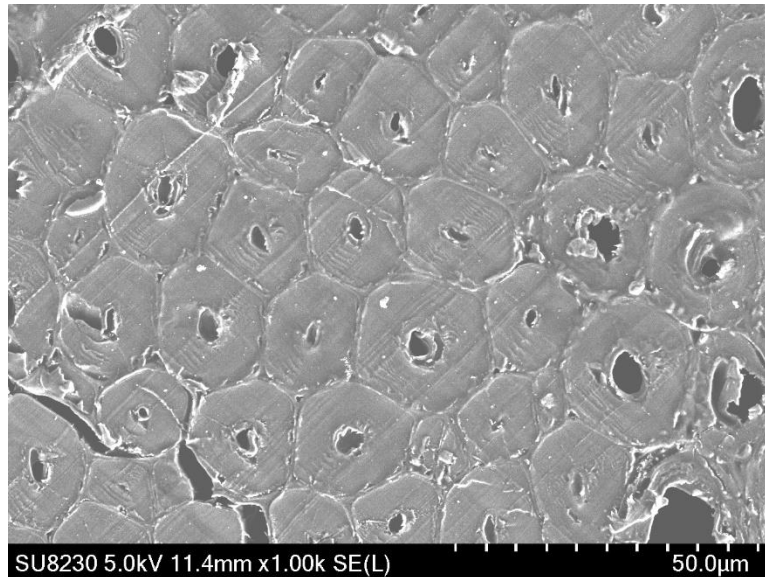


Figure 5-4: SEM micrograph of solid fibers close to the epidermis layer. The density of solid material in these areas is high and represents most of the solid material of the ADL culm. These solid fibers are found surrounding the vascular bundles within the ADL cross-section and form a “ring” of solid material for each bundle.

Previous research on the effects of moisture on vibrational performance in ADL have only considered the macro-level mechanisms for changing behaviour with respect to vibrational characterisation, including internal friction measurements [5], [55]. Internal friction is a useful measure of material damping due to energy loss within a medium and can be considered important in woodwind reeds where increased internal damping would decrease the elastic response of the reed (i.e., increased hysteresis between input and output excitation waves). Evidence of cell wall collapse from repeated wetting-drying cycles has been described generally [5] and shown to decrease internal friction ($\tan \delta$) values with increased exposure to moisture cycling, in terms of the first flexural vibration mode. It is not clear the degree to which macroscale dimensional shrinkage (in part due to parenchyma cell collapse) contributes to this decrease in internal friction versus other changing material properties that do not remain constant with repeated exposure to

changing moisture conditions. These changing material properties have not been well studied at the microstructural level, especially in terms of the solid fibers within the vascular bundles that contribute most significantly to bending stiffness (static and dynamic).

5.2.2 Nanoindentation

Nanoindentation measurements were performed on the cell wall of solid single fibers within the vascular bundle, similar to those performed previously on moso bamboo [61], [67]. In addition to single load-displacement indents, at least two other indents were performed on each solid fiber wall in order to compare the load-displacement curves obtained from different analytical techniques. Measurements were also taken on the parenchyma cell walls of well controlled saturation cycle samples.

Extraction of viscoelastic parameters from depth-sensing experiments has been accomplished using several techniques, including (but not limited to) phenomenological approaches [66], the correspondence principle [68] and fitting of constitutive equations to the entire load-hold-unload curve [63]. The analysis of time-dependent nanoindentation results is complicated by the short time periods of load application, thermal drift and difficulty in separating elastic versus plastic effects. Thus, the reliability and magnitude of extracted material properties/parameters can be model dependent. For this reason, several models are compared during the present study that have previously been used for viscoelastic nanoindentation analysis. These are compared for consistency of results in the Appendix.

Considering the analysis of the models provided in Appendix it is observed that general trends in the data are not model dependent and suggests a fundamental shift in material behaviour during the aging process. Given this finding, sample discussion is limited to the VEP and phenomenological findings as the strain-rate model does not provide additional information. Results of differences between real reeds will only be discussed in terms of E_{VEP} and n_{VEP} results. Comparisons of aging (due to moisture cycling) dependent changes between solid fibers (within the vascular bundle) and parenchyma cells (matrix) is only discussed in terms of E_1^* , E_2^* , η_1 and η_2 parameters. This is a practical limitation as the parenchyma cell walls are only 3 to 6 microns in thickness and thus a smaller load (as is used to compute E_1^* , E_2^* , η_1 and η_2) was required. In this way, the resulting indentation footprint was reduced, mitigating the effects of the parenchyma

cell wall-boundary on the results. Therefore, the elastic and viscous parameters of interest are limited to those shown in Table 5-1 and remembering that sample trends are not model dependent.

Table 5-1: Parameters (elastic and viscous) of interest relevant to the presentation and discussion of sample results henceforth.

Experimental Technique	Elastic Parameters	Viscous Parameters
Viscous-elastic-plastic (VEP)	E_{VEP}	n_{VEP}
Phenomenological (Maxwell-Voigt Model)	E_1^*, E_2^*	η_1, η_2

5.2.3 Thermogravimetric Analysis

The aging process in wood type materials has been shown to induce changes in both the crystallinity and crystallite size of cellulose microfibrils [69], and these changes can result in cell wall mechanical response changes. The importance of the lignin to cellulose ratio in viscoelastic behaviour has also been discussed for resonant wood [70], where it is noted that lignins have a much more viscoelastic response than the other constituents of the cell wall. Despite this, the structure of the lignin is also important, with condensed lignin providing additional stiffness to the cell wall suggesting a reduction in internal friction, as the lignin is bound much more efficiently to the surrounding cellulose microfibrils. In the present work the potential influence of these parameters to viscoelasticity have been investigated using x-ray diffraction and thermogravimetric analysis (TGA). Calibrations for the thermal stability (using TGA) of cellulose, hemicellulose and lignin have been completed elsewhere [71] by deconvoluting the individual contributions of these components to pyrolysis rate in differential TGA curves. This was completed using a calibration that considered pyrolysis of pure cellulose, pure lignin and pure hemicellulose components separately, and then fitting the differential TGA curves of wood chips to the base data via a minimization function (sum of squares). In this way, inter-sample variations of relative amounts of cellulose, hemicellulose and lignin can be approximated.

5.2.4 X-ray Diffraction Analysis

XRD data was obtained using a Bruker D8 Discover x-ray diffractometer between 2theta values of 5 and 50 degrees, using K_{Cu} radiation (40kV). The step size was 0.005 with a total scan

time of 300 seconds per step. Samples were tested at ambient conditions (23°C and 20% RH) after dehydration at 100°C for 1 hour to achieve an equilibrium moisture content (5 to 7%) per sample and minimize the impact of moisture on crystallinity comparisons [72]. Instrumental peak broadening was taken into account using calibrations present in the Diffrac EVA+ software suite [73]. Peak broadening due to crystallite strain was assumed to be significantly smaller than size broadening for the [200] reflection and it was not accounted for, similar to [74]. This is not critical for the present study, as the primary goal was to assess differences between samples of this set and not to compare absolute values with previously published results for wood and bamboo-like materials.

5.2.5 Internal Friction

Internal friction is an important parameter for illustrating the macroscopic effects of viscoelasticity in samples. The present study assessed $\tan \delta$ values using elliptical plots (Lissajoues) of stress versus strain for samples excited at specific frequencies. This analysis method is similar to that previously used for bamboo [75]. Samples were taken from raw ADL to match the samples used for nanoindentation experiments. Testing was completed between 100 and 1000 Hz as the audio range of frequencies is of specific interest for reeds. Relative humidity was controlled during testing such that data was obtained in dry (~0% RH), moist (50 and 80% RH) and saturated (fully wetted) states. Samples were also allowed to equilibrate with the test conditions for 24 hours prior to running the experiment. Measurements of $\tan \delta$ were obtained by analysing the input strain and output stress waveforms and calculating the phase shift between them. Samples were tested in longitudinal and transverse orientations (where the longitudinal orientation is the same as that used for nanoindentation testing).

5.2.6 Reed and *Arundo donax L* Samples

Samples of *Arundo donax L* were taken from cross-sections of manufactured woodwind reed components. These samples were prepared such that the longitudinal direction of the stem was parallel to the axis of nanoindentation loading. Sample surfaces were prepared at the Goodman Cancer Research Centre, McGill University in the Histology Core facility. Samples were initially

embedded in paraffin wax before cutting on a sliding microtome (Lecia brand). No further treatment as performed on the surface to prevent damage to the cell walls, as surface roughness measurements of approximately 5 to 10 nm RMS indicated the surface was suitable for indentation testing.

The diagram provided in Figure 5-5 depicts the areas from which experimental specimens were taken from reed and raw ADL samples. In total 16 reed samples and 4 raw ADL samples were used. The reed samples consisted of 8 sections taken from the heel of the reed and 8 taken from the tip.

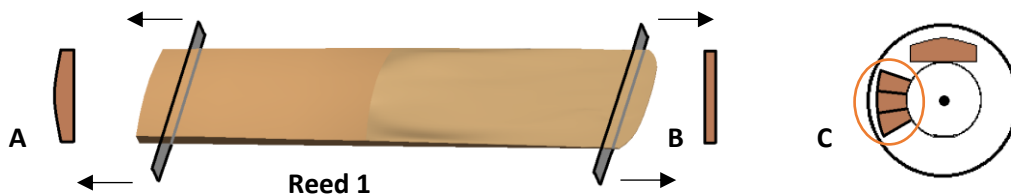


Figure 5-5: Schematic of the samples used for experimentation. A) represents the heel sections that were taken from aged reeds for nanoindentation, XRD and TGA testing. B) represents the matching tip sections also taken for testing. These samples comprised the complete set of reed heel – tip pairs. C) the region outlined in red depicts the saturation cycle samples taken from single internode regions. The orientation of a typical reed is shown for comparison. The longitudinal axis of the ADL culm is denoted by a dot in C).

In this way, a matching sample set was created from each of the 8 reed components. This allowed the results to be compared for intra-reed sample variation and capture any aging/fatigue effects that occur during real playing. The 4 raw ADL samples used were taken from the exact same ADL stem internode region (i.e., same piece of raw material) and each artificially aged using saturation cycling. These specimens included 0 (unused), 5, 25, and 50 cycle samples to capture the effects of repeated wetting and drying on viscoelastic properties. Aging via saturation was completed

using deionized water at ambient temperature (23 to 25°C) and 60 to 70% RH. This process was automated using a programmable pump system where samples were saturated for 1 hour at a time and allowed to equilibrate back to the controlled RH level for 5 hours afterwards. The 1-hour saturation time was chosen to simulate a typical playing session for real reeds. Both the reed and raw ADL saturation samples were taken from the same batch of material (i.e., growing region and age were the same) as provided by the manufacturer in order to minimize variability due to different harvested batches.

Reed samples were played by a professional saxophone musician for 2.5 months, or until they were considered to have reached their end-of-life state. Each reed was played for the same amount of time and had been stored at ambient temperature and 70% relative humidity. In use playing conditions resulted in the reeds being exposed to 1 saturation and drying cycle per playing session for a total of 40 sessions. Samples taken from the heel of the reed are never truly saturated as only the tip of the reed is fully wetted by the musician. Thus it was possible to compare changes between samples taken from the same reed.

5.3 Results

5.3.1 Reed Heel – Tip Nanoindentation

Nanoindentation results for the reed heel and tip sections were analysed in terms of elastic and viscous parameters, the details of which are found in the Materials and Methods section and Appendix A. Samples that exhibited significant drift rates ($> 0.05 \times \text{creep rate}$) over the creep segments were removed from the dataset. Results for each sample represent an average value (E_{VEP} , η_{VEP} , E_1^* , E_2^* , η_1 and η_2) of all single fiber and parenchyma data points with standard error, obtained through model fitting. Typical indentations on solid fiber cell walls are shown in Figure 5-6 along with the profile of an indent (atomic force microscopy micrographs). Results for reed heel and tip n_{VEP} parameters are found in Figure 5-7.

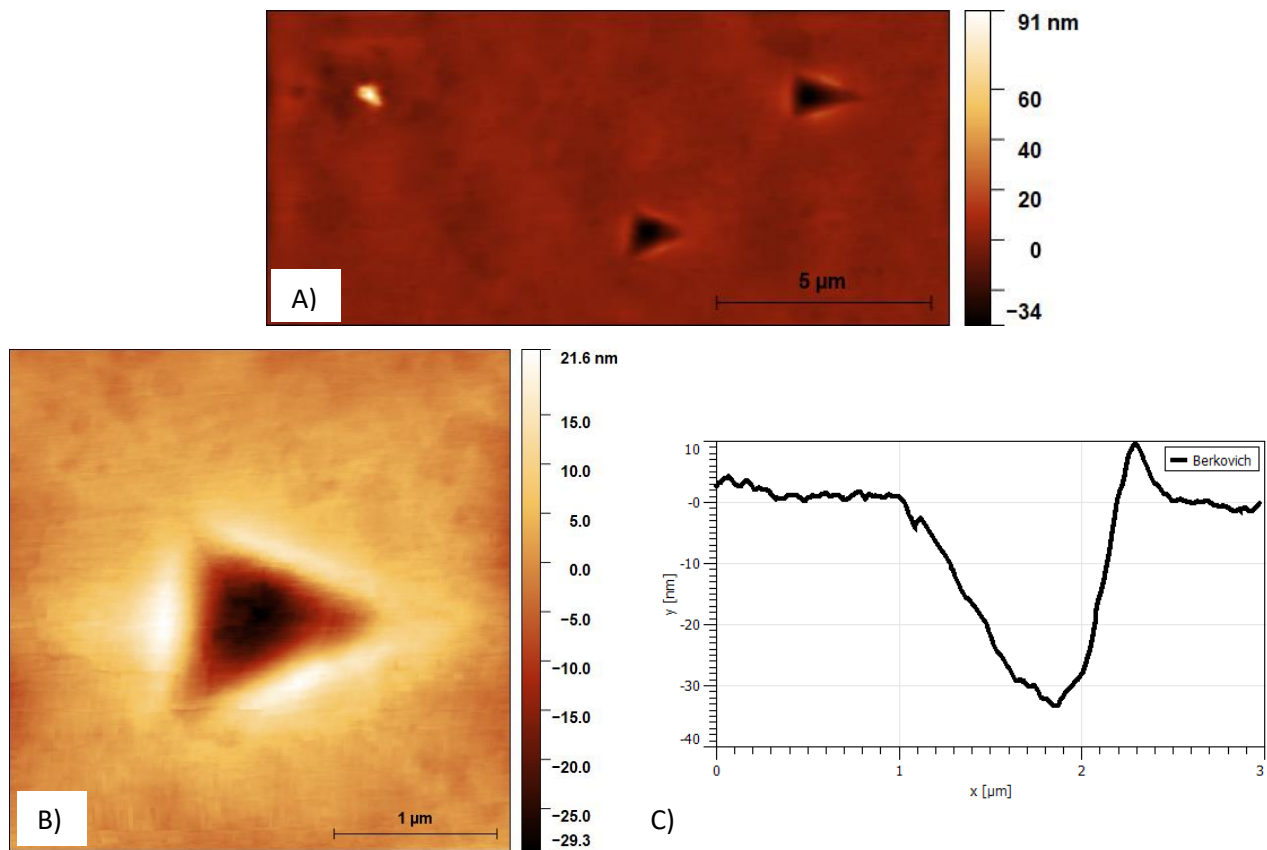


Figure 5-6: AFM micrographs of Berkovich indents. A) Multiple indents on a single fiber wall, B) typical shape of a single indent and C) the indentation profile depicting size.

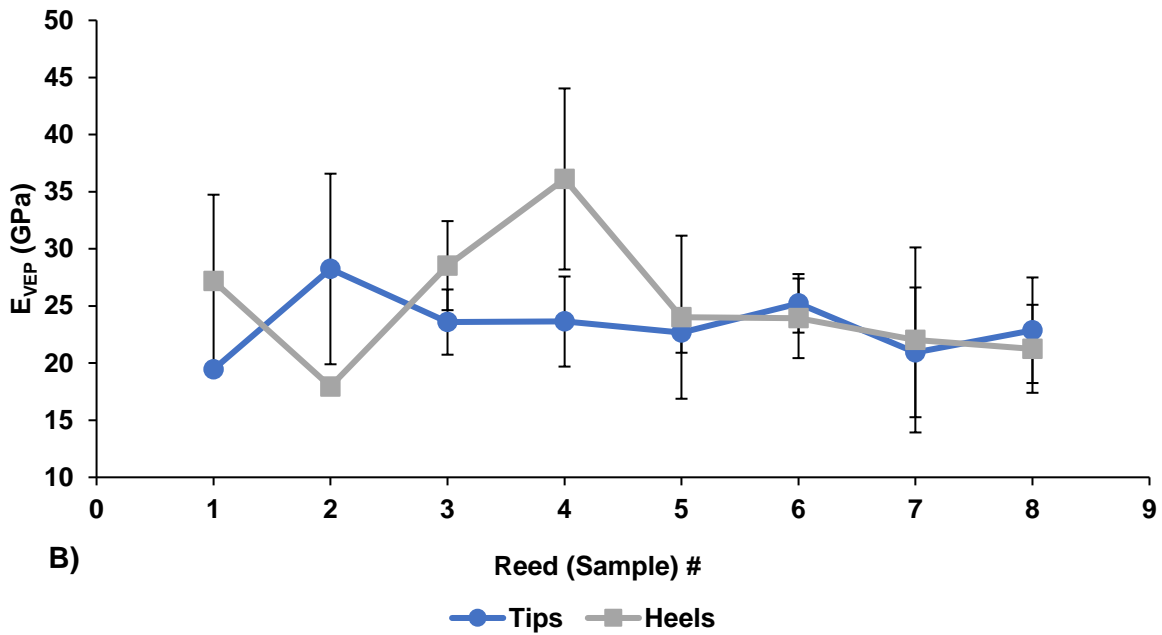
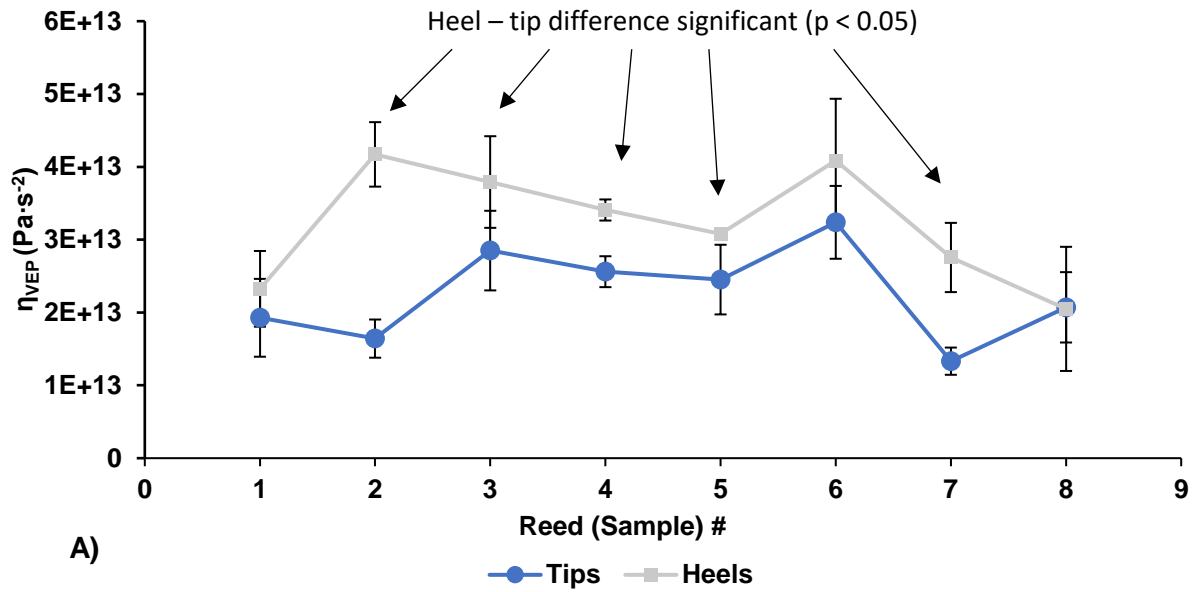


Figure 5-7: A) Viscosity parameters (η_{VEP}) obtained from model fitting to the creep-hold data of reed heel-tip pairs. Significantly different results are highlighted. B) Elastic modulus values obtained from model fitting for the same samples.

All results for elastic modulus are corrected for the properties of the diamond indenter tip, although the solid fibers and matrix of ADL are considerably less stiff than diamond and this correction represents a very small fraction of the measured modulus values [63]. Thus, this step was performed only for completeness. Reed heel viscosity parameters are higher than those of their corresponding tips in 5 of 8 samples, and relatively unchanged in the other three. It appears that over the life of the reed resistance to viscous creep decreases in the solid fibers of the vascular bundles. The unchanged viscosity parameters in three of the reed samples could be attributed to different levels of saturation and slightly reduced playing times during testing. Results for fiber elastic modulus show variable changes between reed heel and tip samples, although there is no clear trend when compared to the viscosity parameters. In terms of the solid fibers, these results suggest that reed aging is dominated by an increase in viscoelastic creep behaviour instead of changes in the elastic response of fibers. Averaging the results for all heels and all tips leads to an overall reduction in the viscosity parameter (η_{VEP}) of 42%. Viscous parameters are greatly reduced for tip fibers relative to heel fibers, also indicating an increasing in viscous creep. Results for elasticity do not indicate any clear trends overall, although reed 2 became more elastic with aging, and reed 4 significantly less elastic. These differences highlight the sample dependent changes that reeds undergo during the natural aging process. Reduced elasticity results (i.e., E_{OP} , E_1^* , E_2^* and E_{VEP}) are corrected using the properties of the diamond indenter tip ($E = 1140$ GPa and $\nu = 0.07$) as in:

$$\frac{1}{E_r} = \frac{1-\nu^2_{sample}}{E_{sample}} + \frac{1-\nu^2_{diamond}}{E_{diamond}} . \quad (5-1)$$

5.3.2 Saturation Cycle Sample Nanoindentation

Saturation cycle samples were analysed in an identical manner to that of the reed heel-tip samples. Unlike the solid fibers of the reed samples, the fibers of these samples exhibited a decreasing trend for both viscosity and elastic modulus with exposure to saturation cycles. Comparing the magnitudes of the viscosity values shows that all reed tips were in between the values of 25- and 50-saturation cycle samples. Elastic modulus values at 50-saturation cycles were 40 to 60% lower than those of the reed tips. Of further interest is the fact that there is an initial increase in viscosity and elasticity at 5 cycles relative to the uncycled case. This likely contributes to the difficulty in assessing reed performance based on their initial characteristics, and illustrates the difficulty faced by manufacturers in categorization. Viscosity and elastic modulus values are

similar at 50-cycles to their initial values ($\eta_{VEP} = 1.94 \times 10^4 \text{ GPa}\cdot\text{s}^2 \pm 0.30 \times 10^4$ and $E_{VEP} = 11.87 \text{ GPa} \pm 1.63$, $\eta_{VEP} = 1.76 \times 10^4 \text{ GPa}\cdot\text{s}^2 \pm 0.37 \times 10^4$ and $E_{VEP} = 13.61 \text{ GPa} \pm 2.54$, respectively) and suggest a shift from solid fibers to parenchyma in the importance of each microstructural component to macroscopic viscous behaviour. As a future study, it would be interesting to study the effects of saliva versus water on the aging process to better understand the differences in fiber elastic modulus between reed and saturation cycle samples.

It is possible that the reed samples were not at the same degradation point at end of life due to slightly dissimilar wetting behaviour and vibrational fatigue. This limitation is due to the similar but not identical playing routines of each of the reeds (where 3 of 8 reed pairs had similar resistance to viscous creep). From the results of the saturation samples, it is likely that some reed tips were at a slightly different point in their fatigue life (as opposed to the well-controlled saturation cycling conditions).

Degradation due to the parenchyma matrix is considered using the phenomenological model presented earlier. Although the parenchyma cell wall is comprised of the same constituents as the solid fiber cell wall, both the ratio of amounts present and the MFA are different [76]. Analysis using this phenomenological model yields values of elastic modulus that are greatly reduced relative to the solid fibers ($E_{parenchyma}^* \leq \frac{1}{2} E_{fiber}^*$). Viscosity parameters are also 25 to 50% lower than those of the solid fibers, suggesting the parenchyma cells contribute more significantly to macroscopic creep. Both viscosity and elastic modulus values are very sensitive to saturation cycles with values at 5 saturation cycles for both dropping by approximately 75% relative to the unused case (0 saturation cycles). These values do recover at 50 saturation cycles to within 20% of the initial conditions.

5.3.3 X-ray Diffraction Analysis

XRD spectra were analysed to yield values for crystallinity index (CI) and volume averaged crystallite size. The data analysis method used in the present work was similar to the peak deconvolution methods discussed previously [77]–[79]. In total, 5 crystalline cellulose peaks were fit to the obtained XRD spectra after the removal of a broad amorphous background peak centered in between 19 and $23^\circ 2\theta$. Peaks were fit using Voigt control parameters with limitations on the Gaussian and Lorentzian components, similar to previous studies [77]. Analysis of volume-

averaged cellulose crystallite sizes was completed using the integral breadth and full-width half-maximum (FWHM) values for the (200), (1-10) and (110) Voigt fitted peaks. These provide values of crystallite width perpendicular to the diffracting planes. Crystallite length was not analysed due to the poorly resolved nature of [004] peaks. The overall CI for each sample was then calculated from the ratio of the 5 crystalline peak area intensities ($A^{Crystall}$) to the amorphous peak area intensity ($A^{Amorphous}$) as:

$$CI = \frac{\sum_1^5 A_i^{Crystall}}{A^{Amorphous}} . \quad (5-2)$$

Although the aim of this analysis was only to compare results between samples within the study and not to other works, care should still be taken in selecting a CI analysis method. This method of peak deconvolution has been shown to be much less sensitive to changes in crystallite size than the Segal method [80]–[82] and thus was chosen for analysis of heel and tip samples where aging induced changes in crystallite size may be important. The d-spacings and apparent crystallite widths for each of the analysed peaks are summarized in Table 5-2.

Table 5-2: d-spacings and apparent crystallite widths for the three main crystalline peaks analysed. All values are reported in nanometers (nm) and include results calculated using the integral breadth and FWHM of fitted peaks.

	d - (1-10)	d - (110)	d - (200)	L (1-10) (IB,FWHM)	L (110) (IB,FWHM)	L (200) (IB,FWHM)
Heel	0.588	0.527	0.402	2.31 +/- 0.56	3.93 +/- 0.38	2.26 +/- 0.08
	+/- 0.027	+/- 0.010	+/- 0.001	2.72 +/- 0.57	4.62 +/- 0.52	2.98 +/- 0.14
Tip	0.594	0.533	0.403	2.31 +/- 0.52	4.72 +/- 0.23	2.34 +/- 0.11
	+/- 0.031	+/- 0.014	+/- 0.001	2.74 +/- 0.53	5.03 +/- 0.25	3.10 +/- 0.18

The aging of reed tips relative to their heels mates through conventional usage shows an increasing CI with aging trend overall. Results for CI values of all reed tip and heel samples are shown in Figure 5-8. This increase in CI is thought to be at the expense of amorphous regions, primarily lignin, and is consistent with previous findings for weathering and aging behaviour in wood XRD studies [83], [84].

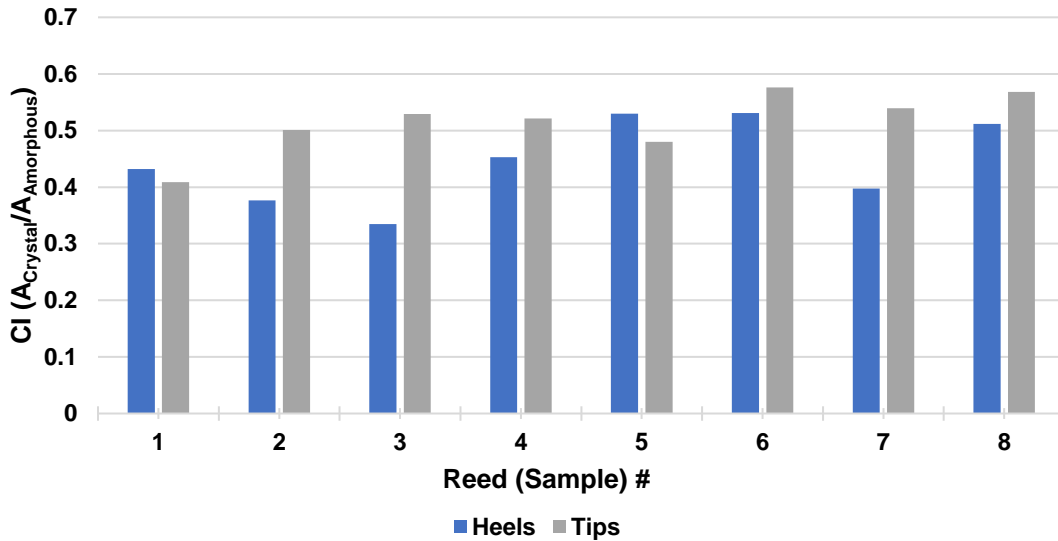


Figure 5-8: CI values for reed heel - tip pairs. Area values for crystalline and amorphous fractions were calculated using 5 crystalline peaks and 1 amorphous peak respectively.

Certainly, for the solid vascular bundle fibers, this result is consistent with a decreasing viscosity parameter (as observed for both reed and saturation cycle samples) where lignin is expected to dominate the viscous behaviour of fibers. Statistically significant differences between CI values for reed samples are not observed, although the changes between heel and tip samples are significant ($p < 0.05$). Average crystallite sizes were calculated using the Sherer equation [85], and the shape factor (K) was taken as 0.9 as in:

$$L = \frac{0.9\lambda}{\beta \cos \theta}, \quad (5-3)$$

where the x-ray wavelength (λ) is taken as 0.15418 nm and β is the integral breadth and is calculated from the ratio of peak height to integrated area (for the case of L_{200} , the (200) crystalline peak is used). Analysis of the (1-10), (110) and (200) peaks shows a slight increase in crystallite width for the (110) and (200) reflections and no change in width for the (1-10) reflection (Table 2). The reported values for these widths are really the volume averaged apparent crystallite sizes within the samples [79].

5.3.4 Thermogravimetric Analysis - TGA

TGA analysis was performed on all reed samples in order to better understand the approximate chemical degradation of cellulose, hemicellulose and lignin constituents. Of particular interest are the differential TGA curves (*mass %/°C*) and the peak positions of thermal decomposition. A typical TGA curve is provided in Figure 5-9 where the main degradation peak due to cellulose pyrolysis is easily visible. The basis for this analysis concentrates on changes in pyrolysis peak positions and peak shapes such that detectible changes can be attributed to changing weight percentages of chemical components (where these components degrade in reed samples during the study).

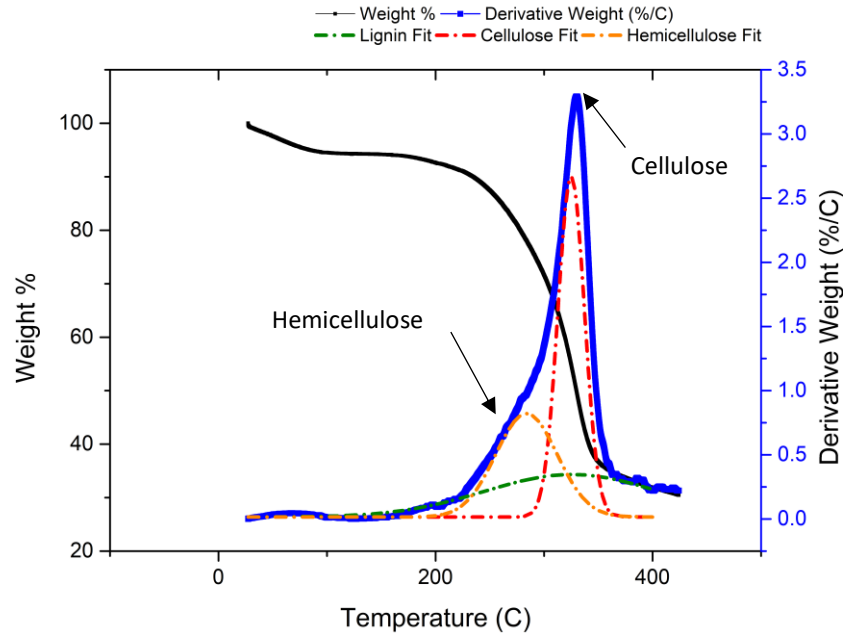


Figure 5-9: A typical TGA curve obtained for tested reed samples. Both the weight % and derivative curves are shown. The main degradation positions for hemicellulose and cellulose are denoted. Fitted peaks for each of the three main constituents analysed are also shown. Note that weight loss up to 100°C is due to equilibrium moisture content and was between 3 and 5% for all samples tested.

Complimentary sets of reed heels and tips were tested in this case, and these samples were taken from the same pieces in each of the nanoindentation, XRD and TGA tests. Results for each of the reed heel-tips pairs are shown in Figure 5-10.

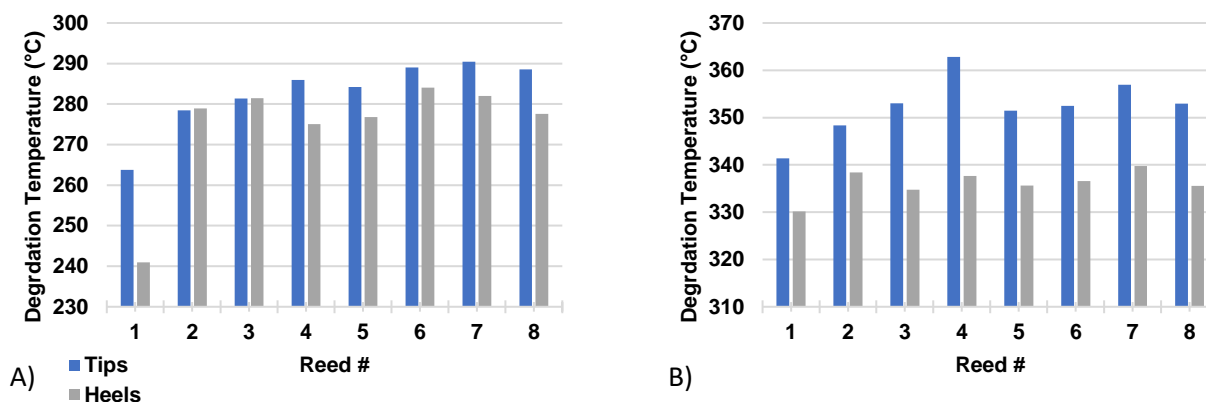


Figure 5-10: A) GA degradation temperatures attributed to the hemicellulose weight fraction of reed heel - tip samples and B) the corresponding degradation temperature attributed to cellulose.

Results are presented as two main peak position temperatures (hemicellulose and cellulose, respectively) where statistically significant results between the heel and tip sample sets are found for the cellulose peaks ($p < 0.001$). If the differential curve is analysed further the main inflection points representative of hemicellulose, lignin and cellulose degradation can be studied using a fitting method previously applied to wood chips [71]. This peak deconvolution was used to approximate the relative amounts of each of the constituents present and these results are shown in Table 5-1. The representative TGA curve provided in Figure 5-9 also depicts the corresponding fitted curve. One primary decomposition curve (approximated as a Gaussian peak) for each of hemicellulose, lignin and cellulose are added together to produce this fitted curve of overall decomposition rate. Using this approximation, lignin degradation is most significant during the aging process between heel and tip pairs. This finding appears in agreement with the general trend of decreasing resistance to viscous creep in solid fibers where it is thought that lignin contributes most significantly to viscous behaviour within the cell wall.

Comparison of initial lignin content with results for several types of bamboo are similar (for bamboo ~27 weight percent and here 31.2 +/- 8.46 weight percent, reported with standard deviation) [62]. The peak deconvolution method used in the present study should be viewed as a method for comparing samples and not taken as reference values for hemicellulose, lignin and cellulose weight percentage values. The fitting method is sensitive to the peak shape used in the

fitting and the positions of peak centers and thus only samples analysed using identical fitting parameters should be compared.

5.4 Discussion

5.4.1 Reed Heel – Tip Pairs

Modulus values calculated from single fibers yield results that are +/- 1.5 GPa of one another indicating that there is consistency within measurements taken from individual fibers and suggesting that variability due to sample surface condition is not significant. The modulus values calculated using the phenomenological approach (especially E_1) are lower than those computed from the VEP model. Despite this variation in absolute value, the trends for saturation cycle dependent modulus are very similar between all modeling approaches (see Appendix). In general, values of reduced modulus compare well with those reported for different species of bamboo [61], [62], [86] when the OP method is considered.

Overall values from reed heel and tip pairs reveal a trend of decreasing creep resistance in aged reed tips. Reed heels are found to be 30 to 50% more resistance to viscous creep (n_{VEP}) than their corresponding tips ($p < 0.03$). Similarly, fitted values for E_1 and η_1 show that reed heels exhibit relatively unchanged values of E_1 and increased values of η_1 (viscous creep resistance) for reed tips compared to the heels ($p < 0.03$). Although a few reed heel-tip pairs exhibit large differences in E_2 values, the overall difference between heel and tip samples is not statistically significant ($p > 0.05$). Despite this, the trend of increasing resistance to viscous creep in reed heels versus tips is also found for the η_2 parameter ($p < 0.01$). These results suggest that for solid fibers the aging process contributes more significantly to their viscous response than elasticity and may highlight the importance of solid fibers on changes that reeds undergo macroscopically (including internal damping).

Examining specific differences in reed tip and heel n_{VEP} values yields a few interesting findings. The fibers of reed tip 7 were much less resistant to viscous creep than those of tips 4, 5 and 6 (in each case, $p < 0.03$). Reed 8 heel fibers exhibited a significant difference from heel 2 and 4 ($p < 0.03$) where the fibers of heels 2 and 4 were substantially more resistant to viscous creep. Additionally, the aging process appears to vary between reeds where reed tip 7 becomes less resistant to viscous creep than other samples (specifically tips 4, 5 and 6). It is important to note

that all reed samples were taken from the same manufactured batch (specially obtained from the manufacturer) and all samples had identical macroscopic stiffness ratings as measured by the manufacturer. This suggests that measured mechanical parameters at the length scale of single fibers could be important in predicting the mechanical behaviour of reeds. Analysis of the artificially aged saturation samples reveals more on the effects of aging on viscoelastic response of solid fibers and parenchyma matrix.

5.4.2 Saturation Cycle Samples

The differences between aged reed samples are difficult to attribute to changes from saturation cycles or other factors such as mechanical fatigue. The tip deflects significantly during playing [40] and this likely contributes to degradation in macroscopic bending stiffness. Thus, the second set of samples were analysed to elucidate degradation due to moisture alone. These well-controlled saturation cycle samples (here referred to as artificially aged samples) reveal the extent to which moisture effects the viscoelastic properties of solid fibers and matrix cell walls with increasing exposure. A similar analysis regime to the reed heel-tip pairs was used for these artificially aged samples to confirm that trends discovered were consistent between methods (refer to Appendix A). The results illustrate an interesting aspect to changes in solid fiber viscous creep response within the first few saturation cycles (n_{sc}). During this initial stage ($n_{sc} \leq 5$) solid fibers experience an increase (~50%) in resistance to viscous creep (η_{VEP}) compared with the unsaturated case. This is accompanied by a large increase in fiber elastic modulus (at $n_{sc} = 0$, $E_{VEP} = 12$ GPa and at $n_{sc} = 5$, $E_{VEP} = 25$ GPa). This trend changes when $n_{sc} > 5$ with both η_{VEP} and E_{VEP} decreasing until they are similar to their initial values at $n_{sc} = 50$. Trends of η_{VEP} and E_{VEP} with increasing n_{sc} are provided in Figure 5-11. When fitted values of η_{VEP} for reed heel – tip pairs and their dependency on n_{sc} are included it is observed that they fit the general trend found for saturation cycle samples.

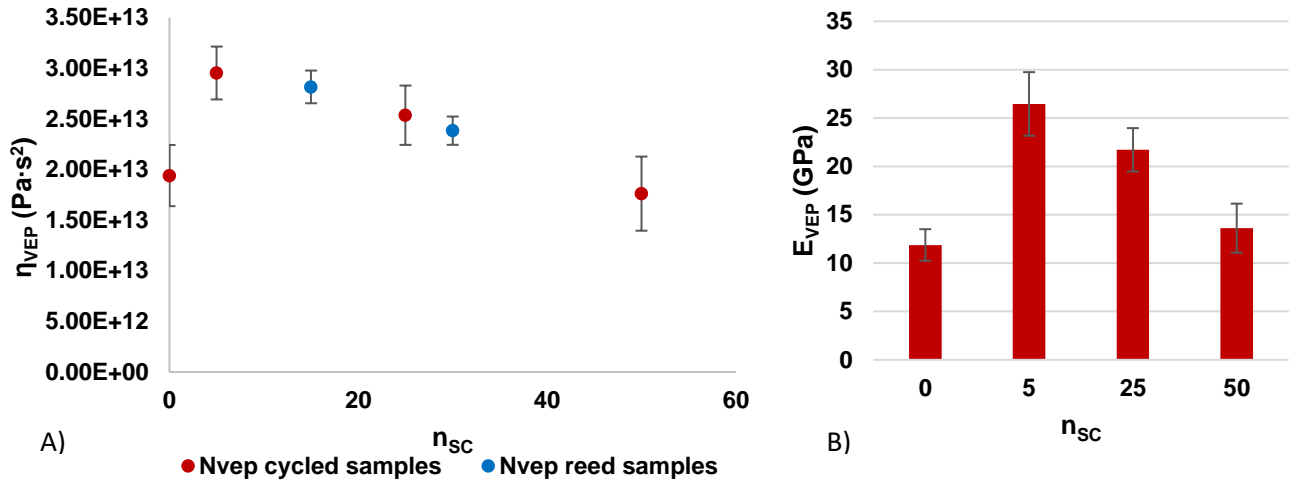


Figure 5-11: A) η_{VEP} viscosity values and their dependency on saturation cycles. Values calculated for reed heel and tip samples are also included for comparison with the general trend. B) E_{VEP} values for cycled samples with respect to number of saturation cycles.

The elastic and viscous parameters for solid fibers are shown in Figure 5-12 with the overall trend of decreasing resistance to viscous creep with aging being evident (for solid fibers of the vascular bundles).

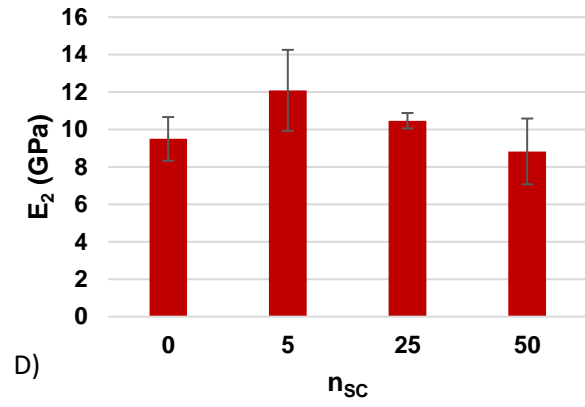
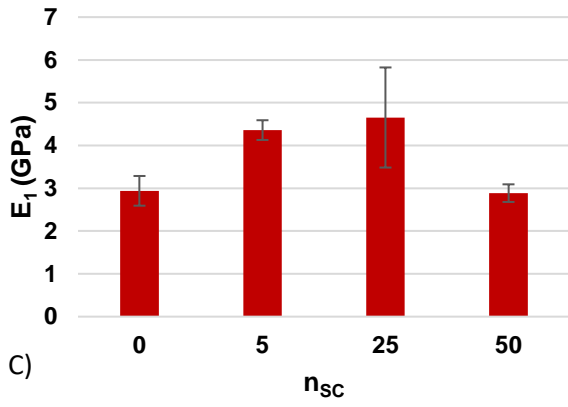
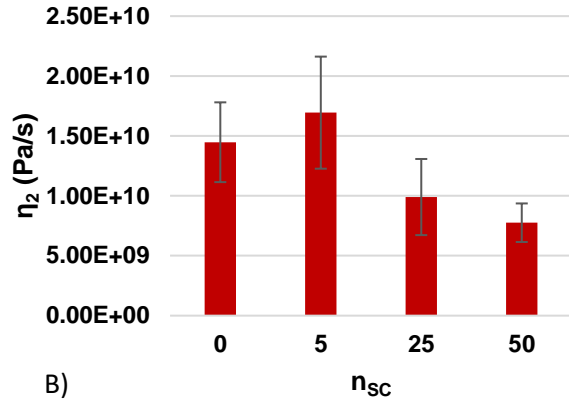
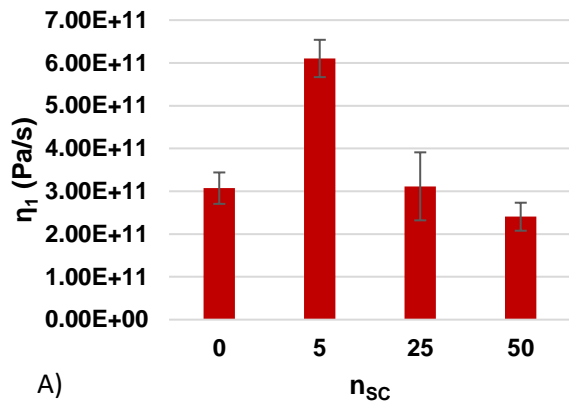


Figure 5-12: Maxwell-Voigt parameters for saturation cycle samples including η_1 , η_2 , E_1 and E_2 (A, B, C, D, respectively).

Regression analysis of η_{VEP} , η_1 and η_2 values indicates that the similarity in trends observed between these methods is significant (for η_{VEP} - η_1 $R^2 = 0.718$, Pearson's $r = 0.85$ and $p < 0.0001$, while for η_{VEP} - η_2 $R^2 = 0.524$, Pearson's $r = 0.72$ and $p < 0.0001$). This presents strong evidence that fundamental degradation mechanisms are contributing to the changing creep and viscous behaviour of solid fibers.

5.4.3 Solid Fibers and Parenchyma Cells

Suggested models for the structure of cellulose microfibrils [87] have previously been hypothesised and it is worth considering these here. Two primary models include series and fibril-structures where the former contains crystalline cellulose regions gapped by amorphous regions and the latter has more long range crystalline regions connected by amorphous (hemicellulose and lignin) surfaces. For the series model upon loading, all of the stress is supported by the smaller crystalline regions. In the fibril model both crystalline and amorphous surfaces bare the input stress. In the context of the present study, the fibril model appears to support the trends observed for E_{VEP} where changes in apparent cellulose crystallite width could result in an increase in measured elastic modulus, followed by a deterioration of E_{VEP} due to degradation of the surface chains. Lignin plays an important role in contributing to the mechanical strength of plant tissues and highly lignified cell walls are quite resistant to compressive forces [88]. Thus, the loss of these amorphous phases during aging are likely important in understanding the changing properties measured in the present study.

Different trends for both viscous creep and elastic modulus are found when results from the parenchyma cells are analysed. Initially, the parenchyma cells exhibit a steep drop in elastic modulus and an increase in viscous creep. The initial values of viscosity and elastic modulus (analysed using the phenomenological approach) for $n_{sc} = 0$ of solid fiber and parenchyma cells are provided in Table 5-3.

Table 5-3: Comparison of Maxwell-Voigt parameters for solid fibers and parenchyma cells of saturation cycle samples.

Maxwell-Voigt Parameters	Solid Fibers	Parenchyma Cells
E_1 (GPa)	9.49 +/- 0.35	7.57 +/- 0.53
E_2 (GPa)	9.50 +/- 1.17	9.45 +/- 1.48
η_1 (GPa·s ⁻¹)	307.31 +/- 36.71	228.86 +/- 21.52
η_2 (GPa·s ⁻¹)	14.48 +/- 3.33	11.77 +/- 2.64

As a comparison, values obtained from Oliver-Pharr analysis are $E_{OP} = 13.86 \pm 0.89$ GPa for solid fibers and $E_{OP} = 7.76 \pm 0.53$ GPa for the parenchyma cells. The initial values ($n_{sc} = 0$) of E_1 and η_1 in this case exhibit the largest differences between solid fibers and parenchyma cells. These E_1 and η_1 parameters suggest the major difference between these microstructural elements is the steady creep behaviour (at least initially and is higher in parenchyma cells). This suggests that there is a difference in the time-dependent response of the parenchyma cells when compared to the solid fibers of the vascular bundles. Differences in the elastic parameters may be related to the microfibril angle within the cell wall. This angle is a measure of the orientation of highly crystalline cellulose microfibrils with respect to the longitudinal axis of the overall fibers (in this case, parallel to the direction of indentation loading). The microfibril angle (MFA) of the cell wall greatly influences the resulting mechanical strength and measured elastic modulus [86], [89]. Differences in MFA between parenchyma cells and solid fibers have recently been characterised in moso bamboo [76] and indicate that the average MFA in the primary cell wall is higher (0-40°) in the parenchyma than in the solid fibers (~50°). Although the structure of ADL is not identical to bamboo there are many similarities and if a parallel is drawn, the smaller MFA of the parenchyma is likely responsible for larger E_1 parameters and effects the time-dependency of the parenchyma differently than the fibers. It should be noted that the MFA is species dependent as the results of MFA investigation by [76] are different to those obtained by [86].

All of the fitted Maxwell-Voigt model parameters for parenchyma cells are plotted in Figure 5-13 with respect to n_{sc} . Parenchyma cells constitute the majority of material volume within ADL and contribute significantly to macroscopic mechanical behaviour. The differences in nano-mechanical response between solid fibers and parenchyma noted here are thus important for understanding the static and dynamic properties of ADL and reeds.

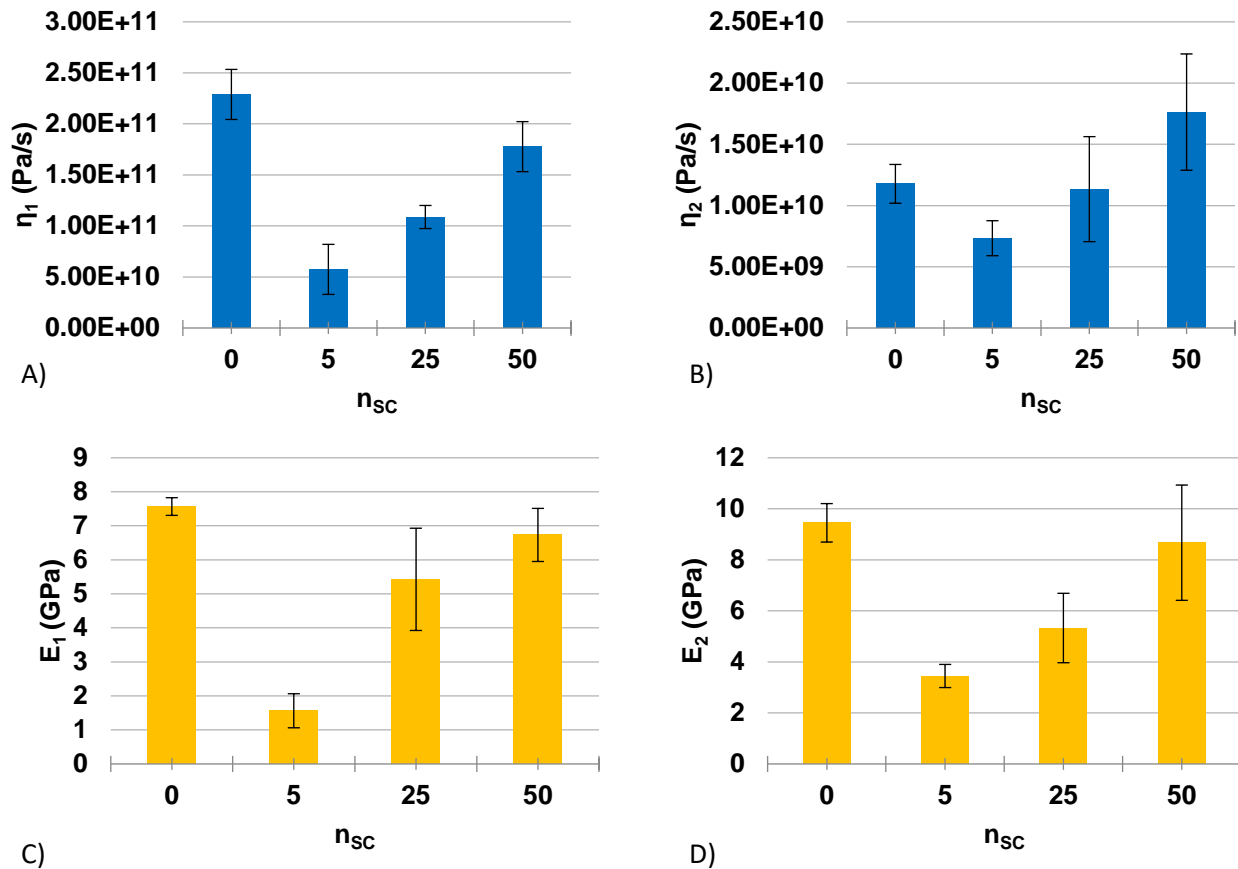


Figure 5-13: Maxwell-Voigt parameters for saturation cycle sample parenchyma cells including η_1 , η_2 , E_1 and E_2 (A, B, C, D, respectively).

A general trend of increasing resistance to viscous creep and increasing elastic modulus is found for all of the parameters (after considering the initial changes below $n_{sc} < 5$ discussed above). This result is markedly different from that obtained from solid fibers and a comparison is given in Figure 5-14.

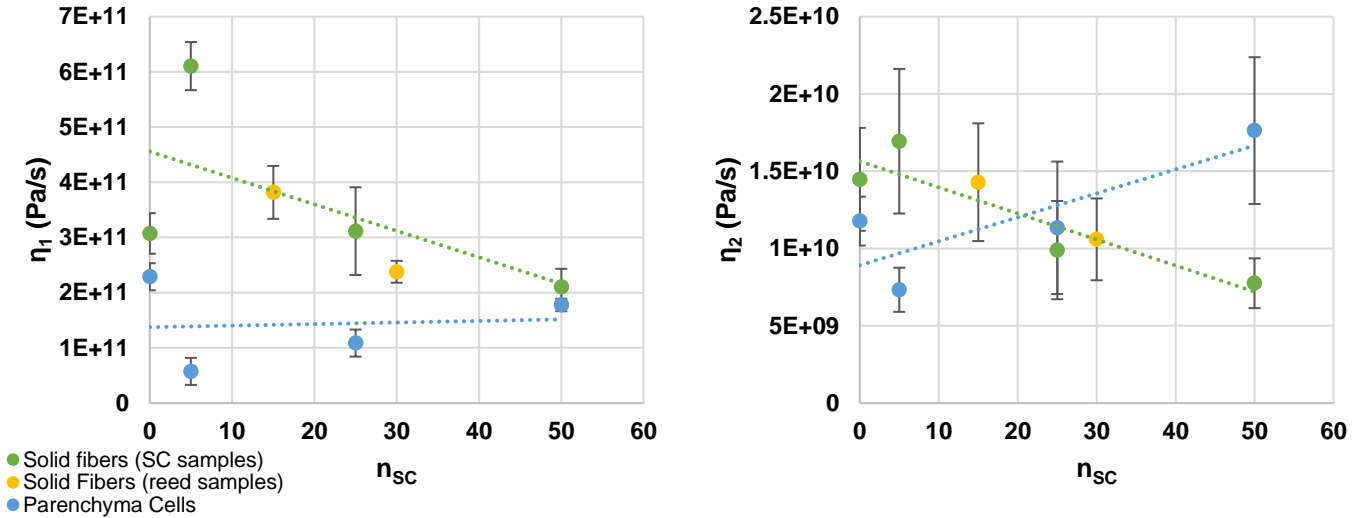


Figure 5-14: Comparison of viscosity parameter values between solid fibers and parenchyma cells. Results from reed heel - tip pairs are also shown. The difference in behaviour with increasing n_{sc} is observed for both η_1 and η_2 .

Results for elastic moduli within the fiber cell wall have been shown to be dependent on moisture content, with the different chemical constituents (primarily hemicellulose and lignin) reacting differently to changes in moisture content [90]. Lignin is particularly sensitive and decreases with increasing moisture content. Samples in the present study were equilibrated to minimize differences in moisture content, although the sensitivity of the E value of lignin to moisture content suggests that the lignification (or delignification) of the fiber cell walls may be important in understanding the contrasting fiber and parenchyma cell trends measured here.

Comparing the results from parenchyma cells with those of the solid fibers in terms of viscous creep indicates that there is an inflection point around $n_{sc} \sim 25$ where parenchyma cells become more resistant to creep than the solid fibers (Figure 5-14). This suggests that although the elastic response of ADL is initially dominated by the solid fibers the parenchyma cells do not contribute as significantly to viscous effects as aging increases and thus consideration should be

given to the relative densities of solid fibers and surrounding parenchyma for predicting aging behaviour.

5.4.4 TGA and XRD

Examination of thermal decomposition curves for reed heel and tip pairs reveals two main regions of interest. The first is associated with hemicellulose degradation [71], [91] while the second represents the major degradation stage due to cellulose pyrolysis [71], [91], [92]. The tested reed tip pairs show no significant difference in onset temperature of hemicellulose degradation ($p > 0.05$). In contrast, there is a significant difference in cellulose degradation temperature ($p < 0.001$). The average temperatures of each degradation peak are summarized in Table 5-4 and are similar to previous values for thermal degradation in wood [71], [93], [94].

Table 5-4: Results of TGA testing for reed heel - tip pairs, specifically changes in hemicellulose and cellulose peak decomposition temperatures.

Sample	Hemicellulose Peak (°C)	Cellulose Peak (°C)
Heel	274.19 +/- 14.97	336.15 +/- 3.15
Tip	282.72 +/- 8.68	352.43 +/- 6.20

As a control, an unused reed from the same batch as the reed heel – tip pairs was analysed and found to have hemicellulose and cellulose peak decomposition temperatures of 253.01 and 322.88 for the heel and 245.03 and 314.11 for the tip, respectively. These values are not significantly different from one another suggesting similar compositions, although they are both lower than values found for the aged reeds. Given this difference, it is likely that the reed heel samples had aged to some degree.

Analysis of the derivative thermogravimetric curves using peak deconvolution suggests that lignin degradation is more significant in reed aging than hemicellulose or cellulose degradation. Using this method lignin was found to be much reduced (in weight percentage) in the

reed tips than their corresponding heels ($p < 0.001$). Calculated weight percentages of hemicellulose, lignin and cellulose for the reed heel – tip pairs are provided in Table 5-5.

Table 5-5: Calculated weight percentages of chemical constituents for reed heel - tip pairs estimated from TGA peak deconvolution (standard deviation provided as error).

Sample	Hemicellulose (w%)	Lignin (w%)	Cellulose (w%)
Heel	32.11 +/- 8.07	31.22 +/- 8.46	36.68 +/- 2.52
Tip	52.14 +/- 4.51	7.94 +/- 4.11	39.92 +/- 3.87

Lignin degradation has also been found in natural weathering of wood at time scales ranging from 1 month [95] to one year or more [83]. One month of natural weathering was found to reduce surface lignin content by 62%. The importance of lignin to the mechanical properties of the cell wall have already been mentioned and the increase in viscous creep of tip solid fibers is likely a by-product of this decrease in lignin.

It can be recalled that although reeds (and more generally ADL) age with time this aging may not be uniform between reeds. Microstructural and/or chemical markers that may indicate more stable reeds are desirable from a manufacturing perspective. Analysis of the TGA results with the nanoindentation creep response of solid fibers found a correlation for heel samples ($R^2 = 0.60$, Pearson's $r = 0.78$ and $p < 0.03$). Here the p-value is a measure of the null hypothesis that non-zero correlation slope is due to chance.

XRD results for the reed heel – tip pairs can be summarized as displaying (change from heel to tip, i.e., with increased aging) increasing crystallinity, increased apparent cellulose crystallite size and no significant change in d-spacing. Within the context of cellulose TGA this result is in agreement with previous studies showing increased thermal stability with increasing crystallite size [91], [96], [97]. Increases in crystallite width have also been found in hydrothermally versus archeologically aged wood [84], with increasing time and temperature of hydrothermal exposure increasing the width of microfibril crystallites. Results between reed

samples show differences in apparent crystallite width indicating inherently different aging patterns, potentially due to different water accessibility levels between the samples. This trend holds true for both the initial reed heel samples and the fully aged tips meaning that detected differences are due to both variability in samples and variability in the aging process. The increasing CI values are also in agreement with trends observed for naturally weathered wood [83]. Specifically looking at the apparent crystallite sizes it can be surmised that the monoclinic cellulose I_{β} crystal structure is most abundant in ADL. The I_{β} structure has been found to be the primary type of cellulose within hardwood and higher plants [91], [98]. Analysis of tip elastic modulus values in relation to apparent crystallite size show a correlation in which tips having larger crystallites exhibit a larger elastic modulus ($R^2 = 0.62$, Pearson's $r = 0.79$ and $p < 0.03$).

A summary of CI and crystallite size dependency on age are shown in Figure 5-15. This illustrates the increasing trend of these elements during the aging process via standard playing by a musician.

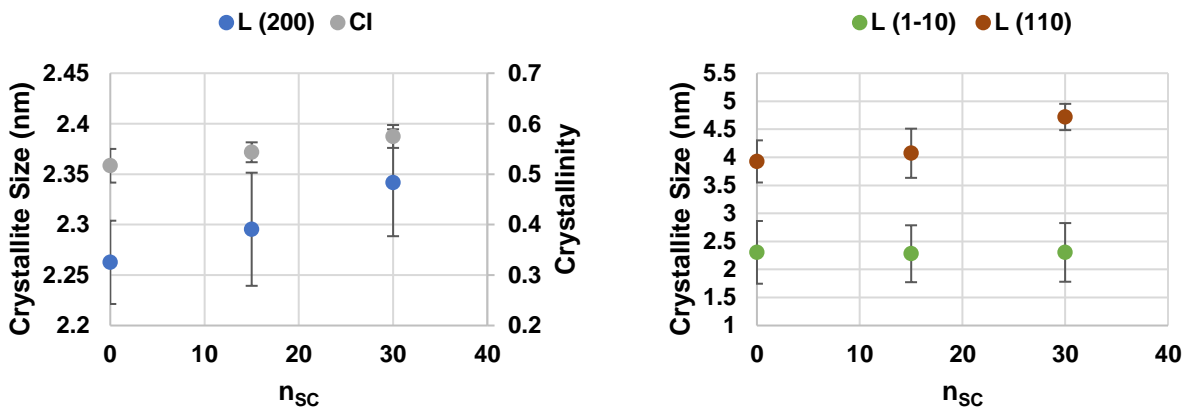


Figure 5-15: Apparent crystallite widths and CI values with respect to n_{sc} (reed heel - tip samples). Increasing trends are observed for the (200) and (110) directions and for crystallinity.

An important limitation to note is that the values of apparent crystallite width (when using integral breadth) are a weighted average [79], [87] and no distinction between microfibril crystallites of the solid fibers versus parenchyma cell walls can be made. An experiment outlining the differences between these two microstructural elements would be an interesting topic for future studies.

5.4.5 Internal Friction

Comparing the results of macroscopic viscoelasticity ($\tan \delta$) with nano-mechanical findings suggests that damping in ADL is controlled via a complex interplay of solid fibers and parenchyma cells. Values obtained at 100% RH will be discussed here as they are most relevant to actual reed usage. Plots of frequency dependent $\tan \delta$ with respect to n_{SC} are shown in Figure 5-16.

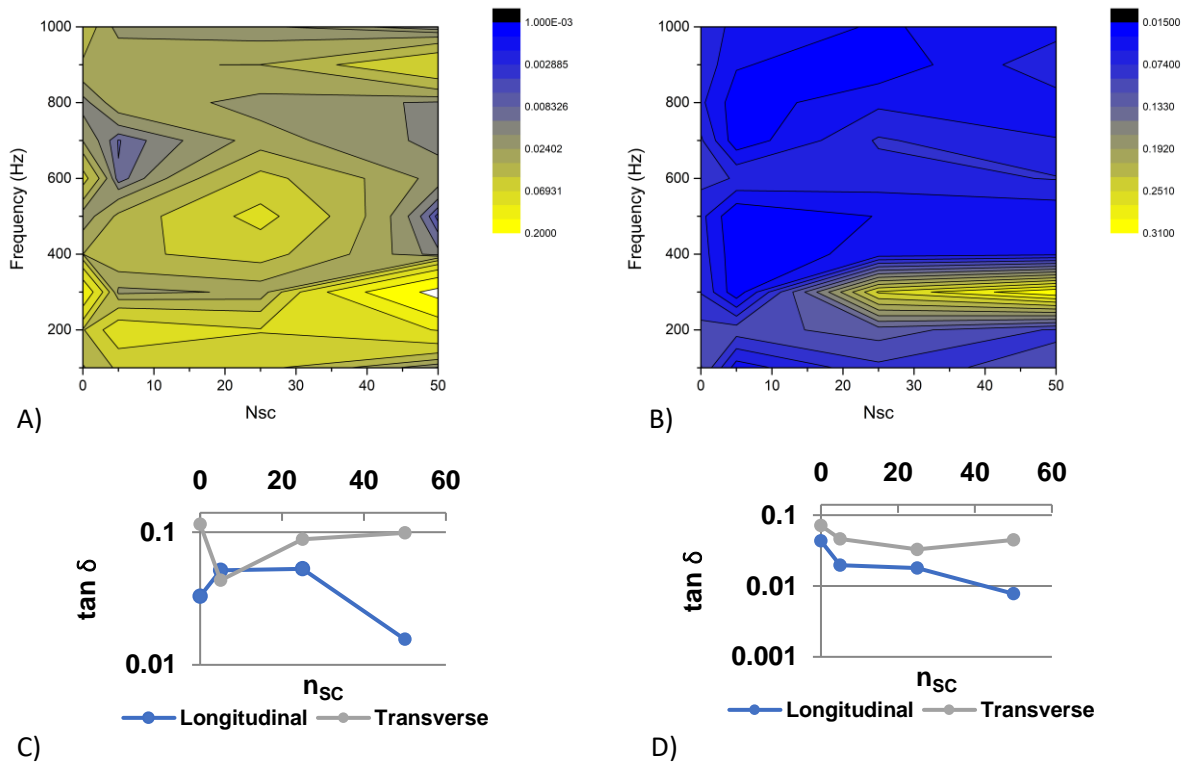


Figure 5-16: A) Longitudinal $\tan \delta$ values for saturation cycle samples. B) Transverse $\tan \delta$ values for saturation cycle samples. C) Values of $\tan \delta$ at 100 Hz and 100% RH with increasing n_{SC} . D) $\tan \delta$ values

Overall, $\tan \delta$ values are lower in the longitudinal direction than in the transverse direction. This seems to agree with the finding that solid fibers (running parallel to this direction) exhibit less viscous creep than the parenchyma cells. For both longitudinal and transverse values, when $f \leq 200$ Hz $\tan \delta$ values increase with increasing values of n_{SC} . This suggests that solid fibers contribute significantly to damping at these frequencies where the trend of decreasing viscosity values with increasing n_{SC} is observed. A similar though less significant trend for $\tan \delta$ is observed at $f \geq 900$ Hz. Longitudinal values of $\tan \delta$ between $400 \leq f \leq 900$ Hz decrease with increasing n_{SC} and

suggest that the viscous behaviour of parenchyma cells significantly contributes to overall damping at these frequencies. Given these results, the importance of the two main anatomical structures of the ADL microstructure to macroscopic damping should be noted. Analysis of their size, volume fraction and distribution may help manufacturers identify more stable reeds and predict their long-term behaviour.

5.5 Conclusions

The present study was designed to evaluate the nano-mechanical properties of microstructural constituents in ADL and their dependency on aging. This aging was completed via actual reed playing representative of real usage and artificial aging using saturation cycling. Elastically, the solid fibers of the vascular bundles did not change significantly when reed heel – tip pairs were compared. Good agreement between E_{OP} and E_{VEP} was observed, while E_1 and E_2 values from the Maxwell-Voigt model were lower by 20 to 30 %, potentially due to the sensitivity of these values to tip-induced plasticity. Despite these differences in modulus values, plasticity does not significantly impact the extracted viscous parameters. Analysis of elasticity in the saturation cycle samples indicated that there is an initial period where solid fibers exhibit an increase in elastic modulus, followed by a near linear decreasing trend until $n_{SC} = 50$. Elasticity in parenchyma cells is found to decrease initially and then increase linearly until $n_{SC} = 50$. This trend is nearly the inverse of that observed for solid fibers and suggests complex rearrangements of cellulose microfibrils and their interaction with hemicellulose and lignin within the cell wall of each anatomical structure during the aging process. Lignin degradation is found to occur in the aged reed samples (via TGA and increasing CI values) and may contribute to the decreasing elastic modulus values measured for solid fibers. Chemical analysis of isolated solid fiber and parenchyma cell samples in ADL would be worthy of investigation in future studies and could explain more localised anatomical aging behaviour. Although no statistically significant difference in solid fiber elasticity was observed for reed heel – tip samples, differences in viscosity were detectable and indicate that reeds of identical manufacturer rating (i.e., bending stiffness) may be further separable by anatomical and nano-mechanical behaviour. Macroscopically, these results suggest that bending stiffness degradation in reeds is primarily controlled by the solid fibers.

Values of viscosity for solid fibers were analysed using η_{VEP} and Maxwell-Voigt η parameters. Both analysis methods yielded similar trends for viscosity evolution with aging.

Overall viscous creep resistance is higher in solid fibers than in parenchyma cells with the fibers exhibiting a decreasing resistance to creep with increasing exposure to moisture. The opposite trend is observed for parenchyma cells and suggests a fundamental shift in the microstructural elements responsible for viscous damping during the aging process. Comparing viscosity results with measurements of $\tan \delta$ on macroscopic samples suggests that solid fibers and parenchyma cells each contribute to damping in different frequency ranges between 100 and 1000 Hz.

These results will aid the development of more naturally responding artificial reeds for woodwind instruments. Furthermore, methods could be developed to better classify ADL reeds using this data and yield more predictable and stable reeds. The differences in nano-mechanical behaviour observed for solid fibers and parenchyma cells suggests that the complex interaction of these two phases is important for controlling macroscopic static and dynamic behaviour. Future work could include the development of composite models to better understand dynamic behaviour at various length scales.

5.6 Appendix - Nanoindentation

5.6.1 Nanoindentation Modeling

In the following, nanoindentation load-displacement analysis is considered with respect to creep-unload constitutive relations (viscous-elastic-plastic), a phenomenological approach and a strain-rate measure of viscous creep resistance. This is performed to assess the elastic and viscous components of ADL fiber behaviour and the relative results between models. Some of the approaches require specialized input loading functions for practical experimentation, each of which are explained below. Results for elasticity (reduced modulus) are compared with the typical Oliver-Pharr [99] approach of unload curve fitting. The use of these models meant that experimentally three indentation points per testing location were used, each with their respective input load function to minimize differences due to intra-sample variability (i.e., for a single ADL fiber, 1 data point consisted of 3 separate indentations, one for each of the models).

5.6.2 Theory – Viscoelastic models

5.6.2.1 Viscous-elastic-plastic Model

The use of the viscous-elastic plastic model was completed experimentally using a trapezoidal loading function with equal loading and unloading times. Note that the segment timings for all loading functions can be found in Table A1 and examples of the loading functions can be found in Figure A-1. The use of this mode yielded one viscous term and one elastic term after fitting the viscous-elastic-plastic relation to the holding and unloading segments, respectively. The details of this model are described below.

A viscoelastic-plastic model for nanoindentation testing using a Berkovich tip can be described following the work of Oyen and Cook [64]. This model consists of elastic, viscous and plastic elements in a time-dependent constitutive relation. The basic premise is that the sum total of all displacements from each element leads to the total displacement observed experimentally when configured in series. Considering these elements, we can write the nanoindentation displacement relation as:

$$h = h_v + h_e + h_p \quad (5-4)$$

where each term represents a contribution from each element of the model [63], [64]. Of particular interest in the present study are the elastic and viscous components of the model. The constitutive differential equation of this model has been solved previously for the case of a Berkovich tip [63] and the creep and unloading portions of the model are provided as:

$$h_{creep}(t) = \frac{P_{max}^{1/2}}{(\alpha_3 \eta_q)^{1/2}} (t - t_r) + h_{load}(t_r), \quad (5-5)$$

$$h_{unload}(t) = k^{\frac{1}{2}} \left(\frac{t_r^{3/2} - (2t_r + t_c - t)^{3/2}}{3/2(\alpha_3 \eta_q)^{1/2}} + \frac{(2t_r + t_c - t)^{1/2} - t_r^{1/2}}{(\alpha_2 E')^{1/2}} \right) + h_{creep}(t_r + t_c). \quad (5-6)$$

The α values are geometric constants specific to the Berkovich tip. The parameters extracted from this model (E' , η_q , where E' and η_q will hereafter be referred to as E_{VEP} and η_{VEP}) provide measures of elasticity and viscosity, respectively.

5.6.2.2 Phenomenological Model

Nanoindentation testing for the phenomenological model required an idealized step-function as the input load-time curve such that the load was the practical approximation of an instantaneous step (within the practical limits of the nanoindentation instrument). Creep parameters are extracted from the hold-segment of the input loading function by fitting 2 elastic and 2 viscous parameters to the output load-displacement curve. Similar to the previous model, details of segment timings and the loading function can be found in Table A-1 and Figure A-1.

The phenomenological approach developed by Fisher and Crisps [66] and considered here and has been used to extract parameters for a 4 element Maxwell-Voigt model where the creep-hold portion of the load-displacement indentation curve is fit. This approach utilizes a step function input, and thus assumes instantaneous application of the load (as previously discussed). The depth-time relation for this model is provided below.

$$h(t) = \frac{\pi}{2} P_0 \cot \gamma \left[\frac{1}{E_1^*} + \frac{1}{E_2^*} (1 - e^{-tE_2^*/\eta_2}) + \frac{1}{\eta_1} t \right] \quad (5-7)$$

Parameters extracted from this model include 2 elasticity terms (E_1^* and E_2^*) and 2 viscosity terms (η_1 and η_2).

5.6.2.3 Strain-rate Sensitivity Model

A conventional creep sensitivity analysis has also been considered here to evaluate the viscoelasticity of single fibers and extract creep related data from the creep-hold segment of the load-displacement curves. This method [65] utilizes the secondary creep rate (steady state, linear) during the hold period of the indentation function and evaluates the creep exponent parameter, n , with larger values representing more creep resistant fibers (i.e., exhibiting a more elastic response). This method provides a general indication of time-dependence, as well as an indication of sensitivity to contact hardness. This method yields a single viscous parameter (the creep exponent)

and thus results are compared with n_{VEP} , the viscous parameter from the VEP model and η_1 and η_2 of the phenomenological model.

The creep exponent is found using a log-log plot of stress strain-rate (the first derivative of the depth-time curve) where the stress under the indenter tip is calculated from the known indenter load and the projected contact area. For a Berkovich tip, this area is found using [100]:

$$A_p = 3\sqrt{3}h_p^2 \tan^2 65.3 = 24.5h_p^2, \quad (5-8)$$

where h_p is the depth beneath contact. From this, the stress can be calculated from

$$\sigma = \frac{P}{A_p} \quad (5-9)$$

where P is the indentation load. The strain rate is calculated from the measured indenter depth, h, at known time, t, as in

$$\dot{\epsilon} = \frac{1}{h} \frac{dh}{dt}. \quad (5-10)$$

The relationship for creep sensitivity can be expressed using equation 5-11, where the slope of the stress-strain rate log-log plot provides the creep exponent (n).

$$\dot{\epsilon} = C\sigma^n \quad (5-11)$$

C is a constant dependent on temperature and has been assumed to equal 1 in the present study.

5.6.2.4 Model Summary and Comparative Results

As a summary, the load functions for each of the methods are provided in Table A1 below including all segment parameters. Samples were allowed to equilibrate with the nanoindentation test chamber for 1 hour prior to testing to minimize thermal drift (conditions 23°C and 20% RH).

Table A-1: Nanoindentation loading schemes for testing of reed and raw ADL samples.

Experimental Technique	Segment Times (load-hold-unload, in s)	P_{max} (μN)
Oliver-Pharr	3-5-3	350
Viscous-elastic-plastic (VEP) and Strain-rate Sensitivity	3-15-3	350
Phenomenological (Maxwell-Voigt Model)	0.1-15-3	75

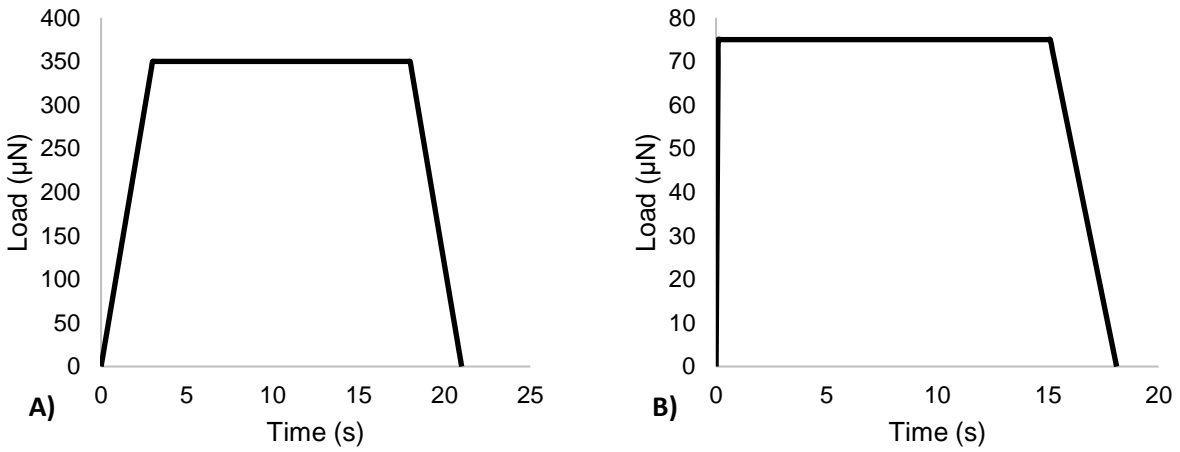


Figure A-1: Experimental load function profiles for the A) the VEP model and B) the Phenomenological model.

Table A-2 also provides a summary of the extracted viscous and elastic parameters of interest from each of the models discussed above. The results of reed heel-tip pair elastic moduli show that there is a relationship between the Oliver-Pharr (OP) and VEP analysis techniques. A linear correlation between the two methods ($R^2 = 0.52$, $p < 0.05$) indicates that results are comparable, although the relationship is not completely 1:1 and OP values tend to underestimate fiber elastic modulus.

Table A-2: Description of parameters extracted from nanoindentation testing at identical sample locations using each of the models considered.

Experimental Technique	Elastic Parameters	Viscous Parameters
Viscous-elastic-plastic (VEP)	E_{VEP}	n_{VEP}
Phenomenological (Maxwell-Voigt Model)	E_1^* , E_2^*	η_1 , η_2
Strain-rate Sensitivity	E^*	n

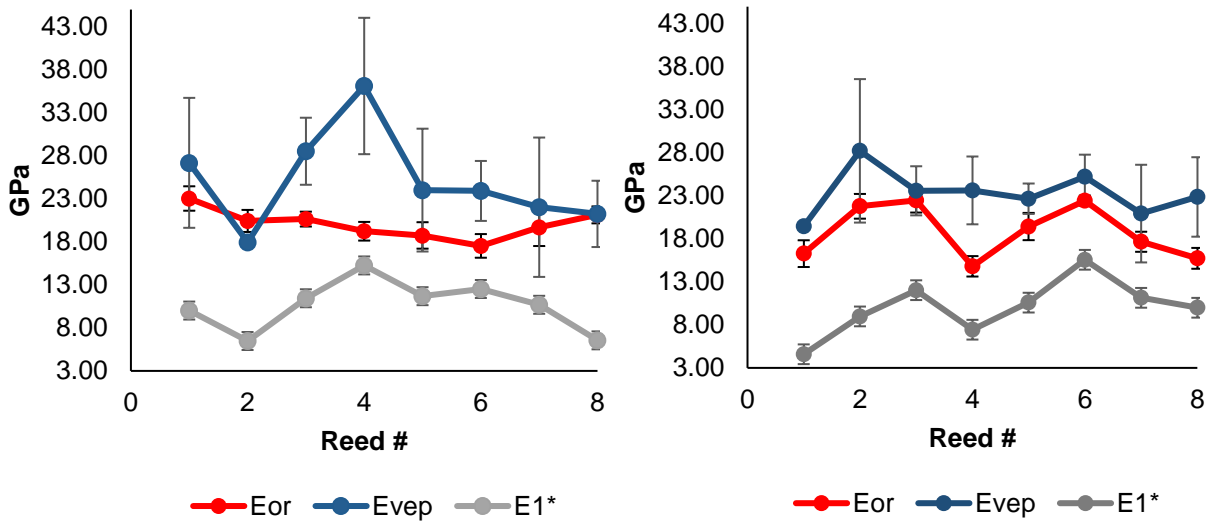


Figure A-2: Comparison of elastic modulus values calculated for solid fibers using both the Oliver-Pharr, VEP and phenomenological methods. Results for reed heels are shown on the left and results for tips on the right.

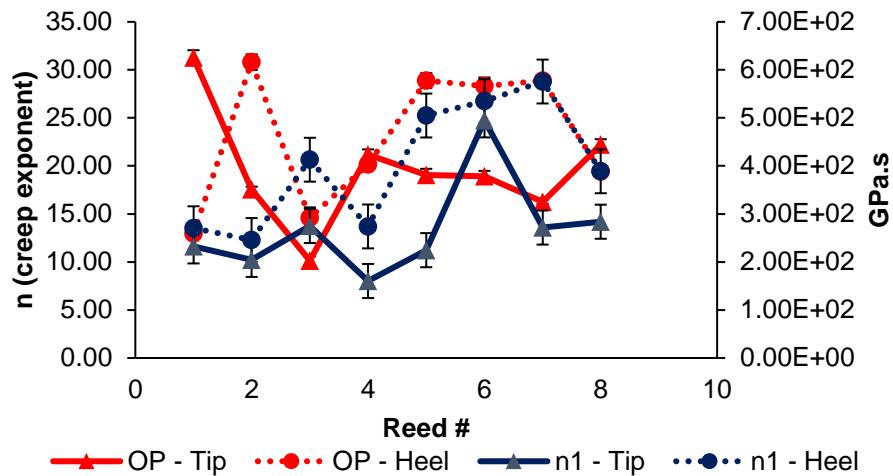


Figure A-3: Comparison between the creep exponent (n) and the viscous parameter (η_1) from the phenomenological model. Results for both reed heels and tips are shown.

The comparison of E values computed from the VEP solution and the phenomenological method shown in Figure A-2 indicate that differences before an after aging (i.e., heel versus tip samples) remain consistent between the two methods. The Oliver-Pharr method does not appear to be as sensitive to differences between samples for the reed heels as there is less inter-sample variability and suggests that either of the two viscoelastic analysis models are more appropriate for discerning aging related changes between samples. Examining the results from strain rate plots shows that the creep exponent, n , is in general higher for the heel samples than the tip samples (Figure A-3). This trend is also observed for the viscous parameters extracted from the VEP and phenomenological models. Note that all results between models were obtained for identical solid fibers, eliminating inter-fiber variability. This creep exponent is a measure of creep resistance and indicates that reed tips are more susceptible to creep at end of life. Given the similarity between models it can be concluded that vascular bundle solid fibers exhibit reduced resistance to viscous creep with exposure to playing (moisture, mechanical vibration) induced aging.

The influence of the nanoindentation time-dependent load-displacement model on the results has also been considered. For a more practical comparison between the samples it was important to evaluate the independence of the general trends observed from the implemented model. The consideration of several models enabled model accuracy to be assessed, as time-

dependent nanoindentation analysis is complicated by several factors, including experimental conditions, sample preparation and the analysis model. Overall, it was found that the results of the phenomenological and VEP models agreed for reed heel-tip comparisons and reed aging results.

The elastic and viscous parameters computed using the phenomenological model exhibit similar trends to the VEP analysis, and additionally all the elastic results (VEP, phenomenological and Oliver-Pharr) are also in reasonable agreement. Overall values from reed heel and tip pairs reveal a trend of decreasing creep resistance in aged reed tips. This result is found using the VEP, phenomenological and creep exponent analysis methods. A comparison of the results is shown in Figure A-4 B). Analysis using the n -exponent in a log-log plot of strain rate versus indentation stress suggests a similar trend of decreasing resistance to viscous creep in reed tips, although there is more scatter in the data ($p > 0.05$) potentially due to the sensitivity of this method to contact hardness.

It should be noted that the E_1 values obtained from the phenomenological model are lower than the modulus values calculated using the VEP or Oliver-Pharr methods. This suggests that there may be some sensitivity to the step-load application, where the increase in load is finite and not instantaneous as in the theoretical framework [66]. For this phenomenological model, E_1 and η_1 are only influenced by the time-dependent creep deformation and not the initial step displacement, meaning that those parameters are still useful for quantifying time-dependent behaviour regardless of potential sensitivity to the step increase in load. An attempt was made to minimize this sensitivity by keeping the applied indentation load low for the step function (75 μN).

Results are also compared for the saturation cycle samples between the VEP and Maxwell-Voigt methods. Although the fitted parameters for viscosity differ in absolute value, the trends observed between the two are similar (analysis with linear relationship between the two). Values of the creep exponent (n) for the creep-hold segment are also provided for these samples. The similarity in trends observed between all three methods suggests a fundamental change in the micro-mechanical response of solid fibers with increasing exposure to moisture cycles. The trend comparison plots for solid fibers of the saturation cycled samples are provided in Figure A-4.

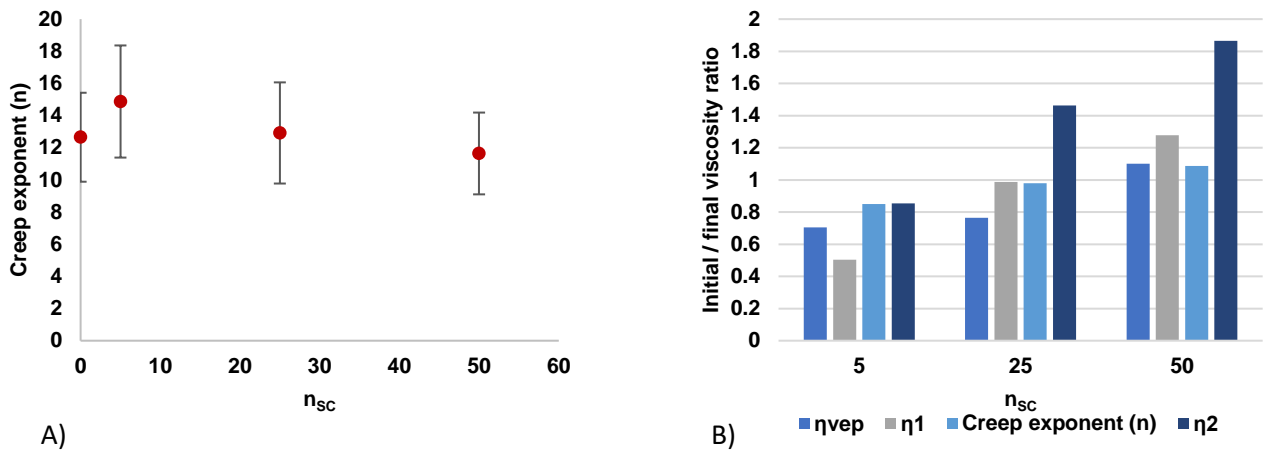


Figure A-4: A) Creep exponent (n) values with respect to n_{sc} for saturation cycle samples (calculated from the creep-hold period). B) Comparison of viscosity values between methods. Here the values are presented as ratios normalized with respect to the initial values (at $n_{sc} = 0$). All results shown are given for solid fibers of the vascular bundles.

The results from aging analysis and model comparison indicate that general trends are consistent and not model dependent. Therefore, consideration of elastic and viscous parameters extracted from either the VEP or phenomenological approach leads to the same conclusions.

Chapter 6

6 Swelling and Moisture Fatigue Behaviour of *Arundo Donax* using Micro-Computed Tomography

C. Kemp¹, Selina Kolokytha², Dominique Derome³, G. Scavone¹

¹Computational Acoustic Modeling Laboratory, Department of Music Research, McGill University

²Centre for X-Ray Analytics, Swiss Federal Laboratories for Material Science and Technology (Empa)

³Laboratory for Multiscale Studies in Building Physics, Swiss Federal Laboratories for Material Science and Technology (Empa)

This chapter is in manuscript form and will be submitted for publication. The experiments outlined in this chapter examine the swelling behaviour of *Arundo donax L* at elevated moisture conditions. Given the degradation in material properties presented in Chapter 5, it was desirable to compare the physiological and morphological changes that the reed material experiences under well controlled moisture cycling experiments. The samples selected for this study were not played by a musician and thus were not exposed to mechanical fatigue. The results of this study help to better understand the roll of moisture in reed degradation when it is isolated from the mechanical component.

Abstract:

The degradation of woodwind instrument reeds (*Arundo donax L*) is not well understood and this work presents the findings of an interdisciplinary investigation into the reed microstructure at

various moisture contents and presents long-term anatomical degradation results previously unconsidered. Although similar to bamboo and sharing properties with wood, few studies have focused on the behaviour and anatomical structure of *Arundo donax L* in moist conditions. As reeds are played in a fully water saturated state, hygromechanical properties are an important aspect of reed vibrational behaviour. In the present study, in-situ swelling of *Arundo* material is analysed using micro computed tomography. Image analysis shows that swelling occurs primarily in the radial and tangential directions and is linearly dependent on moisture state (relative humidity). Localised swelling is found to be significant around vascular structures where moisture absorption is greatest and exceeds measured macroscopic values of swelling strain. Analysis of moisture cycled samples shows a thinning of parenchyma cell wall tissue with increasing exposure to moisture cycles. Significant tortuosity of the parenchyma cell wall is also found and is thought to contribute to the reduced mechanical stability, with respect to bending stiffness of real reeds as they age. Future work could consider chemical analysis of parenchyma cell wall constituent degradation as well as computational analysis of *Arundo* material at different moisture states to study the impact anatomical changes have on vibrational modes.

6.1 Introduction and Background

The vibrating element of single reed musical instruments, such as clarinets and saxophones, is constructed from *Arundo donax L*. This naturally growing member of the grass family has been used in the construction of reeds for centuries [101]. Much variability is observed between reeds in a nominally identical set [8], [102] and usually results in researchers utilizing synthetic reeds for testing purposes [6], [40]. The acoustic literature to date has focused on the study of reed-mouthpiece systems and has mostly neglected the influence of variable reed properties on instrument performance (i.e., reed elastic properties are taken as isotropic and homogeneous). Others have noted the importance of moisture on vibrational properties in rectangular bars of *Arundo donax L* [55] which suggests that inter-reed variability control may require consideration of both moisture state and anatomical structures.

While previous models have been developed to study reed behaviour, they typically consider the reed-mouthpiece system as a second-order oscillator with homogenous properties along the reed tip [39], [103], [104] which may not be accurate given the variable distribution of anatomical elements through the *Arundo* culm [12]. The tip of the reed is approximately 100 to 150 microns

in thickness and the material presents varying spatial distributions of anatomical structures. These distributions likely cause nonuniform swelling and shrinkage locally within the reed microstructure resulting in aging degradation in the form of warping. Reed tip warping is undesirable as it leads to uneven closing of the reed with the mouthpiece, changing flow characteristics and vibration. Studies using artificial player systems designed to study reed-mouthpiece interaction in a controlled way suggest that, for clarinet reeds, tip vibration is quite large and includes both longitudinal and transverse modes [40]. Reed behaviour is also inconsistent and varies with time, increasing the difficulty in assessing typical acoustic and subjective parameters of reeds, such as brightness and ease of playing [8], [45]. It is also difficult to assess the level of saturation that *Arundo* material experiences when reeds are played in the mouth. All of these factors suggest that careful anatomical analysis of moist reeds and reed material is warranted.

Despite recent efforts to examine changes in fundamental bending vibrational modes of reeds exposed to moisture [5], not much is known about microstructural changes with time and playing that can contribute to changing performance. Previous chemical analysis on a small number of clarinet reeds did not yield significant correlations to the prediction of musical quality [41] and compiled anatomical statistics have not considered the influence of moisture [4]. Furthermore, the swelling properties of reeds at elevated humidity states has not been examined thoroughly. It is desirable to observe the in-situ swelling of *Arundo* samples at different humidity levels to better understand the complex interaction between anatomical structures and moisture saturation. This behaviour is similar to that occurring in fully wetted reeds when played in the mouth. Examination of microstructure/anatomical morphological changes in these settings will also help to understand those features that contribute most significantly to reed aging.

6.2 Physiology and Properties of *Arundo Donax*

Arundo donax L is a bamboo-like plant that develops into a tubular culm with node and internode regions as shown in Figure 6-1.

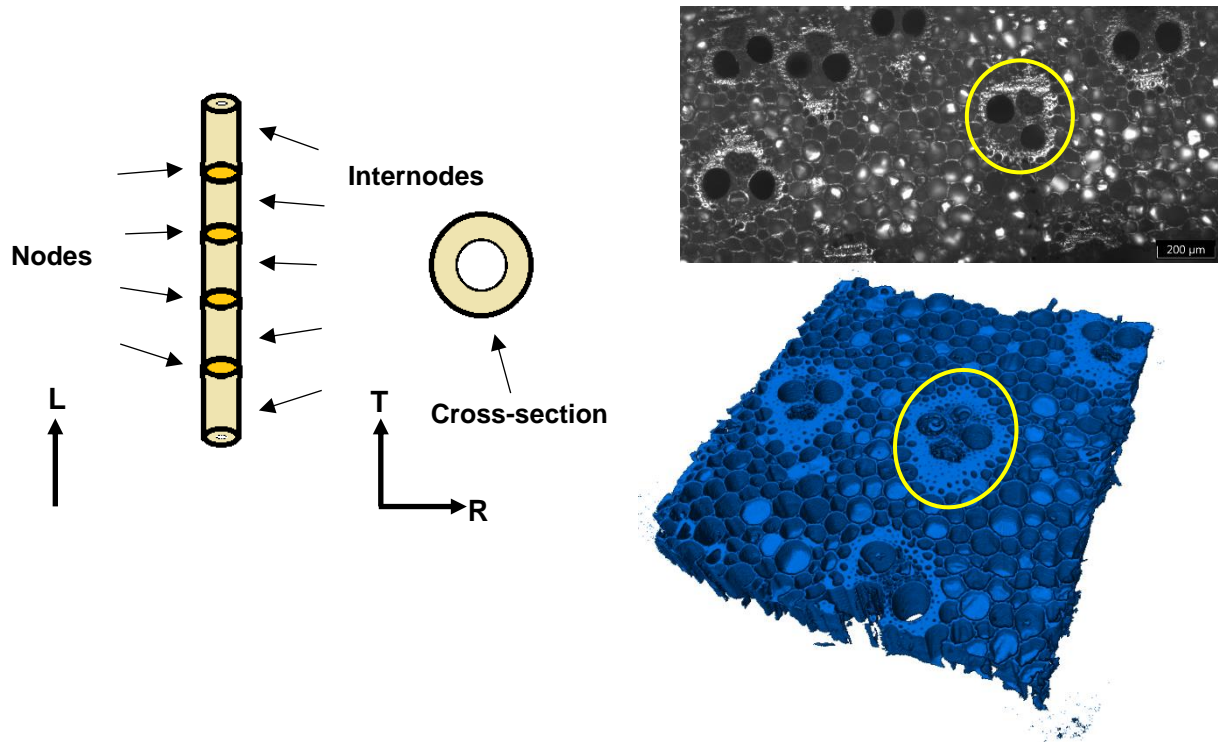


Figure 6-1: Schematic diagram showing a typical *Arundo Donax* stem (without rhizome). The longitudinal direction is provided with respect to the culm and the tangential and radial directions with respect to the cross-section. A cross-section micrograph is also provided. The regions denoted by the yellow circles depict vascular bundles while the surrounding area is parenchyma tissue. Note that the softer, parenchyma tissue is found towards the inner diameter of the culm. This region also constitutes the majority of the inner cortex of the plant.

It is a giant reed of the grass family with a similar cross-section anatomy to that of bamboo [105]. Despite its use for woodwind reeds and as a potential provider of biomass energy [106], it is widely considered to be an undesirable weed. As previously measured [101], [105], the *Arundo* culm can grow up to 4 cm in diameter and 7 mm in wall thickness. Mechanical stability is provided by the vascular structure of inner parenchyma ring, with highly lignified solid bundles providing longitudinal rigidity [12]. This longitudinal direction is considered to be aligned with the direction of culm growth, in terms of the plant's physiology. This mechanical stiffness enables the plant to grow to lengths of several meters and this, combined with desirable damping properties [55], makes it the preferred choice for woodwind reeds. The gradient in spatial density of vascular bundles with respect to the *Arundo* culm wall has a pronounced effect on the mechanical properties of the culm. For bamboo, mechanical measures including tensile strain to failure are higher for the epidermal layer than for the inner, parenchyma-rich layer indicating that solid fibers have greater

ductility potential [107]. Longitudinal values of Young's modulus are also found to be dependent on spatial location within the culm wall, and the internode region that samples are taken from (i.e., modulus values towards the root of the plant are higher than those towards the top section). This dependence of anatomical structure on mechanical properties has been noted for bending of moso bamboo also [62]. The influence of moisture on anatomical structures must be considered for woodwind reeds (i.e., finished reeds used on instruments) as morphological changes of parenchyma cells and vascular bundles is not well understood for their material, *Arundo donax L.*

Woodwind reeds are machined from the *Arundo* culm wall of internode sections. The reed is rigidly clamped to a mouthpiece while playing and it is primarily the tip section that vibrates as an air-flow valve. The reed tip geometry is machined down to the inner layer of the parenchyma ring and no material from the epidermal layer is in contact with the musician's mouth. Anatomically, this results in a vibrating structure that is comprised of parenchyma cells and vascular bundles of the culm's inner diameter. Parenchyma cell wall thickness, size and vascular bundle distribution therefore contribute significantly to the effective mechanical properties of the tip. When moisture is considered, morphological changes in these structures are of importance and must be considered. Kolesik et al. [4] found that high continuity of fiber structures surrounding the vascular bundles was associated with higher quality reeds. Furthermore, smaller proportions of phloem and xylem tissue within the vascular bundles was also correlated to higher quality reeds. The importance of parenchyma tissue is still unclear, as is the effect of these anatomical structures on long term degradation and changes during moisture absorption.

Previous research on in-situ swelling of wood [13]–[15] has utilized micro-computed tomographic (CT) imaging to visualize anatomical structures at specific moisture conditions. X-ray tomography provides morphological data in three dimensions and makes it an ideal candidate for the examination of in-situ *Arundo* swelling. This three-dimensional data also enabled the confirmation of an important *Arundo* physiological assumption, longitudinal symmetry. This longitudinal symmetry has implications for manufacturing settings where analysis of lignified vascular bundle fibers is directly correlated to mechanical stiffness of manufactured reeds (refer to Chapter 4 for more detailed analysis). As compared to typical late- and earlywood, *Arundo donax L* presents vascular structures that are not present in its wood counterparts. The influence of these anatomical structures on in-plane (i.e, tangential and radial) moisture-induced swelling has

not previously been discussed despite its believed importance on the vibrational modes of the reed tip during playing (considered previously in terms of bamboo). Due to the small thickness of typical alto saxophone reeds (100 to 150 microns) at the tip, the influence of local swelling strains would lead to variable warping behaviour (a typical degradation mechanism of reeds).

Binarization and segmentation of tomographic slices is a complicated process and generalized workflows established for specific materials usually require modification for new materials. This complicates the analysis process and care should be taken to prepare the best possible binary images, minimizing the impact of intra-sample variability on statistical measures. Arundo material retains two anatomical structures of interest in terms of importance to real reeds. These are the vascular bundles and parenchyma cells. Segmentation and binarization procedures therefore follow similar workflows to those developed for wood type materials, where the final processed images are binary representations of solid material and pore structures. This means that thresholding procedures should be optimized to the Arundo material intensity and the air volume intensity of tomographic image slices. Subsequent analysis of these binary slices involves extraction of shape and size parameters that quantify the anatomical structures of interest.

Micro-CT analysis can yield much statistical data that are pertinent to *Arundo donax L* anatomical evaluation. For wood and plant type materials, anatomical structure analysis has included phloem and xylem conduit size, parenchyma cell size [108], parenchyma cell wall thickness and lumen diameter [109]. Similar to wood, *Arundo donax L* exhibits strong longitudinal symmetry and thus anatomical statistics are most interesting in the radial and tangential directions. Parenchyma cell wall thickness is of interest as the deterioration of these cells would have a direct impact on the bending rigidity of thin reed tips. Similar types of analysis have been completed for cell wall thickness on early and latewood, although this was only completed on new specimens and did not consider aging behaviour [109]. Measurements of swelling strain can also be completed through registration analysis of tomographic image sets obtained at different moisture conditions [14, p.], [15]. Swelling strains are of particular interest in the tangential-radial plane (representing the cross-section of the Arundo culm) as expansion/shrinkage in these directions would modify the reed tip-opening displacement. The flow performance of the reed-mouthpiece system is very sensitive to this area and geometrical changes due to swelling could influence the free-vibration modes of the reed [110], [111].

The cell wall structure is an important characteristic of wood and bamboo type materials. This structure is comprised of a hierarchical composite layout that contributes to impressive specific strength at the macroscopic scale. Unlike wood, bamboo solid fibers exhibit a very fine multi-layered structure with alternating thin and thick composite layers [112]. For solid vascular bundle fibers in moso bamboo, cellulose microfibrils within the cell walls have been found to be nearly axially aligned with the longitudinal direction, contributing to the fibers' high longitudinal modulus [60]. More specifically, the thick walls contain cellulose microfibrils with a low microfibril angle (MFA), whereas a high MFA is found within the thin layers. Similar to the secondary (S2) layer of typical wood cell walls, the cellulose microfibrils are helically oriented within this layer and embedded in a matrix of amorphous cellulose, hemicellulose and lignin. This high degree of alignment (in terms of MFA) has the effect of drastically increasing the longitudinal modulus relative to parenchyma cells. Previous studies on bamboo found the degree of lignification of the solid fiber cell wall to not significantly impact the modulus of solid cell wall fibers, although it has been shown to impact the modulus of wood cell walls [113]. These distributions of highly crystalline cellulose microfibrils and amorphous (and hydrophilic) lignin are important as the hydrophilic components experience softening and swelling during moisture exposure [114]. Similar to bamboo, the composite microstructure of *Arundo donax L* owes its mechanical performance to rigid vascular bundles and compliant parenchyma cells. Changes to these structures at elevated moisture conditions including swelling strain characterisation will aid in the understanding of long-term reed performance and mechanical degradation, which is pertinent to vibrational behaviour.

6.3 Materials and Methods

For this study, raw samples of *Arundo donax L* obtained directly from a reed manufacturer were used to observe moisture induced swelling and anatomical changes due to repeated moisture cycling. The manufacturer obtains *Arundo* culms from farms in France after they have been allowed to dry at ambient conditions for one year. Culms are then shipped to the manufacturing facility where the node regions are removed and splits are made from the internodes. Micro-CT samples were hand-cut from these splits using a razor blade, as more conventional material preparation techniques such as diamond cutting, laser ablation and grit-polishing can damage the delicate microstructure of the culm. Four samples were cut into 1 mm by 1 mm x 3 mm sections with the 1 mm by 1 mm plane representing the tangential-radial directions. Samples were then

mounted onto brass stems using a small amount of paraffin wax at the base. For mounting, the longitudinal direction (i.e., the 3 mm length) was aligned with the axis of the brass CT stem. This study was comprised of two protocols, with Protocol-1 examining the in-situ swelling behaviour of a single sample (henceforth referred to as Swell-1) and Protocol-2 investigating the deterioration of Arundo samples exposed to increasing levels of moisture cycling. Protocol-2 included three samples named according to their moisture exposure levels, named MC5, MC25 and MC50. A schematic is provided in Figure 6-2.

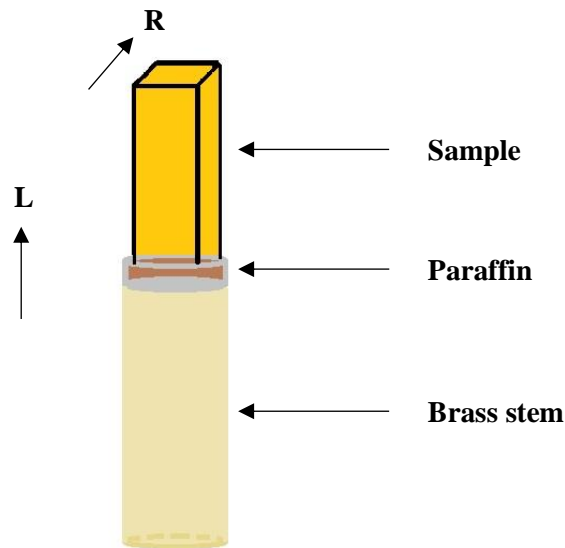


Figure 6-2: Overview of the micro CT sample mounted on the brass stem. Note that the longitudinal and radial directions of the Arundo culm are provided.

Swell-1 (Protocol-1) was repeatedly micro-CT imaged at elevated moisture states. This sample was observed at 5 different moisture contents, including a desiccated state, 50% relative humidity (RH), 80% RH, 90% RH and fully saturated. Arranged chronologically, imaging was performed initially in the desiccated state with subsequent imaging at these successively increasing moisture contents, overall representing a hydration protocol. A final scan was performed upon re-drying to the desiccated state. Prior to X-ray tomographic scanning the sample was conditioned at each respective moisture state for 3 hours to reach an equilibrium moisture content (confirmed by temporal measurements of sample mass). The desiccated state was reached by allowing the sample to dry in a desiccator for 1 day. The in-situ relative humidity was maintained (at room temperature)

through the use of a thin Kapton tube that surrounded the mounting stem during each scan. Although placed in between the sample and the incident x-ray beam, Kapton is generally quite transparent to X-rays. The Kapton tube was connected to a conditioning unit that allowed for the control of RH to approximately +/- 1%.

The samples from Protocol-2 (MC5, MC25, MC50) were cut from the same piece of Arundo internode to minimize inter-sample variability. Each of these samples was exposed to moisture cycling via a saturation-desaturation regime. Each of these samples was exposed to moisture cycling via the regime shown in Figure 6-3.

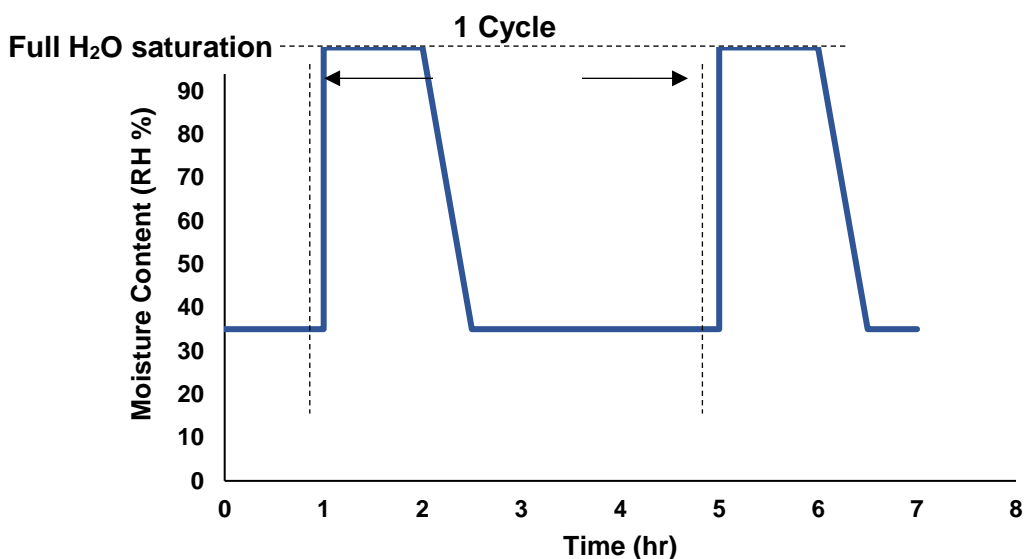


Figure 6-3: Moisture cycling regime implemented for sample conditioning. One complete cycle (saturation to ambient state) is shown, including the ramp-down to 35% RH.

One complete moisture cycle involved full saturation of the sample using deionized water for 1 hour, followed by desorption at 35% RH for 3 hours. This regime was selected to approximate the playing life of a reed used by an active musician. All told, one sample was exposed to 5 cycles, one to 25 cycles and one to 50 cycles (MC5, MC25, MC50, respectively). Automation of the procedure was accomplished using a programmable power switch connected to a pump that submerged the samples in water until the power was turned off and the reservoir allowed to drain.

All measurements were conducted at the Empa Center for X-ray Analytics in Dübendorf, Switzerland using the RX Solutions Easy Tom XL. Mounted samples were fixed to a rotating stage

with the center of rotation of the sample at 6.26 mm from the source and 1156.05 mm from the detector. This allowed space for the Kapton conditioning tube to fit in between the sample and the detector. The X-ray source was set 100 keV and 150 mA, parameters that required tuning due to the low contrast of *Arundo donax L* during X-ray exposure. The field of view was 1.24 x 1.24 mm² producing tomographic slices of 1870 x 1870 pixels in resolution. The effective pixel size was thus 0.66 x 0.66 μm². The exposure time was 15 seconds per projection resulting in a scan time of approximately 6 hours per sample. This exposure included averaging over 10 frames. A total of 1440 projection slices per scan were acquired and then reconstructed to create a tomographic stack of each sample. Pre-processing of the images included ring artifact correction, as well as offset and noise correction, performed by the CT operator.

6.3.1 Image Analysis

Arundo material retains two anatomical structures of interest in terms of importance to real reeds, vascular bundles and parenchyma cells. Segmentation and binarization procedures therefore follow similar workflows to those developed for wood type materials, where the final processed images are binary representations of solid material and pore structures. Subsequent analysis of these binary slices involves extraction of shape and size parameters that quantify the anatomical structures of interest. Images were segmented and binarized using a series of software tools, including Avizo [115] and imageJ [46]. Additionally, the XLib open toolbox for imageJ was used for 3D segmentation of the air volume surrounding the samples resulting in improved thresholding of the sample volume [116]. Overall, image processing involved segmentation of the surrounding air-volume to create a phase mask, followed by grey-level thresholding of the sample volume in Avizo. All images were filtered using a non-local means approach to reduce noise while preserving the sample edges. Binary images of the sample volumes (post-thresholding) were used to analyse several parameters including:

- Local parenchyma cell wall thickness, provided as a frequency distribution over the entire image stack (imageJ – local thickness plugin)
- Parenchyma cell size and shape parameters (imageJ – analyse particles, with thresholds for minimum cell size of 15 μm in diameter).

A subsection of parenchyma cell tissue was extracted from each of the image sets in Protocol-1 to compare volume changes that occur during moisture sorption. This was completed using a label analysis in Avizo to extract the same parenchyma cell volume from each image stack.

The three morphological measures of the parenchyma cells analysed were cell area, solidity (for tortuosity) and cell aspect ratio. These were used to quantify matrix degradation due to the moisture cycling in Protocol-2. The cell area is calculated in imageJ after performing a label analysis on the parenchyma cell structure where the area of each labeled cell is calculated from the number of pixels bound by the cell perimeter. The units are calibrated using the known pixel to micron scale of the CT slice. The labeled cells are further analysed using the solidity calculation in imageJ, calculated as the ratio of cell area to convex area (convex area being the smallest convex region that encloses all points within the cell wall). Tortuosity was analysed to assess deformation along the parenchyma cell wall perimeter from Protocol-2. This measure was estimated using the Skeletonize function in imageJ to generate a binary map of parenchyma cell wall material. The line segments of interest for this analysis form circles (the parenchyma cells) and therefore the solidity factor was used to define tortuosity (instead of the typical skeleton branch length to Euclidian distance ratio). A circle encloses the maximal area for an equal perimeter between two shapes and under this definition as the convex area of the solidity factor decreases the cell wall becomes more tortuous in nature. Therefore, ratio values close to 1 indicate a more circular and less tortuous cell wall. Note that the normal cell area measure (non-convex) is approximated as a circle. The aspect ratio of parenchyma cells was also evaluated to examine elongation of the cell due to repeated moisture cycling.

An open MATLAB image registration routine (described in [117] and [118]) was used for registration of the data sets of different moisture conditions. First, rigid registration (translation and rotation) was used to align the datasets for swelling strain analysis. In-plane swelling strains were obtained through the use of an affine registration (translation, rotation, shear and scaling). Strain in the longitudinal direction was not significant and is not presented here. For wood, this affine process is described in detail in [13], though in general the linear transformation can be described using:

$$T(x) = Ax + t, \quad (6-1)$$

where $\mathbf{T}(\mathbf{x})$ is the linear transformation aligning the deformed and undeformed (reference) images, \mathbf{A} is the affine transformation matrix, \mathbf{x} is the coordinates for the undeformed image and \mathbf{t} is a translation vector. Strains from the image registration procedure are obtained from the Eulerian strain tensor computed from the deformation grid produced during registration. Local deformation in the transverse-radial plane was analysed using a non-rigid B-spline registration [117]. Swelling strains extracted from the registration procedure were calculated using three different image stacks taken from the 1440 full stack, each 250 projections in size. This provided average and standard deviation measures for moisture induced swelling strain.

6.4 Results

An overall view of the image processing results is shown in Figure 6-4. This provides a sample of the three-dimensional Arundo volume segmented from tomographic image stacks.

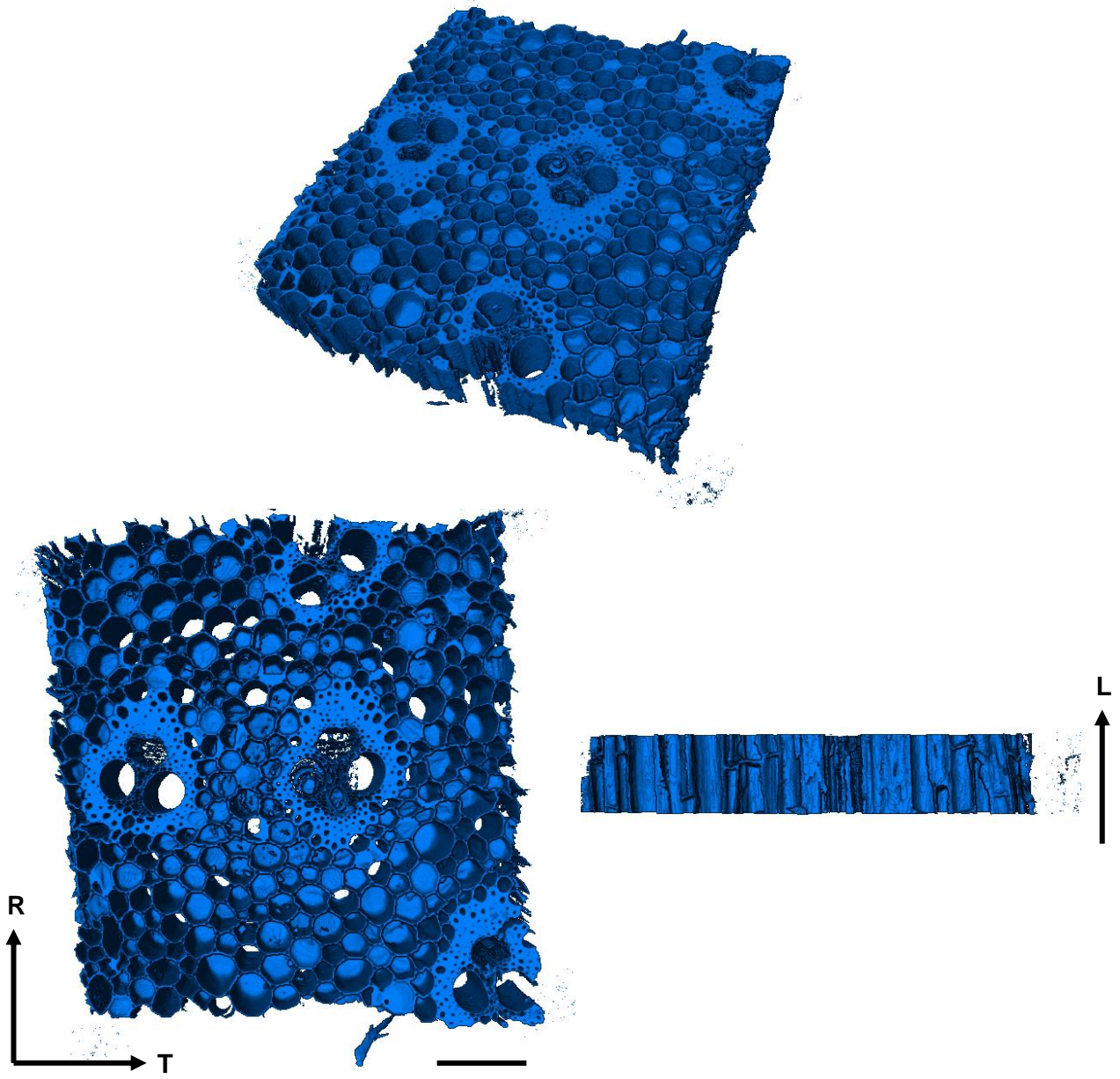


Figure 6-4: Segmented sample extracted from the tomographic image set. A three-dimensional view is shown at the top, along with the radial-tangential plane (bottom-left) and the longitudinal direction (bottom right). This extracted subset represents a 250-slice stack used for data analysis. Note the radial, tangential and longitudinal directions are shown,

Figure 6-5 presents 2D cross-sectional views of the Arundo sample obtained at different levels of RH. This includes moisture states between the dry condition (desiccated) and fully saturated state. A final scan was obtained after de-hydrating the sample back to the desiccated state (the final image in the above figure).

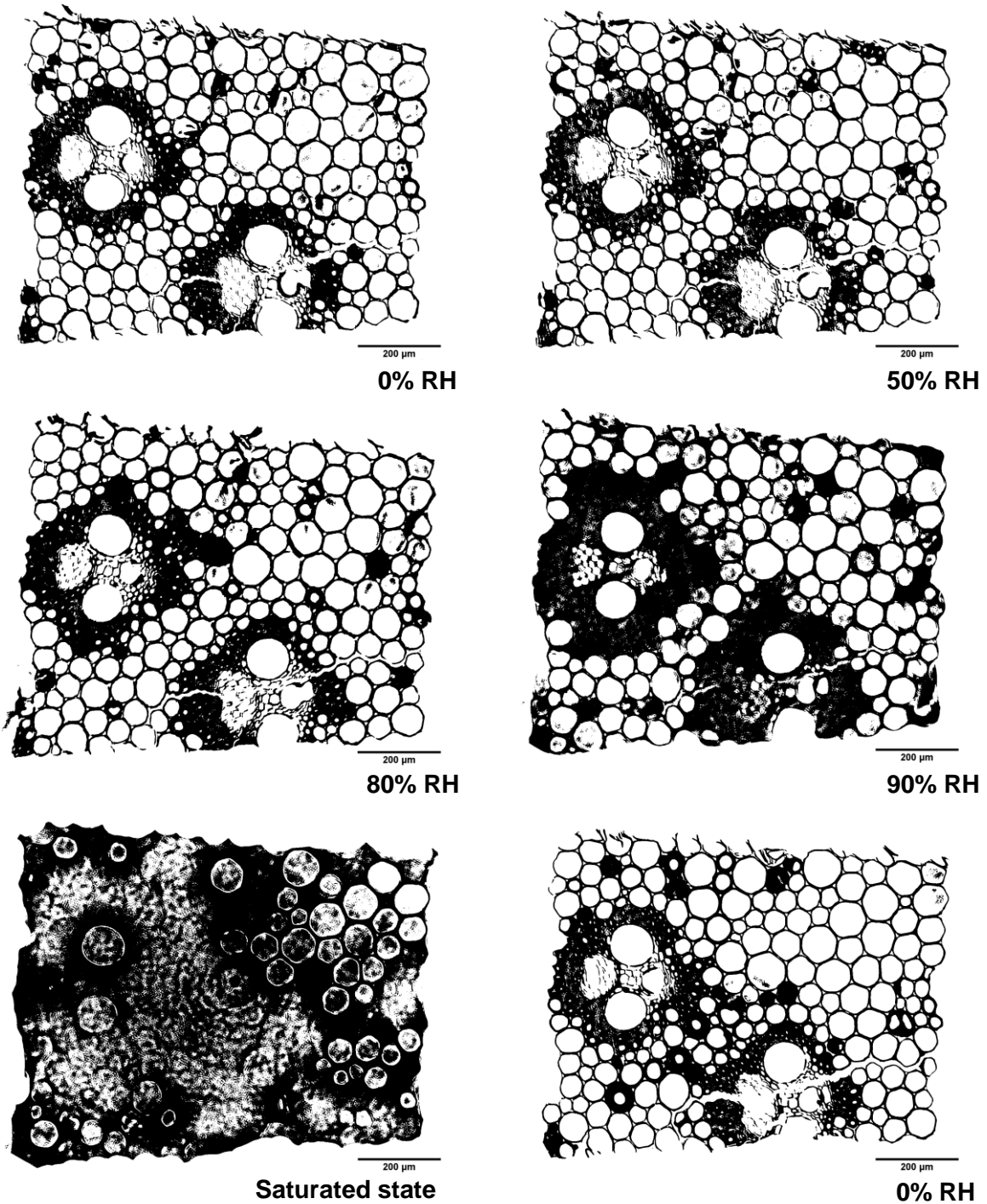


Figure 6-5: 2D binary images of the Swell-1 (Protocol-1) cross section under different moisture contents (as labeled). 200 micron scalebars are provided.

Figure 6-6 presents the results of affine swelling strain analysis. Data is provided for registration performed on the entire sample area as well as for a subsection of the parenchyma. This aided in elucidating the components of the Arundo cross-section contributing most significantly to swelling strain (i.e., vascular structures versus parenchyma cells). All strains are presented with respect to the initial desiccated condition (i.e., non-zero strains are relative to the desiccated state).

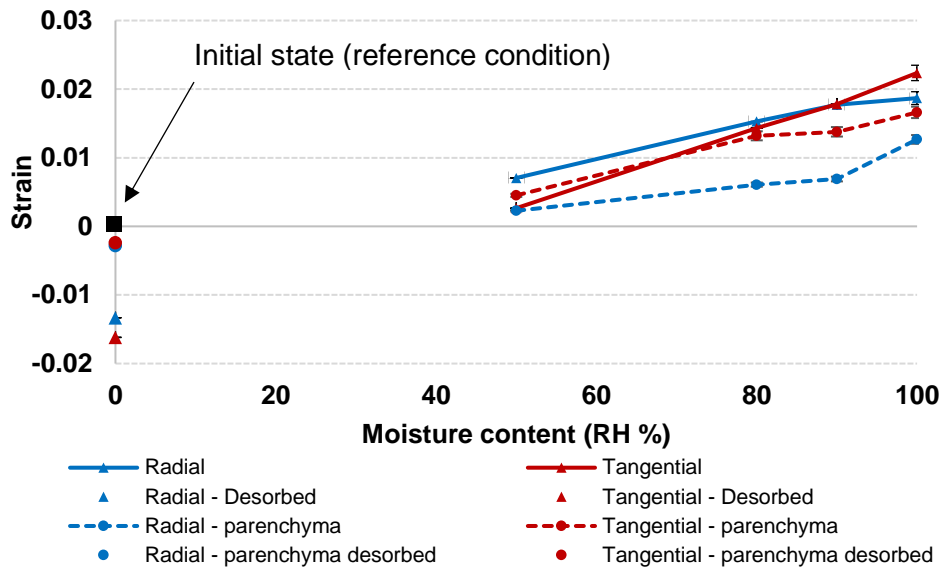


Figure 6-6: Swelling strains (radial and tangential) calculated as an area average across the sample cross-section (solid lines) and calculated for an extracted sub-section of the parenchyma (dashed lines). Strains after desorption following drying from saturated moisture content (plotted as 100% RH) are also provided and depict residual shrinkage following moisture desorption. Results are presented with standard deviations.

Example images from affine registration on the full sample volume are provided in Figure 6-7 and a more localised parenchyma volume in Figure 6-8. These images were used to extract the data presented in Figure 6-6. All images are the binarized versions of the tomographic image stack and have been de-noised.

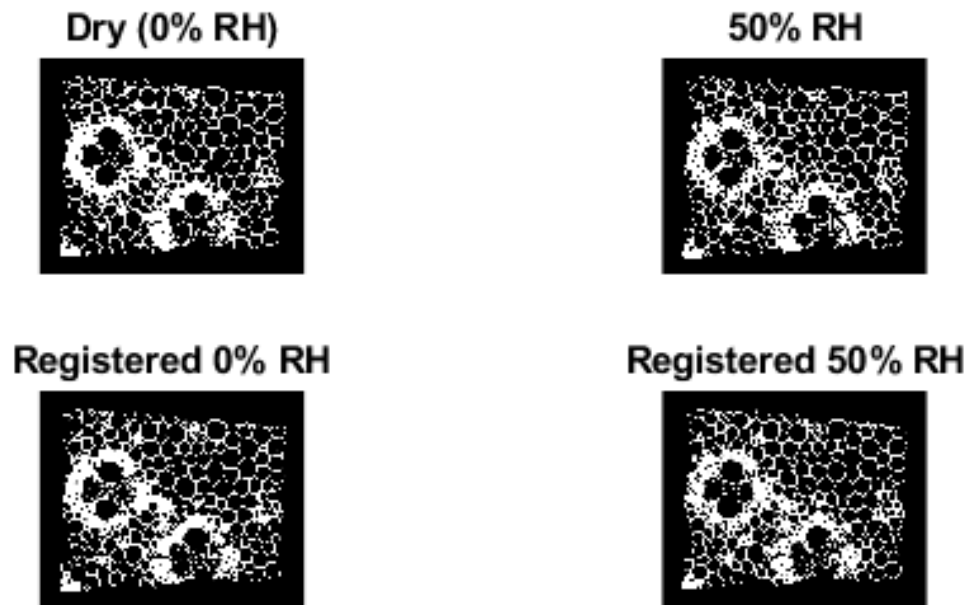


Figure 6-7: Example registration for the dry to 50% RH condition. The images shown were obtained from the thresholding procedure performed on the tomographic image sets.

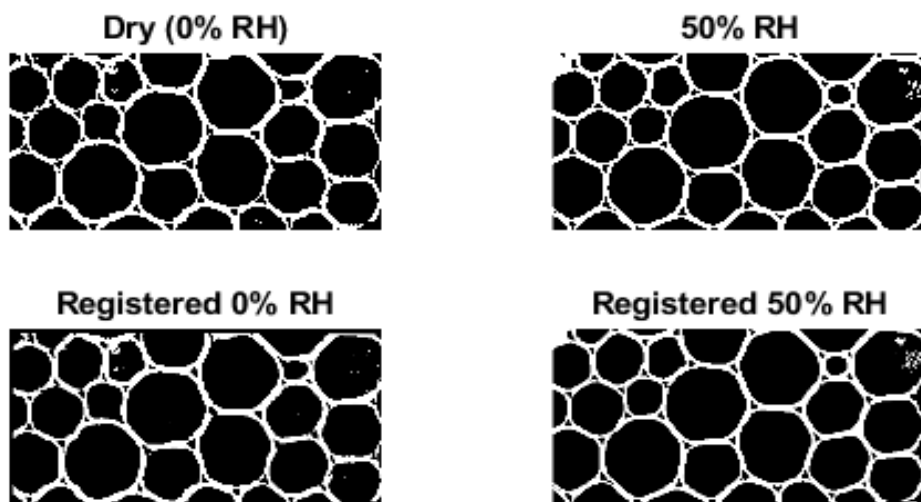


Figure 6-8: Example registration for the dry to 50% RH condition of the extracted parenchyma area.

The images shown in Figure 6-5 all depict the same sample scanned in-situ at different RH levels. The micro CT tomograms were obtained without moving the sample between scans to minimize drift and other rigid body motions that could reduce the accuracy of image registration. Images were aligned using landmark coordinates of highly identifiable anatomical features, primarily the large vessels of the vascular bundles (xylem tissue).

More localized swelling deformation was measured using a b-spline registration on aligned images (Figure 6-9 and Figure 6-10). This was performed on the same image sets as presented above. Results for the fully saturated condition are not shown as noise caused by X-ray scattering from the sample water content prevented repeatable measures from being obtained. Results are plotted for the radial and tangential directions of each sample with equal scalebars for comparison.

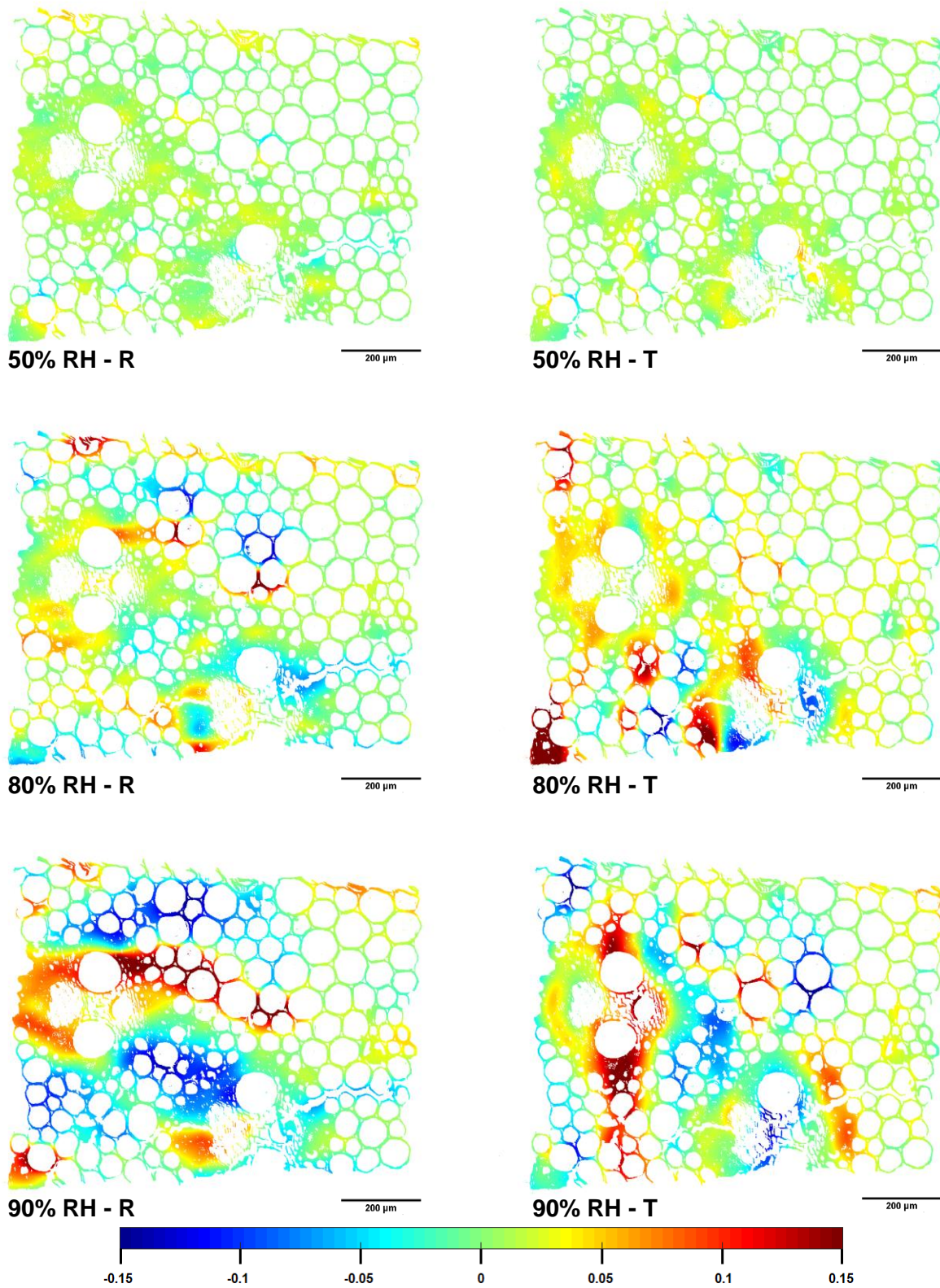


Figure 6-9: Local strain distribution for the radial (left side plots, R) and tangential (right side plots, T) directions at different moisture conditions. Strains were calculated with reference to the initial dry state (desiccated). All contour scales are equal (-0.15 to 0.15 strain).

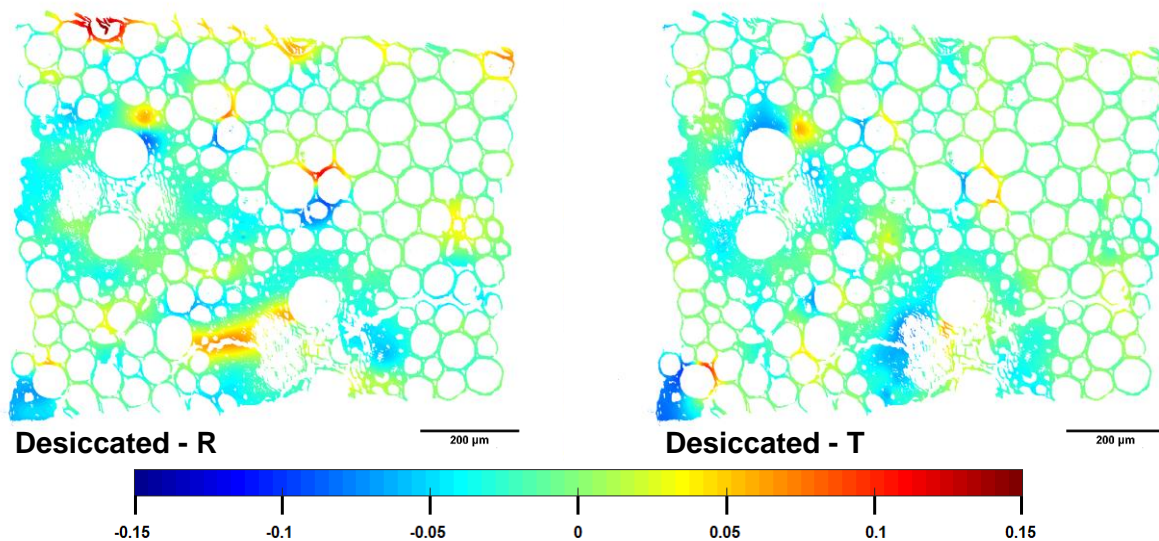


Figure 6-10: Local strain distribution for the radial and tangential directions upon moisture desorption back to the desiccated state. Strain are calculated with reference to the initial dry state. Contour scales are the same as those presented in Figure 7 and 200 micron scalebars are provided.

Changes in the thickness of parenchyma cell walls are presented for the same sample in Figure 6-11. These measurements were performed on a subsection of the parenchyma to avoid the influence of vascular bundles on the thickness statistics (similar to the registration presented in Figure 6-8). Shaded plots highlighting local thickness are provided for the different moisture contents of Protocol-1 and upon desorption to the initial state. Cell wall thickness statistics are presented for the entire image stack as histograms using 15 thickness bins. The results for parenchyma wall thickness are also presented with respect to moisture content in the form of thickness distributions (Figure 6-12).

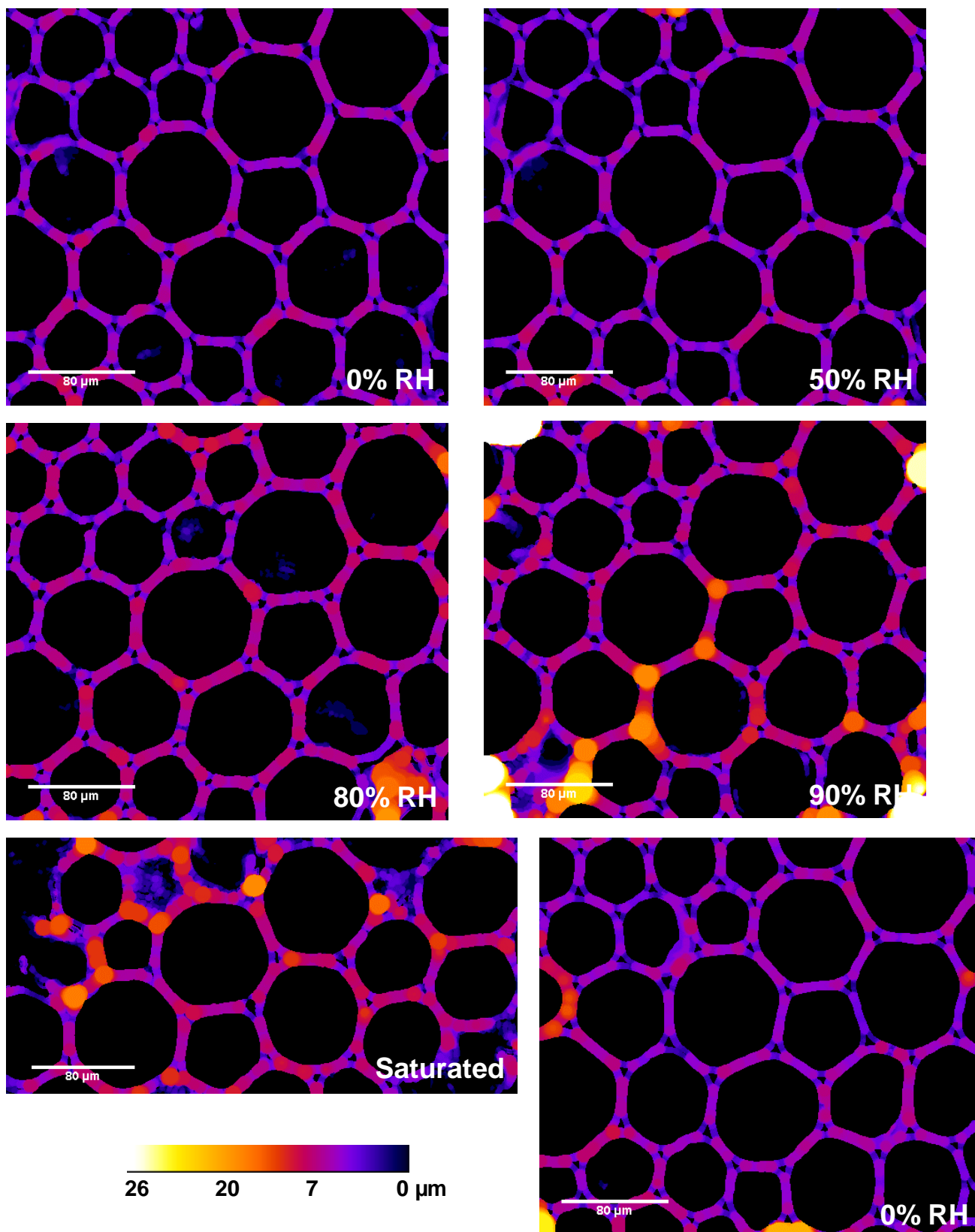


Figure 6-11: Parenchyma cell wall thickness analysis for the in-situ sample. The final 0% RH image represents the sample upon moisture desorption following in-situ moisture conditioning to 100% RH during X-ray acquisition. All scalebars are 80 microns and the same thickness scale is used for all images.

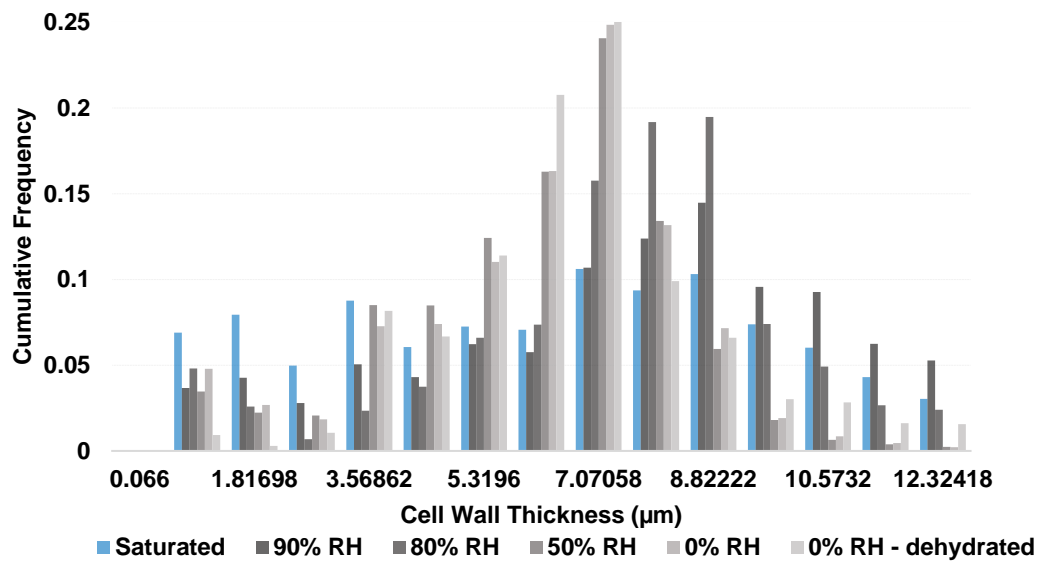


Figure 6-12: Cumulative frequency distributions of the parenchyma cell wall thickness for different in-situ moisture conditions (Protocol-1). Note that the final distribution represents a return to the initial condition (0% RH).

The next set of figures considers the results for Protocol-2 samples. These results were obtained at ambient moisture content. The ambient conditions were recorded during X-ray acquisition and were found to average 24°C and 35 to 40% RH. The samples were given 1 hour to equilibrate with these conditions prior to scanning (following prior storage at 10-15% RH). As previously outlined, the samples of Protocol-2 were artificially aged via moisture cycling to simulate the varying moisture contents experienced by real reeds during playing and storage. Figure 6-13 provides binary images of all three samples as a general overview.

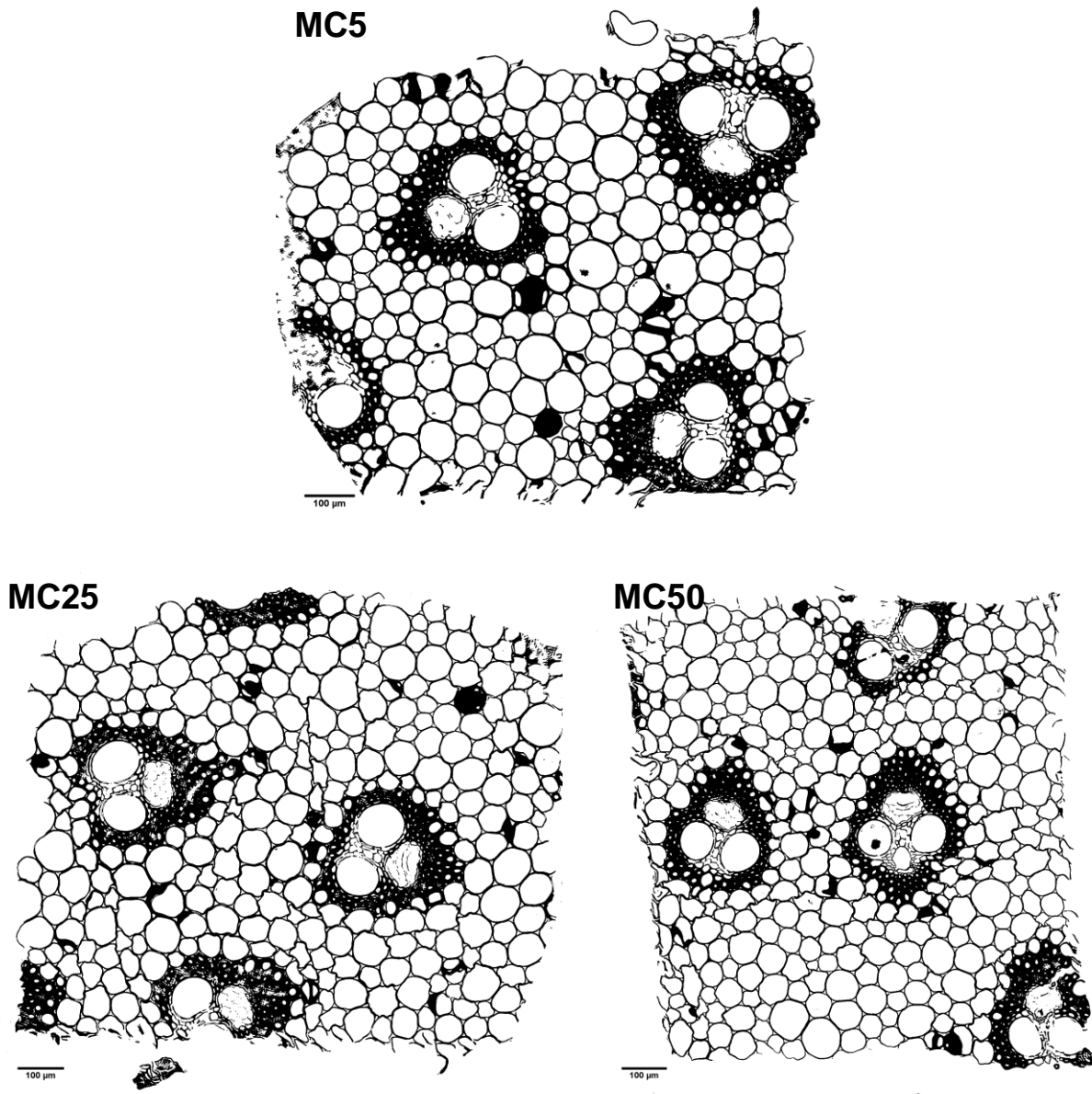


Figure 6-13: Binary tomographic slices of each of the three moisture cycle samples. All scalebars are provided as 100 µm.

Similar to Protocol-1, parenchyma cell wall thickness was analysed for samples MC5, MC25 and MC50 to quantify cell wall degradation due to moisture cycling (Protocol-2). A subsection of each sample was extracted and included only parenchyma tissue to prevent vascular bundles and other structures from influencing the measured distributions. Note that all subsections were of the same micron size.

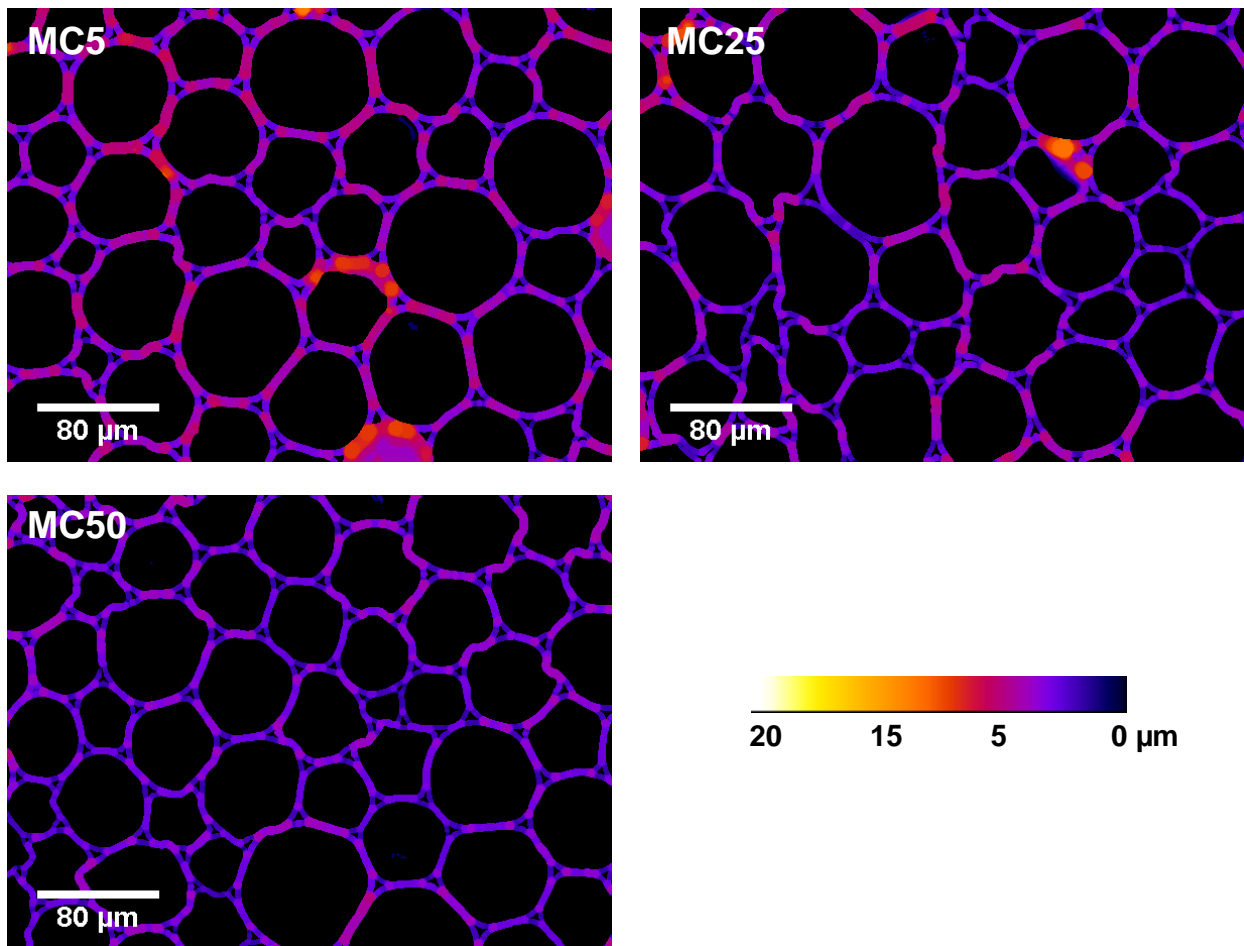


Figure 6-14: Parenchyma cell wall thickness for the moisture cycled samples. All scalebars are 80 µm and the range of cell wall thickness has been equalized for each sample. The thickness scale is also provided.

Histograms of parenchyma cell wall thickness are also provided for these samples in Figure 6-15. In general, wall thickness is observed to depend on the number of moisture cycles the sample has been exposed to.

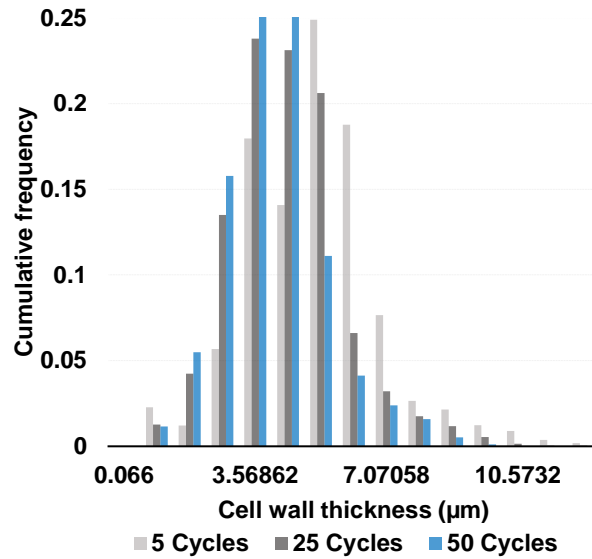


Figure 6-15: Cumulative frequency distributions of parenchyma cell wall thickness for the moisture cycled samples of Protocol-2.

A comparison was also made with a new piece of ADL (taken from the in-situ data set at 50% RH). Figure 6-16 depicts the general trend of decreasing parenchyma cell wall thickness during moisture cycling. It should be reiterated that the moisture cycled samples were taken from the same piece of raw ADL culm to minimize inter-sample wall thickness variability (i.e., changes due to natural variation and not imposed treatments).

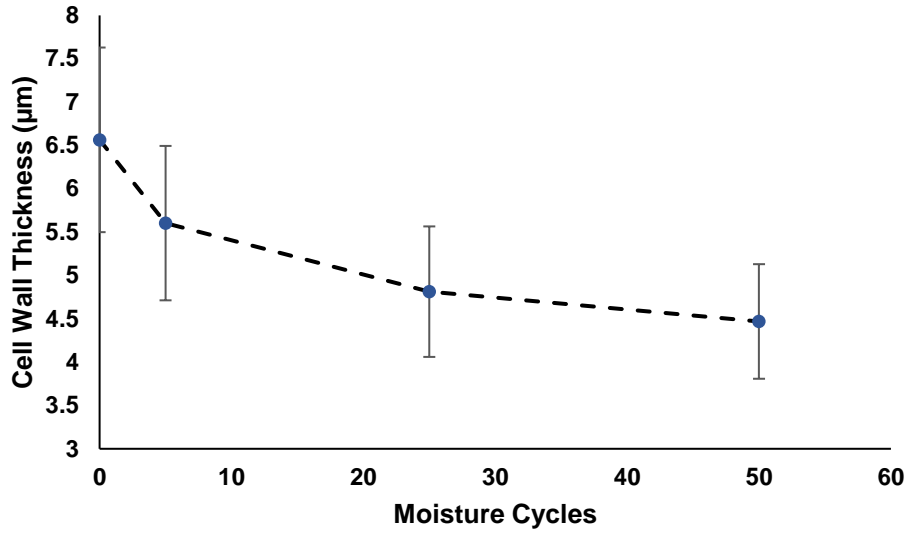


Figure 6-16: Change in parenchyma cell wall thickness with increasing exposure to moisture cycling. Data points at the 5, 25 and 50 cycle marks are taken from Protocol-2 samples, while the zero-cycle position represents data taken from Swell-1 of Protocol-1. Error bars are provided as standard deviation.

Figure 6-17, Figure 6-18 and Figure 6-19 all provide morphological measures of the Arundo anatomical structure. These measures are provided with respect to the number of moisture cycles each sample was subjected to. All collected measurements were obtained from full tomographic stack analysis and the data is therefore representative of roughly 1.25 by 1.25 by 1.25 mm³ of Arundo material (at each level of moisture cycling).

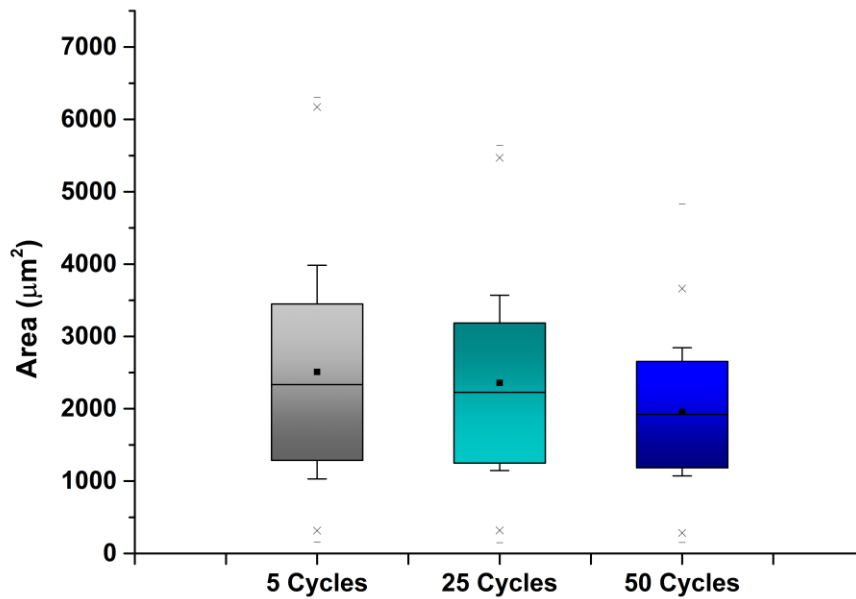


Figure 6-17: Parenchyma cell area calculated for samples MC5, MC25 and MC50 (Protocol-2). The means of each distribution are shown by the solid squares.

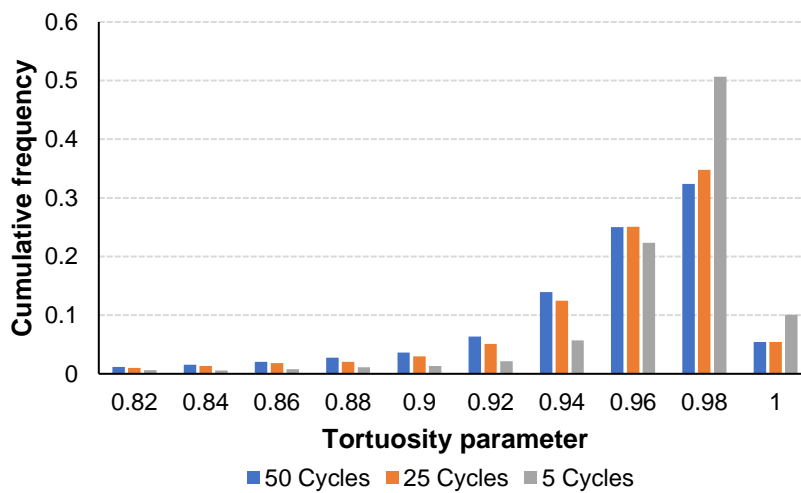


Figure 6-18: Tortuosity parameter as measured using ImageJ (via solidity and cell perimeter parameters). The solidity parameter includes the convex area which is calculated as a polygon that completely encompasses all points along the cell perimeter (idealised as a circle for parenchyma cells). These parameters were calculated slice-wise and are therefore 2-dimensional representations of tortuosity (i.e., tortuosity in the radial-tangential plane of the Arundo cross-section).

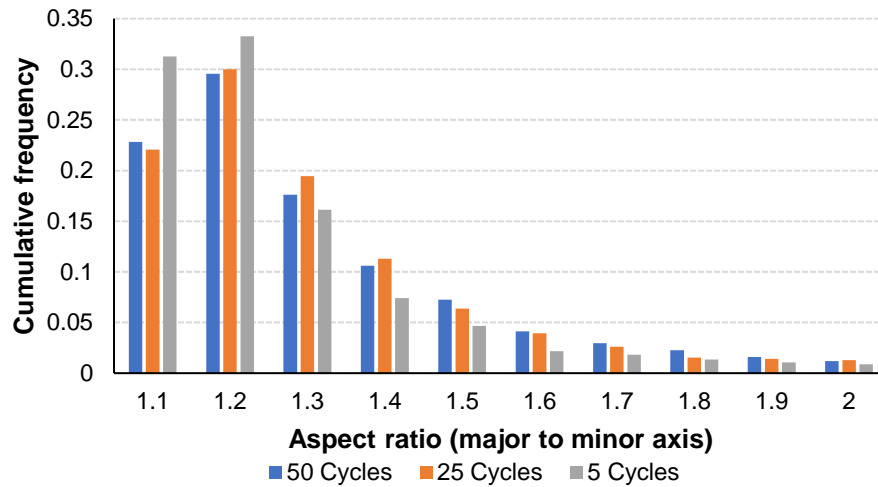


Figure 6-19: Aspect ratio parameter for each of the samples of Protocol-2. This parameter is calculated as the ratio of cell major to minor axis length and larger values indicate more elongated cell morphologies. In general, increasing the number of moisture cycles a sample is exposed to increases the number of cells that experience morphological deformation.

Qualitative analysis of parenchyma tissue extracted from the in-situ swelling strain sample shows the localised deformation of longitudinal cell wall caps during moisture absorption. The extracted tissue samples are shown in Figure 6-20.

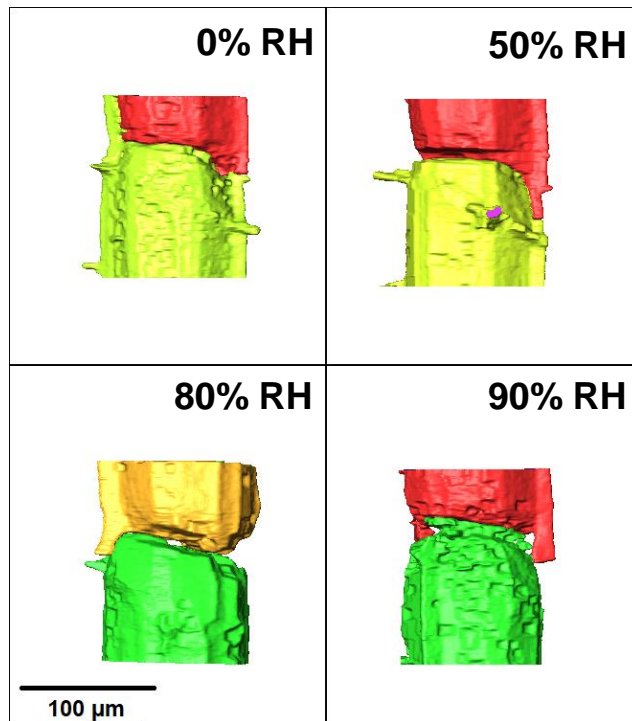


Figure 6-20: Parenchyma tissue swelling and localised deformation in the longitudinal direction during in-situ moisture absorption. A 100 μm scalebar is provided. All parenchyma cell volumes were extracted from the same spatial locations of tomographic image stacks via a labeling analysis in Avizo.

This data shows the importance of cell wall end caps as local shrinkage causes a decrease in parenchyma cell diameter at the joining face between continuous cells (*Arundo donax L* exhibits significant longitudinal symmetry in terms of parenchyma cell lumen continuity). As noted, macroscopic swelling strain in the longitudinal direction is negligible, however this local cell cap strain suggests the importance of longitudinal cell positioning on the mechanical bending stiffness of reed tips. Tip areas that are close to these end caps would experience more heterogeneous strain distributions when compared to average longitudinal swelling behaviour. The local bending stiffness of the cell structure would be reduced in this case due to the geometrical changes of the parenchyma intra-cell interface (i.e., thinning of the support structure).

6.5 Discussion

In terms of swelling strains, the results from in-situ experimentation (Protocol-1) show maximum tangential and radial strains at saturated moisture content and a general positive linear trend between moisture content and swelling strain (in both directions). Radial and tangential swelling, as for wood, have been shown to dominate the overall swelling behaviour of bamboo specimens [119], and this behaviour is also found for *Arundo donax L* presently. Here tangential swelling is larger than radial swelling (~2% and 1.85%, respectively). Radial swelling is more significant for all conditions until full saturation, with tangential swelling becoming the larger of the two at 90% RH. Swelling in both directions exhibits a linear dependency on moisture from the desiccated to fully saturated state, similar to the behaviour observed for wood [120]. When a subsection of the parenchyma tissue from each sample is considered more specifically, tangential swelling becomes the dominant swelling strain over the full range of moisture conditions. Additionally, the swelling strains measured in the parenchyma tissue are lower than those observed for the entire *Arundo* cross-section (i.e., including vascular bundles). In moso bamboo, vascular bundles retain a higher amount of lignified tissue when compared to the surrounding parenchyma cells [60]. Vascular structures also act as the nutrient uptake (including water) mechanisms for higher plants. Examination of the binary cross-section images obtained in-situ show the ingress and diffusion of moisture from the vascular bundles towards the middle sections of the parenchyma tissue. This suggests one possible explanation for the observed decrease in swelling when only the parenchyma is considered, versus the entire cross-section. Here the hydrophilic nature of cell wall amorphous components (cellulose, hemicellulose, lignin) in the vascular bundle fibers lead to increased swelling. Shrinkage strains are also found for both the overall *Arundo* cross-section and the parenchyma tissue upon moisture desorption to a desiccated state. These strains leave the sample with smaller tangential and radial dimensions and are within 10% of one another for the parenchyma tissue. Radial shrinkage strain is higher than tangential for the overall cross-section.

Highly localised swelling around the vascular bundles was also confirmed by analysis of the b-spline registered cross-sections to 90% RH. Radial and tangential swelling strain plots (Figure 6-9 and Figure 6-10) illustrate the highly localised in-plane strains that occur around the vascular bundles. Large strains are also observed in some surrounding parenchyma struts that could lead to cell wall weakening during repeated cycling. These large strain concentrations appear to be vascular swelling accommodation in the parenchyma tissue. As mentioned, overall strains

are lower in the parenchyma tissue and thus this highly localised swelling accommodation likely leads to long term degradation of *Arundo* material. High compressive strains (locally) can also be found between the vascular bundles of the swelling sample suggesting another mechanism for parenchyma cell collapse during moisture cycling. As an alternative perspective, shrinkage in bamboo is known to be restricted by the presence of vascular bundles [121] and suggests that the spatial distribution of bundles in the cross-section is important for the long-term mechanical stability of cycled reeds. These highly localised strains are likely related to warping in real reeds. Warping occurs during the lifespan of reeds, especially if stable moisture conditions are not maintained during storage.

Previous research on *Arundo donax L* has indicated that cell wall recovery can occur following collapse due to moisture exposure, although long term recovery (greater than 14 cycles) after repeated cycling was not considered [5]. Swelling due to the recovery was found to be most significant after the first moisture cycle. The decreasing parenchyma cell area observed presently for samples exposed to increasing moisture cycles suggests that more permanent swelling and shrinkage hysteresis leads to a degradation of the parenchyma. This coupled with the observed decrease in cell wall thickness would lead to a mechanical softening in terms of bending stiffness. For real reeds this has been observed during their lifespan and is pronounced due to the thinness of the tip.

In this work on the in-situ sample, parenchyma cell wall thickness increases with increasing RH. The distribution of cell wall thickness throughout the specimen volume also exhibits decreasing kurtosis with increasing RH suggesting variability in the response of parenchyma tissue to moisture. The initial distribution of cell wall thickness is recovered upon desorption back to the desiccated state, both in terms of mean thickness and distribution kurtosis. Previous studies for wood have attributed microstructural losses to hemicellulose and lignin degradation upon chemical analysis [122]. Although these results were obtained at elevated temperatures (60 to 90°C), the noted stability of cellulose suggests that a similar degradation may occur in the parenchyma tissue of cycled *Arundo* samples. With more specific regard to *Arundo donax L*, loss of reed tangential thickness with exposure to moisture cycles has also been attributed to the loss of water soluble extractives [5].

Morphological observations of changes in parenchyma tissue with exposure to moisture cycling indicate that cells undergo deformation during cycling and exhibit an increase in tortuosity above 5 cycles. Tortuosity can be approximated by the length of a curve relative to its effective length (or Euclidean distance) and a slight modification on this definition is used here (outlined in the methods section). The cell wall was quantified using the skeletonization scheme in ImageJ. A typical binarized tomogram depicting the labeled parenchyma cells and cell wall skeleton network are shown in Figure 6-21.

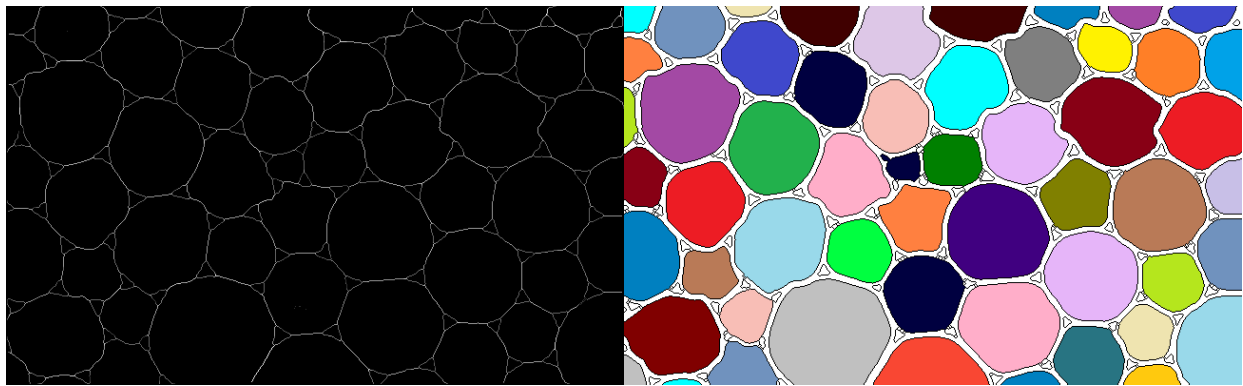


Figure 6-21: Skeletonized (left) and labelled (right) images extracted from the AD-50 binarized image stack. The coloured label provides examples of the parenchyma cells used to extract shape and size statistics.

The parenchyma cell wall structure was used to create a branch skeleton from the binary image. As the tortuosity ratio approaches 1 the measured path (here the cell wall) becomes less tortuous in nature. The MC25 sample exhibited the largest mean value of tortuosity. The trend of increasing tortuosity with increased moisture cycles was reaffirmed by analyzing the ratio of idealized circle perimeter (calculated by imageJ) to actual parenchyma cell perimeter. Ratios less than 1 indicating increased cell perimeter and thus a more tortuous cell wall nature. The same trends (weighted average of idealized circle cell perimeter to actual perimeter were 0.90, 0.88 and 0.86 for Protocol-2 samples MC5, MC25 and MC50, respectively) are observed in this case, suggesting that tortuosity indeed increases with further moisture cycling. Overlap in tortuosity distributions between the samples is also due to the highly confined regions of cell wall deformation, with some surrounding parenchyma cells that do not exhibit significant tortuosity. Despite this, the shift in the tortuosity distribution of sample MC25 is evident when compared to MC5. Furthermore, both MC25 and MC50 tortuosity were larger than that of MC5. It is possible that swelling strains

induced during cycling contribute to the tortuosity observed for parenchyma cells. The cross-section of MC25 contains three vascular bundles that are spatially distributed equally from one another (in terms of Euclidean distance from vessel lumen to vessel lumen). The inability of the surrounding parenchyma matrix to accommodate swelling strains during cycling may have contributed to the higher tortuosity observed for this sample. As previously mentioned, vascular bundles are important anatomical structures for limiting shrinkage strains in bamboo [121].

The aspect ratio is found to increase with increasing moisture cycling suggesting a change in parenchyma cell shape. Protocol-2 samples exposed to 25 to 50 moisture cycles exhibit significant cell elongation relative to the 5-cycle state. The mechanisms for this deformation would be similar to those responsible for changes in tortuosity, and coupled with the noted decrease in cell wall thickness and increase in tortuosity would contribute to the reduced mechanical stability of the parenchyma matrix, especially in the radial direction (the direction of applied vibration during reed bending/playing).

Qualitative analysis of parenchyma tissue swelling shows the importance of cell wall end caps as local shrinkage causes a decrease in parenchyma cell diameter at the joining face between continuous cells (*Arundo donax L* exhibits significant longitudinal symmetry in terms of parenchyma cell lumen continuity). As noted, macroscopic swelling strain in the longitudinal direction is negligible, however this local cell cap strain suggests the importance of longitudinal cell positioning on the mechanical bending stiffness of reed tips. Tip areas that are close to these end caps would experience more heterogeneous strain distributions when compared to average longitudinal swelling behaviour. The local bending stiffness of the cell structure would be reduced in this case due to the geometrical changes of the parenchyma intra-cell interface (i.e., thinning of the support structure).

Although not presented here, a mechanically fatigued (1Hz compression) *Arundo* sample was also scanned for comparison with the moisture cycled samples. In terms of sample morphology, no significant changes were observed for either the vascular bundles or parenchyma tissue. This suggests that fatigue in played reeds is primarily due to moisture cycling and moisture induced anatomical changes that alter the mechanical properties of the reed (macroscopically). During playing, reeds undergo bending vibration and cell densification may occur mechanically,

similar to the tortuosity observed for moisture cycled samples. Analysis of this densification in real reeds would be of interest for future studies.

6.6 Conclusions

In this study the effects of in-situ moisture saturation and moisture cycling on swelling and anatomical structures have been studied for the musical reed material *Arundo donax L.* In-situ X-ray tomography swelling analysis showed that both radial and tangential swelling strains exhibit a linear dependence on RH, behaviour that is similar to swelling observed in wood. After desorption to the desiccated state, there are residual shrinkage strains in both the radial and tangential directions. Localised analysis of the parenchyma tissue indicated that swelling strains in these regions were slightly lower than when the entire *Arundo* cross-section was considered. As the vascular bundles act as the nutrient transport structures, higher swelling strains surrounding these bundles are thought to be the result of significant moisture absorption and diffusion. Under fully saturated conditions, the majority of parenchyma cells surrounding the vascular bundles saturate with water illustrating the important role that water plays in real reed performance. The effect of this saturation and swelling on bending vibration would be an interesting topic for future studies. The large local radial and tangential strains in these areas cause highly localised deformation of parenchyma cell walls that can result in permanent damage over repeated cycles. There is also a notable increase in parenchyma cell wall thickness during moisture absorption that recovers upon desorption.

Degradation and anatomical changes due to moisture cycling have also been examined in separate *Arundo* samples (Protocol-2). Similar to the in-situ samples, X-ray tomography was used to scan samples exposed to 5, 25 and 50 cycles of moisture cycling. Image analysis of tomographic slices found that parenchyma cell wall thickness decreased with increasing number of moisture cycles. Comparison with a new (non-cycled) sample of *Arundo donax L.* confirmed a non-linear decay in parenchyma cell wall thickness from 0 to 50 cycles. Parenchyma cell shape parameters were also extracted to quantify deterioration of parenchyma tissue. No significant anatomical changes in the vascular bundles were identifiable during the analysis. Local parenchyma cell tortuosity, solidity and area (idealized using a circular geometry) all exhibited changes between 5 and 25 moisture cycles with tortuosity increasing and solidity and cell area decreasing. In real usage, reeds experience mechanical softening with respect to bending stiffness. This softening is

likely the result of a loss of transverse stiffening components of the cell wall (i.e., lignin) in addition to geometric softening due to parenchyma cell collapse and wall thinning.

In terms of future work, computational mechanical analysis of parenchyma tissue at 5, 25 and 50 moisture cycles could yield information regarding changes in transverse stiffness and vibrational modes pertinent to real reeds and would be an avenue for future research. In relation to cell wall thinning, FTIR spectral analysis of vascular and parenchyma tissue could reveal the depolymerization of lignin and hemicellulose cell wall components. Comparison of parenchyma cell tortuosity between moisture-cycled and played reeds could better highlight the influence of vascular bundles on the deformation of surrounding parenchyma tissue. The locations of vascular bundles within the culm vary from reed to reed and their influence on tortuosity likely contributes to variable reed stiffness.

The results of this study will help to better understand the degradation of reeds and their mechanical performance in the saturated state. The changes in anatomical structure observed with increasing RH and moisture cycling could aid manufacturers in identifying more stable *Arundo* material in terms of swelling strains and local heterogeneity.

Chapter 7

7 Conclusions

In this research, the degradation of played alto saxophone reeds during their useful life was investigated through the use of spatially dependent bending stiffness evaluation. The reeds were played over two and a half months by a professional jazz musician and found to lose 30 to 60% of their initial stiffness in the tip region of the reed vamp. Stiffness degradation was also observed further towards the heart of the vamp, with a reduction in initial stiffness of 5 to 25%. Subjective rankings of reed stiffness by the musician were found to correlate well with the softest and stiffest reeds of the set. Examination of off-axis (relative to the vamp centerline, longitudinally) bending stiffness and subjective rankings found a positive correlation, indicating that the musician was sensitive to stiffness asymmetry. Reeds with a large difference in on- and off-axis stiffness were perceived as being stiffer by the musician. Anatomical investigation into several shape and spatial parameters with respect to vascular bundles was also conducted. Analysis of these features within the cross-sections of reed heel samples found significant positive correlations between on-axis stiffness and vascular bundle area fraction. Using this data in addition to other parameters (solid fiber fraction, parenchyma cell strut thickness, vascular bundle spatial density), a composite model of bending stiffness was created to predict the stiffness of reeds. This model successfully predicted the stiffness of all reeds used in the playing study within 5% using only anatomical data obtained from optical microscopy. This approach is more accurate than the average bending stiffness sorting method employed by manufacturers and suggests a possible improved method for product quality control.

Investigation into the degradation of reeds and *Arundo donax L* material was extended to multiple length scales using nanoindentation, XRD and TGA characterisation methods. Samples were taken from played and un-played portions of reeds, and well-controlled moisture cycled samples. A fundamental difference in degradation behaviour was observed between vascular bundle fibers and parenchyma cell walls for all samples. Overall solid fibers exhibited larger

indentation moduli than the parenchyma cell walls. Both of these structures experienced only modest decreases in longitudinal moduli with moisture related aging. A large difference between vascular bundles and parenchyma cell walls was observed with respect to viscous behaviour. Viscoelastic parameters extracted from nanoindentation depth-time curves indicated that solid fibers were initially more elastic, with viscosity increasing as moisture exposure was increased. For the parenchyma cell wall, viscosity decreased with increasing exposure to moisture cycles. TGA results indicated a decrease in the lignin content of all aged samples (in terms of mass fraction, relative to hemicellulose and cellulose) relative to new samples taken from the same reed. The increase in solid fiber viscosity with increasing moisture cycles was attributed to this loss of lignin, as these fibers are known to be highly lignified which increases transverse stiffness between microfibrils. The crystallinity (via XRD) of aged versus new samples was found to increase, along with a slight increase in cellulose crystallite length. This increasing crystallinity was attributed to decreasing mass fractions of amorphous components (primarily lignin and hemicellulose) and increasing crystallite size due to longitudinal alignment of amorphous components of cellulose microfibrils during moisture induced swelling (similar to results observed for wood). Macroscopically, testing of $\tan \delta$ for new and aged samples indicated a decrease in longitudinal damping at frequencies above 800 Hz, and an increase in transverse damping.

In-situ swelling analysis of *Arundo donax L* samples was also performed using a micro CT approach. Analysis focused on the tangential-radial plane (i.e., a typical reed cross-section) as longitudinal swelling was found to be negligible. Swelling in *Arundo donax L* was found to be linearly dependent on relative humidity. Some hysteresis between the absorption and desorption directions was also observed, with some residual shrinkage strains (compressive) remaining upon desiccation from the fully saturated state. Volumetric strains were found to be 1.80% and 2.25% for the radial and tangential directions, respectively. Analysis of a subsection of the tomographic dataset corresponding to parenchyma cells indicated slightly larger radial and tangential strains than for the entire cross-section, indicating that local strains surrounding vascular bundles can cause cell collapse of parenchyma cells, reducing in-plane strain. Analysis of local strains surrounding vascular bundles were indeed found to be large relative to the total swelling strain. These bundles facilitate moisture transport in the *Arundo* culm and lead to the large swelling strains observed. The effects of moisture cycling were also investigated using image analysis of tomographic stacks. Parenchyma cell size and cell wall thickness were both found to decrease with

increasing exposure to moisture cycles. Tortuosity of the cell wall was also observed for samples exposed to greater than 25 complete saturation cycles. These morphological changes in the parenchyma matrix are thought to decrease the mechanical stability of aged reeds, especially in terms of bending stiffness.

7.1 Contributions to Original Knowledge

- The first long term degradation study of real, played alto saxophone reeds was conducted and evaluated with respect to objective and subjective stiffness. Anatomical analysis of the reed microstructure was also conducted and correlated to bending stiffness measurements.
- A novel technique for bending stiffness evaluation of reeds was developed. This method probed reed tips at six different spatial locations, producing a stiffness map and providing measures of stiffness asymmetry. Stiffness characterisation using this methodology is much improved relative to typical average measures used by manufacturers as it is sensitive to local differences in reed microstructure.
- A model was developed with improved accuracy and sensitivity for stiffness prediction in manufactured reeds. The inputs to this model could be captured through optical methods during manufacturing and screening of raw *Arundo donax L* material could be completed in this way to produce more consistent reeds.
- Nano-mechanical parameters for anatomical structures of *Arundo donax L* were quantified in terms of elasticity and viscoelasticity. Additionally, the sensitivity of these parameters to moisture cycling was evaluated, yielding the first systematic study of reed fatigue at the microstructural scale.
- In-situ swelling of *Arundo donax L* was evaluated under highly controlled experimental conditions to evaluate the dependency on relative humidity. The effects of moisture cycling on anatomical structures was evaluated in three dimensions using tomographic datasets.

7.2 Suggestions for Future Work

- The methodology employed for nanoindentation reed fatigue evaluation could be extended to dynamic nanoindentation. This would yield frequency dependent changes in dynamic modulus and $\tan \delta$ values with moisture cycling.

- Finite element modeling could be used to study changes in reed tip vibrational models due to the effects of morphological changes in anatomical structures with moisture cycling.
- A parametric study of the dynamic behaviour of reeds could be undertaken using the micro CT data obtained during swelling evaluation. The development of a finite element model using this data could allow changes in anatomical structure spatial arrangement to be correlated with changes in vibrational parameters. This would be useful for assessing the performance of raw *Arundo donax L* material prior to reed manufacturing, and for selecting desirable material for specific requirements.

8 References

- [1] R. E. Perdue, “Arundo donax—Source of musical reeds and industrial cellulose,” *Econ. Bot.*, vol. 12, no. 4, pp. 368–404, Oct. 1958.
- [2] E. Obataya and M. Norimoto, “Acoustic properties of a reed (*Arundo donax* L.) used for the vibrating plate of a clarinet,” *J. Acoust. Soc. Am.*, vol. 106, no. 2, pp. 1106–1110, Aug. 1999.
- [3] S. Glave *et al.*, “Quality indicators for woodwind reed material,” *Nucl. Instrum. Methods Phys. Res. Sect. B Beam Interact. Mater. At.*, vol. 150, no. 1–4, pp. 673–678, Apr. 1999.
- [4] P. Kolesik, A. Mills, and M. Sedgley, “Anatomical Characteristics Affecting the Musical Performance of Clarinet Reeds Made from *Arundo donax* L. (Gramineae),” *Ann. Bot.*, vol. 81, no. 1, pp. 151–155, Jan. 1998.
- [5] H. Akahoshi and E. Obataya, “Effects of wet–dry cycling on the mechanical properties of *Arundo donax* L. used for the vibrating reed in woodwind instruments,” *Wood Sci. Technol.*, vol. 49, no. 6, pp. 1171–1183, Nov. 2015.
- [6] V. Chatziioannou, A. Hofmann, and M. Pàmies-Vilà, “An artificial blowing machine to investigate single-reed woodwind instruments under controlled articulation conditions,” *Proc. Meet. Acoust.*, vol. 31, no. 1, p. 035003, Dec. 2017.
- [7] J. Petiot, P. Kersaudy, G. Scavone, S. McAdams, and B. Gazengel, “Modeling of the subjective quality of saxophone reeds,” *Proc. Meet. Acoust.*, vol. 19, no. 1, p. 035028, May 2013.
- [8] B. Gazengel, J. P. Dalmont, and J. F. Petiot, “Link between objective and subjective characterizations of Bb clarinet reeds,” *Appl. Acoust.*, vol. 106, pp. 155–166, May 2016.
- [9] C. E. Lawton, G. Jeronimidis, A. J. Pretlove, and J. R. Barnett, “Anatomical factors affecting the quality of oboe reeds made from *Arundo donax* L.,” *Pac. Reg. Conf. 3rd Recent Adv. Wood Anat. 1994 Rotorua N. Z. Recent Adv. Wood Anat.*, pp. 308–315, 1996.
- [10] M. Kawasaki *et al.*, “Structural observations and biomechanical measurements of clarinet reeds made from *Arundo donax*,” *Microsc. Res. Tech.*, vol. 80, no. 8, pp. 959–968.
- [11] D. J. Casadonte, “The clarinet reed: an introduction to its biology, chemistry, and physics /,” The Ohio State University, 1995.

- [12] H.-C. Spatz, H. Beismann, F. Brüchert, A. Emanns, and T. Speck, “Biomechanics of the giant reed *Arundo donax*,” *Philos. Trans. R. Soc. B Biol. Sci.*, vol. 352, no. 1349, pp. 1–10, Jan. 1997.
- [13] D. Derome, M. Griffa, M. Koebel, and J. Carmeliet, “Hysteretic swelling of wood at cellular scale probed by phase-contrast X-ray tomography,” *J. Struct. Biol.*, vol. 173, no. 1, pp. 180–190, Jan. 2011.
- [14] A. Patera *et al.*, “Micro-Scale Restraint Methodology for Humidity Induced Swelling Investigated by Phase Contrast X-Ray Tomography,” *Exp. Mech.*, vol. 54, no. 7, pp. 1215–1226, Sep. 2014.
- [15] A. Rafsanjani, M. Stiefel, K. Jefimovs, R. Mokso, D. Derome, and J. Carmeliet, “Hygroscopic swelling and shrinkage of latewood cell wall micropillars reveal ultrastructural anisotropy,” *J. R. Soc. Interface*, vol. 11, no. 95, p. 20140126, Jun. 2014.
- [16] H. Qing and L. Mishnaevsky Jr., “3D hierarchical computational model of wood as a cellular material with fibril reinforced, heterogeneous multiple layers,” *Mech. Mater.*, vol. 41, no. 9, pp. 1034–1049, Sep. 2009.
- [17] L. Mishnaevsky Jr. and H. Qing, “Micromechanical modelling of mechanical behaviour and strength of wood: State-of-the-art review,” *Comput. Mater. Sci.*, vol. 44, no. 2, pp. 363–370, Dec. 2008.
- [18] S. Koponen, T. Toratti, and D. P. Kanerva, “Modelling elastic and shrinkage properties of wood based on cell structure,” *Wood Sci. Technol.*, vol. 25, no. 1, pp. 25–32, Jan. 1991.
- [19] D. J. Gardner, N. C. Generalla, D. W. Gunnells, and M. P. Wolcott, “Dynamic wettability of wood,” *Langmuir*, vol. 7, no. 11, pp. 2498–2502, Nov. 1991.
- [20] S. Holmberg, K. Persson, and H. Petersson, “Nonlinear mechanical behaviour and analysis of wood and fibre materials,” *Comput. Struct.*, vol. 72, no. 4–5, pp. 459–480, Aug. 1999.
- [21] N. G. Jústiz-Smith, G. J. Virgo, and V. E. Buchanan, “Potential of Jamaican banana, coconut coir and bagasse fibres as composite materials,” *Mater. Charact.*, vol. 59, no. 9, pp. 1273–1278, Sep. 2008.
- [22] J. F. Vincent, “Structure of wood,” *Curr. Opin. Solid State Mater. Sci.*, vol. 3, no. 3, pp. 228–231, Jun. 1998.

- [23] G. Sinn, A. Reiterer, and S. E. Stanzl-Tschegg, "Surface analysis of different wood species using X-ray photoelectron spectroscopy (XPS)," *J. Mater. Sci.*, vol. 36, no. 19, pp. 4673–4680, Oct. 2001.
- [24] C. P. Neto *et al.*, "Variations in chemical composition and structure of macromolecular components in different morphological regions and maturity stages of *Arundo donax*," *Ind. Crops Prod.*, vol. 6, no. 1, pp. 51–58, Feb. 1997.
- [25] E. Obataya, T. Ono, and M. Norimoto, "Vibrational properties of wood along the grain," *J. Mater. Sci.*, vol. 35, no. 12, pp. 2993–3001, Jun. 2000.
- [26] A. K. Bledzki and O. Faruk, "Wood Fibre Reinforced Polypropylene Composites: Effect of Fibre Geometry and Coupling Agent on Physico-Mechanical Properties," *Appl. Compos. Mater.*, vol. 10, no. 6, pp. 365–379, Nov. 2003.
- [27] M. Meier-Schellersheim, I. D. C. Fraser, and F. Klauschen, "Multi-scale modeling in cell biology," *Wiley Interdiscip. Rev. Syst. Biol. Med.*, vol. 1, no. 1, pp. 4–14, 2009.
- [28] R. Talreja and C. V. Singh, "Multiscale Modeling for Damage Analysis," in *Multiscale Modeling and Simulation of Composite Materials and Structures*, Y. W. Kwon, D. H. Allen, and R. Talreja, Eds. Springer US, 2008, pp. 529–578.
- [29] M. L. Knothe Tate, "Top down and bottom up engineering of bone," *J. Biomech.*, vol. 44, no. 2, pp. 304–312, Jan. 2011.
- [30] T. K. Bader, K. Hofstetter, C. Hellmich, and J. Eberhardsteiner, "The poroelastic role of water in cell walls of the hierarchical composite 'softwood,'" *Acta Mech.*, vol. 217, no. 1–2, pp. 75–100, Feb. 2011.
- [31] V. Bucur, "Wood structure anisotropy and ultrasonic parameters," in *Acoustics of Wood*, 2nd ed., Berlin Heidelberg: Springer-Verlag, 2006, pp. 141–170.
- [32] L. N. McCartney, "Multiscale Modeling of Composites Using Analytical Methods," in *Multiscale Modeling and Simulation of Composite Materials and Structures*, Y. W. Kwon, D. H. Allen, and R. Talreja, Eds. Springer US, 2008, pp. 271–316.
- [33] F. V. Souza and D. H. Allen, "Multiscale modeling of impact on heterogeneous viscoelastic solids containing evolving microcracks," *Int. J. Numer. Methods Eng.*, vol. 82, no. 4, pp. 464–504, Apr. 2010.
- [34] R. Hill, "A self-consistent mechanics of composite materials," *J. Mech. Phys. Solids*, vol. 13, no. 4, pp. 213–222, Aug. 1965.

- [35] V. Kouznetsova, M. G. D. Geers, and W. a. M. Brekelmans, “Multi-scale constitutive modelling of heterogeneous materials with a gradient-enhanced computational homogenization scheme,” *Int. J. Numer. Methods Eng.*, vol. 54, no. 8, pp. 1235–1260, Jul. 2002.
- [36] S. Le Conte and S. Vaiedelich, “A Wood Viscoelasticity Measurement Technique and Applications to Musical Instruments: First Results,” *J. Violin Soc. Am.*, vol. 21, no. 1, pp. 112–118, Jun. 2007.
- [37] M. Spycher, F. W. M. R. Schwarze, and R. Steiger, “Assessment of resonance wood quality by comparing its physical and histological properties,” *Wood Sci. Technol.*, vol. 42, no. 4, pp. 325–342, Apr. 2008.
- [38] S. Amada and R. S. Lakes, “Viscoelastic properties of bamboo,” *J. Mater. Sci.*, vol. 32, no. 10, pp. 2693–2697, May 1997.
- [39] F. Avanzini and M. van Walstijn, “Modelling the Mechanical Response of the Reed-Mouthpiece-Lip System of a Clarinet. Part I. A One-Dimensional Distributed Model,” Jun-2004. [Online]. Available: <https://www.ingentaconnect.com/contentone/dav/aaua/2004/00000090/00000003/art00014>. [Accessed: 28-Jun-2018].
- [40] Picart P., Leval J., Piquet F., Boileau J. P., Guimezanes T., and Dalmont J. P., “Study of the Mechanical Behaviour of a Clarinet Reed Under Forced and Auto-oscillations With Digital Fresnel Holography,” *Strain*, vol. 46, no. 1, pp. 89–100, Jan. 2010.
- [41] S. Glave *et al.*, “Quality indicators for woodwind reed material,” *Nucl. Instrum. Methods Phys. Res. Sect. B Beam Interact. Mater. At.*, vol. 150, no. 1, pp. 673–678, Apr. 1999.
- [42] P. G. Dixon and L. J. Gibson, “The structure and mechanics of Moso bamboo material,” *J. R. Soc. Interface*, vol. 11, no. 99, p. 20140321, Oct. 2014.
- [43] J. N. Heinrich, “The Basson Reed,” *J. Int. Double Reed Soc.*, vol. 7, p. 1743, Jun. 1979.
- [44] J. Backus, “Vibrations of the Reed and the Air Column in the Clarinet,” *J. Acoust. Soc. Am.*, vol. 33, no. 6, pp. 806–809, Jun. 1961.
- [45] J.-F. Petiot, P. Kersaudy, G. Scavone, S. McAdams, and B. Gazengel, “Investigation of the Relationships Between Perceived Qualities and Sound Parameters of Saxophone Reeds,” *Acta Acust. United Acust.*, Oct. 2017.

- [46] J. Schindelin, C. T. Rueden, M. C. Hiner, and K. W. Eliceiri, "The ImageJ ecosystem: An open platform for biomedical image analysis," *Mol. Reprod. Dev.*, vol. 82, no. 7–8, pp. 518–529.
- [47] C. A. Schneider, W. S. Rasband, and K. W. Eliceiri, "NIH Image to ImageJ: 25 years of image analysis," *Nat. Methods*, vol. 9, no. 7, pp. 671–675, Jul. 2012.
- [48] J. Schindelin *et al.*, "Fiji: an open-source platform for biological-image analysis," *Nat. Methods*, vol. 9, no. 7, pp. 676–682, Jul. 2012.
- [49] S. Amada, Y. Ichikawa, T. Munekata, Y. Nagase, and H. Shimizu, "Fiber texture and mechanical graded structure of bamboo," *Compos. Part B Eng.*, vol. 28, no. 1, pp. 13–20, Jan. 1997.
- [50] F. Shadmehri, B. Derisi, and S. V. Hoa, "On bending stiffness of composite tubes," *Compos. Struct.*, vol. 93, no. 9, pp. 2173–2179, Aug. 2011.
- [51] L. J. Gibson and M. F. Ashby, *Cellular solids structure and properties*, 2nd ed. Cambridge University Press, 1997.
- [52] J. Chung and A. M. Waas, "The micropolar elasticity constants of circular cell honeycombs," *Proc. R. Soc. Lond. Math. Phys. Eng. Sci.*, vol. 465, no. 2101, pp. 25–39, Jan. 2009.
- [53] H. Altenbach and A. Oechsner, Eds., *Cellular and Porous Materials in Structures and Processes*. Wien: Springer-Verlag, 2010.
- [54] A. Cernescu, J. Romanoff, H. Remes, N. Faur, and J. Jelovica, "Equivalent mechanical properties for cylindrical cell honeycomb core structure," *Compos. Struct.*, vol. 108, pp. 866–875, Feb. 2014.
- [55] E. Obataya and M. Norimoto, "Acoustic properties of a reed (*Arundo donax* L.) used for the vibrating plate of a clarinet," *J. Acoust. Soc. Am.*, vol. 106, no. 2, pp. 1106–1110, Jul. 1999.
- [56] A. E. Lord, "Viscoelasticity of the giant reed material *Arundo donax*," *Wood Sci. Technol.*, vol. 37, no. 3–4, pp. 177–188, Dec. 2003.
- [57] Speck O. and Spatz H.-C., "Mechanical Properties of the Rhizome of *Arundo donax* L.," *Plant Biol.*, vol. 5, no. 6, pp. 661–669, Feb. 2008.

- [58] F. Avanzini and M. van Walstijn, “Modelling the Mechanical Response of the Reed-Mouthpiece-Lip System of a Clarinet. Part I. A One-Dimensional Distributed Model,” *Acta Acust. United Acust.*, vol. 90, no. 3, pp. 537–547, Jun. 2004.
- [59] G. Chen, H. Luo, S. Wu, J. Guan, J. Luo, and T. Zhao, “Flexural deformation and fracture behaviors of bamboo with gradient hierarchical fibrous structure and water content,” *Compos. Sci. Technol.*, vol. 157, pp. 126–133, Mar. 2018.
- [60] X. Wang, H. Ren, B. Zhang, B. Fei, and I. Burgert, “Cell wall structure and formation of maturing fibres of moso bamboo (*Phyllostachys pubescens*) increase buckling resistance,” *J. R. Soc. Interface*, vol. 9, no. 70, pp. 988–996, May 2012.
- [61] L. Zou, H. Jin, W.-Y. Lu, and X. Li, “Nanoscale structural and mechanical characterization of the cell wall of bamboo fibers,” *Mater. Sci. Eng. C*, vol. 29, no. 4, pp. 1375–1379, May 2009.
- [62] P. G. Dixon *et al.*, “Comparison of the structure and flexural properties of Moso, Guadua and Tre Gai bamboo,” *Constr. Build. Mater.*, vol. 90, pp. 11–17, Aug. 2015.
- [63] S. E. Olesiak, M. L. Oyen, and V. L. Ferguson, “Viscous-elastic-plastic behavior of bone using Berkovich nanoindentation,” *Mech. Time-Depend. Mater.*, vol. 14, no. 2, pp. 111–124, May 2010.
- [64] M. L. Oyen and R. F. Cook, “Load–displacement behavior during sharp indentation of viscous–elastic–plastic materials,” *J. Mater. Res.*, vol. 18, no. 1, pp. 139–150, Jan. 2003.
- [65] R. R. Chromik, D.-N. Wang, A. Shugar, L. Limata, M. R. Notis, and R. P. Vinci, “Mechanical Properties of Intermetallic Compounds in the Au–Sn System,” *J. Mater. Res.*, vol. 20, no. 8, pp. 2161–2172, Aug. 2005.
- [66] A. C. Fischer-Cripps, “A simple phenomenological approach to nanoindentation creep,” *Mater. Sci. Eng. A*, vol. 385, no. 1, pp. 74–82, Nov. 2004.
- [67] M. K. Habibi, L. Tam, D. Lau, and Y. Lu, “Viscoelastic damping behavior of structural bamboo material and its microstructural origins,” *Mech. Mater.*, vol. 97, pp. 184–198, Jun. 2016.
- [68] S. Campbell, M. Oyen, and V. Ferguson, “Viscous Behavior in Berkovich Nanoindentation of Bone,” in *Proceedings of the SEM Annual Conference*, Albuquerque, New Mexico, USA, 2009, vol. 14.

- [69] P. A. Penttilä *et al.*, “Effects of pressurized hot water extraction on the nanoscale structure of birch sawdust,” *Cellulose*, vol. 20, no. 5, pp. 2335–2347, Oct. 2013.
- [70] I. Brémaud, J. Ruelle, A. Thibaut, and B. Thibaut, “Changes in viscoelastic vibrational properties between compression and normal wood : roles of microfibril angle and of lignin,” *Holzforschung*, p. voir DOI, 2013.
- [71] L. Gašparovič, Z. Koreňová, and L. Jelemenský, “Kinetic study of wood chips decomposition by TGA,” *Chem. Pap.*, vol. 64, no. 2, pp. 174–181, Apr. 2010.
- [72] U. P. Agarwal, S. A. Ralph, C. Baez, R. S. Reiner, and S. P. Verrill, “Effect of sample moisture content on XRD-estimated cellulose crystallinity index and crystallite size,” *Cellul. 245 1971-1984*, vol. 24, no. 5, pp. 1971–1984, 2017.
- [73] *DIFFRAC.EVA*. Billerica, Massachusetts, USA: Bruker.
- [74] C. Driemeier, W. D. Santos, and M. S. Buckeridge, “Cellulose crystals in fibrovascular bundles of sugarcane culms: orientation, size, distortion, and variability,” *Cellulose*, vol. 19, no. 5, pp. 1507–1515, Oct. 2012.
- [75] S. Amada and R. S. Lakes, “Viscoelastic properties of bamboo,” *J. Mater. Sci.*, vol. 32, no. 10, pp. 2693–2697, May 1997.
- [76] K. Hu, Y. Huang, B. Fei, C. Yao, and C. Zhao, “Investigation of the multilayered structure and microfibril angle of different types of bamboo cell walls at the micro/nano level using a LC-PolScope imaging system,” *Cellulose*, vol. 24, no. 11, pp. 4611–4625, Nov. 2017.
- [77] M. Wada, T. Okano, and J. Sugiyama, “Synchrotron-radiated X-ray and neutron diffraction study of native cellulose,” *Cellulose*, vol. 4, no. 3, pp. 221–232, Sep. 1997.
- [78] Garvey Christopher J., Parker Ian H., and Simon George P., “On the Interpretation of X-Ray Diffraction Powder Patterns in Terms of the Nanostructure of Cellulose I Fibres,” *Macromol. Chem. Phys.*, vol. 206, no. 15, pp. 1568–1575, Jul. 2005.
- [79] Langford J. I., “A rapid method for analysing the breadths of diffraction and spectral lines using the Voigt function,” *J. Appl. Crystallogr.*, vol. 11, no. 1, pp. 10–14, Feb. 1978.
- [80] L. Segal, J. J. Creely, A. E. Martin, and C. M. Conrad, “An Empirical Method for Estimating the Degree of Crystallinity of Native Cellulose Using the X-Ray Diffractometer,” *Text. Res. J.*, vol. 29, no. 10, pp. 786–794, Oct. 1959.

- [81] S. Park, J. O. Baker, M. E. Himmel, P. A. Parilla, and D. K. Johnson, “Cellulose crystallinity index: measurement techniques and their impact on interpreting cellulase performance,” *Biotechnol. Biofuels*, vol. 3, p. 10, May 2010.
- [82] P. Ahvenainen, I. Kontro, and K. Svedström, “Comparison of sample crystallinity determination methods by X-ray diffraction for challenging cellulose I materials,” *Cellulose*, vol. 23, no. 2, pp. 1073–1086, Apr. 2016.
- [83] F. Lionetto, R. Del Sole, D. Cannoletta, G. Vasapollo, and A. Maffezzoli, “Monitoring Wood Degradation during Weathering by Cellulose Crystallinity,” *Materials*, vol. 5, no. 10, pp. 1910–1922, Oct. 2012.
- [84] T. Inagaki, H. W. Siesler, K. Mitsui, and S. Tsuchikawa, “Difference of the Crystal Structure of Cellulose in Wood after Hydrothermal and Aging Degradation: A NIR Spectroscopy and XRD Study,” *Biomacromolecules*, vol. 11, no. 9, pp. 2300–2305, Sep. 2010.
- [85] P. Scherrer, “Bestimmung der Größe und der inneren Struktur von Kolloidteilchen mittels Röntgenstrahlen,” *Nachrichten Von Ges. Wiss. Zu Gött. Math.-Phys. Kl.*, vol. 1918, pp. 98–100, 1918.
- [86] S. Mannan, J. P. Knox, and S. Basu, “Correlations between axial stiffness and microstructure of a species of bamboo,” *Open Sci.*, vol. 4, no. 1, p. 160412, Jan. 2017.
- [87] Y. Nishiyama, “Structure and properties of the cellulose microfibril,” *J. Wood Sci.*, vol. 55, no. 4, pp. 241–249, Aug. 2009.
- [88] D. G. Hepworth and J. F. V. Vincent, “Modelling the Mechanical Properties of Xylem Tissue from Tobacco Plants (*Nicotiana tabacum* ‘Samsun’) by Considering the Importance of Molecular and Micromechanisms,” *Ann. Bot.*, vol. 81, no. 6, pp. 761–770, Jun. 1998.
- [89] T. A. Tabet and F. Abdul Aziz, “Cellulose Microfibril Angle in Wood and Its Dynamic Mechanical Significance,” in *Cellulose*, IntechOpen, 2013.
- [90] S. Youssefian, J. E. Jakes, and N. Rahbar, “Variation of Nanostructures, Molecular Interactions, and Anisotropic Elastic Moduli of Lignocellulosic Cell Walls with Moisture,” *Sci. Rep.*, vol. 7, no. 1, p. 2054, May 2017.
- [91] M. Poletto, A. J. Zattera, M. M. C. Forte, and R. M. C. Santana, “Thermal decomposition of wood: Influence of wood components and cellulose crystallite size,” *Bioresour. Technol.*, vol. 109, pp. 148–153, Apr. 2012.

- [92] D.-Y. Kim, Y. Nishiyama, M. Wada, S. Kuga, and T. Okano, “Thermal Decomposition of Cellulose Crystallites in Wood,” *Holzforschung*, vol. 55, no. 5, pp. 521–524, 2005.
- [93] F. C. Beall and H. W. Eickner, “Thermal degradation of wood components: a review of the literature.,” *Res. Pap. U. S. For. Prod. Lab.*, no. No. FPL 130., 1970.
- [94] G. A. Zickler, W. Wagermaier, S. S. Funari, M. Burghammer, and O. Paris, “In situ X-ray diffraction investigation of thermal decomposition of wood cellulose,” *J. Anal. Appl. Pyrolysis*, vol. 80, no. 1, pp. 134–140, Aug. 2007.
- [95] P. D. Evans, P. D. Thay, and K. J. Schmalzl, “Degradation of wood surfaces during natural weathering. Effects on lignin and cellulose and on the adhesion of acrylic latex primers,” *Wood Sci. Technol.*, vol. 30, no. 6, pp. 411–422, Nov. 1996.
- [96] U.-J. Kim, S. H. Eom, and M. Wada, “Thermal decomposition of native cellulose: Influence on crystallite size,” *Polym. Degrad. Stab.*, vol. 95, no. 5, pp. 778–781, May 2010.
- [97] M. Poletto, H. L. Ornaghi Júnior, and A. J. Zattera, “Native Cellulose: Structure, Characterization and Thermal Properties,” *Materials*, vol. 7, no. 9, pp. 6105–6119, Aug. 2014.
- [98] M. Wada, T. Okano, and J. Sugiyama, “Allomorphs of native crystalline cellulose I evaluated by two equatorial d-spacings,” *J. Wood Sci.*, vol. 47, no. 2, pp. 124–128, Apr. 2001.
- [99] W. C. Oliver and G. M. Pharr, “An improved technique for determining hardness and elastic modulus using load and displacement sensing indentation experiments,” *J. Mater. Res.*, vol. 7, no. 6, pp. 1564–1583, Jun. 1992.
- [100] A. C. Fischer-Cripps, *Nanoindentation | Anthony C. Fischer-Cripps | Springer*, 2nd ed. Springer-Verlag New York, 2004.
- [101] R. E. Perdue, “Arundo donax—Source of musical reeds and industrial cellulose,” *Econ. Bot.*, vol. 12, no. 4, pp. 368–404, Oct. 1958.
- [102] J. Petiot, P. Kersaudy, G. Scavone, S. McAdams, and B. Gazengel, “Modeling of the subjective quality of saxophone reeds,” *Proc. Meet. Acoust.*, vol. 19, no. 1, p. 035028, May 2013.
- [103] V. Chatziioannou and M. van Walstijn, “Estimation of Clarinet Reed Parameters by Inverse Modelling,” *Acta Acust. United Acust.*, vol. 98, no. 4, pp. 629–639, Aug. 2012.

- [104] K. Takahashi, H. Kodama, A. Nakajima, and T. Tachibana, “Numerical Study on Multi-Stable Oscillations of Woodwind Single-Reed Instruments,” *Acta Acust. United Acust.*, Dec. 2009.
- [105] R. Pilu, R. Bucci, F. C. Badone, M. L. and oni, “Giant reed (*Arundo donax* L.): A weed plant or a promising energy crop?,” *Afr. J. Biotechnol.*, vol. 11, no. 38, pp. 9163–9174, May 2012.
- [106] L. Corno, R. Pilu, and F. Adani, “*Arundo donax* L.: A non-food crop for bioenergy and bio-compound production,” *Biotechnol. Adv.*, vol. 32, no. 8, pp. 1535–1549, Dec. 2014.
- [107] G. Lokesha, B. G. Vijayasimha Reddy, T. Yella Reddy, and M. Venkatarama Reddy, “Experimental Determination of Tensile Properties of Bamboo Structure,” *Int. J. Mech. Prod. Eng.*, vol. 5, no. 11, pp. 143–146, Nov. 2017.
- [108] S. Sevanto *et al.*, “Is desiccation tolerance and avoidance reflected in xylem and phloem anatomy of two coexisting arid-zone coniferous trees?,” *Plant Cell Environ.*, vol. 41, no. 7, pp. 1551–1564, Jul. 2018.
- [109] D. Derome, W. Zillig, and J. Carmeliet, “Variation of measured cross-sectional cell dimensions and calculated water vapor permeability across a single growth ring of spruce wood,” *Wood Sci. Technol.*, vol. 46, no. 5, pp. 827–840, Sep. 2012.
- [110] A. R. Da Silva, Y. Shi, and G. Sacvone, “Computational analysis of the dynamic flow in single-reed woodwind instruments,” *Proc. Meet. Acoust.*, vol. 19, no. 1, p. 035043, May 2013.
- [111] Y. Shi, A. R. da Silva, and G. P. Scavone, “LBM Simulation of the Quasi-Static Flow in a Clarinet,” in *Proceedings of the Third Vienna Talk on Music Acoustics*, University of Music and Performing Arts Vienna, pp. 35–42.
- [112] N. Parameswaran and W. Liese, “On the fine structure of bamboo fibres,” *Wood Sci. Technol.*, vol. 10, no. 4, pp. 231–246, Dec. 1976.
- [113] W. Gindl, H. S. Gupta, and C. Grünwald, “Lignification of spruce tracheid secondary cell walls related to longitudinal hardness and modulus of elasticity using nano-indentation,” *Can. J. Bot.*, vol. 80, no. 10, pp. 1029–1033, Oct. 2002.
- [114] J. Berthold, M. Rinaudo, and L. Salmeñ, “Association of water to polar groups; estimations by an adsorption model for ligno-cellulosic materials,” *Colloids Surf. Physicochem. Eng. Asp.*, vol. 112, no. 2, pp. 117–129, Jul. 1996.

- [115] *Avizo*. Hillsboro, Oregon, USA: FEI Visualization Sciences Group.
- [116] B. Münch, L. H. J. Martin, and A. Leemann, “Segmentation of elemental EDS maps by means of multiple clustering combined with phase identification,” *J. Microsc.*, vol. 260, no. 3, pp. 411–426, Dec. 2015.
- [117] D. Rueckert, L. I. Sonoda, C. Hayes, D. L. G. Hill, M. O. Leach, and D. J. Hawkes, “Nonrigid registration using free-form deformations: application to breast MR images,” *IEEE Trans. Med. Imaging*, vol. 18, no. 8, pp. 712–721, Aug. 1999.
- [118] S. Lee, G. Wolberg, and S. Y. Shin, “Scattered Data Interpolation with Multilevel B-Splines,” *IEEE Trans. Vis. Comput. Graph.*, vol. 3, pp. 228–244, 1997.
- [119] T. K. H. Tang, “Preservation and drying of commercial bamboo species of Vietnam,” University of Hamburg.
- [120] C. Skaar, *Wood-Water Relations*. Berlin Heidelberg: Springer-Verlag, 1988.
- [121] W. Liese, *The Anatomy of Bamboo Culms*. BRILL, 1998.
- [122] P. D. Evans and P. D. Evans, “Degradation of wood surfaces by water,” *Holz Als Roh-Werkst.*, vol. 48, no. 5, pp. 159–163, May 1990.
- [123] I. G. Ritchie and Z.-L. Pan, “High-damping metals and alloys,” *Metall. Trans. A*, vol. 22, no. 3, pp. 607–616.
- [124] I. G. Ritchie, “Improved resonant bar techniques for the measurement of dynamic elastic moduli and a test of the Timoshenko beam theory,” *J. Sound Vib.*, vol. 31, no. 4, pp. 453–468, Dec. 1973.
- [125] Lars Berglund, “Cellulose-based nanocomposites,” in *Natural fibers, biopolymers, and biocomposites*, 1st ed., Taylor & Francis, 2005, pp. 807–817.
- [126] Z. Liu, Z. Jiang, Z. Cai, B. Fei, Y. Yu, and X. Liu, “Dynamic mechanical thermal analysis of moso bamboo (*Phyllostachys heterocycla*) at different moisture content,” *BioResources*, vol. 7, no. 2, pp. 1548–1557, Feb. 2012.
- [127] Satish Kumar, KS Shukla, Tndra Dev, and PB Dobriyal, “Bamboo Preservation Techniques: A Review,” International Network for Bamboo and Rattan, Oct. 1994.
- [128] V. Bucur, “Ageing of Wood,” in *Handbook of Materials for String Musical Instruments*, Springer International Publishing, 2016, pp. 283–323.

A. Appendix

This appendix presents a study published in *MRS Advances* that explored damage mechanisms in artificially aged Arundo Donax material. This study examined some preliminary results of material testing using optical microscopy, XRD and damping measurements. Sample preparation and testing techniques were developed here and used in future work (Chapters 4, 5 and 6). Samples used in this study were not used in any of the other chapters presented and thus the paper is provided here as an appendix.

A.1 Microstructure Contributions to Vibrational Damping and Identification of Damage Mechanisms in *Arundo Donax L*: Reed Cane for Woodwind Instruments

Connor Kemp¹ and Gary Scavone¹

¹Computational Acoustic Modeling Laboratory, McGill University, 555 Sherbrooke Street West, Montreal, QC, Canada.

Abstract:

Natural cane reeds (Latin name *Arundo Donax L* and here termed ADL) have been used on woodwind instruments for centuries with little change. The reed acts as a mechanical valve controlling the energy input into the musical instrument and it is the musician's first option for altering the instrument's sound and response characteristics. Despite this, their consistency, variable performance, durability and sensitivity to ambient conditions make it difficult for the musician to find and maintain a reed that responds to their liking. Thus it is desirable to examine the material, microstructural and anatomical properties of the reed and their contributions to vibrational performance with input from mechanical engineers, materials scientists and musicians.

The current study is part of an on-going research project, and this paper presents preliminary results. In the present work raw samples of ADL obtained from a manufacturer in pre-cut form are sectioned into longitudinal and transverse specimens for mechanical characterisation. Prior to testing, samples are conditioned using an incubation system to 37 degrees Celsius and 90% relative humidity, mimicking in-use conditions of the reed. Initial microstructure analysis of each specimen is completed using optical microscopy to quantify fiber spatial arrangement, size and the existence of micro-cracks along the fiber-matrix interface. X-ray diffraction is also used to quantify the fraction of crystalline cellulose present in each sample. Specimens are then excited over a specific frequency range similar to that of in-use reeds using pressure waves in a non-contact setup. Values of internal friction are obtained as logarithmic decrement values for frequency-dependent decay. One set of specimens is then subjected to cyclic mechanical loading at low

frequency ($< 1\text{Hz}$) and stresses up to 15MPa . The other set is maintained at the given environmental conditions using the incubator and aged through temperature and humidity cycling. Comparisons of post-testing microstructure damage and internal friction measurements are then completed to delineate specific degradation mechanisms due to mechanical/fatigue deterioration and moisture cycling. Internal friction is found to be dependent on both frequency, moisture and cyclic loading. Furthermore, the existence of microstructural cracks contributes to increasing decrement values at high frequencies in both fatigued and moisture cycled samples. Statistically significant correlations are discovered between logarithmic decrement and vascular bundle orientation at 700 Hz and logarithmic decrement and parenchyma cell diameter at 1000 Hz . Reductions in internal friction below 400 Hz indicate a decreasing loss modulus (E'') with increased moisture cycles, although this trend will be tested against a larger sample set in further work.

A.2 Introduction

The reed is a small piece of cane (*Arundo Donax L.*, here termed ADL) that is used on many woodwind instruments as the primary vibrating element. This element controls the volume flow of air into the air column and is critically important to the sound produced by the instrument. Reeds are often found to be highly variable, both in terms of static stiffness and produced sound. Despite this, little research has been conducted on the material properties and microstructural contributions to this variability. Furthermore, little is known about the reed material ADL in terms of its elastic, plastic, dynamic, degradation and damping properties. An example of an ADL microstructure is provided in Figure 1. This work presents a proposed methodological framework to study structural changes in reed material (ADL) when exposed to in-use conditions and the framework is demonstrated using four compression samples.

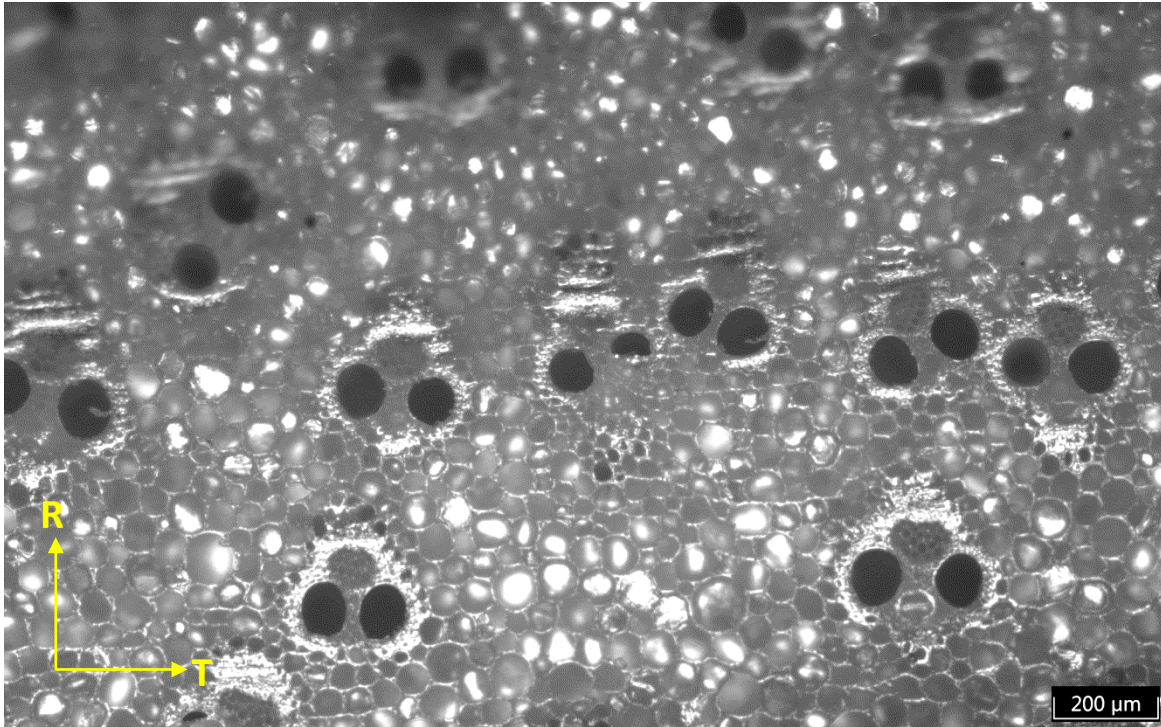


Figure 1: ADL microstructure as a cross-section through the stem. This orientation shows fibers and vascular bundles aligned in the longitudinal direction.

Similarities can be drawn to bamboo in terms of the structures present in this material, primarily the vascular bundles, fiber cap and parenchyma matrix. Like bamboo and most wood materials, ADL can be considered as elastically orthotropic with fibers aligned in the longitudinal direction of the stem. For this material the three important directions are axial/longitudinal, radial (R in Figure 1) and tangential/transverse (T in Figure 1). Stiffness in ADL is provided by the fibers and fiber caps within the porous matrix of parenchyma. Fibers and fiber caps can be observed as the light sections surrounding the large, open vessels (lumen) of Figure 1. Reeds are manufactured with their cross-section aligned with the longitudinal direction of the stem. Despite this and sophisticated machining techniques, natural variations in stem size and straightness can cause misalignment with the fibers resulting in less predictable stiffness. The reed tip is also $\sim 100\mu\text{m}$ in thickness which contributes to this variability as there is no separation of length scales. This tip is also exposed to large strains, likely large enough to induce permanent deformation [40].

To complicate matters further it is also well known that reed properties can change during their useable lifespan. As reeds are played in a fully humidified state (and stored either in a dry or semi-humidified state), changes in elastic and damping properties are not well understood. Also the roles that moisture degradation and mechanical degradation (here, cyclic fatigue loading from playing) play in contributing to these changing properties have not been examined for ADL. The present study is part of ongoing research and presents preliminary observations of changes in the dynamic behavior (damping properties) of ADL due to cyclic mechanical loading and moisture cycling. Both of these cases are chosen to mimic the in-use conditions that a reed is routinely exposed to, namely induced mechanical oscillations of the reed tip and humidity changes between playing conditions and storage conditions.

In the context of materials science, this study considers damping properties via internal friction measurements of the logarithmic decrement of free vibration. This method is chosen due to the constraints of sample geometry and size, and its elegance of simplicity. The logarithmic decrement has been used frequently as a measurement of internal friction and can be measured using resonant bar techniques, the torsion pendulum, or high frequency driven oscillation, to name just a few. Here the resonant bar technique (similar to [55]) is used and is outlined in detail in a subsequent section. X-ray diffraction is also used to observe differences in the crystalline fraction of cellulose between each. Measured differences in internal friction are compared with XRD measurements and microstructural parameters in an effort to correlate material properties with sample performance. Given the limited number of samples tested to-date (4), only trends in the data are discussed as opposed to absolute values of internal friction, microstructural features and crystallinity.

A.3 Experiment

The present study consists of two main components including cyclic mechanical loading and relative humidity (RH) cycling. Measurements of internal friction are taken before, during and after each step of the experimental procedure. There were four material specimens in total, including two of each material orientation as shown in Figure 2 (two samples transverse to the long-axis of the stem and two samples parallel to the long axis). For reference, the micrograph provided in Figure 1 is a cross-section of the stem wall microstructure (inner to outer diameter).

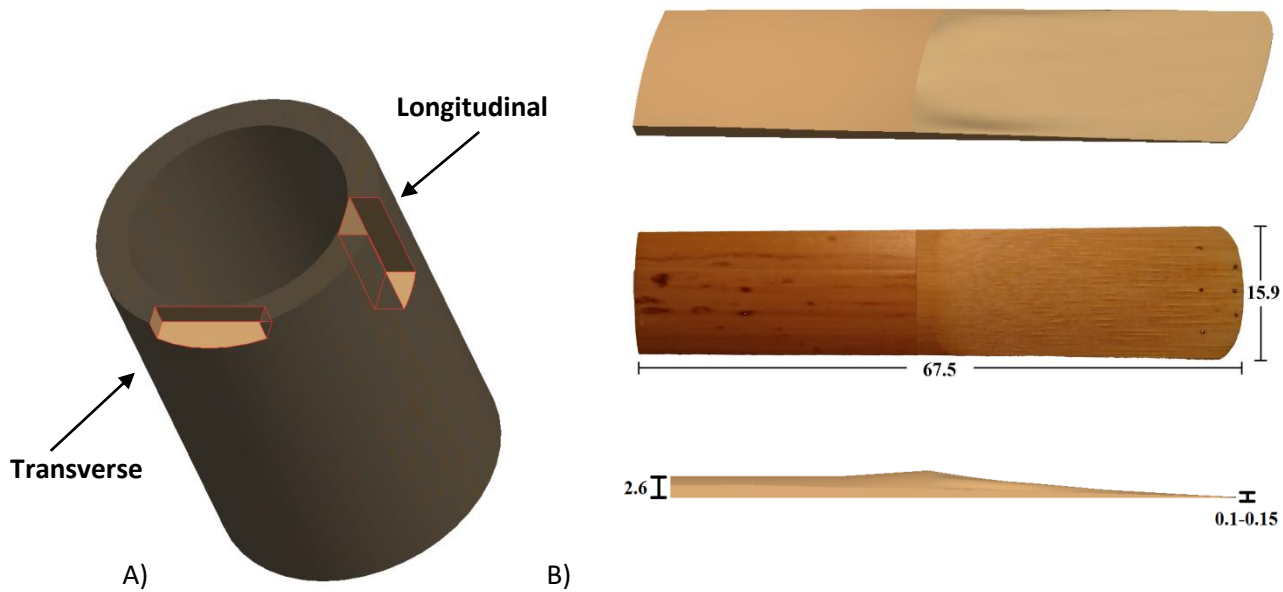


Figure 2: A) Orientation of samples used in the study with respect to the ADL stem geometry. The longitudinal sample is aligned along the length of the stem. B) Dimensions (in mm) and geometry of a typical alto saxophone reed. Note that the reed is machined from the wall of the stem and aligned with the longitudinal direction.

Each sample was a prismatic bar with equal dimensions (provided in Table 1) as this geometry lent itself well to both compression loading and bending resonance. Parallel/longitudinal samples were aligned with the fiber direction of ADL while transverse samples had a cross-section aligned with the tangential direction of the stem. The upper limit of sample thicknesses was limited by the raw ADL wall thickness. Table 1 also provides the naming convention used henceforth for the samples.

Table 1: Specimen identifiers and dimensions (in mm). Dimensions are given as a rectangular bar.

Sample	W (width)	H (height)	L (length)	Mass (g)
Longitudinal 1 (L1)	4.30	2.83	12.88	0.095
Longitudinal 2 (L2)	4.13	2.96	12.88	0.095
Transverse 1 (T1)	3.93	2.70	12.62	0.085
Transverse 2 (T2)	3.92	2.60	12.68	0.085

A.3.1 Cyclic Mechanical Loading

Samples L2 and T2 were used for the mechanical deformation component of the study. Fatigue loading was conducted on an ADMET 2.5kN material testing system using circular compression platens to prevent off-axis loading. A cycling frequency of 0.1Hz was used until 270 complete cycles had been reached. A preload was applied to each of the samples, although this load was different for sample L2 and T2 due to the added compliance of the T2 sample. This was observed from the additional strain measured for an equal load in the transverse samples, due to the loading direction being perpendicular to the fibers in the sample. Therefore, L2 was preloaded to 10 MPa and then cycled with an amplitude of +/- 4.1 MPa, fully compressive. T2 was preloaded to 7 MPa and then cycled at +/- 2.35 MPa. This entire iteration was completed two times, each with at least 24 hours in between to allow for residual strain to completely relax. Residual strain is of concern due to the large relaxation times associated with viscoelastic materials such as ADL.

A.3.2 Moisture Cycling

Samples L1 and T1 were used for the moisture cycling portion of this study. Samples were initially measured and weighed to quantify the moisture uptake during each cycle of the test. For this cycling, each sample was placed in a temperature and humidity controlled incubator at 37°C and 90% relative humidity (RH) for 24 hours. It should be noted that in-use reeds are in contact with saliva. The moisture parameters used here were taken as a first approximation of in-use conditions, where variables including pH levels, wetting preferences (i.e., not all musicians prepare reeds the same way) and embouchure (i.e., amount of the reed fully inside the mouth) were neglected. By incubating the samples at the given temperature and RH values, inter-sample variability was controlled. Given the length of incubation for each sample, moisture content was not at equilibrium. After the test, samples were then measured and weighed again before being returned to the incubator at 45°C and ambient RH to dry for 24 hours. This formed a complete cycle for the test and was repeated once. This single repeat was completed as a method of observing initial changes to the ADL material as noted by musicians upon playing a new reed for the first several sessions (where reeds are not exposed to moisture for the same length of time by all musicians).

A.3.3 Internal Friction Measurements

Measurements of internal friction were taken prior to beginning mechanical loading or moisture cycling in order to obtain an initial value for each sample. The resonant bar method [123] was used to excite each sample at frequencies between 100 and 1000 Hz (100 Hz intervals) and the resulting decay waveform was recorded upon cessation of the driving force. As these samples are extremely small with little mass, care was taken to position the specimens upon ultra-thin wire guides $0.224L$ from each end (where L is ~ 13 mm for each sample). These positions have been shown to be the nodal positions for prismatic bars of rectangular cross section in fundamental flexural vibration modes [124]. Excitation was completed using a compression driver (JBL 2426H) connected to a signal generator. Excitation tones were pure sinusoids and were applied for 2 seconds with the corresponding decay being measured for a further 1 second. Samples were positioned on the guide wires in the center of the compression driver with the specimen long-axis parallel to the driver face. This was done to ensure flexural excitation. The corresponding displacement amplitudes were measured at the center of the specimen on the opposite face using a STIL confocal white-light sensor. The entire experimental setup for these measurements is provided in Figure 3.

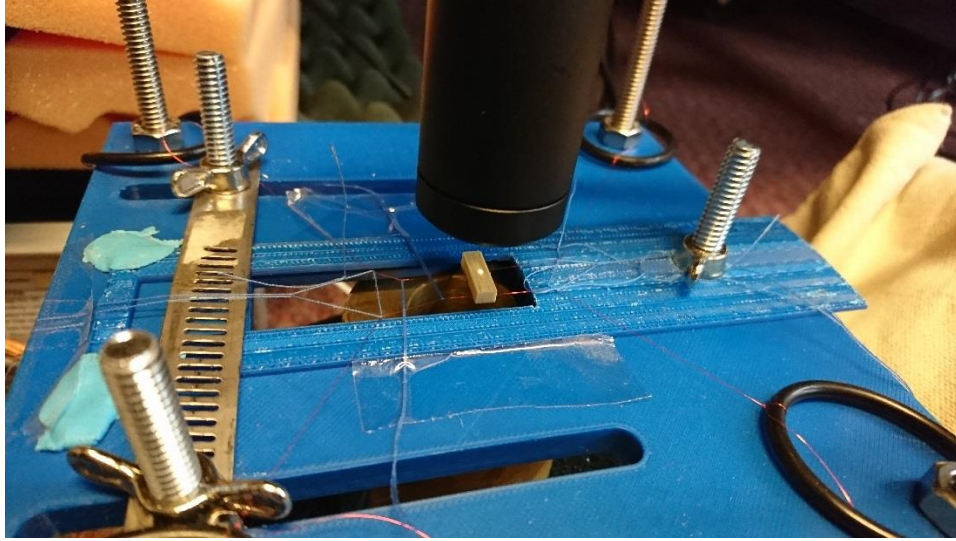


Figure 3: Experimental setup for internal friction measurements depicting the sample, confocal displacement sensor and compression driver.

The main advantage of this setup in comparison with the typical torsion pendulum is the complete free-free nature of sample vibration with no physical contact of any kind (i.e., no attached mass to alter the resonance of the system).

The logarithmic decrement for internal friction measurements is calculated as the relative magnitude of successive peaks in the decay amplitude plot. In order to obtain an average value over the entire decay the decrement, Δ , is calculated as follows:

$$\Delta = N^{-1} \ln \frac{A_1}{A_{N+1}} \quad (1)$$

where A_1 is the first decay peak amplitude and A_{N+1} is the $N+1$ th decay peak amplitude. An example decay curve is provided in Figure 4.

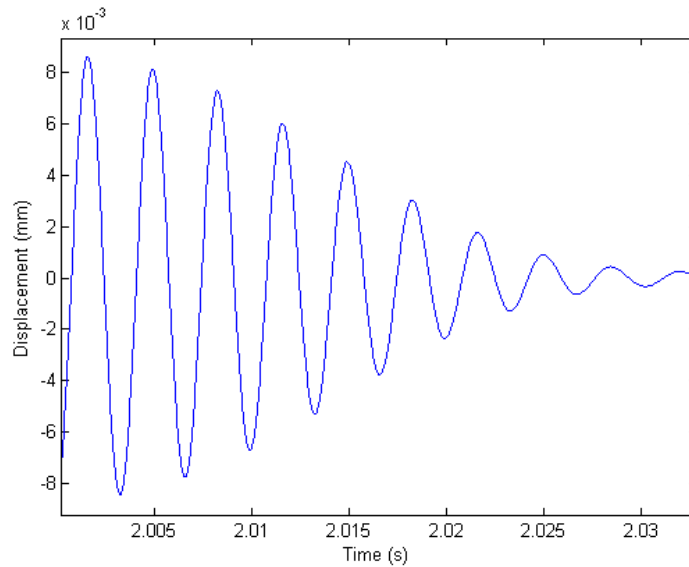


Figure 4: Sample displacement decay curve obtained at 300Hz excitation.

In total, 10 of these measurements were made per sample, per trial. To observe internal friction changes, measurements were made immediately following the first moisture cycle (samples still at 37°C and 90% RH) and 1 hour following the first 270 cycles of mechanical loading. In this way, the effects of moisture and residual strain on internal friction could be captured. These measurements were repeated one day later (24°C and ambient RH) after samples L1 and T1 had dried and samples L2 and T2 had fully relaxed. Once completed, the process was repeated again for another 24 hr/270 cycle moisture/mechanical loading.

A.3.4 Materials Quantification

Microstructural analysis of each sample was completed through optical microscopy of cross-sections. Micrographs of samples at 5, 20, 50 and 100x were obtained in order to evaluate the distribution of microstructural features pertinent to ADL. Some of these features are illustrated in Figure 5 below.

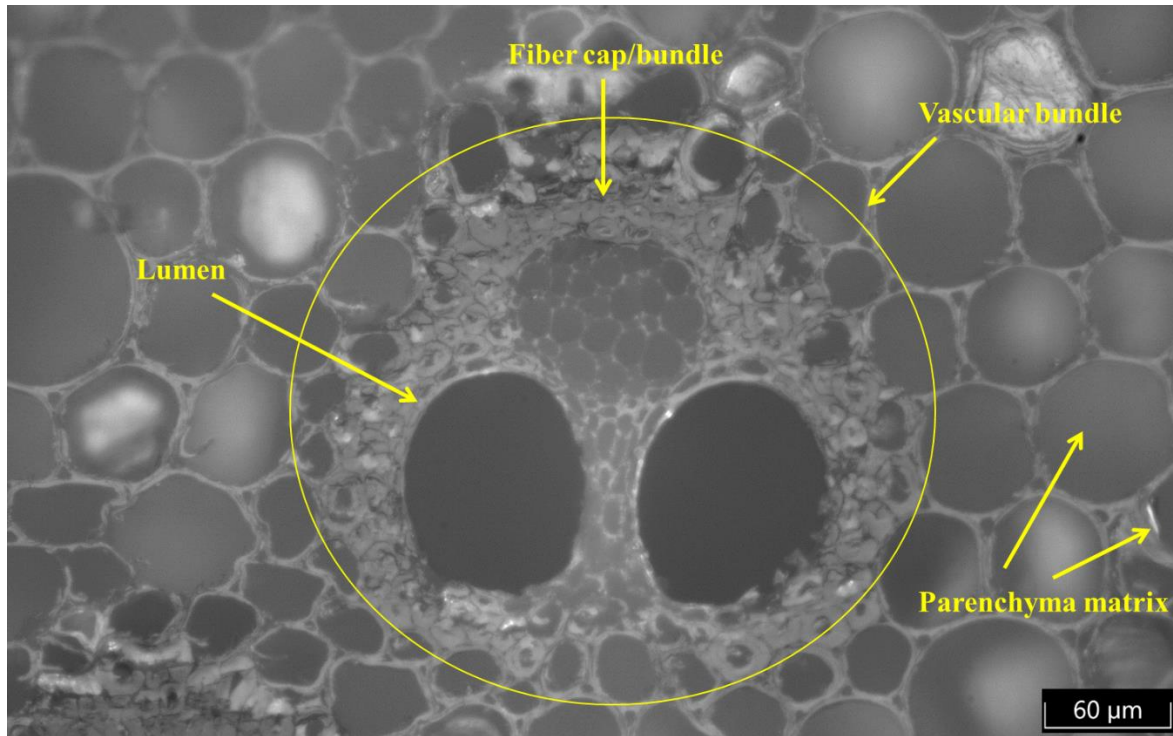


Figure 5: Optical micrograph of ADL indicating several microstructural features.

Analysis of these features over a relatively large cross-sectional area ($\sim 2 \times 1$ mm) provided average values for vascular bundle size, lumen diameter, parenchyma matrix diameter, fiber bundle size and vascular bundle orientation (in degrees relative to the sample surface). As an example, the vascular bundle illustrated in Figure 5 was considered to have an orientation of 0° as it is aligned with the surface.

The effects of moisture on the ADL material structure was also examined through the use of XRD measurements. Measurements were made on samples L1 and T1 prior to moisture cycling, and post moisture cycling for each trial. A Bruker X8 diffractometer was used with a Cu x-ray source and 2θ values ranging from 2 to $\sim 110^\circ$. For the case of ADL, this enabled the measure of relative phase changes between trials.

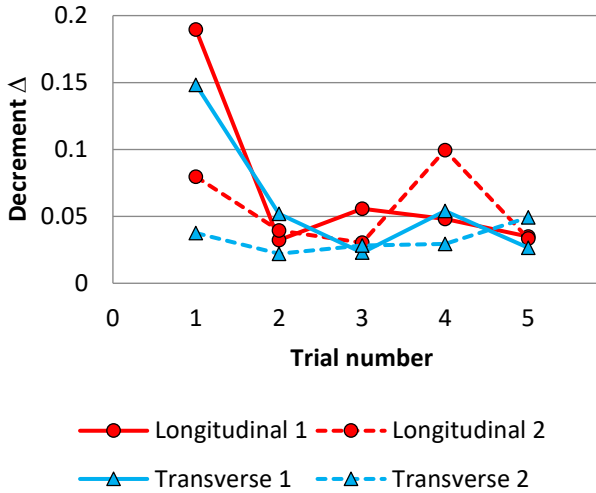
A.4 Discussion

Figures 6 and 7 depict internal friction variation with frequency for all samples. Analysis of internal friction measurements shows that behavior differs between low (< 400 Hz) and high frequencies (up to 1000 Hz). As a general observation, it appears that internal friction between

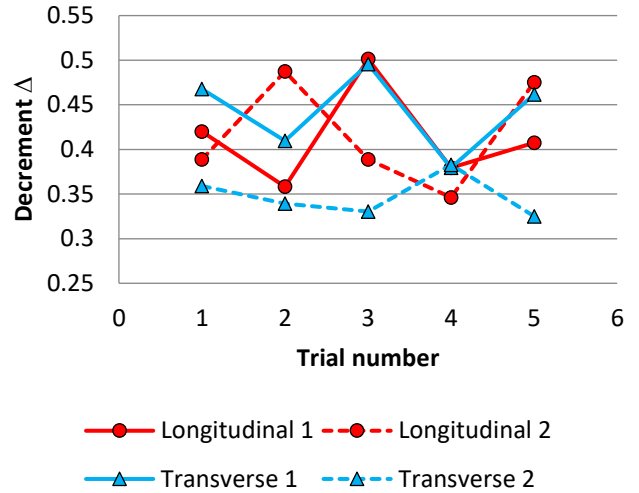
sample groups differs more significantly at frequencies < 400 Hz, while a general trend appears for all samples above 600 Hz. Each trial number indicates one of the 5 data points taken for logarithmic decrement values from 100 Hz to 1000 Hz (i.e., trial 1 contains 10 data points for each sample) over the course of the experiment. The timeline of the experiment is provided in Table 2, where trial 1 is the first set of measurements taken and trial 5 is the last. In the subsequent plots, the solid lines indicate samples having undergone moisture cycling, while dashed lines indicate compression loading samples.

Table 2: Experimental timeline for all ADL samples. The arrows indicate the conditioning that followed the previous trial. The type of conditioning performed on each sample is also indicated.

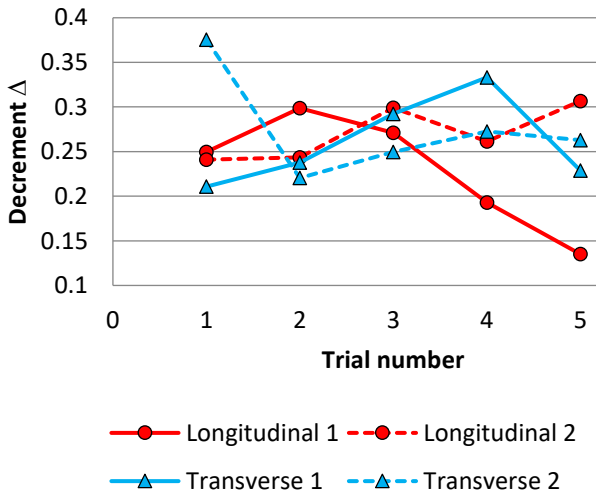
Timeline	Conditioning (Samples L1 and T1)	Conditioning (Samples L2 and T2)
	<ul style="list-style-type: none"> ● Longitudinal 1 ▲ Transverse 1 	<ul style="list-style-type: none"> - - ● - - Longitudinal 2 - - ▲ - - Transverse 2
Trial 1 →	<i>Initial characterisation</i>	
	24 hrs. at 37°C and 90% RH	Compression loading - 270 cycles
Trial 2 →	<i>Measurement 2</i>	
	24 hrs. at 45°C and ambient RH	24 hr. strain relaxation
Trial 3 →	<i>Measurement 3</i>	
	24 hrs. at 37°C and 90% RH	Compression loading - 270 cycles
Trial 4 →	<i>Measurement 4</i>	
	24 hrs. at 45°C and ambient RH	24 hr. strain relaxation
Trial 5	<i>Measurement 5</i>	



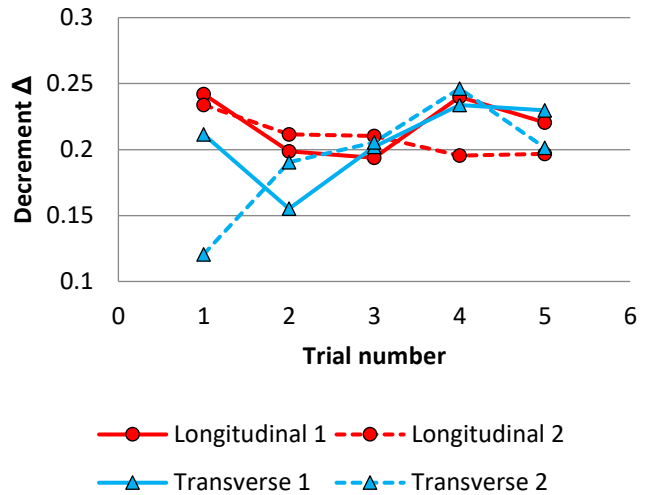
A) 100 Hz



B) 200 Hz



C) 300 Hz

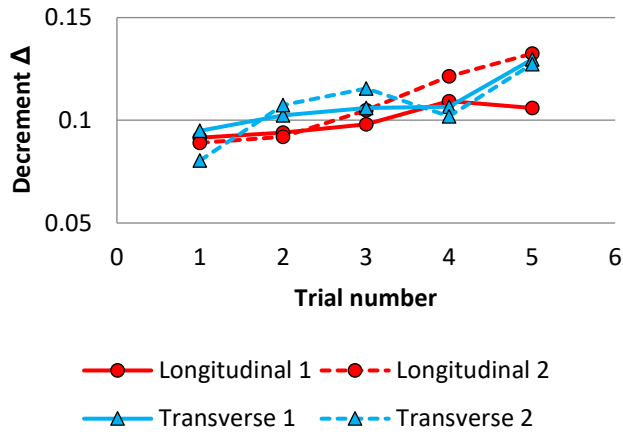


D) 400 Hz

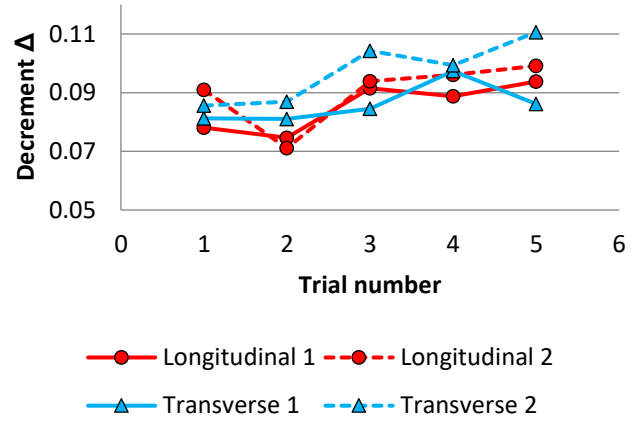
Figure 6: Plots of internal friction given as the logarithmic decrement versus trial number for all samples. (a) 100 Hz, b) 200 Hz, c) 300 Hz, d) 400 Hz)

The low frequency internal friction results shown here do not exhibit any overall trends, however there are a few interesting sample differences. The internal friction of L2 at 100Hz seems to exhibit a dependency on strain relaxation as illustrated by the difference between trials 4 and 5.

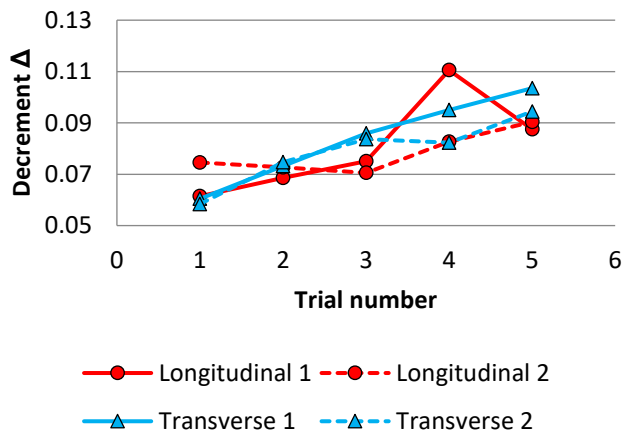
Examination of the initial versus final plots of internal friction for each sample indicates that the 100 Hz decrement value converges for all samples, suggesting that mechanical loading and moisture cycling has a similar effect on low frequency damping. Further examination indicates that this trend does not continue for the 200 Hz case. Here the largest differences (when compared to initial values) are observed for the mechanically loaded specimens (L2 and T2). $\Delta L_{200\text{Hz}}$ increases compared to its initial value while $\Delta T_{200\text{Hz}}$ decreases by a similar amount relative to its initial value. This can be further observed by examining the plots of initial internal friction and final internal friction (after completion of all testing) in Figure 8.



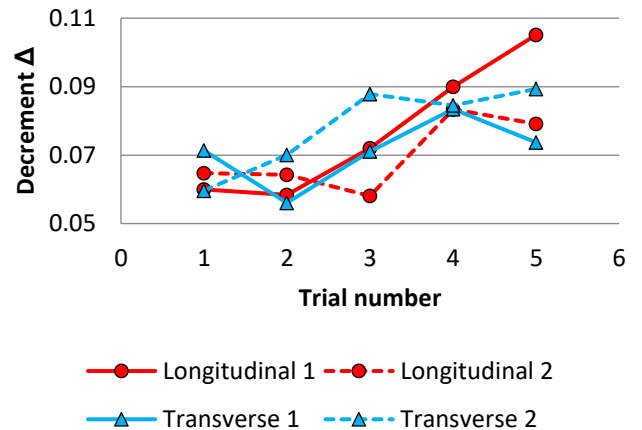
A) 700 Hz



B) 800 Hz



C) 900 Hz



D) 1000 Hz

Figure 7: Plots of internal friction given as the logarithmic decrement versus trial number for all samples. (a) 700 Hz, b) 800 Hz, c) 900 Hz, d) 1000 Hz)

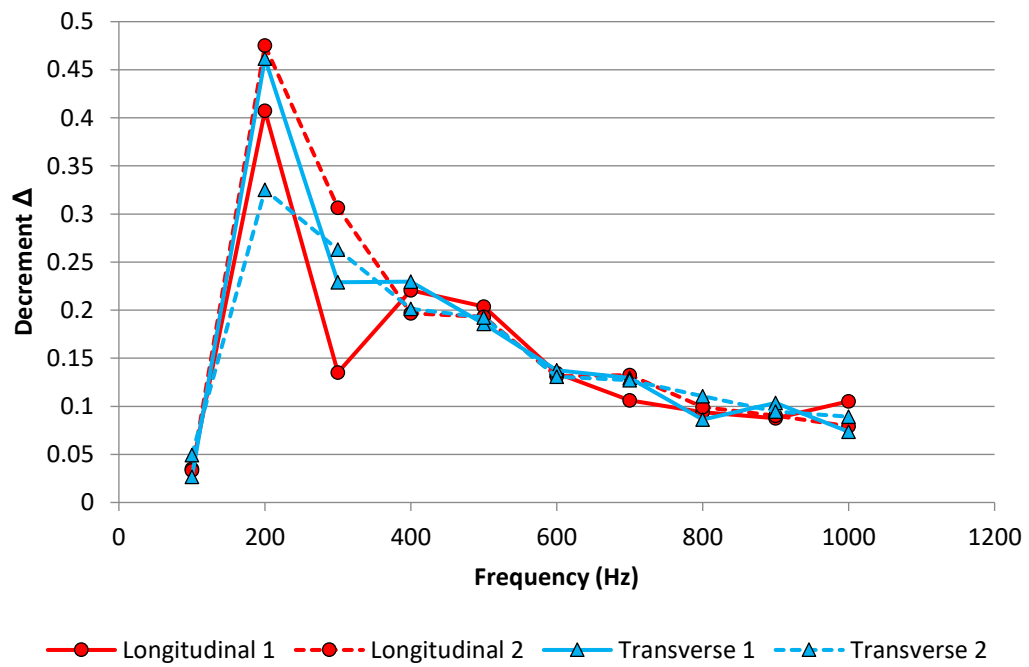
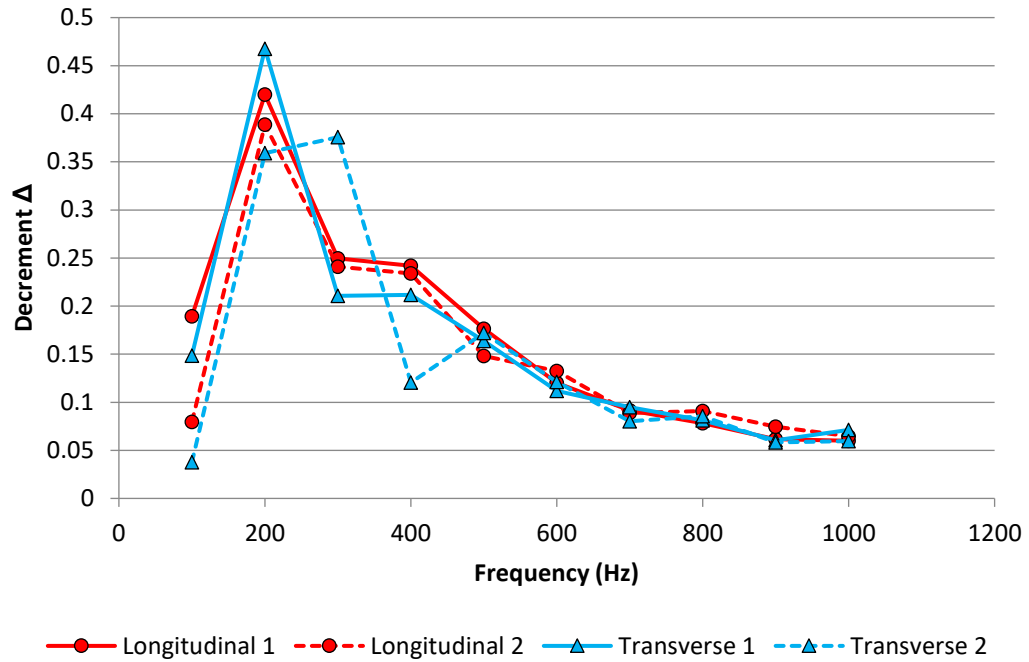


Figure 8: Top: decrement versus frequency values for all samples prior to testing. Bottom: the same results for all samples post testing.

For the case of $f = 700$ Hz, examining the trends of L1 and L2, it appears that both mechanical and moisture cycling contribute to increasing internal friction, although the rate of increase is larger for mechanical loading. Also of interest is the recovery of the 900 Hz internal friction value for L1 between the final moisture cycle measurement and the final measurement in dry conditions. This could be indicative of the increased molecular mobility of cellulose within the fiber cap at 90% RH which adds to dissipative forces. Work on cellulose nanocomposites has suggested that increased molecular mobility (above the glass transition temperature) contributes to changes in the complex modulus of the material [125]. For moso bamboo, studies have also shown the storage modulus to be dependent on temperature and moisture (decreasing with overall moisture content and decreasing with increasing temperature) [126]. The glass transition temperature of hemicelluloses in moso bamboo has also been shown to be below 30°C, a fact which compares favorably with the assertion that increased molecular mobility is increasing internal friction for the 900Hz L1 sample at 90% RH.

Examining the results between 200 and 400 Hz more closely, it can be seen that moisture cycling has a larger effect on internal friction than mechanical loading for the case of the longitudinal samples. Specifically, at 200Hz both L1 and T1 appear to be significantly effected by moisture cycling with internal friction values decreasing with each moisture cycle. This also occurs for the 100Hz internal friction values and will be discussed in a subsequent section within the context of changing crystallinity values for L1 and T1. For the transverse samples, both mechanical loading and moisture cycling result in a large absolute change in internal friction (relative to initial values). In fact, moisture cycling appears to consistently lower the internal friction of sample L1, while cyclic mechanical loading has the opposite effect. This could be related to sample L1 having a very low average vascular bundle orientation angle indicating an increased contribution of solid fibers to recoverable, elastic energy propagation due to more homogeneous moisture expansion (this is investigated further in the microstructural analysis section).

Looking at the data for moisture uptake (24 hrs. at 90% RH) of samples L1 and T1 it is found that the maximum linear expansion is found in the width direction for L1 3.6% (corresponding to the tangential direction). For T1, a maximum linear expansion of -1.97% is found in the height direction (corresponding to the radial direction). This suggests that the material behaves very anisotropically with regards to expansion and contraction, a fact that has been

mentioned in previous work on bamboo preservation [127]. It could be suggested then that the majority of residual strains due to moisture cycling would be absorbed in the parenchyma matrix due to its lower volumetric density. This data will be confirmed with longer term exposure to 90% RH.

Overall it appears that there is an internal friction peak near 200 Hz. Tests were not conducted below 100 Hz as previous results for bamboo [75] indicate that there is little internal friction dependency on frequency in this range. Although all samples appear to exhibit similar decrement values above 700 Hz, it should be noted that in terms of loss angle these small differences represent changes of 10° to 20°. Changes of this magnitude would result in a much larger viscous component of stress-strain phase lag.

A.4.1 Microstructural Analysis

The results of microstructural analysis are not surprising given that the four samples were machined from the same raw stem. It can be noted however that the variation in vascular bundle orientation is indicative of significant spatial variability within the single stem and may be of importance for ensuring reed tip uniformity. The results are illustrated in Figure 9.

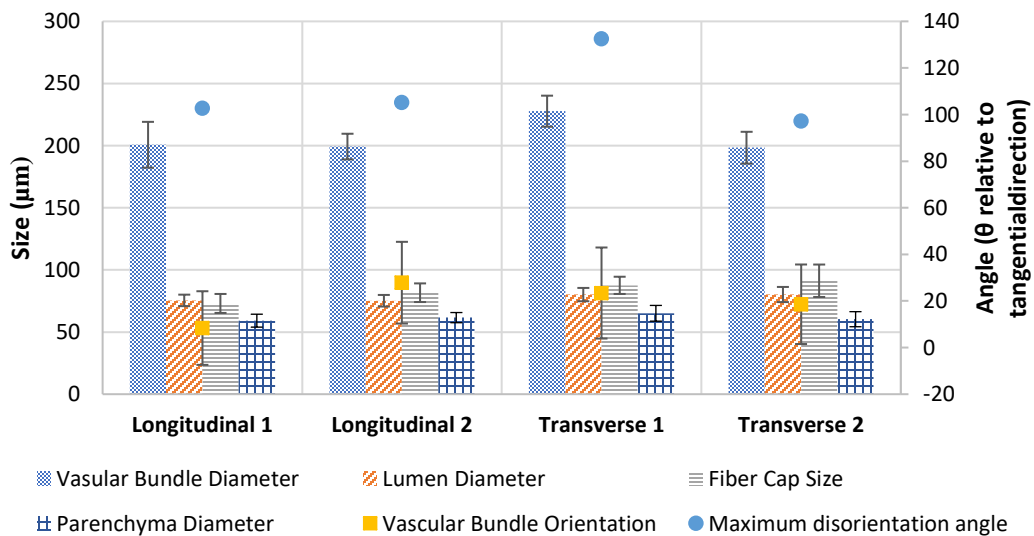


Figure 9: Microstructural results for each of the samples as measured using optical microscopy. Error bars indicate standard deviation.

The results shown in Figure 9 compare favorably with previously obtained results for reed cross-sections [9, 10]. The influence of these microstructural features on decrement values was investigated using regression analysis (with 95% confidence). For Trial 5 decrement values (the final test of each sample), a statistically significant result was obtained for vascular bundle diameter effects on internal friction at 700 Hz. Here a positive linear trend is observed where increasing vascular bundle angle (with respect to parallel alignment with the tangential direction) corresponds to increasing decrement values (F-test, $p = 0.0435$). For Trial 1 a similar observation is made for the relationship between parenchyma matrix diameter and internal friction. In this case, at 1000 Hz a positive linear trend indicates that increasing parenchyma diameter increases the logarithmic decrement (F-test, $p = 0.0259$). Increasing the size of the parenchyma cells would increase the hemicellulose and amorphous cellulose weight fractions within the sample and thus increase viscoelasticity and the effects of loss mechanisms, making this an expected result.

The power of this analysis will be improved in future work by increasing the number of samples within the data set.

Inspection of the micrographs confirms the existence of cracks within the material (provided in Figure 10), both along the fiber-matrix interface and within the fiber cap. The consequences of this with regards to internal friction have been mentioned for the case of $f = 800$ Hz.

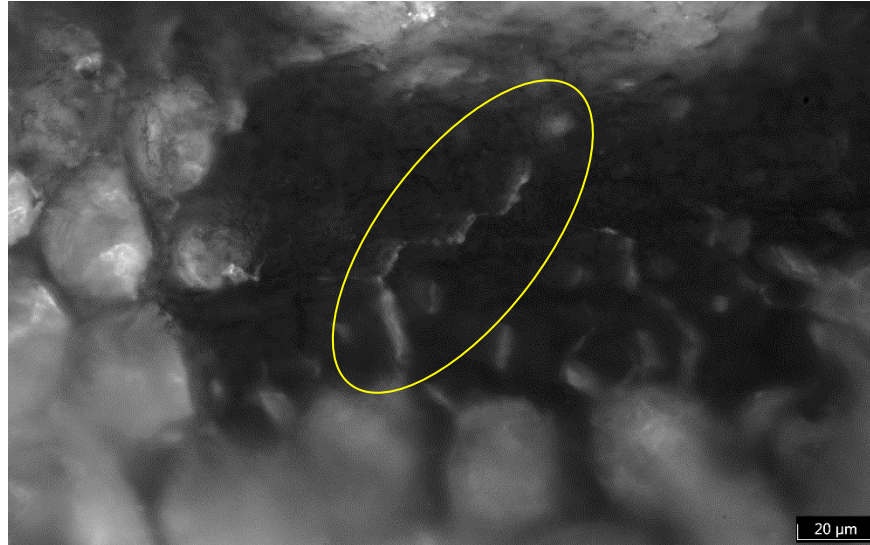


Figure 10: Micrographs of sample L1 depicting cracks within the fiber cap (top) and at the interface between the fiber cap and the parenchyma matrix (bottom).

For the case of sample L1 the nucleation of these cracks is likely the result of local differences in swelling behavior. Bamboo, a similar material to ADL, expands most significantly in the longitudinal direction [75] and for the case of sample L1 this could explain the large relative increases in internal friction above 700 Hz. These relative differences in internal friction are shown in Figure 11, where differences between Trial 1 and Trial 5 decrement values for each sample are presented as fractions of the initial value. These increases in decrement values could be attributed

to the nucleation and growth of the noted cracks in between the fiber cap and matrix. This would result in a larger phase lag between these two microstructural entities for a propagating stress wave due to more viscous dissipation. While these cracks are small, the effect would contribute to high frequency internal friction values more significantly than low frequency values. This is because cracks along the fiber-matrix interface would result in large local elasticity changes (when the material is thought of as a phase weight-averaged composite) and the ratio of propagation wavelength to crack length decreases (further increasing dissipation). Results are also given for sample L2 in Figure 12. Here large cracks within the fiber cap and significant parenchyma matrix deformation are observed. This is considered an expected result for a mechanically cycled sample.

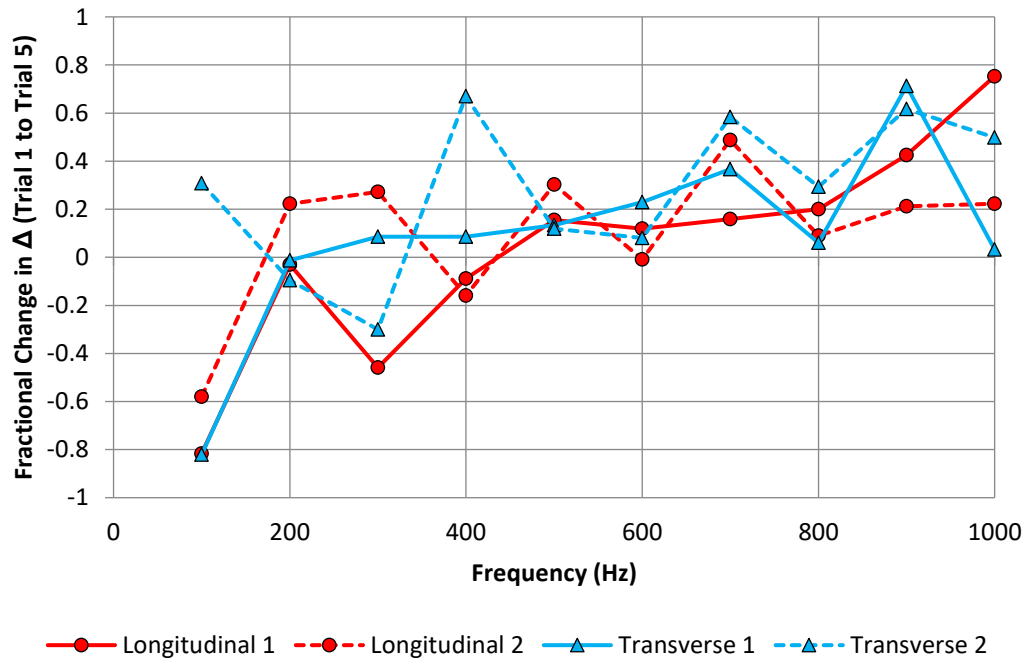


Figure 11: Change in decrement values from Trial 1 to Trial 5 for all samples. Negative values indicate a decrease in internal friction relative to the initial value, while positive values indicate an increase.

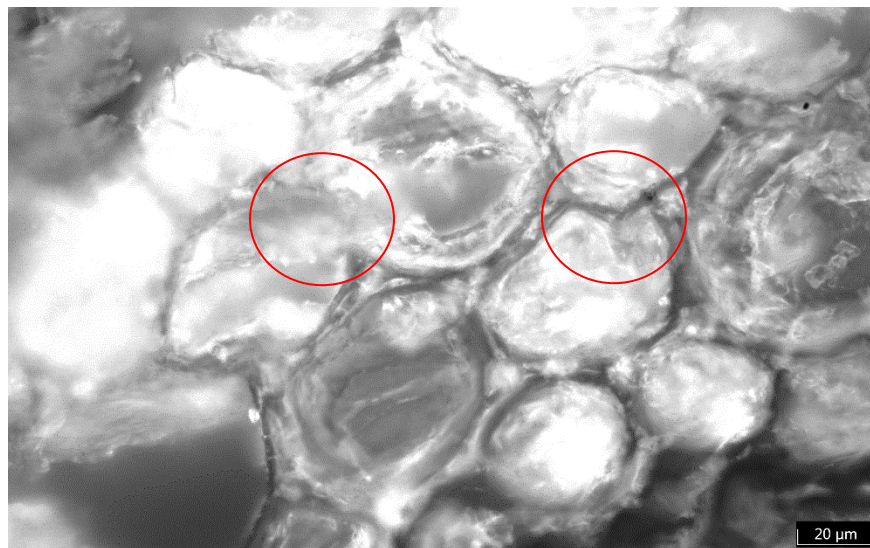
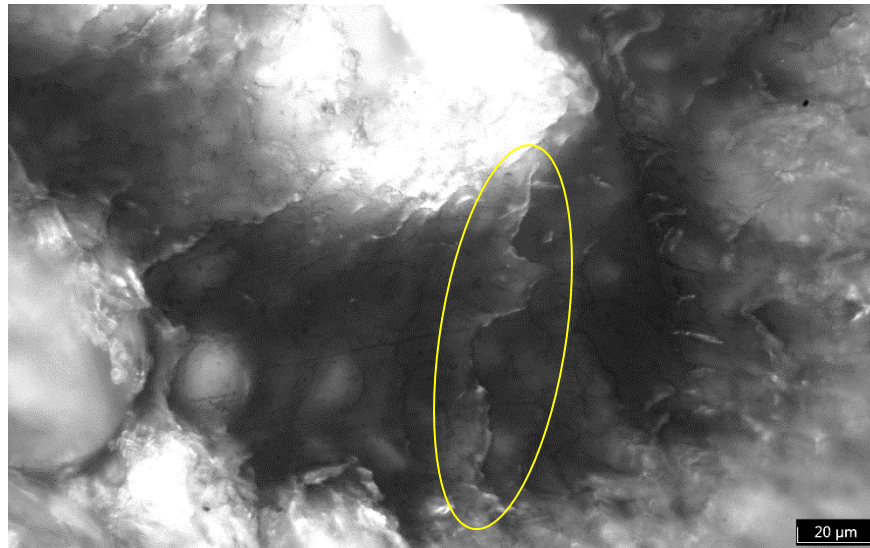


Figure 12: Micrographs of sample L2 depicting cracks within the fiber cap (top) and deformation and cell wall breakage within the parenchyma matrix (bottom).

The large increases in decrement values at 1000 Hz for the T2 sample may be explained by the complete separation of the fiber structure from the remaining vascular bundle (Figure 13). If the material is imagined as a either a Voigt (equal strain) or Reuss (equal stress) composite, the propagation of waves through the sample involves each of the phases present. In the case of T2, the resulting load sharing would be shifted mainly to the surrounding parenchyma matrix, increasing viscous dissipation as the out-of-phase response of the matrix and fiber structure increases.

Crystallinity was measured using the results of XRD measurements through the peak deconvolution method [81]. The main peak observed is for the (002) I_β-cellulose reflection, as shown in Figure 14. Percent crystallinity was 21.36 % for L1 and 26.06% for T1 initially. This is an expected result as the samples were cut from the same raw stem.

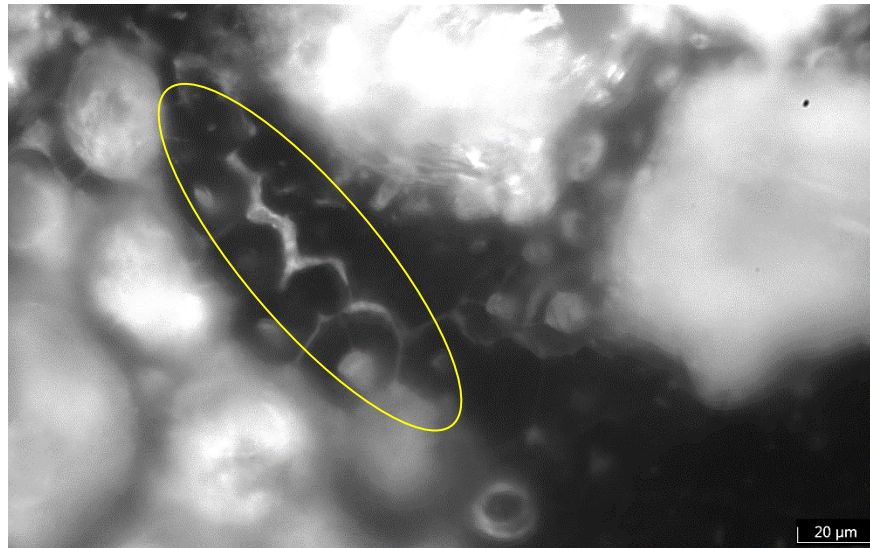


Figure 13: Complete separation of fiber cap from the vascular bundle in sample T2.

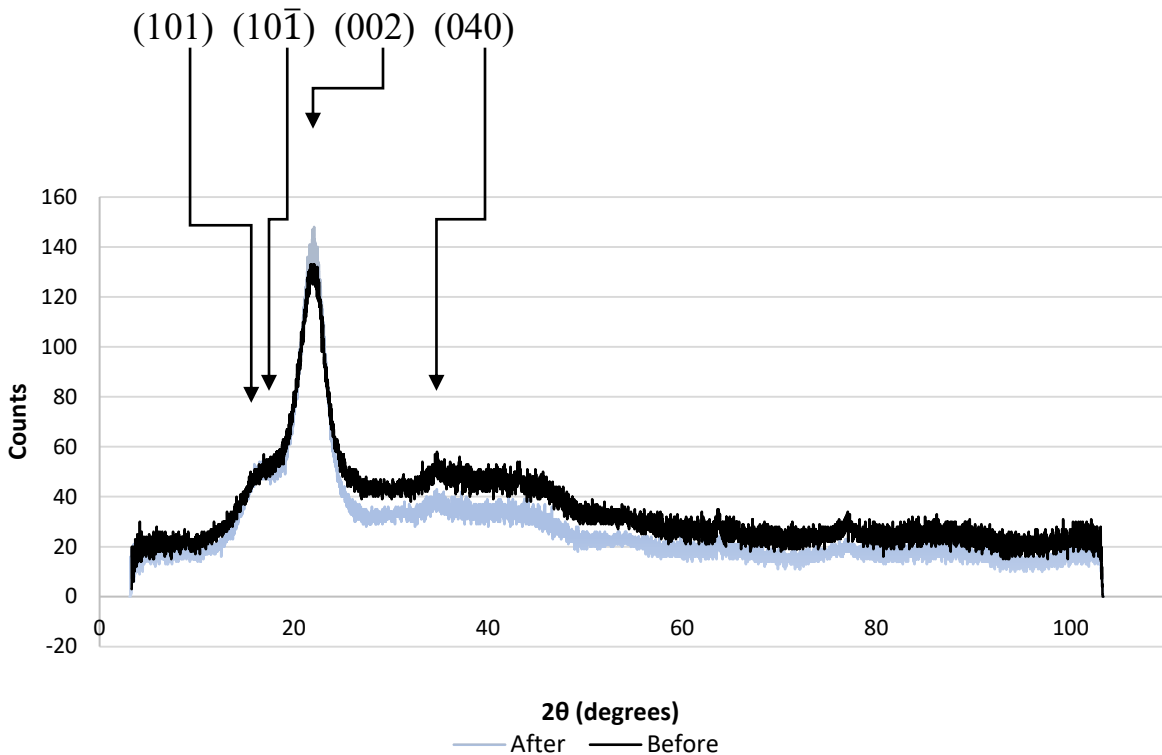


Figure 14: Before testing and after testing (both iterations) XRD spectra for sample L1. Indices of peak reflections are also provided. The lower spectrum represents the results after moisture cycling (measured after trial 5).

It is expected that normal usage of reeds (and ADL material) would contribute to changes in crystallinity due to the lower pH of saliva versus deionized water. Changes in crystallinity over time are currently being examined for real in-use reeds using the XRD technique.

Recent work on viscoelasticity in bamboo [67] indicates that at frequencies above ~10Hz the viscoelastic contributions of the solid fibers and parenchyma matrix begin to equally control the dynamic behavior of the material. This manifests itself in the form of constantly increasing loss modulus (E'') values with increasing frequency. The loss modulus is related to the logarithmic decrement and represents viscous loss in the material. This could help explain the increase of internal friction (when comparing the initial to final values, as in Figure 11) observed in the present study above 700 Hz where the contributions of the parenchyma matrix and solid fibers (specifically their amorphous components) dominate the dynamic behavior. Previous research [128] on wood used in violins has indicated that specimens with larger crystalline cellulose volume fractions result in reduced loss tangent values (where the loss tangent, $\tan\delta$ is related to the logarithmic decrement by $\tan\delta = \Delta/\pi$). For this reason, ADL specimens from different stems are currently being evaluated

with XRD to evaluate the importance of sample crystallinity on low frequency (< 300 Hz) internal friction.

A.5 Summary and Future Work

The preliminary work in this study has shown that internal friction of ADL (as measured by the logarithmic decrement) exhibits a sensitivity to frequencies in the range of 100 to 1000 Hz. Additionally, both mechanically loading (fatigue) and moisture cycling of samples results in changes to these measurements that are not fully recovered. The variability in sample behavior for specimens cut from a single stem internode lends credence to the musical knowledge of inter-reed variability within a package (for this case inter-stem variability has been controlled). It was also discovered that mechanically fatiguing samples and moisture cycling them contributes to internal friction results in similar ways for high frequencies (increases the logarithmic decrement) and in different ways for low frequencies (more inter-sample variation, dependent on material orientation). These two test cases are common for in-use reeds and may explain why musicians do not find reeds to behave similarly (due to different loading conditions associated with embouchure pressure).

For samples at high frequency (> 700 Hz), increasing internal friction with further trials was attributed to the development of cracks within the microstructure of each sample. For the moisture cycled samples, these cracks are a result of highly anisotropic swelling/shrinkage within the solid fiber bundles. Cracks in the mechanically loaded samples were most prevalent in the transverse sample, which was an expected result given the low E and E' moduli value in the tangential direction relative to the longitudinal direction. Analysis of microstructural features indicates subtle differences between samples, mainly vascular bundle orientation, fiber cap size and parenchyma cell diameter. At 700Hz, a statistically significant result was found via regression analysis of vascular bundle orientation versus internal friction where increasing orientation angle corresponded to increasing decrement values. At 1000Hz, a similar positive relationship between parenchyma cell diameter and internal friction was observed. Both of these results suggest that reeds comprised of high angle vascular bundles and large parenchyma cells would exhibit increased internal losses at 700 Hz and 1000 Hz.

Future work will include further analysis of XRD measurements, including estimate of cellulose crystallite size for comparison with literature values for wood and bamboo. Analysis of XRD measurements between samples will be performed and could elucidate the origins of initial internal friction variability, specifically at frequencies below 300 Hz. These results are not discussed here as further testing of a greater number of samples is required. Additionally, consideration of moisture content variation of in-use reeds (during and between playing) needs to be considered in order to validate and/or understand the limitations of using high (>90%) RH values for simulated degradation. This will also enable more long-term studies of crystallinity change with moisture cycling. Measurements of internal friction using a shaker rig will also be completed to compare free-free results with fixed-free. In this case internal friction will be measured by extracting the Lissajous curve between stress and strain ($\tan\delta$) and comparing new results with the current data. Decrement values will also be measured for longitudinal modes in addition to flexural bending (as was the case in this portion of the study). Similar results obtained for bamboo have indicated significant anisotropy in internal friction measurements [75]. Future XRD measurements will be statistically tested with internal friction values to evaluate potential correlation. Comparison with previous work on bamboo [75] will also be made by testing samples at frequencies < 100 Hz.

Measurements of loss angle will also be made through fatigue testing (0.1 Hz) of specimens with strain gauges (phase lag between stress and strain). Through a conversion of loss angle values to logarithmic decrement values, comparison will be made with the current results. This will also facilitate comparisons of samples between stems as only intra-stem variability was observed presently. Finally, nanoindentation tests on fiber bundles and parenchyma cell walls will be completed in order to capture potential changes in reduced modulus with moisture cycling and variations through thickness of the stem wall.

A.6 Acknowledgments

The authors wish to acknowledge Dr. Francois Barthelat of the Laboratory for Advanced Materials and Bioinspiration at McGill University for helpful discussions and equipment access. The same thanks are also extended to Dr. Larry Lessard of the Advanced Composite Materials Lab at McGill University for microscopy access. Discussions with Dr. Shang in the department for Materials and Mining Engineering at McGill University also helped in analyzing XRD measurements.